Ph.D. degree in Molecular Medicine (curriculum in Computational Biology)

EUROPEAN SCHOOL OF MOLECULAR MEDICINE (SEMM),
Univeristy of Milano and University of Naples

A fistful of molecules: cells escape an operational mitotic checkpoint through a stochastic process

Candidate:
Paolo Bonaiuti
IFOM
Matricola R10720

Supervisor:
Dr. Andrea Ciliberto
IFOM

Anno Accademico 2017-2018

Contents

List of abbreviations

SAC	Spindle Assembly Checkpoint
MCC	Mitotic Checkpoint Complex
APC/C	Anaphase-Promoting Complex/Cyclosome
FCS	Fluorescence Correlation Spectroscopy
FCCS	Fluorescence Cross-Correlation Spectroscopy
ODE	ordinary differential equation
n	number of observations
N	number of biological independent replicates

List of Figures

List of Tables

Marco Polo describes a bridge, stone by stone.

'But which is the stone that supports the bridge?' Kublai Khan asks.

'The bridge is not supported by one stone or another,' Marco answers, 'but by the line of the arch that they form.'

Kublai Khan remains silent, reflecting. Then he adds: 'Why do you speak to me of the stones? It is only the arch that matters to me.'

Polo answers: 'Without stones there is no arch.'

Italo Calvino, Invisible cities

Abstract

The cell-cycle culminates with the segregation of sister chromatids in the two newborn daughter cells. Correct chromosome segregation is a fundamental step in ensuring the transmission of unaltered genetic material. The molecular machinery that physically carries out chromosome segregation is the mitotic spindle, whose components, microtubules, attach to kinetochores, multiprotein structures situated at the centromeric region of each chromosome. During prometaphase, microtubules bind kinetochores so that each pair of sister chromatids is pulled towards the two poles of the cell. Anaphase starts, thanks to the cleavage of cohesin rings that hold sister chromatids together, when the correct bipolar attachment is achieved. Chromosomes, freed from cohesin, migrate evenly to the two daughter cells, both inheriting the same genetic material.

The presence of unattached kinetochore at anaphase onset is dangerous, since it may lead to unbalanced ploidy of daughter cells, with severe consequences for their survival. For this reason, attachment of kinetochores is overseen by a control mechanism, the Spindle Assembly Checkpoint, or SAC. The SAC halts anaphase progression until all kinetochores are attached to microtubules. Spindle poisons activate the SAC and halt cell progression for several hours. However, cells eventually adapt to the SAC and enter anaphase, regardless of the presence of the drug. Adaptation is extremely variable in time, and the origin of this large variability is unknown. Moreover, whether cells adapt to an active SAC or if they enter anaphase as a consequence of SAC silencing, is an open question.

With this work, we demonstrate that budding yeast cells adapt to an active SAC. This statement is supported by single-cell experiments on cells carrying both a marker for SAC activation and for anaphase onset. Based on these data, we built a quantitative model of the SAC network, to investigate the origin of variabiliy in adaptation times. The parameters of this model were directly measured, if not available in literature. In particular, we found that the complex that promotes anaphase onset, APC/C, is present in very low amounts, giving a prominent role in adaptation to the inherent stochasticity of chemical interactions. In our model, random fluctuations in the number of molecules of the active form of APC/C drive the onset of anaphase in mitotically-arrested cells. We then verified that, as predicted by the model, increasing the synthesis of Cdc20, a protein required for the SAC and coactivator of APC/C, increases adaptation propensity, but does not change its stochastic nature. Our conclusions support the idea that adaptation is a stochastic process, and that adaptation propensity is the same for all cells.

Chapter 1

Introduction

> Cell reproduction occurs by an elaborate series of events called the cell cycle, whereby chromosomes and other components are duplicated and then distributed into two daughter cells. A complex network of regulatory proteins governs progression through the steps of the cell cycle. Morgan [2007]

As suggested by this quote by David Morgan, the goal of what is known as cell cycle is cell reproduction, which is essential for all living beings. For unicellular organisms, this event generates an entire new organism. The faithful transmission of genetic information lies at the heart of cell reproduction. For this reason, the two main events in the cell cycle are, as presented in the quote, chromosome duplication and their segregation. Each of the two events occurs in a different phase of the cell cycle: chromosome duplication occurs in *interphase*, while chromosome segregation in *M phase*. The result of a complete cell cycle is the birth of two cells, which carry the same genetic material of the mother cell.

Interphase is further subdivided into G1, S and G2 phases. During G1 phase (or Gap 1), the cell grows in size, and monitors the environment before starting a new round of cell division. If conditions are not appropriate, the cell enters a resting state, called G0. If conditions are favorable, the cell triggers the irreversible cascade of events that will lead to cell division. The first key step of this cascade happens during S phase (or Synthesis), when the chromosomes are duplicated. At the end of this phase, the pairs of identical chromosomes, called sister chromatids, are tightly linked together. After S phase, there is an additional gap phase, G2, which monitors the safe progression in the next cell-cycle stage. Next, the cell segregates its chromosomes during *mitosis*, and physically divides in two during *cytokinesis*. These are the two phases comprising M phase. In the next section, we will address mitosis, the phase of the cell cycle most relevant for this study.

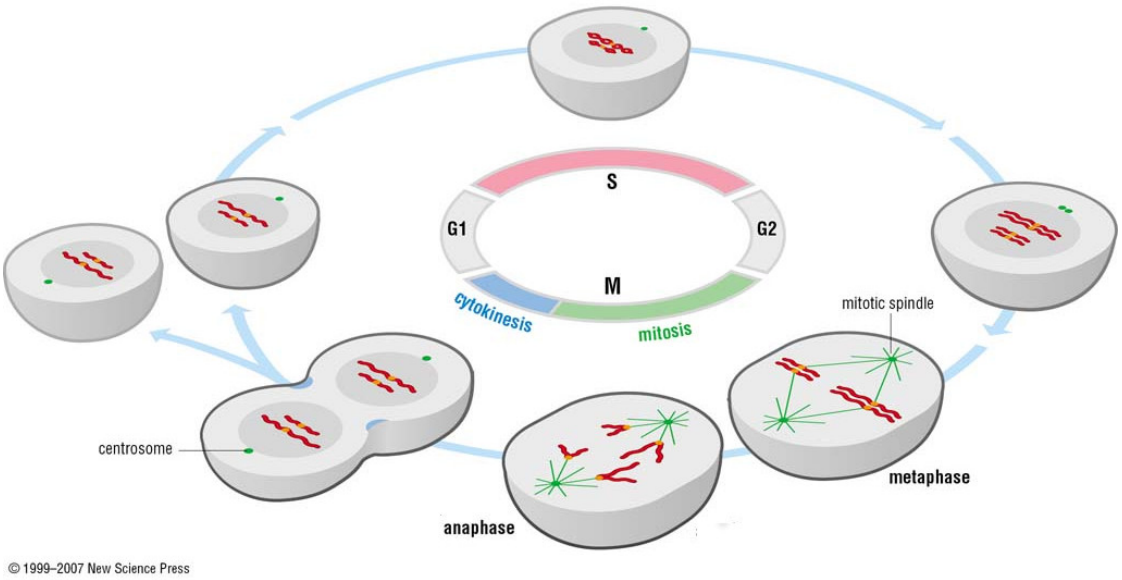

Figure 1.1: Eukaryotic cell cycle.
Depicted in red are the chromosomes, in green the mitotic spindle and the microtubule organizing centers (centrosomes in vertebrates, spindle pole bodies in yeasts). Yellow dots on chromosomes are the kinetochores.
Image taken from Morgan [2007].

1.1 Mitosis

During mitosis, sister chromatids are segregated into two daughter cells. Chromosome segregation is operated by the mitotic spindle, which is the molecular machinery that physically attaches to chromosomes and pulls them to the opposite poles of the cell at the end of mitosis. The mitotic spindle is formed by microtubules, tubuline polymers, and is nucleated from microtubule-organizing centers (or MTOCs, called spindle pole bodies in yeasts, and centrosomes in animal cells).

At the beginning of mitosis, sister chromatids are held together by cohesin Michaelis et al. [1997], a ring-shaped protein complex Gruber et al. [2003]. During *prophase*, the first stage of mitosis, sister chromatids undergo condensation, which facilitates their movement. At the same time, the MTOCs migrate towards the opposite poles of the cell and start nucleating the mitotic spindle. *Prometaphase* starts with the breakdown of the nuclear envelope, in animal cells but not in yeast, and continues until all sister chromatids are attached to microtubules, when *metaphase* starts. The opposite forces pulling sister chromatids align them on the metaphase plate, which is localized at the center of the spindle.

The onset of *anaphase* is marked by the cleavage of cohesin rings, that allows the separation of sister chromatids Michaelis et al. [1997]. The mitotic spindle elongates and pulls the separated chromatids towards the opposite MTOCs, that move outward. *Telophase* and *cytokinesis* are the final steps of cell division, when chromatids migration stops, chromosomes decondense, and the cell is pinched in two. In animal cells, two nuclear envelopes reform around the separated genetic material.

The regulation of the whole mitotic process is controlled by the Cyclin-dependent kinase 1 (Cdk1,

or Cdc28 in budding yeast), that by phosphorylating its substrates drives the major mitotic events: chromosome condensation, spindle formation and elongation, separation of sister chromatids Morgan [2007]. The regulatory subunits of Cdk1 are the cyclins. In budding yeast there are four mitotic cyclins, Clb1-4, with partially overlapping functions Bloom and Cross [2007]. Clb2 is considered the main mitotic cyclin, since it accounts for roughly 70% of the mitotic activity of Cdk1 Surana et al. [1991]. Its levels rise at the beginning of mitosis, and they start diminishing at anaphase onset. Clb2 degradation is completed by the end of mitosis Sullivan and Morgan [2007]. Since the activity of Cdk1 depends on obligatory association with a cyclin, Cdk1 activity is related to Clb2 levels. However, binding to cyclins is a necessary condition, but it is not sufficient for Cdk1 activation: other post-translational modifications, often organized in feedback loops, are needed Morgan [2007]. Cdk1 enzymatic activity peaks at metaphase and declines to minimal values before mitotic exit Sullivan and Morgan [2007]. The decline in kinase activity is not sufficient for mitotic exit: the dephosphorylation of Cdk1 substrates is also required. In budding yeast, the main responsible for the dephosphorylation of Cdk1 substrates is Cdc14 Visintin et al. [1998], which is released from the nucleolus, and thus activated, in early anaphase Visintin et al. [1999].

We now focus on metaphase-to-anaphase transition in budding yeast, the cell-cylce stage and the organism investigated in this study.

1.1.1 Metaphase-to-anaphase transition

During the final stages of S phase and prometaphase, microtubules emanating from the two MTOCs start capturing chromosomes Tanaka et al. [2005]. The binding of microtubules to chromosomes is mediated by multiproteins structures called *kinetochores*, located at the centromeric region of each chromosome Santaguida and Musacchio [2009]. These structures provide not only the docking site for microtubule attachment (one per kinetochore in budding yeast), but also the tension-sensing machinery that can halt the progression into anaphase until complete biorientation is provided (see Section 1.1.2). Due to the stochastic nature of the attachment process, improper microtubule-kinetochore attachments can occur before the correct biorientation is achieved. The whole process is highly dynamic, and involves elongation/shrinkage of the microtubule fibers Huang and Huffaker [2006] as well as attachment/detachment from kinetochores of incorrectly attached microtubules Tanaka et al. [2002]. As soon as all the sister chromatids pairs are correctly bioriented, the forces pulling them towards the opposite MTOCs align them on the metaphase plate, and anaphase onset follows.

For anaphase to take place, two proteins need to be degraded: securin (Pds1 in yeast) and Clb2. Pds1, when degraded, releases its binding partner separase, whose protease activity induces cohesin cleavage Cohen-Fix and Koshland [1999]. Pds1 is thus the main inhibitor of anaphase, since its degradation triggers the cascade of event that allows sister chromatids separation. At anaphase onset, also Clb2 starts being degraded. Both Pds1 and Clb2 are substrates of a complex known as the

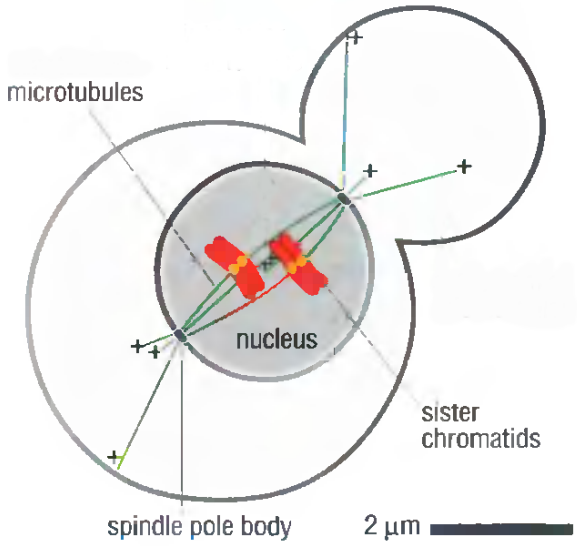

Figure 1.2: Mitotic spindle
Formation of mitotic spindle in budding yeast, nucleated from the two opposite spindle pole bodies. Image adapted from Morgan [2007].

Anaphase Promoting Complex, or Cyclosome (APC/C), which induces proteasomal degradation of specific substrates by polyubiquitination Lim et al. [1998].

APC/C structure and activation

APC/C is a highly conserved E3 ubiquitin ligase composed, in different organisms, by at least 13 subunits (see Table 1.1). It can be subdivided into three subdomains with different functions: a catalytic core, a structural platform, and a structure called "arc lamp", composed by a sandwich of subunits containing multiple 34-residues tetratricopeptide (TPR) repeats Primorac and Musacchio [2013]. The catalytic core is composed by $APC2$ and $APC11$. The structural platform is composed by three large subunits, $APC1$, $APC4$ and $APC5$. The "arc lamp" is composed by several subunits, among which Cdc27, Cdc16 and Cdc23. These three subunits, highly conserved, form symmetric homodimers and are thus present in two copies in APC/C Zhang et al. [2010]. Sandwiched between the C-terminal region of Cdc23 and $APC1$, $APC4$ and $APC5$, lies Mnd2. This is a non-essential APC/C subunit, responsible for the mitotic turnover of the APC/C coactivator Cdc20 Foster and Morgan [2012], Mansfeld et al. [2011], Uzunova et al. [2012], Alfieri et al. [2016]. The two mitotic coactivators of APC/C, Cdc20 and Cdh1, dock to APC/C at the same binding site Primorac and Musacchio [2013], and are thus mutually exclusive. The two proteins are structurally related, and share three important motifs involved in the interaction with APC/C: the IR motif at the C-terminus, and the C-box and KILR motifs at the N-terminus.

APC/C activation at the metaphase-to-anaphase transition depends on its binding with Cdc20. Indeed, cells carrying temperature-sensitive *cdc20-1* mutation die at the restrictive temperature during a metaphase arrest Lim et al. [1998]. APC/C^{Cdc20} targets both Pds1 and Clb2, albeit APC/C^{Cdc20} does not completely degrade Clb2 Yeong et al. [2000]. The completion of Clb2 degrada-

Vertebrates	*S. Cerevisiae*
$APC1$	$APC1$
$APC2$	$APC2$
$APC3$	$CDC27$
$APC4$	$APC4$
$APC5$	$APC5$
$APC6$	$CDC16$
$APC7$	not present
$APC8$	$CDC23$
$APC9$	$APC9$
$APC10$	$DOC1$
$APC11$	$APC11$
$CDC26$	$CDC26$
$APC13$	$SWM1$
$APC15$	$MND2$
$APC16$	Unknown

Table 1.1: Composition of APC/C in vertebrates and budding yeast
Table adapted from Primorac and Musacchio [2013].

tion is operated in late anaphase by APC/C bound to its coactivator Cdh1, that substitutes Cdc20. Cdh1 is one of the common substrates of Cdk1 and Cdc14, and is activated by Cdc14 via dephosphorylation. Cdk1 and Cdh1 are mutual antagonists, since Cdk1 inactivates Cdh1 by phosphorylating it Zachariae et al. [1998], and Cdh1 inactivates Cdk1 by degrading its binding partner Clb2 Visintin et al. [1998]. Cdh1, as opposed to Cdc20, is not essential for cell viability, since Clb2 is degraded by APC/C^{Cdc20} to levels compatible with mitotic exit Wäsch and Cross [2002].

Regulation of APC/C^{Cdc20} activity and Cdc20 protein levels

APC/C^{Cdc20} is regulated by different mechanisms, including the regulation of Cdc20 levels. In particular, while APC/C is present throughout the whole cell cycle, Cdc20 is not. Cdc20 is virtually absent from mitotic exit until late S-phase, when its synthesis is triggered and sustained until anaphase onset Pan and Chen [2004], Robbins and Cross [2010], Prinz et al. [1998]. Cdc20 synthesis partially depends on the transcriptional inhibitor Yox1, which is inhibited by Cdk1 during mitosis Liang et al. [2012]. By silencing Yox1, Cdk1 favours Cdc20 synthesis, and in turns APC/C activation. Cdk1 activity is necessary to sustain Cdc20 production, since Cdk1 inhibition causes a drop in Cdc20 mRNA and protein levels that arrests cells in metaphase Liang et al. [2012], Vernieri et al. [2013]. s Cdk1 facilitates APC/C activation also by increasing the binding affinity of APC/C with Cdc20 by phosphorylating three APC/C subunits, Cdc16, Cdc23 and Cdc27. As opposed to transcriptional regulation, this mechanism is not essential: cells carrying non-phosphorylatable forms of the TPR subunits Cdc16, Cdc23 and Cdc27 are viable, albeit mildly delayed in the cell cycle Rudner and Murray [2000]. Viability of non-phosphorylatable APC/C-mutant is likely due to residual binding affinity, lower than wild-type but sufficient to drive an unperturbed metaphase-to-anaphase transition.

Cdc20 synthesis is balanced by fast degradation. Both asynchronous and prometaphase-arrested cells show a Cdc20 half-life of $\sim$ 10 minutes Pan and Chen [2004], Foe et al. [2011], Foster and

Morgan [2012]. Cdc20 degradation solely depends on APC/C Foe et al. [2011], Nilsson et al. [2008], and thus occurs via ubiquitination. During prometaphase arrest, Cdc20 ubiquitination occurs mainly through an *in cis* mechanism Foe et al. [2011]. This means that APC/C ubiquitinates and targets to degradation a Cdc20 molecule bound to it. Cdc20 degradation relies on the same IR and C-box domains used to bind and degrade Pds1 and Clb2 Foe et al. [2011]. The fast synthesis and degradation of Cdc20 imply fast dynamics for reaching the steady-state levels of the protein (see Section 1.2.1).

The *in cis* mechanism of degradation persists as long as APC/C^{Cdc20} is present. In late anaphase, when Cdh1 substitutes Cdc20 in activating APC/C, Cdc20 degradation is driven by an *in trans* mechanism: Cdc20 is recognized by APC/C^{Cdh1} as a substrate, ubiquitinated and targeted for degradation. As for other APC/C^{Cdh1} substrates, Cdc20 binding to APC/C^{Cdh1} is mediated by D-boxes. During G1 phase, when Cdc20 synthesis is absent, APC/C^{Cdh1} completes Cdc20 degradation Huang et al. [2001], Foe et al. [2011].

As can be noticed from this brief description, Cdk1, APC/C and Cdh1 regulations are interdependent: Cdk1 induces APC/C activation by sustaning Cdc20 synthesis and APC/C-Cdc20 binding, while APC/C^{Cdc20} reduces Cdk1 activity by inducing the degradation of the Cdk1 regulatory partner Clb2. This is a negative-feedback loop. In contrast, Cdk1 and Cdh1 are in a positive-feedback loop, since they inhibit each other: Cdk1-dependent phosphorylation inhibits Cdh1, while unphosphorylated Cdh1, bound to APC/C, inhibits Cdk1 by inducing Clb2 degradation. The transition of Cdk1 from a 'high activity' state to a 'low activity' state marks the difference between metaphase and anaphase. Completion of Cdk1 inactivation is necessary for regular cell-cycle progression Gérard et al. [2015].

1.1.2 The Spindle-Assembly Checkpoint

The metaphase-to-anaphase transition is a delicate step in the cell cycle. If securin cleavage occurs before chromosome biorientation is completed, DNA segregation can lead to uneven partitioning of genetic material, giving rise to daughter cells carrying more or less chromosomes than euploid cells. This condition, typical of cancer cells, is called *aneuploidy*, and it is largely detrimental, inducing severe unbalancing in the transcriptome and proteome of the cell Pavelka and Rancati [2013], Tang and Amon [2013].

To avoid this fate, eukaryotic cells developed a highly conserved mechanism, called the *spindle-assembly checkpoint* (SAC). In the presence of uncorrect attachment, the SAC is activated by a signaling cascade that starts from unattached kinetochores and leads to the formation of a complex that inhibits APC/C. In this way, the SAC halts anaphase progression until correct kinetochore-to-microtubule attachment. Drugs that impair microtubules formation, such as nocodazole, benomyl, or vinka alkaloids, inhibit kinetochore-to-microtubule attachment and thus activate the SAC. In the experiments presented in Sections 3.1 and 3.3, cells are arrested using nocodazole.

While in mammalian cells the SAC is activated at every cell cycle, in budding yeast it is not. However, budding yeast SAC-defective cells, such as *mad1*Δ, *mad2*Δ or *mad3*Δ, in unperturbed condition exibit higher chromosome missegregation rates than wild-type cells, albeit still very low ($\sim 1\%$ versus $\sim 0.01\%$) Warren et al. [2002]. Moreover, disabling the SAC by *MAD1* or *MAD2* deletion anticipates the APC/C^{Cdc20}-dependent degradation of the S-phase cyclin Clb5 in unperturbed budding yeast cells Lu et al. [2014]. These finding suggest a role for the SAC also in unperturbed budding yeast cell-cycle.

SAC-signaling cascade

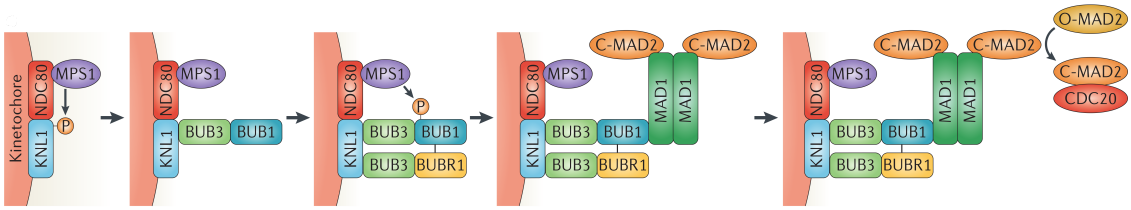

Figure 1.3: SAC signalling at unattached kinetochore
The SAC signalling pathway from unattached kinetochore in higher eukaryotes. The budding yeast homolog of BubR1, Mad3, creates a stable complex with Bub3 but this complex does not localize at kinetochore.
Image taken from London and Biggins [2014a].

One of the most upstream event in the SAC-signaling cascade is the phosphorylation of Ndc80, a member of the outer kinetochore, operated by the protein kinase Aurora B, which induces the localization of Mps1 Nijenhuis et al. [2013], Santaguida et al. [2011], Kemmler et al. [2009], Heinrich et al. [2012]. Mps1 plays a crucial role in SAC activation and, accordingly, its overexpression arrests cells by ectopically activating the SAC-signalling cascade Hardwick et al. [1996]. Mps1 phosphorylates Knl1/Spc105, another member of the outer kinetochore, on different repeats of the MELT (Met-Glu-Leu-Thr) motif London et al. [2012]. Phosphorylated MELTs are recognized by Bub3, that localizes at kinetochores in complex with Bub1 and, in higher eukaryotes, in complex with BubR1 Primorac et al. [2013], Shepperd et al. [2012], Kiyomitsu et al. [2011]. In contrast, the budding-yeast homolog of BubR1, Mad3, does not localize at unattached kinetochore Gillett et al. [2004], even though it forms a stable complex with Bub3 Hardwick et al. [2000]. The formation of the complexes Bub3:Bub1 and Bub3:Mad3 does not depend on SAC signaling Hardwick et al. [2000], Brady and Hardwick [2000].

Next, Mps1 phosphorylates Bub1, inducing the recruitment of Mad1 London and Biggins [2014b], Faesen et al. [2017]. Mad1, bound to Mad2, forms a heterotetrameric complex whose presence at kinetochores is sufficient to induce a SAC arrest Maldonado and Kapoor [2011]. For this reason, in the present work we use Mad2 localization at kinetochores as a readout of active SAC signaling (Sections 3.1 and 3.3). As a consequence of its localization, Mad1:Mad2 complex induces the conversion of cytosolic Mad2 from an open (O-Mad2) to a closed conformation (C-Mad2) in what has been named the "template model" De Antoni et al. [2005], Luo and Yu [2008], Mapelli et al. [2007]. The

Mad2 conformational change facilitates its binding to Cdc20 De Antoni et al. [2005], Mapelli et al. [2007], giving rise to Mad2:Cdc20 which is the seed for the formation of the *mitotic checkpoint complex* (MCC), the diffusible complex that inhibits APC/C (see next section).

In this view, kinetochores act as a catalytic platform to allow Mad2 conformational change and thus facilitate Mad2-Cdc20 binding. Interestingly, it is possible to form Mad2:Cdc20 independently of the kinetochores by compensating the low-affinity of O-Mad2 for Cdc20 with high levels of Mad2 itself. Indeed, Mad2 overexpression induces a SAC-arrest, independently of kinetochores Mariani et al. [2012]. In the experiments presented in Section 3.5, cells are arrested in mitosis using this method.

The SAC-signaling pathway can be diverted by several changes. The lack of any Mad or Bub protein results in SAC defectiveness. This mutated phenotype, in benomyl-treated cells, allowed the identification of Mads and Bubs sets of genes in the original works by the labs of Murray and Roberts Hoyt et al. [1991], Li and Murray [1991]. The same phenotype results from impairment in the localization of Mad1 or Bub3 at kinetochore, and from mutations that lock Mad2 in the open conformation De Antoni et al. [2005], Maldonado and Kapoor [2011], Primorac et al. [2013]. Not only Mad3 deletion, but also its overexpression leads to SAC-defects, albeit mild, likely by competing for Bub3 with Bub1, resulting in reduced amount of Bub1:Bub3 complex signaling at kinetochores King et al. [2007]. Also Cdc20 mutations that impair the binding with Mad2 (such as *cdc20-127*) bypass the checkpoint arrest Hwang et al. [1998].

Importantly, although the strenght of the SAC, measured as effective inhibition of APC/C or as number of signaling molecules, depends on the number of unattached kinetochores Collin et al. [2013], Aravamudhan et al. [2016], Dick and Gerlich [2013], one single unattached kinetochore can inhibit anaphase progression Rieder et al. [1995].

The mitotic checkpoint complex

The main APC/C inhibitor is the mitotic checkpoint complex, or MCC. It consists of Cdc20, Mad2, Bub3 and BubR1/Mad3 Fraschini et al. [2001], Sudakin et al. [2001], Chao et al. [2012]. The levels of Mad2, Mad3 and Bub3 do not change during a cell cycle Pan and Chen [2004], Hardwick et al. [2000], Fraschini et al. [2001], while, as we mentioned above, Cdc20 synthesis and degradation are highly cell-cycle regulated. MCC is formed by the binding of two subcomplexes: Cdc20:Mad2 and Bub3:BubR1/Mad3 Kaisari et al. [2016]. As we mentioned, Cdc20:Mad2 binding is SAC-dependent, while Bub3:BubR1/Mad3 is not. To inhibit APC/C, MCC binds the active APC/C^{Cdc20}, resulting in an APC/C^{inhib} complex comprising two molecules of Cdc20 Izawa and Pines [2015], Alfieri et al. [2016]. APC/C^{inhib} cannot target its substrates for degradation, which impedes anaphase onset. APC/C^{inhib} disassembly induces the disassembly of MCC Alfieri et al. [2016].

1.1.3 Prolonged mitotic arrest and adaptation

In physiological mitosis, chromosome biorentation is achieved in minutes, resulting in APC/C activation, which is followed by the degradation of securin/Pds1 and Clb2, and anaphase onset. Prolonged impairment of proper microtubule-kinetochore attachment is a rare event, usually induced by drugs that interfere with the process (e.g: nocodazole). In particular, several compounds used in cancer therapy aim at killing cancer cells by arresting their proliferation via SAC activation. However, even if the stimulus is not removed, cells eventually escape the arrest in a process named *adaptation* or *slippage*.

This phenomenon is present in both lower and higher eukaryotes, and has been investigated only in recent years. In the presence of prolonged spindle-damage, cells face two dangerous options: either they divide with improperely attached kinetochores, or they are delayed indefinitely before anaphase onset, and die during the arrest. Adaptation would thus be a sort of "last survival chance", albeit risky. On the other hand, since this condition is very unlikely to happen in nature, it is possible that cells had not faced any evolutionary pressure to face this kind of stress, and that adaptation is a side-effect of the SAC pathway that evolved to deal with milder conditions.

One common feature of adaptation is the extreme variability in the duration of the mitotic arrest. Not only different organisms or cell-lines exibit different responses to different treatments, but also genetically identical cells display a profound variability in the respons to the same stimuls Gascoigne and Taylor [2008, 2009], Rossio et al. [2010], Vernieri et al. [2013], Heinrich et al. [2013]. The source of this variability is unclear. With the present work, we aim to shed light on this theme.

Two opposed models for adaptation

The mechanism of adaptation is unclear. One hypothesis is that cells bypass an active SAC. This model, known as "slippage model", was first proposed by Brito and Rieder in 2006 Brito and Rieder [2006]. The authors explained the slow and constant degradation of Cyclin B with an incomplete inhibition of APC/C^{Cdc20} by an active SAC. When Cyclin B levels decrease, cyclins cannot sustain Cdk1 mitotic activity and cells progress into anaphase.

Another model claims that during adaptation SAC is silenced, although not satisfied. In other words, adapting cells progress into anaphase because the 'halt signal' from SAC is switched off, even if the conditions are not suitable for anaphase onset. In particular, Bub1 degradation Goto et al. [2011] or lack of Bub3-Mad1 interaction at kinetochores Rossio et al. [2010] have been proposed as upstream events triggering adaptation. However, these observation are in contrast with the presence at kinetochores of Mad2 and BubR1 observed by Brito and Rieder. Moreover, several adaptation studies in budding yeast were performed by inducing SAC-arrest independently of kinetochores, by overexpressing Mad2 Rossio et al. [2010], Vernieri et al. [2013], and here SAC-silencing cannot be an explanation for adaptation.

Feedback loops in metaphase-to-anaphase transition

Several feedback loops are involved in the anaphase transition. As shown before, in an unperturbed metaphase-to-anaphase transition, Cdk1 and APC/C are involved in a negative-feedback loop: Cdk1 induces APC/C activation by sustaining Cdc20 synthesis and its binding to APC/C, while APC/C^{Cdc20} targets for destruction Cdk1 regulatory subunit, Clb2. When instead cells are arrested by the SAC, at least three positive-feedback loops are involved. First, Mps1 triggers the SAC-response that inhibits APC/C, while APC/C induces the degradation of Mps1 Palframan et al. [2006]. Second, Cdk1 activates the SAC, which inhibits APC/C^{Cdc20}, while APC/C^{Cdc20} induces the inactivation of Cdk1 Rattani et al. [2014], D'Angiolella et al. [2003]. This feedback, if present in budding yeast, is not essential to sustain an active SAC Vernieri et al. [2013]. Third, the protein phosphatase $PP2A^{Cdc55}$ inhibits the formation of APC/C^{Cdc20} by dephosphorylating APC/C on some of the residues phosphorylated by Cdk1. APC/C^{Cdc20}, in turns, inhibits $PP2A^{Cdc55}$ by blocking the degradation of its inhibitor, separase Vernieri et al. [2013], Queralt et al. [2006]. These positive-feedback loops can be responsible for the switch-like transition to anaphase, and its irreversibility.

It is important to underline that Cdc20 is required for adaptation to occur, while Cdh1 is dispensable Vernieri et al. [2013]. For this reason, in the present work we focus on APC/C activation operated only by Cdc20.

1.1.4 Adaptation as experimental approach

In this study, adaptation is not only a research subject, as explained in the previous paragraphs, but also a tool to investigate the behavior of the SAC network in physiological conditions. Challenging cells with a non-physiological prolonged mitotic arrest, helped us in getting insights into SAC network dynamics. By studying adaptation we also aimed at better understanding the SAC.

1.2 Mathematical approaches

In the present work, we investigate the SAC protein network during a prolonged mitotic arrest, considering events downstream SAC signaling. The most upstream event we include in our analysis is the binding between Mad2 and Cdc20, triggered by the presence of unattached kinetochores. The protein network that we consider is thus a subset of the reactions described in the previous sections. Its detailed description can be found in Section 3.2.1, while a visual representation is depicted in Figure 1.4.

Graphical representations of protein networks, as the one in Figure 1.4, are useful for a intuitive summary of all the relationships included in the system, but can hardly give deeper insights into the protein dynamics. To investigate this aspect, it is convenient to translate the protein network into mathematical terms. In the following sections we present the two mathematical tools used in this

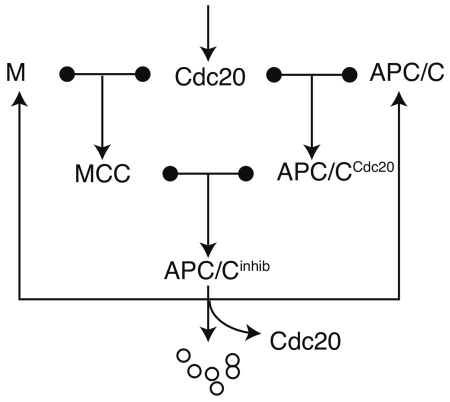

Figure 1.4: Scheme of the SAC protein network investigated in this work

work: ordinary differential equations and stochastic simulations.

1.2.1 Ordinary differential equations as a tool to describe protein network dynamics

Ordinary differential equations, or ODEs, describe the deterministic evolution of a system. In the present work, ODEs describe protein networks, having protein concentrations as temporal variables. ODEs system can be analysed in two ways: either analytically or numerically. The analytical approach is based on mathematical operations on symbolic equations, while the numerical approach is based on computer simulations, and it is often used when analytical solutions cannot be obtained.

The translation from protein networks to ODEs is made possible using what is called *law of mass action*, proposed first in 1864 by two Norwegian scientists, Cato M. Guldberg and Peter Waage Guldberg and Waage [1864]. This law describes the reaction of chemical compounds, both dynamically and at equilibrium. We are now mainly interested in its dynamical version, whose statement is often cited as "the rate of a reaction is directly proportional to the product of the masses of the reagents involved".

We now apply the law of mass action to two examples. Since the protein network we are interested in (Figure 1.4) is based on association/dissociation and synthesis/degradation reactions, the two examples are two simple 'modules', one composed by an association/dissociation reaction and one by synthesis/degradation. We translate the two modules into an ODEs system and investigate its dynamics with mathematical tools. The same approach used on these examples produces the mathematical model investigated in this study (ODEs system (3.1)), starting from the protein network (Figure 1.4).

First module: association/dissociation

The first module that we investigate is an association/dissociation reaction. A and B are substrates, neither produced nor degraded, of the complex AB. The reaction that forms the complex is reversible, and reactants and product are in solution. We can depict the reaction as:

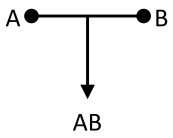

or as:

$$A + B \rightleftharpoons AB.$$

where the double arrows and the bullet points represent, in the two visualizations, the reversibility of the reaction.

The law of mass action claims that the association reaction occurs at a rate $a[A][B]$, where square brackets indicate the concentrations of the substances, and a is the association constant. The dissociation reaction occurs at a rate $d[AB]$, where d is a constant. To have both the rates with dimensions of $concentration \cdot time^{-1}$, a has dimensions of $time^{-1}\, concentration^{-1}$, while d has dimensions of $time^{-1}$. Since a rate is by definition a change over time, we can use these values in temporal derivatives of the concentrations. Association reduces the amount of free A and B, and increases AB. The viceversa is true for the dissociation reaction. We will thus have the following ODEs system:

$$\begin{cases} \dfrac{\mathrm{d}[A]}{\mathrm{d}t} = d[AB] - a[A][B] \\ \dfrac{\mathrm{d}[B]}{\mathrm{d}t} = d[AB] - a[A][B] \\ \dfrac{\mathrm{d}[AB]}{\mathrm{d}t} = -d[AB] + a[A][B] \end{cases} \tag{1.1}$$

The complete description of the system needs an additional information, that is the value of the variables at time 0: $[A_0]$, $[B_0]$ and $[AB_0]$.

There is a way to simplify the system in (1.1). Since the the two substrates are not produced nor degraded, their total amount is constant over time. If we identify them as A_{tot} and B_{tot}, we can write:

$$[A_{tot}] = [A] + [AB] = [A_0] + [AB_0]$$
$$[B_{tot}] = [B] + [AB] = [B_0] + [AB_0].$$

Equations like these are called *conservation laws*, and are a very useful to reduce the number of variables in an ODEs system. Specifically, if we write

$$[A] = [A_{tot}] - [AB]$$
$$[B] = [B_{tot}] - [AB],$$

we can have a full description of the system keeping track only of the dinamic of $[AB]$ and the total

amount of the substrates. The full system is:

$$\begin{cases} [A] = [A_{tot}] - [AB] \\ [B] = [B_{tot}] - [AB] \\ \frac{\mathrm{d}[AB]}{\mathrm{d}t} = -d[AB] + a\Big([A_{tot}] - [AB]\Big)\Big([B_{tot}] - [AB]\Big) \end{cases} \tag{1.2}$$

The first thing we can study is the equilibrium, or the *steady state*, of the system, that is when the temporal derivative is 0. We thus have:

$$\begin{aligned} \frac{\mathrm{d}[AB]}{\mathrm{d}t} = 0 &= -d[AB] + a\Big([A_{tot}] - [AB]\Big)\Big([B_{tot}] - [AB]\Big) \\ 0 &= -\frac{d}{a}[AB] + [A_{tot}][B_{tot}] - [AB]\Big([A_{tot}] + [B_{tot}]\Big) + [AB]^2 \\ 0 &= [AB]^2 - [AB]\Big([A_{tot}] + [B_{tot}] + \frac{d}{a}\Big) + [A_{tot}][B_{tot}] \end{aligned}$$

which is a second degree equation. Its solutions are therefore

$$[AB]_{1,2} = \frac{\Big([A_{tot}] + [B_{tot}] + \frac{d}{a}\Big) \pm \sqrt{\Big([A_{tot}] + [B_{tot}] + \frac{d}{a}\Big)^2 - 4[A_{tot}][B_{tot}]}}{2} \tag{1.3}$$

Only the '$-$' solution can give $[AB] < [A_{tot}], [B_{tot}]$, and thus it is the only biologically relevant solution. From this equation we can see that the steady state of the system only depends on the total amount of the reactants, and on the ratio between d and a, not on their absolute values. We will use this important general property of steady states in Section 3.2.3.

Another way to write the ODEs system at equilibrium leads us to an important parameter, the dissociation constant K_D. We can write:

$$\begin{aligned} \frac{\mathrm{d}[AB]}{\mathrm{d}t} = 0 &= -d[AB] + a[A][B] \\ d[AB] &= a[A][B] \\ K_D = \frac{d}{a} &= \frac{[A][B]}{[AB]} \end{aligned} \tag{1.4}$$

The ratio $\frac{d}{a}$ is the K_D. The lower the K_D, the stronger the affinity between A and B. K_D can be interpreted in a very physical way. If $[B] = K_D$, then $[A] = [AB]$. In other words, if $[B]$ equals the dissociation constant, which has dimensions of a concentration, the free A and the complex AB are present in the same concentration, and thus half of the total A is in the complex. We can see it graphically in Figure 1.5

To investigate the dynamics of the ODEs system in (1.2), it is possible to find the explicit formula

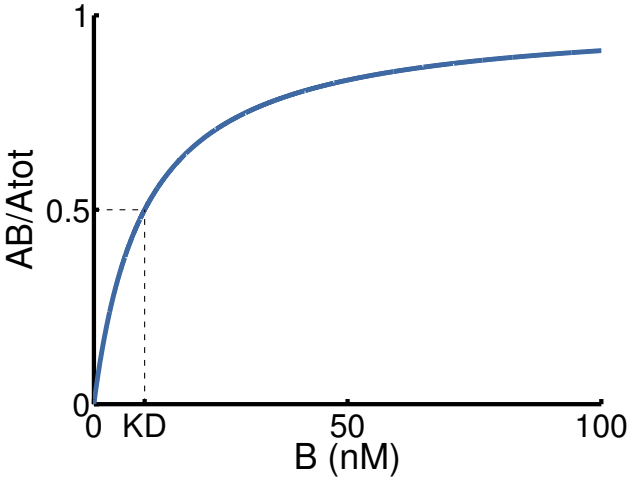

Figure 1.5: Interpretation of K_D
K_D is the value that free B assumes to have, at steady state, half of total A in the complex AB. Smaller K_D means less B needed to produce the complex, that means higher affinity between A and B.

of its solution. This means finding the explicit formula of a function of the time $F(t)$ that satisfies

$$\frac{\mathrm{d}F(t)}{\mathrm{d}t} = -dF(t) + a\Big([A_{tot}] - F(t)\Big)\Big([B_{tot}] - F(t)\Big).$$

However, the explicit formula is not more understandable than the ODEs system (1.2) itself, and thus we do not write it here. To circumvent this problem, it is possible to simulate the system numerically and plot the result (see Figure 1.6). It is important to notice that, in contrast with Figure 1.5, on the x-axis we have time. This plot represents the deterministic dynamic of the system. In Section 1.2.2 we will see how the stochastic dynamic of the same system behaves.

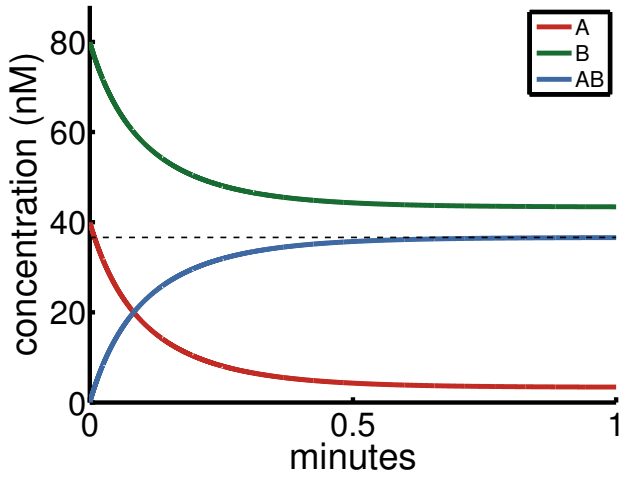

Figure 1.6: Deterministic simulation of the association/dissociation module
Dashed line is the steady-state value for AB. The initial number of molecules for the three species, and the association and dissociation constant, are in the same range as those of the association between MCC and APC/C^{Cdc20} in the protein network analysed in the main text.

Bifurcation diagrams

Before moving to the synthesis/degradation module, we investigate the association/dissociation module with another tool, called *bifurcation diagram*. This plot describes the steady-state value of a network as function of one of the parameters, named *bifurcation parameter*. Studying the steady-state value of a network is an approximation: the dynamics of the system is neglected, and only the value at equilibrium is studied. This method underlies the idea that the system quickly reaches the steady state.

To plot a bifurcation diagram, steady states are usually identified by simulating numerically the dynamics of the system over a long time, until equilibrium is reached, since we do not know the explicit mathematical relationship between the bifurcation parameter and the steady-state value.

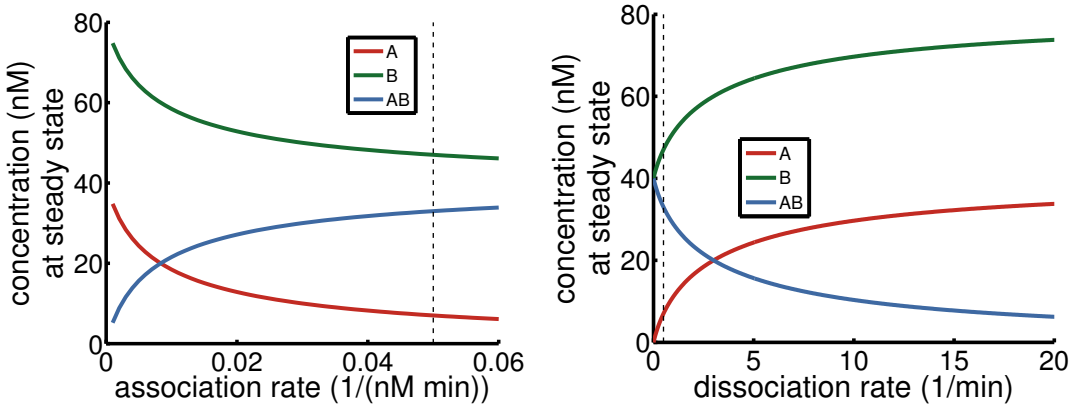

Figure 1.7: Bifurcation diagram for association/dissociation module
a) Bifurcation diagram having the association constant a as bifurcation parameter. By modulating its value, we modulate the steady-state values for the three species. Higher a values facilitate the formation of the complex AB. d is set to 0.5 (dashed line in panel **b**).
b) Bifurcation diagram having the dissociation constant d as bifurcation parameter. Higher d values reduce the formation of the complex AB, and freed A and B. a is set to 0.05 (dashed line in panel **a**). The initial number of molecules and the baseline association and dissociation constants, are in the same range as those of the association between MCC and APC/C^{Cdc20} in the protein network analysed in the main text.

We can plot two bifurcation diagrams for the association/dissociation module, one having the association constant a as bifurcation parameter (Figure 1.7(a)), one having the dissociation constant d as bifurcation parameter (Figure 1.7(b)). It is worth noticing that also other parameters can be used, for example $[A_{tot}]$ or $[B_{tot}]$, or combinations of parameters such as the $\frac{d}{a}$ (i.e: K_D). By comparing the two panels in Figure 1.7, we notice that the effect of changing a is stronger than changing d. In particular, once a is greater than 0.02, the system almost does not respond to changes in its value. On the other hand, d influences the steady-state values of the three species on a broader range of values, from 0 to 10. In both panels there is a *saturation effect*. This means that the effect of changing the bifurcation parameter levels off. In this module the saturation is due to the limiting amount of the three molecular species. A similar effect plays a key role in the biological problem presented in this work. Bifurcation diagrams are thoroughly used in Section 3.2.

Second module: synthesis/degradation

We have seen in the previous sections the behavior of a basic module of association/dissociation. Now we investigate how a basic module of synthesis/degradation behaves. Graphically we can depict the new module as:

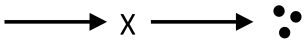

or as:

$$\rightarrow X \rightarrow$$

where the left arrows represent synthesis, while the right arrows represent degradation.

The degradation reaction, depends on the concentration of X present, and will thus occur at a rate $D[X]$, where D is the degradation constant with dimensions of $time^{-1}$. Synthesis, unlike degradation, does not depend on X, and its rate is s, a constant with dimensions of $concentration \cdot time^{-1}$. Only one variable is present, and so a single ODE, with its initial state, describes the system:

$$\begin{cases} \dfrac{\mathrm{d}[X]}{\mathrm{d}t} = s - D[X] \\ [X(0)] = X_0. \end{cases}$$

Using the technique of the separation of the variables, we can find an analytic solution that describes this system:

$$[X(t)] = \frac{s}{D} + K_0 e^{-Dt}$$

where K_0 is a constant, defined by imposing that $[X(0)] = [X_0]$. If, for example, $[X_0] = 0$, we have that $K_0 = -\frac{s}{D}$ and thus

$$[X(t)] = \frac{s}{D}\left(1 - e^{-Dt}\right)$$

There is only one steady state, $\frac{s}{D}$, for all the starting values. Similarly to the association/dissociation module, the steady state only depends on the ratio of the parameters, not on their absolute values. The impact of s and D on the dynamics can be noticed comparing the dark-green and violet curves in Figure 1.8: the two curves have the same steady-state value, but s and D are twice as big for the violet curve than for the dark-green. As a consequence, the steady state is reached much faster in the violet curve.

Also synthesis/degradation reactions can be analysed using bifurcation diagrams. In Figure 1.9 we analyse the system using s and D as bifurcation parameters. Since the steady-state value is $\frac{s}{D}$, it depends linearly on s and inversely on D. It is important to notice that, as opposed to the association/dissociation module, no saturation effect is present in this module. The saturation effect comes back when combining synthesis and association, as we will see in Section 3.2.5, analysing the protein network investigated in this work.

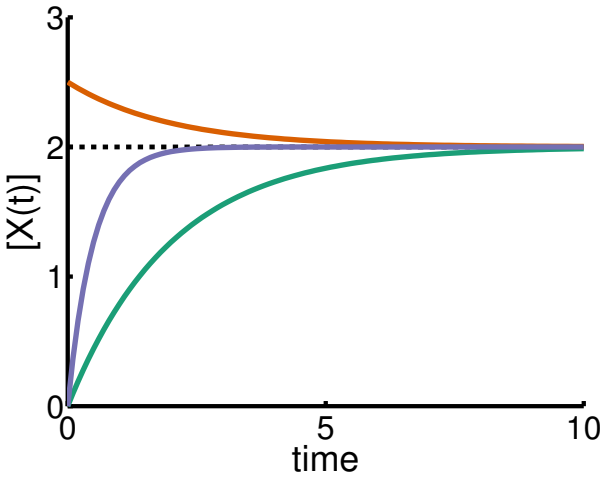

Figure 1.8: Plot of the exact analytical solution of the synthesis/degradation module Dashed line is the steady state value, which is common for all the curves. The orange line represents the evolution of a system starting above the steady state value, while the dark-green and violet lines start below the steady state. Violet line has s and D twice bigger than the other curves, and thus reaches faster the steady state.

1.2.2 Stochastic simulations using Gillespie algorithm

Ordinary differential equations (ODEs) provide deterministic descriptions of the behavior of protein networks. As we just saw, they are an extremely powerful and accessible tool to investigate network properties. However, this deterministic description neglects the intrinsic stochastic behavior of chemical reactions. The description of the chemical process, given by ODEs, can be interpreted as the average over several runs of the process. As long as the different runs are similar to their average, ODEs provide all the necessary details. On the other hand, when the differences between the runs cannot be neglected, other tools must be used Vilar et al. [2003].

The variability in different runs has several causes. For example, the system can be highly sensible to random events, as in the case of stochastic activation of genes Vilar et al. [2003]. Or proteins can be present at very low concentration, resulting in large fluctuations over the mean value of molecule number. What is important to notice is that stochasticity is always present in biochemical networks, but it becomes non-negligible when protein numbers are very small.

To describe the stochastic behavior of biochemical reactions, one of the most commonly used method is the *Gillespie algorithm*, developed in the 70s by Daniel Gillespie Gillespie [1976, 1977]. This algorithm simulates the dynamics of a protein network down to the single molecule, in contrast with ODEs that simulate average concentrations. The implementation of the algorithm is not a goal of this Introduction, since Gillespie algorithm can be simulated with standard packages using different programming languages (as an example: Maarleveld et al. [2013]). However, we aim at presenting some key feature of this method.

To explain the features of Gillespie algorithm, or stochastic-simulation algorithm (SSA), we use as a simple example the same association/dissociation module used in Section 1.2.1, where two proteins

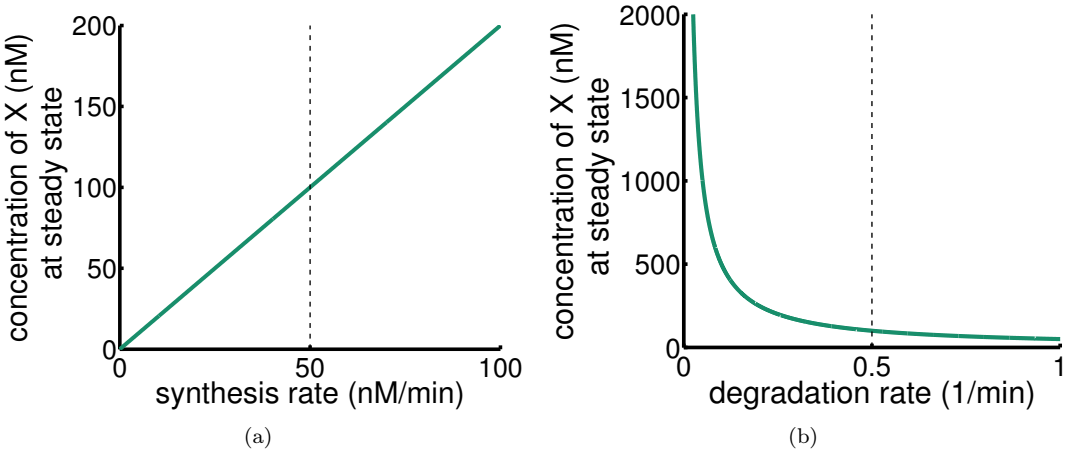

Figure 1.9: Bifurcation diagram for synthesis/degradation module
a) Bifurcation diagram having the synthesis rate s as bifurcation parameter. The steady state changes linearly, without any saturation effect. D is set to $0.5min^{-1}$ (dashed line in panel **b**).
b) Bifurcation diagram having the degradation constant D as bifurcation parameter. Higher d increase the degradation and thus reduce the amount of protein at steady state. s is set to $50nM\ min^{-1}$ (dashed line in panel **a**).

A and B bind, producing the complex AB via a reversible association. For the sake of clarity, we propose again the visual representation:

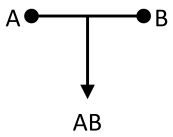

The algorithm is composed by few steps, repeated in cycles.

First, for each of the reactions comprising the network, the probability per unit of time and per unit of molecule is determined. If P_a and P_d are the probability of association and dissociation, respectively, and N is the number of molecules of each species, we have:

$$\begin{cases} P_a = a\dfrac{N_A}{V}\dfrac{N_B}{V} \\ P_d = d\dfrac{N_{AB}}{V} \end{cases}$$

where V is the volume where the reactions take place. The equations are the same as those used in the ODEs system.

Then, the algorithm extracts a random number X, $0 < X \leq (P_a + P_d)$. If $0 < X \leq P_a$, it executes the association reaction, while if $P_a < X \leq (P_a + P_d)$, it executes the dissociation reaction. In the case of association it decreases A and B by one unit, and increases AB by one unit. In the case of dissociation, it decreases AB by one unit, and increases A and B by one unit.

Then it extracts a random number Y, between 0 and 1, and advances time by

$$\Delta t = -\frac{\log Y}{P_a + P_b}.$$

Then the algorithm runs another step: computes reaction rates, chooses the occurring reaction, updates the system variables, advances time and so on.

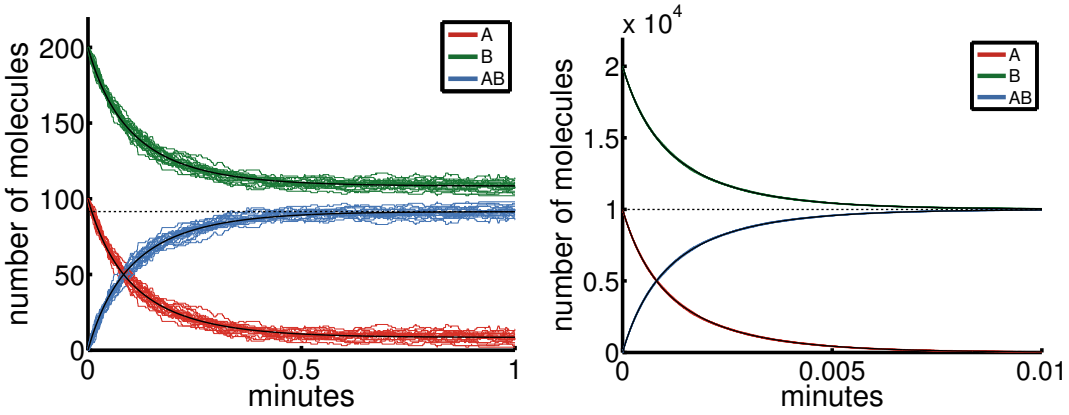

(a) Low number of molecules

(b) High number of molecules

Figure 1.10: Comparison between deterministic and stochastic simulation of the association/dissociation module, in the presence of low or high number of molecules
Deterministic (black lines) and stochastic (colored lines) simulations of the association/dissociation module. Right panel has 100 times higher molecule number than left panel.
In the right panel, black lines almost overlap thin colored lines. Dashed line is the steady-state value for AB.

This algorithm has several interesting features. First, given two subsequent values of time $t_1 < t_2$, the status of the system at time t_2 only depends on the status of the system at time t_1, not on the history of the system before t_1 Gillespie [1976]. This property is called Markov property, and, in brief, describes the fact that the process is *memoryless*. Another interesting feature is that the time of each reaction is exponentially distributed, and so is the time between two reactions. Finally, as demonstrated in Gillespie's papers, the average behavior of the stochastic trajectories overlaps the solution of the ODE system that describes the same protein network. An example of this similarity can be appreciated in Figure 1.10, where we simulated the association/dissociation module discussed in this section. While simulations of ODEs procede smoothly, the stochastic simulations have discrete steps. This is because ODEs variables assume continuous concentrations values, while stochastic simulation variables assume only integer values, since the variables are number of molecules. From the figure it is possible to appreciate that ODEs simulation is the average of the stochastic simulations.

What is fundamental to notice by comparing Figure 1.10(a) and Figure 1.10(b), is that the difference between stochastic simulations and ODEs is more significative when the number of molecules is smaller. In the model discussed in the main text, molecule number is in the same order of magnitude as in the simulations in Figure 1.10(a), and the role of stochasticity is fundamentamental to drive cells into anaphase.

1.2.3 The Ornstein-Uhlenbeck process

The result of simulating the Gillespie algorithm is a stochastic process. With this term is defined a set of indexed random variables, where the index usually represent time. An introduction on this mathematical object and its application (also to biology), can be found, for example, in Aletti et al. [2006]. In the Gillespie algorithm, the random variables are the molecular species, indexed on the steps of the algorithm. Each step represents a progress in time, but steps are not equally spaced in time, since, as we saw in the previous section, also time-increments are defined with a random variable.

We now want to focus on a specific stochastic process, used in the Results chapter as possible description of the dynamics of APC/C^{Cdc20}, the key molecular species of the biological problem tackled in these pages. This process is the Ornstein-Uhlenbeck process, named after two Dutch physicists, Leonar Ornstein and George Eugene Uhlenbeck, who first derived its formulation in 1930 Ornstein and Uhlenbeck [1930]. The Ornstein-Uhlenbeck process is a stochastic process with three properties: it is stationary, it is Gaussian and it is Markov.

Stationary means that its mean value does not change over time: its displacement, defined as the distance between the system at two subsequent times $t_1 < t_2$, have mean 0. *Gaussian* means that the displacements are distributed as a Gaussian distribution, that has mean 0 for the stationarity property. *Markov* means that the process satisfies is memoryless, as we just mentioned.

Another property of Ornstein-Uhlenbeck process that we will use in Results chapter, regards its autocorrelation function. The autocorrelation function is a measure of the auto-similarity of a stochastic process. We will thoroughly use this object in the next section, applied to fluorescence intensity traces. In the present case, it is defined as follows: let X be a stochastic process with mean μ and variance σ^2, and X_t its realization at time t. The autocorrelation function $G(\tau)$ of X is

$$G(\tau) = \frac{\mathbb{E}\big[(X_t - \mu)(X_{t+\tau} - \mu)\big]}{\sigma^2}, \tag{1.5}$$

where $\mathbb{E}$ is the expected value over t, and $(X_t - \mu)$ represent the distance from the mean at time t. This distance can be thought as fluctuation of the stochastic process around the mean value. In other words, at the numerator we find the expected value of the product between the fluctuation at time t and the fluctuation at time $t+\tau$. Fluctuations are both positive and negative, and thus the numerator goes to 0 for great values of τ. For an Ornstein-Uhlenbeck process, the autocorrelation has a peculiar shape, that is the exponential shape. Specifically, for Ornstein-Uhlenbeck process

$$G(\tau) = e^{-\tau}. \tag{1.6}$$

A derivation of this equation ca be found, for example, in [Kampen, 2007, eq (3.12), page 84].

Our interest in Ornstein-Uhlenbeck process lies in the specific behavior of its first-passage time.

First-passage time is defined as the time needed for a stochastic process to *first* reach a specific value (e.g: the time it takes for a stock to duplicate its value) Redner [2001]. The first-passage time we are interested in, is the time needed for APC/C^{Cdc20} to first hit the 'anaphase threshold', that is an arbitrary value that triggers anaphase onset.

An Ornstein-Uhlenbeck process has exponentially distributed first-passage time, provided that the threshold is far enough from the mean value Nobile et al. [1985]. Finding similarities, as done in Section 3.2.4, between APC/C^{Cdc20} and an Ornstein-Uhlenbeck process, thus, gives us a theoretical explanation of why we found exponentially distributed first-passage time for APC/C^{Cdc20} (Figure 3.4).

1.3 Fluorescence (Cross-)Correlation Spectroscopy

Two of the key reasonings in the work presented in these pages rely on quantification of proteins and protein complexes. First, to know the amount of Cdc20 interactors, all the members of MCC and several APC/C subunits have been measured (Figure 3.6(b)). The presence of these proteins in very low amount is the main driver of the stochastic behavior of adaptation. Second, to test the predictions of the model linking the amount of MCC and of the inhibited form of APC/C (APC/C^{inhib}) to *CDC20* gene copy number (Figure 3.10(a)), the concentration of both MCC and APC/C^{inhib} have been measured (Figure 3.20(a)).

In both cases, we needed the measurements to be quantitative. Not only: since both MCC and APC/C^{inhib} are present in very low amount in the cell, the technique used to measure their concentration had to be highly sensitive. For these reasons, we decided to perform these measurements using Fluorescence Correlation Spectroscopy (FCS) and Fluorescence Cross-Correlation Spectroscopy (FCCS), which are quantititative technique to measure protein and protein complexes concentration, respectively. We give here a general overview of the two techniques. For general remarks, see Rigler and Elson [2001], Bacia et al. [2006], Ries et al. [2010], Schwille and Hausten [2002]. Slaughter and Li [2010] is an inspirational paper on the topic. Bacia and Schwille [2007] collects practical guidelines.

FCS and FCCS are single-molecule methods aimed at measuring several properties of fluorescently labeled particles. They are based on the fluctuations in fluorescence intensity, measured in a confocal volume at single-photon resolution. Each acquisition lasts longer than in normal confocal microscopy and, unlike this technique, the confocal volume does not change its position inside the cell. Since the confocal volume does not move, intensity fluctuations are caused by changes in the fluorescent particles inside the volume. Specifically, fluctuations are caused by particles entering or exiting the confocal volume, or by particles changing their emission for other reasons, such as folding-unfolding dynamics, chemical reactions or photophysical changes. A visual representation of intensity fluctuations caused by particle dffusion is given in Figure 1.11(a).

For these fluctuation to be noticeable, we need both high sensitivity in the photon-counting process

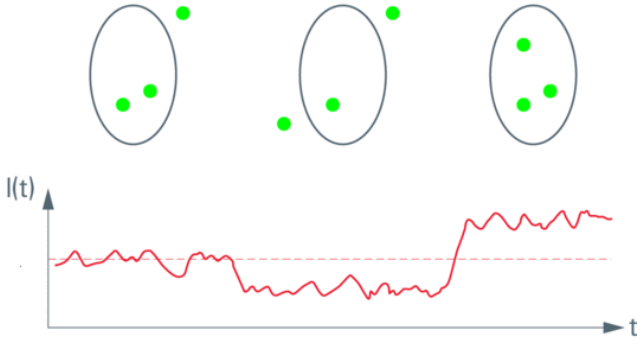

(a)

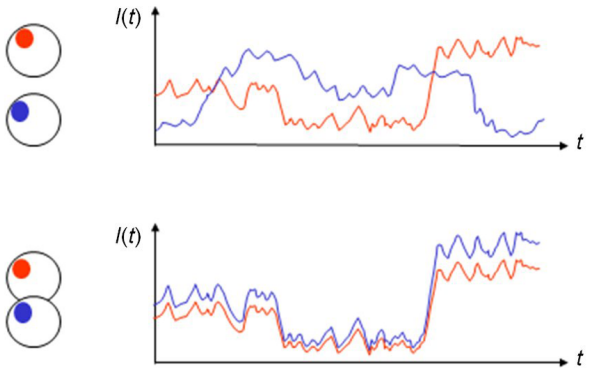

(b)

Figure 1.11: Visual representation of FCS and FCCS intensity traces
a) Visual representation of fluorescence intensity over time, one labeled protein. The oval represents the confocal volume, while the green dots are the fluorescent particles. Solid red line is the measured intensity over time, $I(t)$, the dashed line is its average. As long as two molecules are in the confocal volume, $I(t)$ has the same value of its mean. Once a molecule leaves the confocal volume, the intensity is reduced. The intensity increases with three molecules in the confocal volume. The larger fluctuations derive from changes in molecule number in the confocal volume, but noise is unavoidable, and cause smaller fluctuations. Image adapted from http://www.leica-microsystems.com/science-lab/fluorescence-correlation-spectroscopy/. **b**) Visual representation of fluorescence intensity over time, two labeled proteins, either freely diffusing or codiffusing. If the two particles are not interacting (upper panels), their diffusion is mutually independent. If, on the other hand, the two particles form a complex (lower panels), they diffuse together. Since they enter and exit the confocal volume together, their fluorescent traces fluctuate together. We can measure the complex by measuring the similarity between the two traces. Image adapted from http://www.leica-microsystems.com/it/prodotti/microscopi-confocali/metodi-confocali/fccs/

and low average number of photons detected per unit of time. The first goal have been achieved in the last decades with the great improvements in technical equipments (for an overview of the microscope settings, see Schwille and Hausten [2002], Bacia and Schwille [2007]). The second goal can be achieved by reducing the number of labeled proteins measured per unit of time. To do so, it is possible to limit the detection volume, and measure the proteins of interest at low concentration. For this reason, the optimal settings for FCS limit the confocal volume to less than one femtoliter, and investigate proteins in the nanomolar concentration range.

Even if FCS and FCCS are microscopy techniques, they do not return any image. Instead, the output is the fluorescence intensity, which can be analysed with mathematical tools to investigate properties of fluorescent particles. In particular, it is possible to measure absolute concentrations. Several other quantities can be investigated (e.g: diffusion time, rotational behavior...) but since

in this study we used these techniques to measure concentrations, we will cover only this aspect of FCS/FCCS.

Before entering into the mathematical part, it is necessary to distinguish between FCS and FCCS. FCS deals with only one fluorescent trace at a time. This means, excluding more advanced techniques (e.g: Fluorescence Lifetime Correlation Spectroscopy (FLCS) Kapusta et al. [2012]), studying one protein. FCCS, instead, deals with two fluorescent traces, resulting from the emission of two proteins tagged with spectrally distinct fluorophores, using two distinct laser lines to excite them. With this technique, we can measure the complex formed by the two tagged proteins using their codiffusion, as depicted in Figure 1.11(b).

1.3.1 Correlation functions and the model used to fit them

In FCS, the fluctuations in fluorescence intensity are processed by autocorrelation analysis. This operation, already mentioned in Section 1.2.3 about the Ornstein-Uhlenbeck process, consists in measuring the similarity of the intensity trace I at a given time t with the same function at time $t+\tau$, averaged over all the t. In other words, each trace is compared with itself, shifted in time, and the autosimiliarity is measured. In mathematical terms:

$$G(\tau) = \frac{\mathbb{E}\big[(I_t - \mu)(I_{t+\tau} - \mu)\big]}{\mathbb{E}(I_t)^2} \tag{1.7}$$

where, as in equation (1.5), $(I_t - \mu)$ is the fluctuation in the intensity I at the time t, and $\mathbb{E}$ indicate averaging over t. The different denominator in this equation compared to equation (1.5), is used to link $G(0)$ with the average number of particles in the volume, as we will see soon. In Figure 1.12, we show a visual representation of what autocorrelation means. $G(\tau)$ is high for small values of τ, meaning that the curve has the maximal similarity with itself at small time shifts, and the similarity fades to 0 for bigger values of τ.

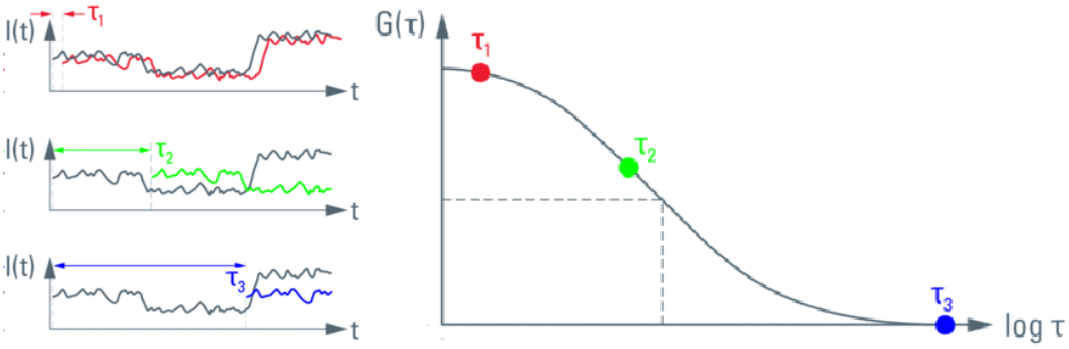

Figure 1.12: Visual representation of autocorrelation
The intensity $I(t)$ (black line) is shifted in time (τ_1 red curve, τ_2 green curve and τ_3 blue curve). The similarity betwenn the black and the coloured curves is the autocorrelation $G(\tau)$ for the different values of τ (right panel). Each dot on $G(\tau)$ correspond to a curve. Notice that time shift in x-axis is in log scale. Adapted from http://www.leica-microsystems.com/science-lab/fluorescence-correlation-spectroscopy/.

The autocorrelation obtained from the measured fluctuations is then fitted with a model. The choice of the model depends on the properties of the system. For example, if the diffusion occurs in three dimensions (e.g: freely diffusing protein) or in two dimensions (e.g: membrane protein), if the protein is actively transported (e.g: protein involved in secretory pathway), if different populations of the protein diffuse with different speed (e.g: free protein VS protein bound to DNA). For our system, the best choice is the two-component model, assuming triplet-like blinking state. *Two-component* means that the protein of interest can be found in two populations, ideally the free molecule or the molecule bound to a slower diffusing complex (for us: APC/C or MCC). More subpopulations can be present, but we decided not to add more components to the model to avoid overfitting. *Triplet-like blinking state* means that the model takes into account the blinking of the fluorophore, that is a quantum process operating on a very short time-scale ($< 100\mu s$), that shall not be mistaken for very fast diffusing molecule.

The explicit equation describing the model is:

$$G(\tau) = \left(1 - \Theta_T + \Theta_T e^{-\frac{\tau}{\tau_T}}\right)\frac{1}{N}\left(\sum_{j=1}^{2} f_j \frac{1}{1+\frac{\tau}{\tau_{D,j}}}\sqrt{\frac{1}{1+\frac{1}{\kappa^2}\frac{\tau}{\tau_{D,j}}}}\right). \tag{1.8}$$

The first parenthesis takes into account the triplet state of the fluorophore, and is significant only on the characteristic triplet state time-scale τ_T (usually much smaller than $\tau_{D,j}$). Θ_T accounts for the amount of autocorrelation depending on the triplet state. N is the average number of particles in the confocal volume. f_j is the fraction of the j-th component, meaning $f_1 + f_2 = 1$. $\tau_{D,j}$ is the diffusion time of the j-th component, and finally κ is the optical parameter related to the shape of the Gaussian confocal volume. If z is the vertical radius of the Gaussian confocal volume, and ω the lateral radius, κ is defined as $\kappa = \frac{z}{\omega}$. What is important to notice from equation (1.8) is that

$$G(0) = \frac{1}{N}, \tag{1.9}$$

and thus we can measure the average number of particles knowing $G(\tau)$.

The core of the model is the term of the summation, that describes the behavior of an homogeneous population of fluorescent particles:

$$G(\tau) = \frac{1}{N}\frac{1}{1+\frac{\tau}{\tau_D}}\sqrt{\frac{1}{1+\frac{1}{\kappa^2}\frac{\tau}{\tau_D}}}. \tag{1.10}$$

In Figure 1.13 we can see the dependency of $G(\tau)$ on two of the three parameters present: the average number of particles in the volume, N, and the diffusion time, τ_D. By increasing N, the fluctuation caused by a particle entering or exiting the confocal volume becomes neglectable. We can think of trying to find out whether a person had entered or left our living room or an overcrowded concert hall. The higher N, the less the impact of fluctuations, the smaller $G(0)$. By increasing τ_D we speed up

the particle. The faster it moves, the shorter it takes for the autosimilarity of the intensity to decay to 0 (see Figure 1.12).

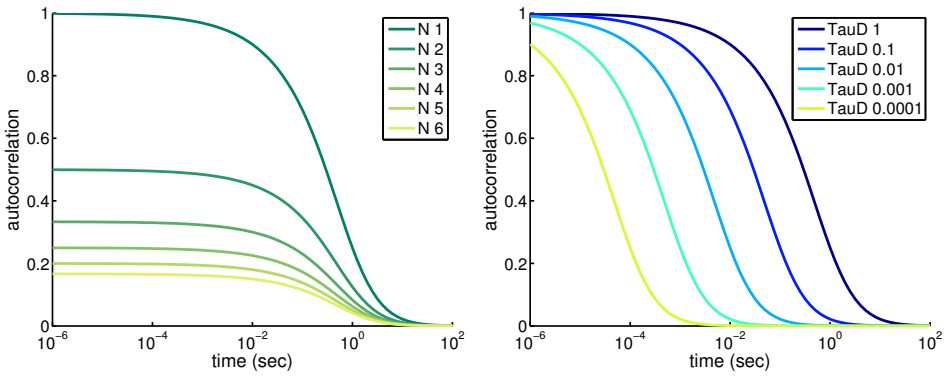

Figure 1.13: How FCS curves respond to changes in the parameters
Changes in N and τ_D on the core component of the model, presented in equation (1.10).

1.3.2 Computing the acquisition volume knowing the diffusion coefficient

We have seen how to measure the number of particles in the confocal volume (equation (1.9)). To measure the concentration, we need to measure the effective confocal volume V. In order to do it we take advantage of dyes with known diffusion coefficient D, which is related to the diffusion time τ_D by the equation that defines it:

$$\tau_D = \frac{\omega^2}{4\,D}$$

From spatial integration [Rigler and Elson, 2001, page 364, section 17.2.2] we can express the effective volume V as

$$V = \pi^{3/2}\,\omega^2\,z.$$

We can then compute

$$\begin{cases} D = \dfrac{\omega^2}{4\,\tau_D} \\ V = \pi^{3/2}\,\omega^3\,\kappa \end{cases}$$

That gives us

$$\begin{aligned} \frac{D^3}{V^2} &= \frac{\omega^6}{(4\,\tau_D)^3}\,\frac{1}{\pi^3\,\omega^6\,\kappa^2} \\ &= \frac{1}{(4\,\kappa^2\,\pi\,\tau_D)^3} \end{aligned}$$

and finally

$$V = \kappa\left[4\,\pi\,\tau_D\,D\right]^{3/2}. \tag{1.11}$$

This last equation gives us a way to compute the effective volume from the knowledge of D and from the parameters obtained by fitting the autocorrelation curve to the model.

1.3.3 A note of caution on the overlapping volume

With the equation (1.11) we can compute the effective confocal volume for each of the two channels. When we perform FCCS we also need to know the 'effective overlapping volume', that is the volume where we can effectively measure cross-correlation. This is not a trivial problem, since the volumes for the two channels do not often have the same size, since the latter depends on the laser wavelength, and volumes are not always concentric.

Moreover, the effective volumes are not rigid sphere, but rather regions of the space where the probability of detecting a photon is higher, given that this probability is non-zero in the whole space. For this reason we have the counterintuitive result that the 'effective overlapping volume' is bigger than the smallest of the two. It is actually a sort of a geometrical average of the two [Rigler and Elson, 2001, page 366, eq (17.10)].

We will not measure the 'effective overlapping volume' with analytical formulas, but by measuring double-labeled dyes and setting the 'effective overlapping volume' such that the concentrations C_g, C_r and C_{rg} have the same value.

1.3.4 Measuring concentrations

We have seen how to measure the number of particles, N, and the effective volume, V, from the fitted parameters. Now we discuss how to get from these numbers to the concentration of the proteins and of their complexes. We call G_{rr} and G_{gg} the fitted $G(0)$ of the autocorrelation functions of *r*ed and *g*reen channels, respectively. From these values we can thus compute the absolute concentration (in moles) of the two fluorescent proteins, by using the following equation:

$$C_i = \frac{1}{G_{ii} V_i N_a} \qquad \text{for } i = r, g \tag{1.12}$$

where N_a is the Avogadro constant and V_i is the acquisition volume for the *g*reen or the *r*ed channel. To compute the concentration of the complex we used the following equation (see [Rigler and Elson, 2001, page 367, eq (17.15)]):

$$C_{rg} = G_{rg} V_{rg} N_a C_r C_g \tag{1.13}$$

where the subscript rg refers to the cross-correlation (i.e: the complex). V_{rg} is the overlapping volume, computed as explained previously. Note that, unlike the concentration of the interacting proteins (see equation (1.12)) where $G(0)$ and the concentration are inversely proportional, the concentration of the complex is drectly proportional to the $G(0)$ of the cross-correlation function, G_{rg}.

In this Introduction, we gave an overview of the biological problem examined in this work, and of the tools we used to address it. Adaptation to the SAC was investigated with the help of a mathematical model, analysed using both its deterministic and stochastic versions. Some of the key

predictions of the model were tested and confirmed using single-cell microscopy and FCCS.

Aim of the thesis

This thesis analyses the phenomenon of adaptation to the Spindle Assembly Checkpoint (SAC). It is organized in two main parts. First, we address whether cells adapt to an active SAC, or if cells rather escape the mitotic arrest after SAC silencing. Then, we build and analyse a quantitative model of the SAC network. Model predictions are experimentally tested, aiming at unraveling the origin of the well-known large variability in adaptation times.

The main results and reasoning presented in these pages are in press in the manuscript *'Cells escape an operational mitotic checkpoint through a stochastic process'*, Bonaiuti P, Chiroli E, Groß F, Corno A, Vernieri C, Štefl M, Cosentino Lagomarsino M, Knop M and Ciliberto A, *Current Biology*.

Chapter 2

Materials and Methods

In this chapter, protocols are presented in the same order as the results in Chapter 3. The first section (Section 2.1) includes information that are common in every use of a technique, such as the characteristics of the microscope for single-cell experiment, or the G1 arrest protocol for synchonizations. All the other details, experiment-specific, are presented in the subsequent sections. In this way, we try and give the reader a complete overview of the protocol used to produce each figure, from strain creation to cell growth and data analysis.

2.1 General information

Strains, genetic manipulation, media and plasmids

All yeast strains (Table 4.4) were derivatives of or were backcrossed at least three times to W303 (*ade2-1, trp1-1, can1-100, leu2-3,112, his3-11,15, ura3*). Where not otherwise specified, chromosomal deletions or tagging in both haploid and diploid strains were generated by one-step gene replacement Longtine et al. [1998], then checked by polymerase chain reaction (PCR). In every case, strains obtained from transformation were then successfully tested for viability at different temperatures (23 °C, 30 °C and 37 °C) and with Ethanol/Glycerol as carbon source to check mitochondrial functionality. Homozygous diploid strains were obtained by crossing two haploids with the same genotype, by isolating zygotes and by checking the ploidy by FACS analysis of DNA content of cycling cultures.

Where not otherwise specified, synchronizations were carried out at 30 °C. To arrest cells in G1, α-factor was added at $3\,\mu g/ml$ to log-phase culture. After 60-90 minutes, a second α-factor administraton was given, at half the previous concentration ($1.5\,\mu g/ml$). After 120-150 minutes from the first administration, cells were released from G1 arrest. Nocodazole (Sigma-Aldrich) was used at $15\,\mu g/ml$.

A complete list of the plasmids used in this study can be found in Table 4.5.

Protein extract and western blot analysis

TCA protein extracts for western blot analysis were prepared according to Fraschini et al. [1999], and proteins were transferred on a nitrocellulose membrane (Amersham). Commercial primary antibodies were used as follows: Clb2 (sc-9071; Santa Cruz Biotechnology, Inc.) at 1:1.000, Cdc28 (sc-6709; Santa Cruz Biotechnology, Inc.) at 1:100, Cdc20 (sc-6731; Santa Cruz Biotechnology, Inc.) at 1:500, Pgk1 (D660; Invitrogen) at 1:5000. Secondary antibodies were from Bio-Rad Laboratories and proteins were detected by an enhanced chemiluminescence system (Invitrogen) according to the manufacturer's instructions. Blots were acquired as digitalized images by a Chemidoc XRS+System (Bio-Rad Laboratories). Signal was quantified using ImageJ or Image Lab software.

Image acquisition - single-cell experiments

Single-cell experiments were performed growing cells at 30 °C in microfluidic chambers (CELLASIC). Time-lapse movies were recorded using a DeltaVision Elite imaging system (Applied Precision) based on an inverted microscope (IX71; Olympus) with a camera (CoolSNAP HQ2; Photometrics) and a UPlanFL N 60x (1.25 NA) oil immersion objective lens (Olympus). GFP, Venus and mCherry were acquired using single bandpass filters (EX475/28 EM523/36 for GFP and Venus, EX575/25 EM632/60 for mCherry). The phototoxicity of the acquisition setting of each experiment was measured by comparing the cell cycle duration in excited and non-excited cells, for which we detected no significant difference. The coexistence of excited and non-excited fields of view was made possible by *ad-hoc* scripting of DeltaVision acquisistion software.

Image analysis - single-cell experiments

Images were projected, when needed, and mounted using an automated pipeline written in Fiji Schindelin et al. [2012].

We have aimed at analyzing as many cells as possible, with the limitations that come with the microfluidic technology. We have found that experiments with around 100 cells per condition give reproducible results. All the cells imaged have been analyzed, without any selection step except those explicitly mentioned when presenting the results or the method.

All the cells were segmented using the software Phylocell (developed by Gilles Charvin and colleagues Charvin et al. [2008] and available on GitHub Charvin [2017]). Pixels in the segmented areas of mother and daughter cells were analyzed together until cells divide. The mean value of the background, identified as the nonsegmented area, was subtracted for each frame. Fluorescence traces were analyzed using custom softwares in MATLAB.

2.2 Single-cell experiment for Mad2-Bub3 colocalization

This section refers to Figure 3.1(b).

Bub3-mCherry was created by one-step tagging, based on S-primers strategy Janke et al. [2004], placing the tag immediately before the STOP codon. We used three tandem copies, with different codon usage, of a monomeric mCherry. The different codon usage is to prevent genetic rearrangement. This fluorophore was engineered by Susanne Trautmann (plasmids pST70 in Boeke et al. [2014]). Bub3-mCherry was successfully tested for SAC proficiency. Mad2-3GFP fusion was a gift by Tomo Tanaka (Centre for Gene Regulation and Expression, College of Life Sciences, University of Dundee, Scotland, UK).

To control for green-to-red bleedthrough we used a strain carrying only Mad2-GFP (yAC1513), together with the target strain carrying also Bub3-mCherry (yAC3266). Cells were grown in YP medium (1% yeast extract, 2% Bacto Peptone, 80 mg/l adenine) supplemented with 2% glucose (YPD). Cells were arrested in G1 and released into nocodazole. Two hours after, a sample of the arrested colture was taken, briefly sonicated and centrifuged. Surnatant was partially removed to concentrate the cells. A drop of the culture was placed on an 2% agar layer to immobilize cells, and imaged.

GFP was acquired using 10% of the lamp power for 0.07 seconds each Z-stack, mCherry using 10% lamp power for 0.15 seconds. To scan the whole height of the cell, 20 Z-stacks 0.3 μm spaced were acquired. To enhance the hypothetical green-to-red bleedthrought we acquired the two channels before moving to a different Z-stack. Images were deconvolved using SoftWorx software, and their maximum intensity projection was used to have a 2D image. As can be noticed in Figure 2.1, no bleedthrough is recorded.

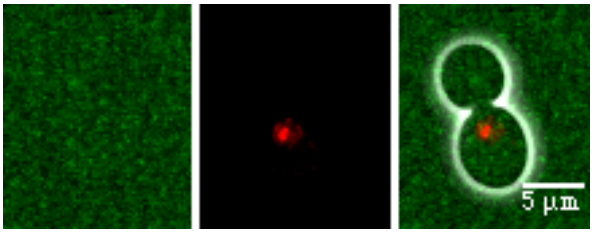

Figure 2.1: Negative control for bleedthrough in Mad2-Bub3 colocalization experiment. The brightenss in GFP channel is higher than in the positive result shown in Figure 3.1(b), to enhance the absence of signal. One cell representative of all the cell recorded ($\sim$ 30). Details of the experiment in Section 2.2.

2.3 Single-cell adaptation experiments in nocodazole - haploids

This section refers to single-cell experiments performed on haploid wild-type and *CDC20 NX* strains. Results are presented in Section 3.1 and 3.3. The protocol used on *mad3*Δ cells is presented in Section 2.5. The protocol used on diploid strains is presented in Section 2.6.

Strains, media and reagents

Cells were grown in YP medium (1% yeast extract, 2% Bacto Peptone, 80 mg/l adenine) supplemented with 2% glucose (YPD). Cells were arrested in G1 and released into nocodazole. One hour after the

release, α-factor was administered at $12.5\mu g/ml$, together with nocodazole, to avoid S-phase after adaptation.

Clb2-mCherry was created as Bub3-mCherry (see Section 2.2). Its complete functionality has been tested by checking viability of *CLB2*-mCherry *clb1*Δ. Mad2-3GFP fusion is the same used for Mad2-Bub3 colocalization experiment.

Image acquisition

Images were acquired every 10 minutes for 700 minutes. Mad2-GFP was acquired using 11 Z-stacks spaced $0.3\,\mu m$, each acquired for 0.07 seconds at 10% lamp power. Images were deconvolved using SoftWoRx software, and projected using the maximum intensity projection. Clb2-mCherry was acquired at 10% lamp power for 0.5 seconds, with a single Z-stack to reduce photodamage of the cells. The coexistence of different Z-stacks was made possible by *ad-hoc* scripting of the DeltaVision acquisition procedure.

Image analysis - Clb2 dynamics

Clb2-mCherry mean signal was smoothed using a Savitsky-Golay filtering. Its accumulation was used as readout of mitotic entry, and identified as the maximum of the second derivative after budding (as in Charvin et al. [2010b]). Exit from the mitotic arrest was detected as the starting time of Clb2 degradation. To measure this event, we first verified the presence of Clb2 degradation, recognized as a drop in fluorescence level of at least 25% of the peak value. Once the degradation was identified, the time of its start was determined as the frame where the second derivative had its minimum value.

Image analysis - Mad2 localization

Mad2-GFP localization was determined using a localization index defined using the Laplacian of Gaussian operator. This operator smooths out the noise and enhances edges between dark and bright areas of the image Marr and Hildreth [1980]. Since, with our settings, the kinetochore occupies roughly a 3x3 pixels square, we used the Laplacian of Gaussian of size 3. For the smoothing parameter σ we choose 2. The resulting matrix of the filter is:

$$\begin{bmatrix} -0.0085 & 0.0038 & -0.0085 \\ 0.0038 & 0.0187 & 0.0038 \\ -0.0085 & 0.0038 & -0.0085 \end{bmatrix} \tag{2.1}$$

The effect of this filtering are shown in Figure 2.2. We used the maximum of the filtered image as localization index.

To define a threshold above which Mad2 was defined as localized, we observed that the Mad2 localization index drops rapidly from high to low values when cells adapt. This result can be appreciated

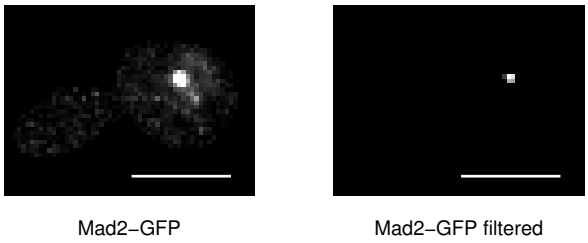

Figure 2.2: Effect of the Laplacian of Gaussian filtering on Mad2-GFP signal.
Mad2-GFP raw image (left) was filtered using the Laplacian of Gaussian filter presented in equation (2.1). The resulting image is in the right panel. The scales of the two images are very different: raw fluorescent values range from 0 to ∼1500, the filtered values from 0 to ∼40. Scale bars are 5 μm.

by plotting the number of cells with Mad2 localization index above a chosen value in function of time (see Figure 2.3). The curves representing values from 7 to 10 are close to each other, especially in their descending dynamics around 200 minutes. This means that in the majority of cells Mad2 localization index changes from indicating complete localization (> 10) to complete delocalization (< 7). This result gave us the freedom to choose any value within the interval. We chose the highest value, 10. It is worth noticing that in G1, when Mad2 is not localized at kinetochores (see Section 1.1.2), the localization index is much lower (99th percentile = 6.5).

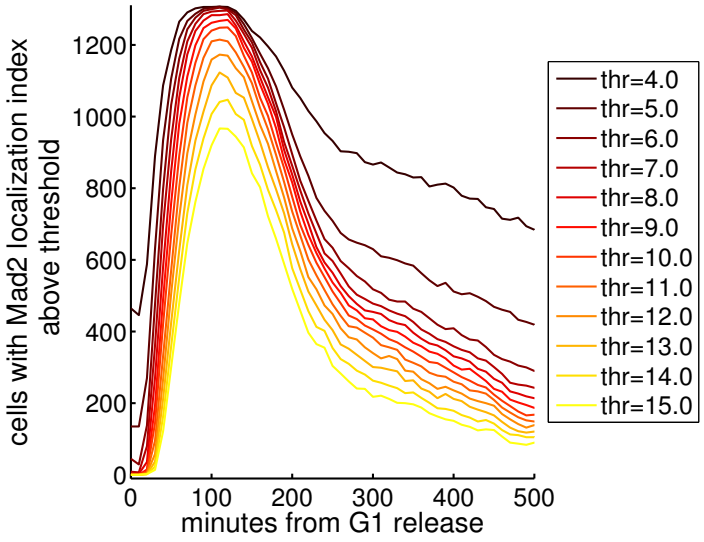

Figure 2.3: Mad2 localization index threshold.
Cells carrying MAD2-GFP CLB2-mCherry and 1, 2, 3, or 5 copies of *CDC20* (yAC3538, yAC3565, yAC3555, yAC3552) were arrested in G1 and released into nocodazole, and their Mad2 localization index was measured in time. In this graph, the number of cells with Mad2 localization index above threshold are plotted versus the time from G1 release into nocodazole. Every curve represents a different value of the threshold, listed in the legend. N: 3; n: 1310. For a complete overview of the database of observations see Table 4.1. Image taken from Bonaiuti et al. [2017].

Image analysis pipeline

We excluded from subsequent analysis cells where Mad2 is not localized when Clb2 degradation starts (i.e.: Mad2 localization index is below 10) and cells where Mad2 delocalizes while Clb2 is stable. On the remaining cells, we computed the empirical cumulative distribution function of the adaptation times. This curve was fitted with an exponential function after a delay. The rate of the exponential

curve gives the adaptation propensity. Rates normalized on wild-type are used as hazard ratios in the final comparison presented in Section 3.3.3.

To summarize the analysis pipeline we list here all its steps:

1. segment each cell;
2. extract the information in the segmented area of mother and daughter cells together, remove the background, compute the mean value of Clb2 and the localization index of Mad2 in time;
3. compute Clb2 accumulation and degradation times, and evaluate the Mad2 localization status at the time of Clb2 degradation;
4. from Figure 2.3, define a threshold for Mad2 localization index based on steepness of the curves around 200 minutes, and on Mad2 localization index value during G1;
5. according to the threshold, identify cells where Mad2 is localized or not at the time of Clb2 degradation. Figure 3.2(d) and 3.14 are produced at this step;
6. exclude cells where Mad2 is not localized at the time of Clb2 degradation, and cells where no Clb2 degradation is recorded. Figure 3.3 is produced after the exclusion;
7. compute the empirical cumulative distribution function of adaptation times, and fit it with an exponential after a delay (Figures 3.4 and 3.15(a));
8. compute hazard ratio of each strain normalizing the rate with the one of wild-type.

An analysis of the robustness of the results presented in Figures 3.2(d), 3.3, 3.4, 3.14 and 3.15(a) is presented in Appendix A.

2.4 Mathematical model

This section refers to results presented in Section 3.2.

We converted the wiring diagram shown in Figure 3.5 into a System Biology Markup Language (SBML) model of biochemical reactions that could be used for simulations in Python. Deterministic simulations were carried out using the Python package 'SloppyCell' Myers et al. [2007], Gutenkunst et al. [20107]. Stochastic simulations were performed with the Python package 'StochPy' using Gillespie's direct method Maarleveld et al. [2013].

Parameters for the model are discussed in Section 3.2.2. To measure Cdc20 degradation we used cells carrying *his3-11,15::HIS3tetR-GFP, ura3::3XURA3tetO112* (yAC1070, gift by Simonetta Piatti, Centre de Recherche en Biologie Cellulaire de Montpellier, CNRS, Montpellier, France). Samples for western blot analysis were fixed in cold $NaN_3\,1mg/ml$. More details of the protocol can be found in the caption of Figure 3.6(a) To compare Cdc20 levels with those of APC/C subunits, we used *CDC23-Myc9*, *Myc9-CDC20*, *CDC27-Myc9*, *APC5-Myc9* and *APC4-Myc9* strains (gift by Wolfgang

Zachariae, Laboratory of Chromosome Biology, Max Planck Institute of Biochemistry, Martinsried, Germany). Details of the protocol can be found in the caption of Figure 3.6(c). To measure protein concentration we used FCCS, the details of the protocol used to produce Figure 3.6(b) can be found in Section 2.7.

2.5 Creation and characterization of strains with additional copies of *CDC20*

This section refers to results presented in Section 3.3.1.

Plasmid construction and genetic manipulation

CDC20 sequence from -411bp to +391bp was amplified by overlap extension PCR on the plasmid used for Cdc20 tagging in Shirayama et al. [1998] and on pAC130 and cloned in YipLac204 to obtain plasmid pAC138 for *TRP1* tagging. This plasmid was digested with KpnI and *CDC20* sequence was cloned in YipLac211 to obtain plasmid pAC142, for *URA3* tagging. pAC138 and pAC142 integrations at *TRP1* and *URA3* loci were obtained by digestion with EcoRV and copy number was evaluated by Southern blot (for integration at *TRP1*) or qPCR (for integration at *URA3* or *TRP1*), see Figure 3.12(a) and 3.12(b). To test for *CDC20* functionality, in the strains carrying additional copies of *CDC20* both the endogenous *CDC20* and *CDH1* were removed and viability was verified.

Quantification of extra *CDC20*

To estimate additional *CDC20* copy number, we performed quantitative PCR (qPCR) on genomic material using *MND2* as reference gene. To quantify the number of insertions at *TRP1* locus (Figure 3.12(a)) we also included in the analysis strains carrying extra copies of *CDC20* but deleted for the endogenous gene. qPCR output for yAC2398 (*trp1::CDC20::TRP1, CDC20*) was approximately twice as for the wild-type strain. For yAC2400 (*trp1::CDC20::TRP1 (2X), CDC20*) it was three times compared to wild-type. Accordingly, when we deleted endogenous *CDC20* in yAC2398 we had the same signal as in the wild-type, while we had approximately twice as much with the same deletion in yAC2400. yAC2398 was then used as parental for *CDC20 2X* strains and yAC2400 for *CDC20 3X*.

To measure gene copy number in the selected *URA3* transformant yAC2675, we created a calibration set composed by the haploid wild-type and two diploid strains with different *CDC20*/*MND2* ratios. We run a qPCR analysis using *MND2* as normalizer (Figure 3.12(b)). The results suggest that haploid transformant yAC2675 (unknown number of *CDC20* integrations at *URA3*) carry two additional copies of *CDC20*. The *CDC20 5X* strains carry the additional *CDC20* from this *URA3* transformant and the two copies at *TRP1* locus from yAC2400.

*cdc20*Δ was a gift from Fred Cross (Center for Studies in Physics and Biology, The Rockefeller

University, New York, USA). *pds1::18MYC-PDS1::LEU2* strain used for diploid construction was a gift by Simonetta Piatti (Centre de Recherche en Biologie Cellulaire de Montpellier (CRBM), CNRS, Montpellier, France)

Benomyl plates

This paragraph refers to Figure 3.13(a).

To prepare benomyl plates we melted YPD solid agar, then cooled it to 65 °C. $100X$ Benomyl solution in DMSO was added to the cooled melted agar, then plates are poured and left drying for one hour under a chemical hood. Benomyl concentration in plates was $12.5\mu g/ml$. DMSO was used as negative control at 1% concentration. Drop test with coltures at stationary phase was performed right after drying of the plates, to avoid degradation of the compounds.

Single-cell adaptation experiments in nocodazole - *mad3*Δ

These paragraphs refers to Figure 3.13(b).

Cells carrying MAD2-GFP CLB2-mCherry and 5 copies of *CDC20* or *mad3*Δ were arrested in G1 and released into nocodazole, without any further medium change, to allow cell rebudding after mitotic exit. Images were acquired as presented in Section 2.3.

SAC-deficient cells (*mad3*Δ) have a shorter mitosis than SAC-proficient strains, and thus Clb2 is degraded before mCherry can mature. For this reason, in the experiments of Figure 3.13(b) we cannot measure mitotic arrest as the time between Clb2 accumulation and degradation. Instead, we kept track of the time between the first and the second budding (i.e., between entry into S-phase after G1 release and after adaptation).

mad3::TRP1 was a gift by Peter de Wulf (University of Trento, Centre for Integrative Biology, strain PDW747).

2.6 Single-cell adaptation experiments in nocodazole - diploids

This paragraph refers to results presented in Figure 3.15(b).

Cells were grown in YP medium (1% yeast extract, 2% Bacto Peptone, $80\,mg/l$ adenine) supplemented with 2% glucose (YPD), and released into nocodazole without any synchronization. Images were acquired and mounted as in haploid experiments (Section 2.3), the only difference being the spacing of the Z-stacks ($0.3\,\mu m$ for haploids, $0.38\mu m$ for diploids). Clb2 signal was used to identify mitotic entry and exit, as discussed in Section 2.3, while Mad2 levels were not used in image analysis, for reasons explained in Section 3.3.2.

2.7 FCCS experiments

This section refers to results presented in Section 3.4. For an overview of the technique, see Section 1.3.

Strains, media and reagents

Cells were grown at 23 °C in synthetic complete medium, prepared using yeast nitrogen bases lacking folic acid and riboflavin (CYN6501; ForMedium, Hunstanton, UK) to reduce medium fluorescence, and supplemented with 2% glucose, and 1% Bacto Peptone (BD, USA) to maximize nocodazole effect in synthetic medium Taylor-Mayer et al. [1988].

Plasmid construction and genetic manipulations

To reduce cell autofluorescence, the mutated *ade2-1* gene normally present in W303 genetic background was replaced by one-step gene replacement with wild-type *ADE2* gene, amplified by PCR from plasmid pRS402 Brachmann et al. [1998].

Gene deletion was performed with one-step tagging based on S-primers strategy Janke et al. [2004]. Gene tagging was performed as explained for Bub3-mCherry in Section 2.2, using monomeric mCherry and a monomeric yeast-enhanced version of GFP (myeGFP), in three tandem copies and with different codon usage, engineered by Susanne Trautmann (plasmids pST70 and pST72 in Boeke et al. [2014]). Strains in which Mad2, Mad3 or Bub3 have been tagged were successfully tested for SAC proficiency.

cdc16-6A and *cdc27-5A* were gift from Andrew Murray (Department of Molecular and Cellular Biology and Center for Systems Biology, Harvard University, Cambridge, MA, ADR2032). *bub3*Δ strain was a gift by Simonetta Piatti (Centre de Recherche en Biologie Cellulaire de Montpellier (CRBM), CNRS, Montpellier, France). For details on additional copies of *CDC20* see Section 2.5.

Data acquisition

To immobilize cells, glass bottomed well chambers (Imaging Plate 5241-20; Zell-Kontakt, Germany) were pre-treated for at least 30 minutes with Bioconect (UCT, USA) followed by one ethanol and one water wash steps and incubated overnight at 4 °C with 1% ConcanavalinA (C2010; Sigma), followed again by two wash steps with water. At the time of the sampling, cells were briefly sonicated, then loaded in the chamber. Approximately 15 minutes after loading, medium and floating cells were carefully removed from wells and 150 μl of new medium was added. G1-phase cells were measured after growing 120 to 180 minutes in α-factor containing medium. Metaphase cells were measured 150 to 210 minutes after release in nocodazole from G1.

The experiments were performed in a room with controlled temperature ($\sim$ 23 °C), using a MicroTime 200 (PicoQuant, Berlin, Germany) time-resolved confocal microscope, controlled using both SymphoTime64 software (PicoQuant) and a custom written Java program (using libraries from Im-

ageJ Schneider et al. [2012] and μManager Edelstein et al. [2010]). Cells were excited using a $485\,nm$ pulsed laser diode head (LDH-D-C-485, PicoQuant), pulsing at $20\,MHz$ and a $561\,nm$ continuous-wave laser (Cobolt Jive, Cobolt). Power for both lasers was set such that count rates for both fluorophores were below 1% of pulse rate ($20\,MHz$) to avoid detector dead-time artifacts Nishimura and Kinjo [2005] and reduce photobleaching. Emitted light passed through band-pass emission filters [ET525/50 and ET632/60; Chroma Technology, VT, USA]. For more details on the microscope settings, see Šteflova et al. [2016].

Objective ring-collar was optimized at the beginning of each day to maximize the signal. The laser beam was positioned in the nucleus, identified by the signal from Mad2-GFP for MCC and APC/C^{inhib} measurements, or from Cdc23-mCherryfor APC/C measurements (Figure 3.7). Bright-field images were used to check the correct phase of the cell cycle of the acquired cells. Only one measurement per cell was performed, lasting 45 seconds. .

Data analysis

Auto- and cross-correlation functions were computed using FluctoAnalyzer Wachsmuth et al. [2015], correcting for background autofluorescence and green-to-red bleedthrough. The correction values were computed using control strains as in Maeder et al. [2007]. The background control strain has the same genetic background as target strains, and carries no fluorescent proteins. Bleethrough control strain carries Don1 tagged with the same GFPs used in the target strains.

The resulting functions were fitted, using FluctoAnalyzer, to a two-components model, assuming triplet-like blinking state. An explanation of the model can be found in Section 1.3. We first fitted the optical parameter κ using the calibration dyes. There is a κ for the green and one for the red channel, since the lasers have different wavelengths. This value is constant throughout the whole measurement session, since it only depends on the optical settings.

To compute acquisition volumes we fitted the autocorrelation curves of the calibration dyes Atto-488 and Atto-565. Acquisition volumes result from plugging into equation (1.11) κ and τ_D from the fitting, and imposing $420\mu m^2/s$ as the diffusion coefficient D. To measured the effective overlapping volume we used double-labeled probes (In vitro FCCS standards 488-543 nm, IBA, Göttingen, Germany): the overlapping volume was computed such that the concentration of the probe was the same when measured with the signal from either channel or with the cross-correlation.

The automated fitting pipeline returns a database of the fitted parameters, where each observation is a measured cell. This database was analyzed using an automatized pipeline written using RStudio RStudio Team [2015]. Concentrations are then computed as explained in Section 1.3. We identified as unreliable (e.g: trembling cells, laser beam too close to the outer membrane) and removed all measurements with $R^2 < 0.99$ for one of the two proteins ($\sim 5\%$ of the measurements). Similarly, measurements with $R^2 < 0.3$ for the cross-correlation fitting were removed ($< 0.1\%$). The reason why we used a lower quality threshold for the complex is to avoid removing cells where the two proteins

are not interacting (see a discussion on this topic in Section 2.7.1).

In Figures 3.20(a) and 3.20(b), the concentration of the complex was expressed in each cell as fold increase with respect to value of the *CDC20 1X* strain the same day. This is to take into account day-by-day variability. The normalization factor was choosen taking into account that the concentrations are distributed mainly lognormally. For this reason we did not use the mean of the signal, but rather

$$e^{\langle \log X \rangle}$$

where log is the natural logarithm, X the observed data and square brackets indicate the average over all the observations. In our results, statistical significancies are not altered by normalizing using the mean value.

Kolmogorov-Smirnov test was the choice for pairwise comparisons, either one-tail (for control) or two-tails. The following symbols are used: *ns* $p > 0.05$, * $p < 0.05$, ** $p < 0.01$, *** $p < 0.001$, **** $p < 0.0001$. p-values are explicitly written in the caption of each figure.

2.7.1 Quality of the fitting as additional measure of the complex formation

As explained in the Introduction (equation (1.13)), the concentration of the complex (C_{rg}) is zero only if G_{rg} is zero, since the other factors are positive unless the instrument is not correctly set ($V_{rg} = 0$) or one of the two channels gives no signal ($C_r = 0$ or $C_g = 0$). When fitting real measurements we do not have $G_{rg} = 0$, even if the two proteins are not interacting. Indeed, the observed cross-correlation in these cases is often positive (see Figure 2.5(a)). This background signal is negligible if the complex of interest is present at high concentration. In contrast, if the complex itself gives a dim signal, the background must be removed, or at least reduced. Since the complexes we are interested in are present at very low concentrations, we need to tackle this problem.

The background is due to the presence of cross-talk between the two channels (bleedthrough), expecially from the green to the red channel. As shown in Figure 2.4, the right tail of the eGFP spectrum overlaps the 'red filter'. This means that an eGFP can emit photons detected by the 'red counter'. This of course results in synchronous detection in the 'green' and 'red' detectors, which is by definition cross-correlation. The software we used for the analysis, FluctoAnalyzer Wachsmuth et al. [2015], partially corrects for this effect by using an average procedure. However, it does not completely remove it.

Other techniques can be used to improve the bleedthrough removal before computing the cross-correlation. In particular, the lifetime filtering Macháň et al. [2014] uses the information on the fluorophores' lifetimes (that is: the fluorophore-specific time from excitation to emission) to identify photons coming from one or the other emitter. A statistical filter gives, for each time-bin after excitation, a probability that photons falling in that bin belong to one or the other emitter. Removing 'false red photons' identified by the lifetime of the green-emitting fluorohore, removes the bleedthrough,

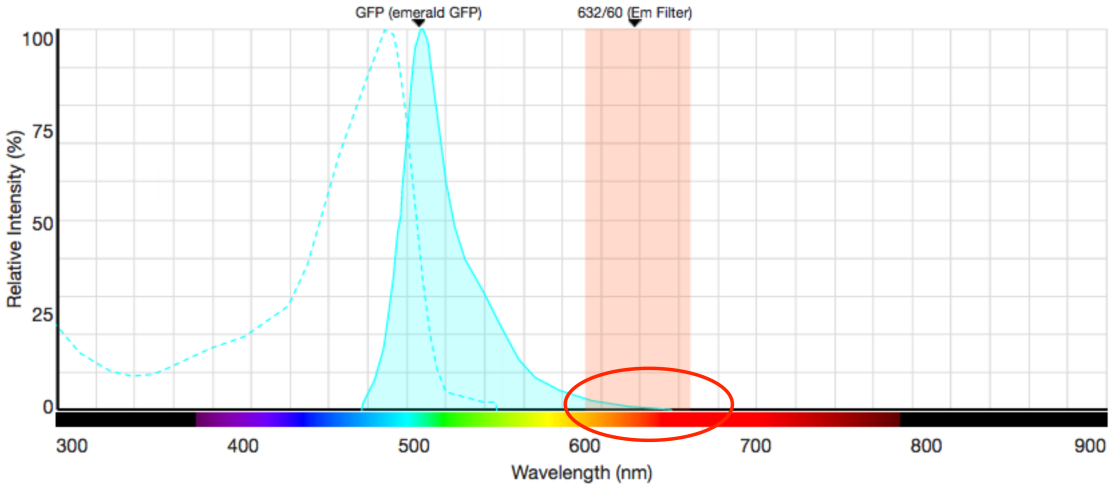

Figure 2.4: Bleedthrough in cross-correlation measurements.
Emission spectrum of eGFP (light-blue filled area) reaches the values of wavelength detected by a 'red filter' (red shaded rectangle). The parameters of the 'red filter' are the same of the filter used in our experiments. In the red circle, the overlap between the spectrum and the filter.
Image produced using http://www.thermofisher.com/it/en/home/life-science/cell-analysis/labeling-chemistry/fluorescence-spectraviewer.html.

photon by photon.

We dealt with the background signal using a different approach, which can be explained by comparing the cross-correlation curves presented in Figure 2.5. Circles are the measured cross-correlation, while the solid line represents the fit. The strain presented in Figure 2.5(a) is a negative control, since it carries eGFP-Don1 and Ste11-mCherry, two proteins that do not interact Maeder et al. [2007]. The other strain, presented in Figure 2.5(b), is a positive control, since it carries Mad2-GFP and Cdc23-mCherry in a condition where the two proteins interact. Curves are processed with the average bleedthrough removal of FluctoAnalyzer Wachsmuth et al. [2015], as we did in the Results chapter. Yet, the $G(0)$ of the negative control is not 0, and thus the measurement does not give zero concentration for the complex. In particular, $G(0)$ for negative and positive controls are roughly the same (0.004 and 0.005).

However, the fitting of the negative control is much worse than the one of the positive. To quantify the quality of each fitting, we used the R^2 returned by FluctoAnalyzer, defined as:

$$R^2 = \frac{\sum_{i=1}^{n}(\hat{y}_i - \bar{y})^2}{\sum_{i=1}^{n}(y_i - \bar{y})^2},$$

where n is the number of the observed values y_i, $\hat{y}_i$ are the fitted value, and $\bar{y}$ is the average of the observed values. As in linear regressions, the maximum value for R^2 is 1. Other properties of R^2 are not retained in non-linear models (such as non-negativity). Albeit suboptimal, we found that R^2 is a good proxy of the quality of fitting.

We used the quality of the fitting, together with the amplitude of the signal, as measures of the quality of the signal detected by the protein pairs we selected to measure MCC and APC/C^{inhib}. Both measures give significant difference between positive and negative controls (see Figure 3.18).

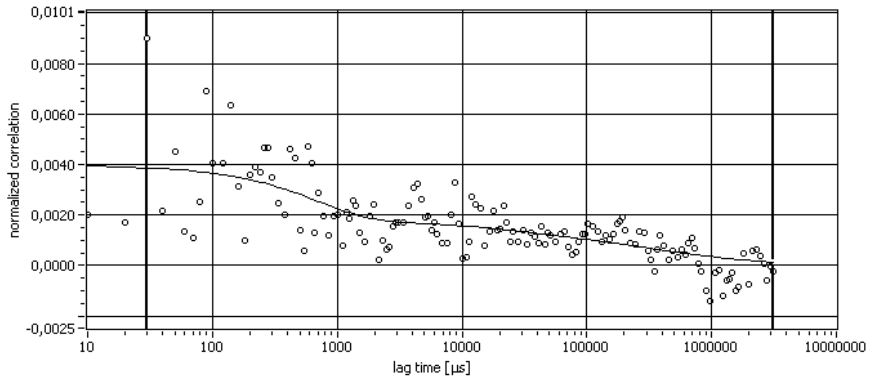

(a) Negative control for cross-correlation

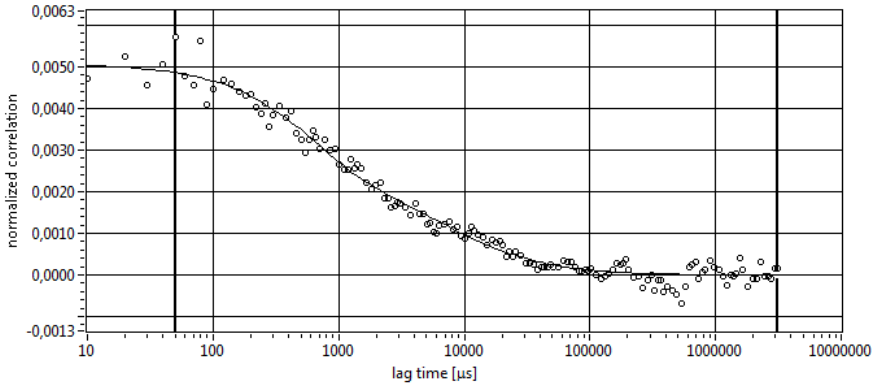

(b) Positive control for cross-correlation

Figure 2.5: Positive and negative control for cross-correlation signal in FCCS.
Croo-correlation data and fitted curves for negative and positive controls.
Negative control carries eGFP-Don1 and Ste11-mCherry, two proteins that do not interact Maeder et al. [2007].
Positive control carries Mad2-GFP and Cdc23-mCherry in a SAC-proficient strain. The cell is arrested in nocodazole, so APC/C^{inhib} is formed and the two proteins interact.

2.8 Pulse experiments and controls

This section refers to results presented in Section 3.5.

Strains, media and reagents

To control for methionine presence or absence, we used synthetic low-fuorescent medium, prepared using nitrogen bases lacking ammonium sulphate, supplemented with ammonium sulphate. The medium is either complete or lacking methionine, supplemented with 2% raffinose (SCR, SCR-met) or 2% raffinose and 2% galactose (SCRG, SCRG-met). Methionine was added at $2\,mM$ or $2.6\,mM$.

Cells were arrested in G1, and supplemented with galactose during the last hour of the arrest to induce *GAL1* promoter. Cells were released into synthetic complete medium, with galactose and raffinose (SCRG). To induce a 'pulse' of exogenous Cdc20, the medium was temporarily switched to SCRG-met. First pulse in Figure 3.23(a) was given at 110 minutes after G1 relase, and lasted 35 minutes. Second pulse in the same figure was given 170 minutes after G1 release, and lasted 35 minutes.

Plasmid construction and genetic manipulation

Plasmid pAC130 carrying *MET3pr-CDC20* construct was synthetized by Epoch Life Science and contains -600bp of *MET3* promoter and *CDC20* ORF from ATG to +392bp. *MET3pr-CDC20* from pl130 was cloned in YipLac211 (KpnI/PstI) and integrated at *URA3* locus by digestion with NcoI. Single integration was checked by Southern blot analysis. *MET3* promoter from plasmid pAC130 was cloned in in PacI/NotI sites of plasmid pGC25 (a gift from Fred Cross, Center for Studies in Physics and Biology, The Rockefeller University, New York, NY 10065, USA; from Charvin et al. [2008]) to obtain *MET3pr*-yEVenus (plasmid pAC136). pAC136 integration was directed at *TRP1* locus by XbaI digestion. Single integration was checked by Southern blot analysis

For the coupling experiment (Figure 3.22(a)), *MET3pr*-mCherry was synthetized by Genscript and cloned in BamHI/EcoRI of Yiplac211 to give plasmid pAC156. It contains 600bp of *MET3* promoter and 392bp of *CDC20* terminator (as in pl130). mCherry sequence has a silent mutation to remove internal NcoI site. pAC156 was inserted at *URA3* site by NcoI digestion. Single integration was checked by Southern Blot.

To obtain plasmid pAC97, *CLN2* promoter from *CLN2pr*-Venus^{degron} (a gift from Fred Cross, Centre for Studies in Physics and Biology, The Rockefeller University, New York, USA, see Charvin et al. [2010b,a]) was swapped with *CDC20pr* (412bp) obtained from the plasmid used for Cdc20 tagging in Shirayama et al. [1998]. *CDC20pr*-Venus^{degron} from pAC97 was cloned by PCR duplication at *CDC20* locus Huber et al. [2014].

HTB2-mCherry was a gift from Fred Cross (Center for Studies in Physics and Biology, The Rockefeller University, New York, USA)

Image acquisition

MET3pr-Venus, *MET3pr*-Venus^{degron} and *CDC20pr*-Venus^{degron} were acquired using a single Z-stack, 10% lamp power, 0.05 seconds. Ht2b-mCherry was acquired with a single Z-stack, 10% lamp power, 0.15 seconds exposition.

Image analysis

To estimate Venus synthesis rate (i.e., activity) from the *MET3pr* or *CDC20pr* (Figures 3.12(d), 3.22(a), 3.22(b), 3.23(d)), the time of promoter activation was identified by the maximum of the second derivative. The raw signal was smoothed using a moving window of size 4. From the moment of promoter activation for a minimum of 40 minutes the signal was fitted with a straight line. Promoter activity was identified as the slope of the fitted line, similarly to what proposed in Charvin et al. [2010b] (see Figure 2.6 for details).

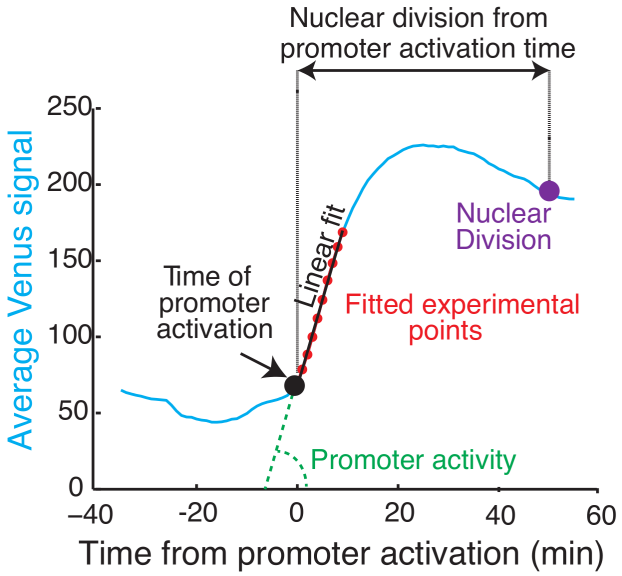

Figure 2.6: Measures obtained from the Venus fluorescence.
Nuclear division (purple dot) was detected by eye using Htb2-mCherry fluorescence. The time of promoter activation was identified by the second derivative of the smoothed fluorescence signal (black arrow). The linear fit was done on experimental data (red dots) for at least 40 minutes after the promoter activation (black line). The slope of the fitted line (green line and angle) was used to compute promoter activity. Image taken from Bonaiuti et al. [2017].

2.9 Single-cell experiments using Cdc20-sfGFP

This section refers to results presented in Section 3.5.1.

Strains, media and reagents

Cells were grown in YP medium (1% yeast extract, 2% Bacto Peptone, 80 mg/l adenine) supplemented with 2% glucose (YPD), arrested in G1 and released into nocodazole.

Plasmid construction and genetic manipulation

N-terminal tagging of *CDC20* with sfGFP was obtained by 'seamless gene tagging' strategy Khmelinskii et al. [2011]. The sequence including sfGFPΔC-I-SceI^{site}-*CYC1term-URA3-NOP1pr*-I-SceI^{site}-sfGFP was amplified by PCR from plasmid pMaM189, and targeted to *CDC20* by designing appropriate oligos. Transformation produced strain yAC3415, in which the correct integration was checked by PCR and fluorescence microscopy. *GAL1pr-I-SCEI* was targeted to *LEU2* locus by digesting plasmid pND32 with SspI. The strain resulting from transformation, yAC3429, was crossed with yAC3415. The *URA3* marker was excised from the resulting strain by growing it onto galactose-containing plates. Correct excision was checked on plates lacking uracile and on plates containing 5-fluoroorotic acid (5-FOA). Finally, *GAL1pr-I-SCEI* was removed by crossing.

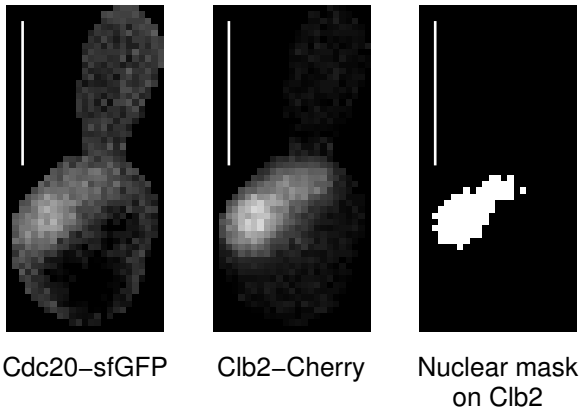

Figure 2.7: Identification of nuclear pixels using Clb2 signal.
The nucleus is identified using a k-means cluster analysis on Clb2-mCherry signal. Cdc20-sfGFP signal was average only on nuclear pixels. Scale bars are $5\,\mu m$.

Image acquisition

Images are acquired using a DeltaVision Elite imaging system with the same components as to the one presented in Section 2.1. The only difference is the camera. Here we used a Scientific CMOS camera (Photonics).

Images were acquired every 10 minutes for 700 minutes using 5 Z-stacks spaced $0.2\,\mu m$. Cdc20-sfGFP was acquired at 10% lamp power for 0.1 seconds each stack, Clb2-mCherry at 10% lamp for 0.2 seconds each stack. Both channels were projected using the average intensity projection.

Image analysis

Clb2-mCherry signal was analysed as explained in Section 2.3. To analyse Cdc20-sfGFP, we measured its nuclear signal. The nucleus was identified by k-means clustering on Clb2-mCherry signal (see Figure 2.7), since this protein accumulates in the nucleus during the mitotic arrest (see Section 1.1.2). For this reason, we can identify the nucleus only between Clb2 accumulation and degradation. This procedure mirrors the one presented and discussed in Vernieri et al. [2013].

Chapter 3

Results

3.1 Clb2 degradation takes place during an active arrest

Two are the possible ways for cells to escape a prolonged mitotic arrest: either after silencing the checkpoint, or in the presence of an active checkpoint. In the first case, the signalling is switched off, and cells restore proliferation in the absence of any 'stop signal'. In the second case, the SAC machinery is active but cells, somehow, overcome it. No clear evidence have been provided so far for either of the two scenarios. To address this point, we followed in real-time, using single-cell fluorescence microscopy, the metaphase-to-anaphase transition and checkpoint activity. We selected as a marker of entry into anaphase the degradation of Clb2 (see Section 1.1.1), and as a marker of checkpoint activity the localization of Mad2 at kinetochores (see Section 1.1.2). To record this information, we used strains carrying the two proteins tagged with fluorophores. Tagging Clb2 with mCherry did not alter its protein dynamics (Figure 3.1(a)). For what concerns Mad2-GFP, in nocodazole it colocalized with Bub3-mCherry (Figure 3.1(b)), which resides at kinetochores during mitosis Kerscher et al. [2003], Gillett et al. [2004] (see Section 1.1.2). This results implies that Mad2-GFP also localizes at kinetochores in nocodazole, as expected in the presence of spindle damage Gillett et al. [2004].

To measure the SAC activity and the length of the mitotic arrest, cells were arrested in G1, released into nocodazole and grown in microfluidic chambers. Cells were prevented from entering into S-phase after adaptation by administration of α-factor, together with nocodazole, one hour after G1-release. A fully automated analysis pipeline identified the duration of metaphase (defined as the time between Clb2 accumulation and degradation) and Mad2 localization. The latter was measured by a 'Mad2 localization index', whose value is high when the protein is localized (see Sections 2.3 for details on the analysis pipeline).

The discrimination between localized and delocalized Mad2 was obtained by applying a theshold: above this value we considered Mad2 as localized, below as not localized. We set this value higher than what we measured in G1-arrested cells, where Mad2 is not localized at kinetochores (see Section 1.1.2).

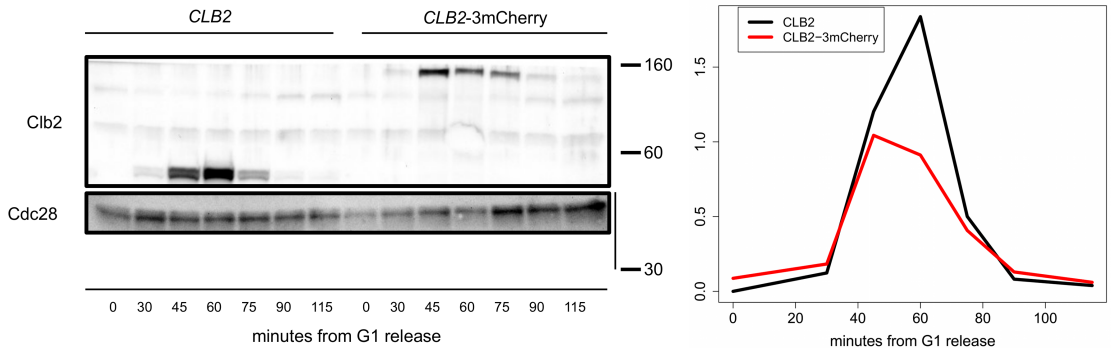

(a)

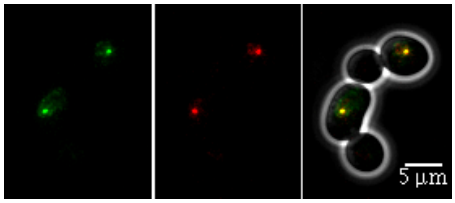

(b)

Figure 3.1: Quality control of tagged protein for adaptation experiments
a) Left panel: Western blot analysis of Clb2 in *CLB2* and *CLB2*-mCherry cells (strains yAC3202 and yAC3509). Cells were arrested in G1, released in fresh medium and sampled at the indicated timepoints. Right panel: Quantification of Clb2 signal, normalized to Cdc28. **b**) Cells carrying Mad2-GFP (in green) and Bub3-mCherry (in red) (yAC3266) were arrested in G1 and released into nocodazole-containing medium, then imaged after two hours. 20 Z-stacks were deconvolved and projected. See Section 2.2 for details on the protocol. Image taken from Bonaiuti et al. [2017].

The identification of cells adapting with localized Mad2 was robust to our choice of the threshold (see Figure 2.3 and Section 2.3 for details). The complete dataset of observations consisted of 326 *CDC20 1X* cells, analyzed in 3 biologically independent replicates (see Table 4.1 for details).

The result of this analysis showed that in the large majority of cells (83%) Mad2 was still localized when Clb2 degradation started. In a much smaller fraction (13%), Mad2 delocalized before Clb2 degradation (Figure 3.2(d)). Examples of fluorescence traces from cells belonging to each of the two groups can be found in Figure 3.2(a) and Figure 3.2(b). In the remaining 4% of cells we could not identify Clb2 degradation even if Mad2 delocalized from kinetochores (Figure 3.2(c)).

Cells where Mad2 was not localized at the time of Clb2 degradation have a median of arrest of 375 minutes as opposed to 120 minutes for cells adapting with localized Mad2. Since the effect of nocodazole may have faded with time, in these cells Clb2 degradation may be a consequence of microtubule repolymerization, although we cannot exclude that they adapt with an alternative mechanism. Our further analyses were performed on cells degrading Clb2 with localized Mad2, as they represented the large majority of our observations.

So far, our analysis focused on SAC activity at the time of Clb2 degradation. To investigate what happens before and after this event, we plotted the distribution of Clb2 levels and Mad2 localization for different time-points around Clb2 degradation (Figure 3.3). Neither of the two proteins changed its readout during 30 minutes preceding Clb2 degradation. However, the levels of Clb2 were largely diminished already 20 minutes after the start of its degradation, which was complete within 40 minutes.

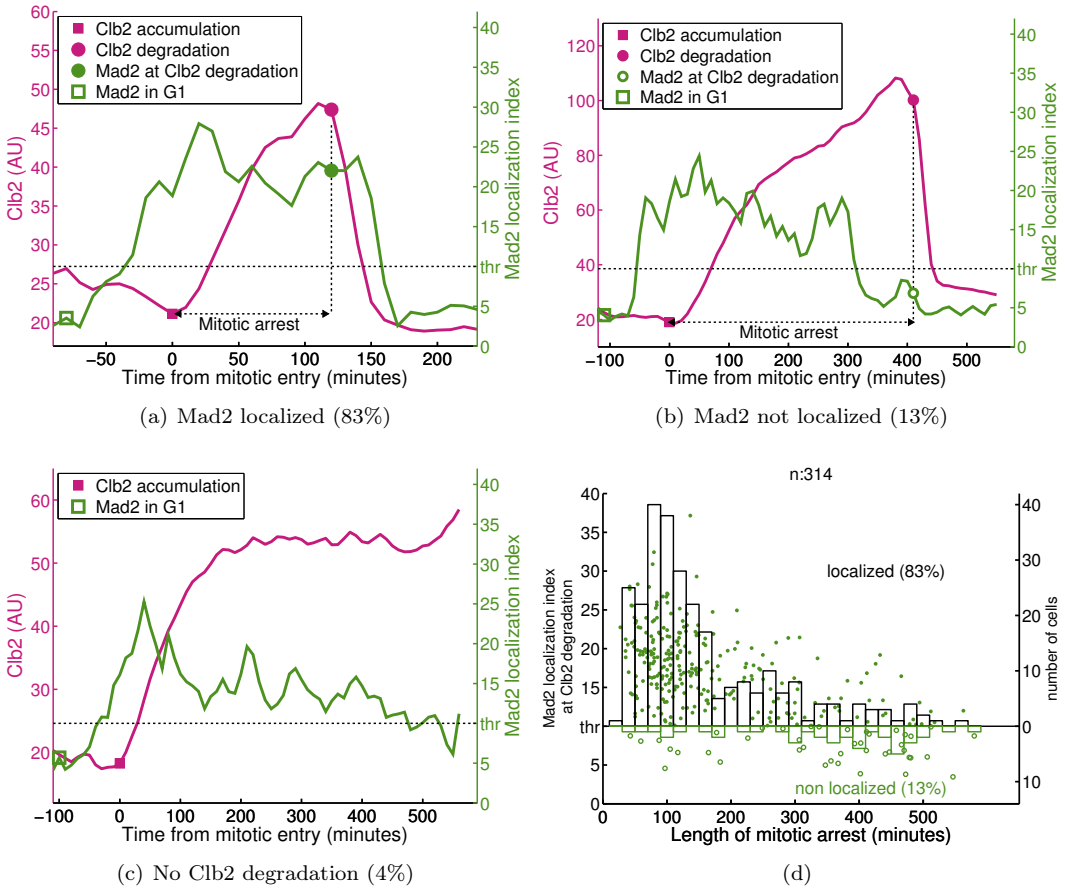

(a) Mad2 localized (83%)

(b) Mad2 not localized (13%)

(c) No Clb2 degradation (4%)

(d)

Figure 3.2: Clb2 degradation occurrs in the presence of Mad2 localized at kinetochores Cells carrying Mad2-GFP Clb2-mCherry (yAC3538) were arrested in G1 and released into nocodazole. **a-c**) Examples of single-cell traces of Clb2-mCherry mean signal and Mad2-GFP localization index. Clb2 accumulation and degradation were automatically identified as explained in Section 2.3. **a**) A cell degrading Clb2 in the presence of localized Mad2. **b**) A cell degrading Clb2 when Mad2 is no longer at kinetochore. **c**) A cell where no Clb2 degradation is recorded. **d**) Scatterplot of Mad2 localization index at Clb2 degradation, for cells where this event takes places (panels **a-b**). Cells with values above threshold are depicted as filled dots, empty otherwise, as in panels **a-b**. The histogram pointing upward refers to cells above threshold, downward to cells below threshold. Number of independent biological replicates (N): 3, number of observations (n): 314 (see Table 4.1 for details on the observation dataset). Image adapted from Bonaiuti et al. [2017].

Mad2 delocalization followed a similar dynamics, but delayed compared to Clb2 degradation and less homogenous, with some cells still having Mad2 localized well after Clb2 degradation.

Thus, our data show that in the large majority of cells anaphase is initiated in the presence of active SAC-signalling by Mad2 at kinetochores. The degradation of Clb2 is followed by a slower and incomplete delocalization of Mad2. These observations are consistent with a 'slippage' model in which cells leave mitosis despite an active checkpoint.

3.2 A model of the mitotic checkpoint reproduces adaptation dynamics

Having demonstrated that cells adapt to an active SAC, we asked how that happens. To this aim, we analysed the phenomenon of adaptation using cumulative distribution functions. When we plotted

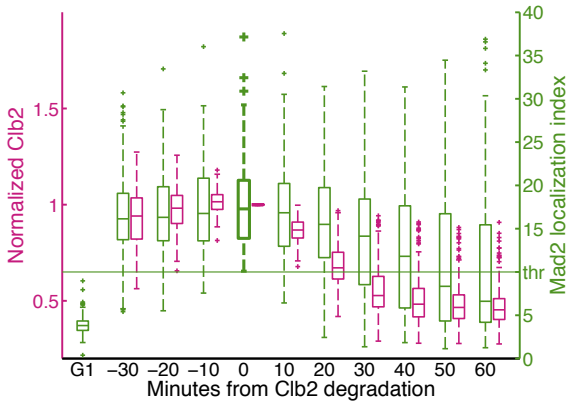

Figure 3.3: After Clb2 degradation, Mad2 delocalization is slow and uncomplete
Boxplots of Mad2 localization index (green) and Clb2 (purple) at the indicated time points before and after Clb2 degradation (t=0). In G1 we show only Mad2 localization. For each cell, Clb2 is normalized on its value when degradation starts. Only cells with Mad2 localized at kinetochores at Clb2 degradation are included (black histogram in Figure 3.2(d)). N: 3; n: 272 (see Table 4.1 for details on the observation dataset).
Image taken from Bonaiuti et al. [2017].

the empirical cumulative distribution function of adaptation times, measured from Clb2 accumulation to Clb2 degradation ('mitotic arrest' shown in Figure 3.2(a)), we observed an exponential-like shape, with no cells adapting in the first 40 minutes (Figure 3.4).

We asked whether this distribution could arise from a model in which the steady-state levels of APC/C^{Cdc20} were kept below a critical 'anaphase threshold' by an operational SAC, but where random fluctuations could overshoot the threshold and drive cells into anaphase.

3.2.1 Construction of the model

To test this idea, we constructed a simple mathematical model of the SAC network and tested whether it can reproduce the observed cumulative distribution of adaptation times. Our model is based on the following core data, explained in detail in Sections 1.1.1 and 1.1.2, and summarized in the protein network depicted in Figure 3.5:

- the only molecular species being synthesized and degraded is Cdc20 Liang et al. [2012], Nilsson et al. [2008], Pan and Chen [2004];
- degradation takes place primarily from the inhibited form of APC/C, *in cis* Foe et al. [2011], Foster and Morgan [2012];
- when the SAC is not active, Cdc20 binds and activates APC/C Primorac and Musacchio [2013];
- when the checkpoint is engaged, it drives the formation of MCC, which can bind and inhibit the active APC/C^{Cdc20} giving rise to the inhibited species APC/C^{inhib} Izawa and Pines [2015], Alfieri et al. [2016].

The protein network depicted in Figure 3.5 can be translated into a system of ordinary differential equations (ODEs), using the law of mass action as explained in Section 1.2.1. Since the binding

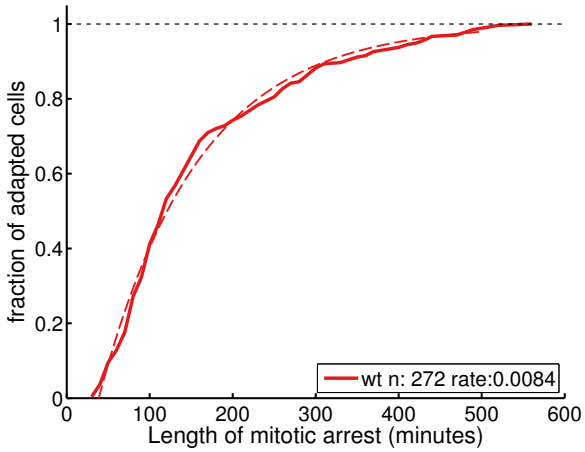

Figure 3.4: The cumulative distribution of metaphase arrest is fitted by an exponential curve
Cells carrying Mad2-GFP Clb2-mCherry (yAC3538) were arrested in G1 and released in nocodazole. We measured for each cell the time spent in metaphase, as defined in Figure 3.2(a). We included cells where Mad2 is localized at kinetochores at the time of Clb2 degradation (black histogram in Figure 3.2(d), example of single-cell trace in Figure 3.2(a)). The observed cumulative distribution of these times is plotted as solid line and fitted with an exponential curve (dashed line). The fitting starts after the delay, and has the rate of adaptation as the only free parameter. N: 3, n: 272 (see Table 4.1 for details on the observation dataset).
Image taken from Bonaiuti et al. [2017].

reactions are reversibile, both an association and dissociation reactions are included. The variables involved in the ODEs are the concentrations of the different molecular species: the concentrations of Mad2, Mad3 and Bub3 are lumped together in a single variable $[M]$, Cdc20 concentration is described by $[C]$, APC/C concentration by $[A]$, MCC by $[MC]$, APC/C^{Cdc20} by $[AC]$, APC/C^{inhib} by $[ACMC]$. The resulting ODE system is the following:

$$\begin{cases} \dfrac{\mathrm{d}[C]}{\mathrm{d}t} = s - a_{MC}[M][C] + d_{MC}[MC] - a_{AC}[A][C] + d_{AC}[AC] + D[ACMC] - D_{bkg}[C] \\ \dfrac{\mathrm{d}[MC]}{\mathrm{d}t} = a_{MC}[M][C] - d_{MC}[MC] - a_{ACMC}[AC][MC] + d_{ACMC}[ACMC] - D_{bkd}[MC] \\ \dfrac{\mathrm{d}[AC]}{\mathrm{d}t} = a_{AC}[A][C] - d_{AC}[AC] - a_{ACMC}[AC][MC] + d_{ACMC}[ACMC] - D_{bkg}[AC] \\ \dfrac{\mathrm{d}[ACMC]}{\mathrm{d}t} = a_{ACMC}[AC][MC] - d_{ACMC}[ACMC] - D[ACMC] - D_{bkg}[ACMC] \end{cases} \tag{3.1}$$

Association and dissociation constants are represented by the parameters a and d, respectively. Subscripts indicate which is the product of the reaction the parameters refer to. In numerical simulations, association and dissociation constants are assumed to be the same for all the reactions (see next paragraph for a robustness analysis related to this assumption). s and D are the parameters for synthesis and degradation, respectively, of Cdc20, the only protein synthesised and degraded. A small background degradation D_{bkg}, introduced for numerical stability, acts on all the molecular species that include Cdc20.

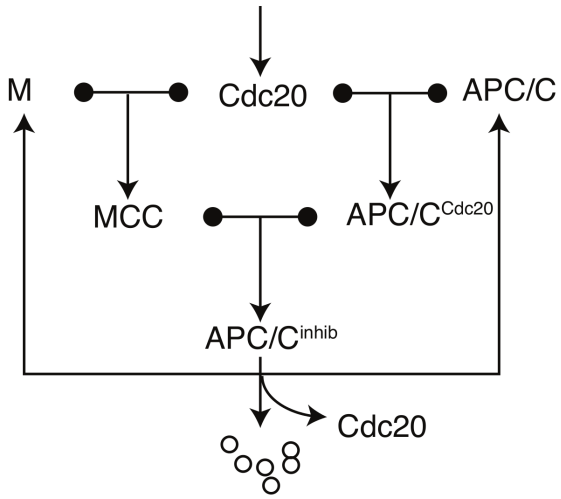

Figure 3.5: Scheme of the SAC protein network
Scheme of the reactions comprising the SAC protein network, as described in Sections 1.1.1 and 1.1.2. The arrow pointing at Cdc20 represents its synthesis. Bullet points in every association/dissociation reaction represent reversibility. The absence of bullet points in APC/C^{inhib} disassembly represents its irreversibility, since it implies the degradation of one molecule of Cdc20.
This same scheme is presented in the Introduction (Figure 1.4).
Image taken from Bonaiuti et al. [2017].

Since the total amounts of APC/C and Mad2, Mad3 and Bub3 are constant, the variables not explicitly included in the ODE system (3.1) can be determined by using the conservation laws:

$$\begin{cases} [A_{tot}] = [A] + [AC] + [ACMC] \\ [M_{tot}] = [M] + [MC] + [ACMC] \end{cases}$$

It is easy to prove that the dynamics of Cdc20 total is:

$$\begin{aligned} [C_{tot}] &= [C] + [AC] + [MC] + 2[ACMC] \\ \frac{\mathrm{d}[C_{tot}]}{\mathrm{d}t} &= \frac{\mathrm{d}[C]}{\mathrm{d}t} + \frac{\mathrm{d}[AC]}{\mathrm{d}t} + \frac{\mathrm{d}[MC]}{\mathrm{d}t} + 2\frac{\mathrm{d}[ACMC]}{\mathrm{d}t} \\ &= s - D[ACMC] - D_{bkg}[C_{tot}] \end{aligned} \tag{3.2}$$

3.2.2 Parameters of the model

Parameters of the model are largely based on experimental results. To estimate synthesis and degradation rates of Cdc20, we first quantified indirectly its concentration during a mitotic arrest, noticing that Cdc20 is expressed roughly as Cdc23 (lower panel, Figure 3.6(c)). Myc-tagging did not alter the levels of either proteins (upper panels, Figure 3.6(c)). To quantify Cdc23 concentration, as well as other APC/C subunits and MCC members, we used Fluorescence Correlation Spectroscopy (FCS), a technique that uses the diffusion of fluorescently-labeled proteins to measure their concentration (see Section 1.3). For Cdc23 concentration, we measured $\sim 70\,nM$ (Figure 3.6(b)). We thus assumed that Cdc20 concentration during mitotic arrest of wild-type strain has the same value. Cdc20 half-life was

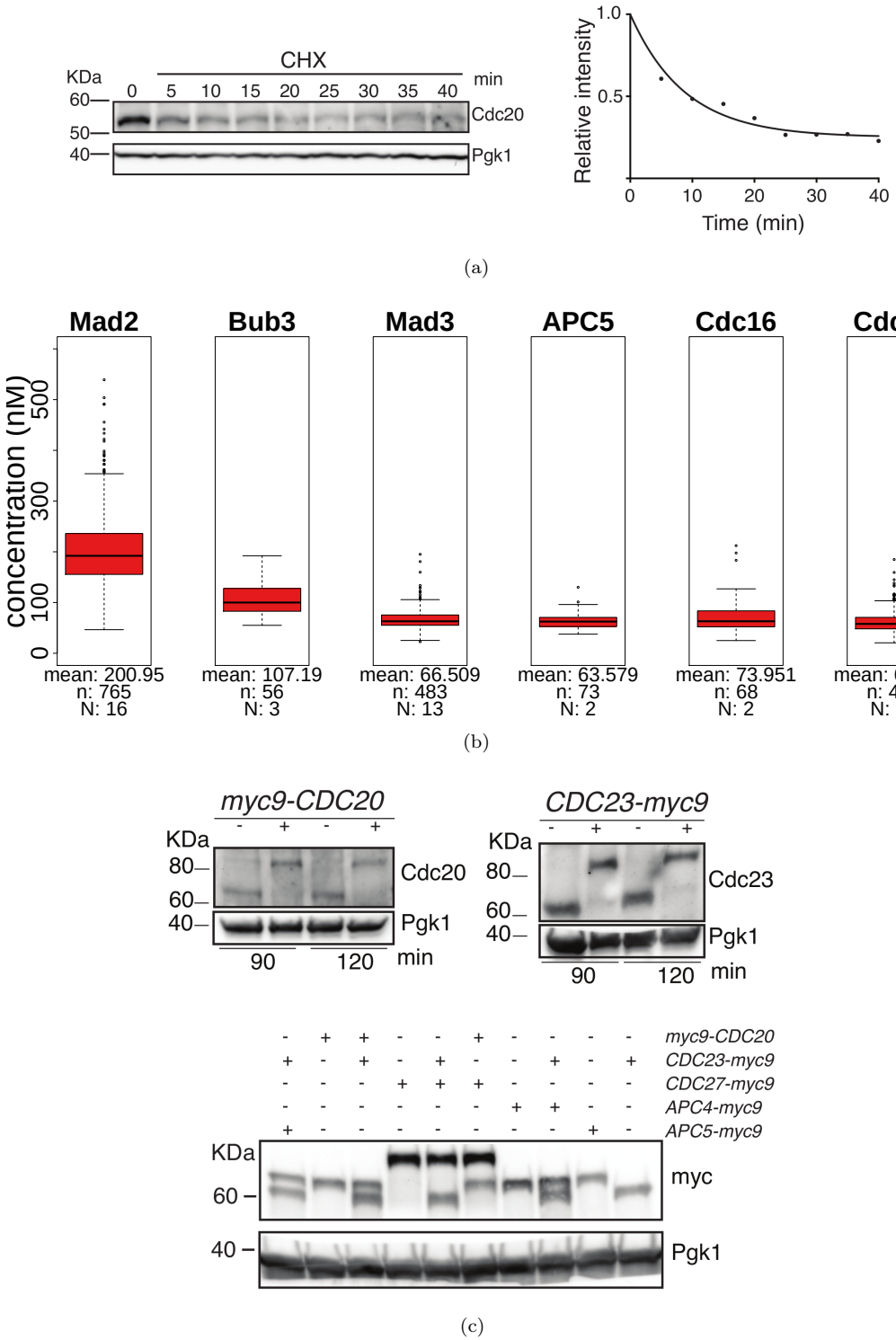

Figure 3.6: Parameter estimation
a) Wild type cells (yAC1070) were arrested in G1 and released into nocodazole. After 120 minutes we added cycloheximde (CHX) and sampled cells for western blotting. Right panel: quantification of the the signal of Cdc20 normalized to Pgk1. The data shown are from single representative experiment out of four repeats. **b**) Cells carrying Mad2-GFP, Bub3-GFP, Mad3-mCherry or Cdc23-mCherry (strains yAC3268, yAC2886 and yAC2940) were arrested in G1 and released into nocodazole at 23 °C. After 150 minutes, for 60 minutes, FCS measurements were performed to estimate the concentration of the protein, as explained in Section 2.7. n and N written at the bottom of each boxplot. **c**) Upper panels: wild-type cells or cells carrying myc9-Cdc20 or Cdc23-myc9 (yAC3202, yAC3307, yAC3371) were arrested in G1 and released into nocodazole. At the indicated time points samples were taken for western blotting. N: 1. Lower panel: cells of the indicated genotypes (strains yAC3430, yAC3307, yAC3367, yAC3365, yAC3436, yAC3353, yAC3261, yAC3427, yAC3262, yAC3371) were arrested in G1 and released into nocodazole. After 110 minutes, samples were taken for protein extract preparation and immunoblotted with anti-myc antibodies. N: 2.
Experiments in panels **a** and **c** perfomed by Elena Chiroli. Image adapted from Bonaiuti et al. [2017].

set to $\sim$ 7 minutes (similar to what measured in Pan and Chen [2004], Foster and Morgan [2012]), by fitting the kinetics of protein degradation in the presence of cycloheximide (Figure 3.6(a)). Synthesis was chosen accordingly, to keep Cdc20 $\sim 70nM$ during an arrest. To ensure the presence of a stable steady state, we introduced the small background degradation rate acting on all molecular species that include Cdc20. This background degradation, APC/C-independent, is chosen arbitrarily to be 5 times smaller than the APC/C-dependent degradation, but a different value would have equally led to a steady-state, as long as the degradation acts on all molecular species that include Cdc20 (see Section 1.2.1). The presence of a steady-state is suggested by the observation that the effects of a transient overexpression of Cdc20 are time-independent (see later, Figure 3.23(a)).

The values of MCC dissociation constant ($K_{D,MC} = \frac{d_{MC}}{a_{MC}}$) and APC/C^{inhib} dissociation constant ($K_{D,ACMC} = \frac{d_{ACMC}}{a_{ACMC}}$) are also based on experimental data. MCC dissociation constant is in the order of nM according to Faesen et al. [2017]. We estimated $K_{D,ACMC}$ indirectly, as follows. IC50 for MCC on APC/C^{Cdc20} was measured to be $4\,nM$ Foster and Morgan [2012]. In first approximation, this result implies that active APC/C^{Cdc20} reaches half-maximal levels at $4\,nM$ of inhibitor, and suggests a value of $K_{D,ACMC}$ around this order of magnitude. Albeit indirectly, these data indicate that $K_{D,MC}$ and $K_{D,ACMC}$ are in the same order of magnitude. We used for both of them $10\,nM$. We found no evidences for $K_{D,AC}$, however, it is reasonable to suppose it is not lower than $K_{D,ACMC}$. We used $10\,nM$ for this dissociation constant too. A robustness analysis on K_Ds is presented in Section 3.2.3. For association constants, which have not been measured, as far as we are aware, we used reasonable numbers. Association of APC/C to MCC or Cdc20 is in the same order of the association constants of the E2 Ubch10 with APC/C Chang et al. [2014]. For MCC formation, we took values comparable with the rate-limiting step, that is Mad2-dimerization Simonetta et al. [2009].

For what concerns the total amount of proteins that interact with Cdc20 in forming MCC, M_{tot}, we used the concentrations measured with FCS (Figure 3.6(b)). Since we found that Mad3 is less abundant than Mad2 and Bub3, and thus limiting in MCC formation, we gave to M_{tot} a value close to its concentration, $80\,nM$.

For what concerns the total amount of APC/C, A_{tot}, we measured the concentration of some of its components, as well as the concentration of the complex. Among the APC/C components that we investigated using both western blot (lower panel in Figure 3.6(c)) and FCS (Figure 3.6(b)), Cdc23 resulted the less abundant, and thus its concentration is an upper limit for A_{tot}. Since Cdc23 is present in two copies in APC/C Primorac and Musacchio [2013], the actual upper limit is half of this value, $\sim 30\,nM$. To directly measure APC/C concentration, we used Fluorescence Cross Correlation Spectroscopy (FCCS). This technique, related to FCS, measures protein-protein interaction using as proxy the codiffusion, in femtoliter volumes, of the proteins of interest detected by fluorescent labeling (see Section 1.3). To measure APC/C formation, we measured the codiffusion of Cdc23 with Cdc16, and of Cdc23 with APC5. All the three subunits are essential in APC/C Giaever

et al. [2002]. Both the protein pairs (Cdc23/Cdc16 and Cdc23/APC5), measure APC/C in very low concentration ($\sim 20nM$), as shown in Figure 3.7. This result is close to the upper limit defined by Cdc23 concentration, and further confirms the low abundance of APC/C. To set the value for A_{tot}, we applied, as conservative choice, a factor 2 to the direct measurement of APC/C. We thus assumed $A_{tot} = 40\,nM$. We will see that the low abundance of complexes, expecially APC/C, plays a key role in the dynamics of adaptation to the SAC. Table 4.3 gives an overview of the parameters and their references.

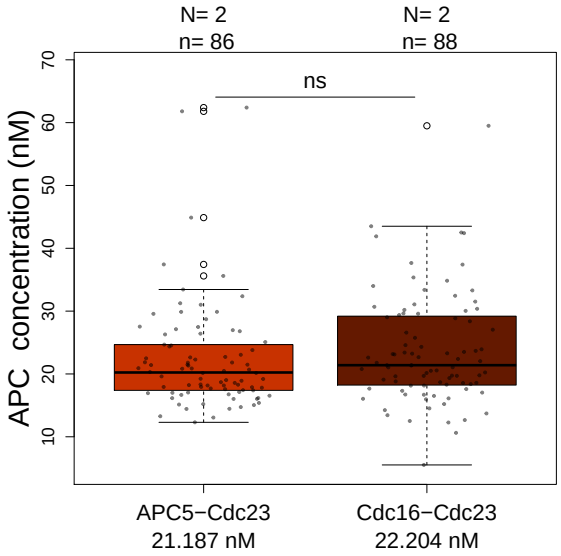

Figure 3.7: Direct measure of APC/C concentration
Cells carrying APC5-GFP and Cdc23-mCherry ('APC5-Cdc23' in the figure, strain yAC2932) or Cdc16-GFP and Cdc23-mCherry ('Cdc16-Cdc23' in the figure, strain yAC2954) were arrested in G1 and released into nocodazole. FCCS measurements were performed after 150-210 minutes, and absolute concentration of APC/C was measured. Kolmogorov-Smirnov two tails test reject the hypothesis of the two distributions being different ($p = 0.314$). The concentrations written in the legend are the central value of the distributions (see Section 2.7), that is the exponential of the mean of the logarithm of the data ($e^{\langle \log X \rangle}$), that takes into account the lognormality of the distributions. See Section 2.7 for details on the protocol.

3.2.3 Robustness of the model to changes in parameter or wiring

The model mainly relies on experimental data, but the values of K_Ds, their homogeneity, and the product of APC/C^{inhib} disassembly, are not well established. Moreover, in our model we made an important assumption, lumping together Mad2, Mad3 and Bub3 in a single variable M. To measure the robustness of the model to these assumptions and less well defined parameters, we used bifurcation diagrams. These plots relate the steady-state value of a variable of a system with the changes of a specific parameter of the system, called bifurcation parameter (see Section 1.2.1). We chose as bifurcation parameter s, the synthesis of Cdc20.

First, we analysed the choice of using a common value for all the K_Ds. As explained previously, in the model we assume that the as and ds, the association and dissociation constants, are equal for the three binding reactions. This means that the K_Ds of the three reactions, defined as $K_D =$

$\frac{d}{a}$, share the same value. In the model we set it to $10\,nM$, in the same order of magnitude as what found for MCC Faesen et al. [2017]. To investigate the robustness of the model, we doubled or halved it to $20\,nM$ or $5\,nM$, and performed a bifurcation analysis on the steady-state levels of APC/C^{Cdc20} and APC/C^{inhib}. The resulting plots are very similar to what obtained when $K_D = 10$ (left plot, Figure 3.8(a)). It is worth noticing that the steady-state levels do not depend on a and d separately, but only on K_D, while a and d determine the dynamics of the system to reach the steady-state (see Section 1.2.1).

The second analysis we performed aimed at investigating how the model behaves if we assume different K_Ds for different reactions. We thus modulated one K_D at a time, while the other two are set to $10\,nM$. We performed this analysis on the estimated $K_{D,AC}$ and $K_{D,ACMC}$, but not on $K_{D,MCC}$, since this value was directly measured Faesen et al. [2017]. The resulting bifurcation diagrams are very similar to the one with $K_D = 10\,nM$ (center and right plot, Figure 3.8(a)). These results show that the system is not sensitive to changes in affinities of the association reactions, suggesting that its response to changes in Cdc20 synthesis only depends on the topology of the network.

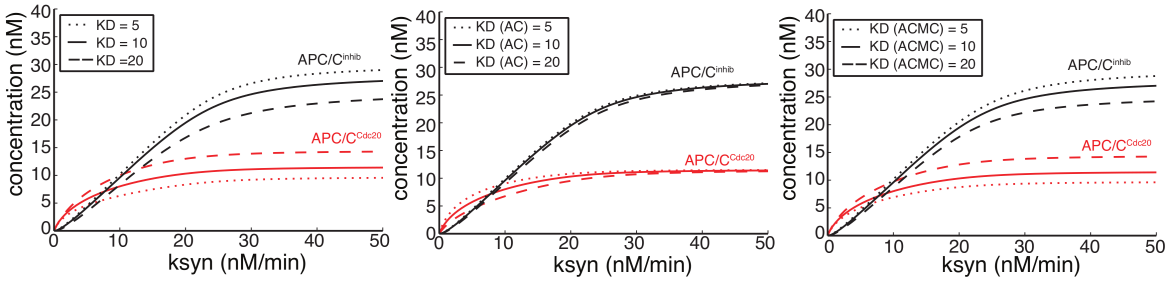

(a) Bifurcation diagrams varying K_Ds

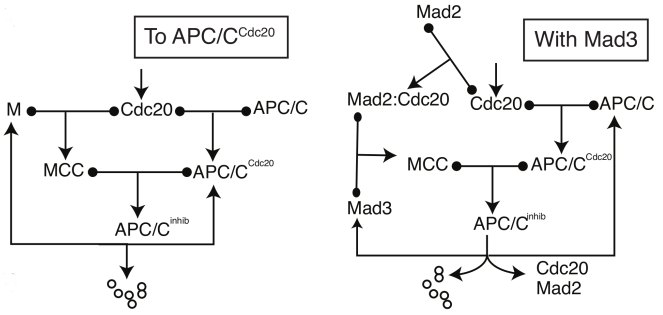

(b) Alternative networks for APC/C^{inhib} disassembly

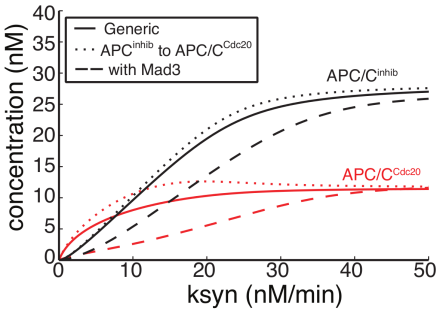

(c) Bifurcation diagrams

Figure 3.8: Analysis of robustness of the model to changes in parameters or wiring
a) Bifurcation analysis of APC/C^{Cdc20} and APC/C^{inhib}, with Cdc20 synthesis as bifurcation parameter. APC/C^{Cdc20} steady-state value is in red, APC/C^{inhib} in black. Solid line describes the system when K_D has the value used throughout the rest of this study. Dotted and dashed lines represent different modulations of K_D, as described in each legend. Left panel: we changed the K_D of all the three binding reactions ($K_{D,AC}$, $K_{D,MC}$, $K_{D,ACMC}$). Center panel: we change the K_D for APC/C-Cdc20 only. Right panel: we change the K_D for APC/C^{Cdc20}-MCC only. **b**) Alternative wirings. In 'To APC/C^{Cdc20}', we assume that APC/C^{inhib} is not broken down into its basic components, but directly into APC/C^{Cdc20} and Mad2+Mad3+Bub3, degrading one molecule of Cdc20. In 'With Mad3', we include Mad2 and Mad3 as separate variables. **c**) Bifurcation analysis ofAPC/C^{Cdc20} and APC/C^{inhib} for the alternative wirings. Solid lines refer to the model described in the main text. Details of the analysis can be found in Section 3.2.3.
Simulations performed by Fridolin Groß. Image taken from Bonaiuti et al. [2017].

In the third analysis, we investigated the robustness of the model in response to changes in the mechanism of APC/C^{inhib} disassembly, the least understood part of the network. In the model, we assume that in this process one molecule of Cdc20 is degradated, while free APC/C, Mad2, Mad3, Bub3 and a second molecule of Cdc20 are released. To investigate how changes in this assumption influence the overall behavior of the model, we ran a simulation assuming that Cdc20 degradation from APC/C^{inhib} gives rise to APC/C^{Cdc20} and free Mad2, Mad3 and Bub3 (left diagram in Figure 3.8(b)). In other words, instead of releasing free APC/C and Cdc20, the process releases the two bound together in an APC/C^{Cdc20} molecule. The bifurcation plot obtained with this modification resembles the one obtained by the 'general model' (Figure 3.8(c)), expecially in its saturating behavior.

The last analysis concerns the variable M, that we used to represent Mad2, Mad3 and Bub3. To relax this assumption, we split the reaction producing MCC in two: first Mad2 binds Cdc20, then their complex forms MCC by binding Mad3 (right panel of Figure 3.8(b)). Bub3, which is a member of MCC, is not included in the network since it is bound to Mad3 throughout the whole cell cycle Hardwick et al. [2000] (see Section 1.1.2 for a detailed discussion on MCC formation). The simulations of this model behave substantially as the 'general model' (dashed lines in Figure 3.8(c)). The results obtained in these two last analyses, where we modified the wiring of the network, show that the fine details on APC/C^{inhib} disassembly or MCC assembly are not relevant for the work discussed in these pages.

3.2.4 Stochastic simulations of the model reproduce adaptation dynamics

As we saw in previous sections, APC/C and Mad3 are present in very low concentration. The presence of low amount of molecules gives a prominent role to the inherent stochasticity of biochemical processes, independently of other sources of noise (e.g: gene expression) Raser and O'Shea [2005]. To include this stochasticity in the analysis of the model, we simulated it using the Gillespie algorithm Gillespie [1977]. This method, explained in detail in Section 1.2.2, describes the evolution of a chemical reaction network, taking into account the stochastic occurrence of molecular reactions.

Stochastic simulations do not deal with concentrations, but with number of molecules. To convert the concentrations measured in Section 3.2.2 for A_{tot} and M_{tot} into number of molecules, we assumed a conversion factor of $2.5\, molecules/nM$, calculated using a nuclear volume of $\sim 4.2\mu l$, corresponding to a nuclear radius of $\sim 1\mu m$ Therizols et al. [2010]. This conversion results in 200 molecules of M_{tot} and 100 molecules of A_{tot} in the stochastic simulations. The same conversion factor was used on every other parameter expressed in nM. Table 4.3 gives an overview of the parameters for the deterministic and stochastic simulations.

Simulations reproduce the experimental behavior of adaptation times

As mentioned at the beginning of Section 3.2, in the model cells transit into anaphase when the amount of active APC/C (APC/C^{Cdc20}) is above an 'anaphase threshold'. This assumption is justified by the presence of feedback loops that control entry into anaphase (see Section 1.1.3). In essence, APC/C^{Cdc20} hitting the threshold in the model represents APC/C^{Cdc20} triggering the feedback loops in a real cell.

We started each simulation from an initial state with no Cdc20 ($[C] = 0$), corresponding to entry into mitosis. As a result of Cdc20 synthesis, APC/C^{Cdc20} levels initially increase, and after a short transient they fluctuate around a steady-state value (see Figure 3.9(a)). Due to the noise, different trajectories (i.e., different cells) cross the 'anaphase threshold' at different times (Figure 3.9(a)). To test whether the simulation produces results that are comparable with the experimental cumulative distribution shown in Figure 3.4, we plotted the cumulative distribution of simulated adaptation times. Indeed, the simulated cumulative distribution (Figure 3.9(d)) shows the same exponential behavior as the experimental one.

The observed and simulated exponential shape of the cumulative distributions, suggests the presence of a homogeneous population, with a unique propensity to adapt shared among all cells. In Appendix B we further support this suggestion with additional evidences.

Theoretical explanation of the exponential behavior of adaptation times

We asked whether we could give a theoretical explanation of the exponential behavior of adaptation times. We defined adaptation time as the time it takes for APC/C^{Cdc20} to first hit the 'anaphase threshold'. This is the definition of first-passage time of a stochastic process (see Section 1.2.3). Thus, we investigated the APC/C^{Cdc20} trajectory as a stochastic process. We know, as explained in detail in Section 1.2.3, that there exists a stochastic process, the Ornstein-Uhlenbeck process, that has exponentially-distributed first-passage time, given that the threshold is far enough from the mean Nobile et al. [1985]. If we demostrate that APC/C^{Cdc20} trajectories are an Ornstein-Uhlenbeck process, or share important similarities with it, and that the threshold is far enough from the mean, we have a theoretical explanation of why APC/C^{Cdc20} first-passage time are exponentially-distributed.

Ornstein-Uhlenbeck process is defined as a stationary Gauss-Markov process. *Stationary* means that its mean value does not change over time, *Gauss process* means that the values it assumes are distributed as a Gaussian distribution, while *Markov process* means that it is possible to make predictions for the future of the process simply by knowing its present state, not its history.

We test if APC/C^{Cdc20} trajectories, after the first transient, have these three properties. First, this process is stationary, since the system is at steady state. Second, this process is Gaussian, as can be noticed both graphically and statistically. Graphically, we can appreciate the great similarities

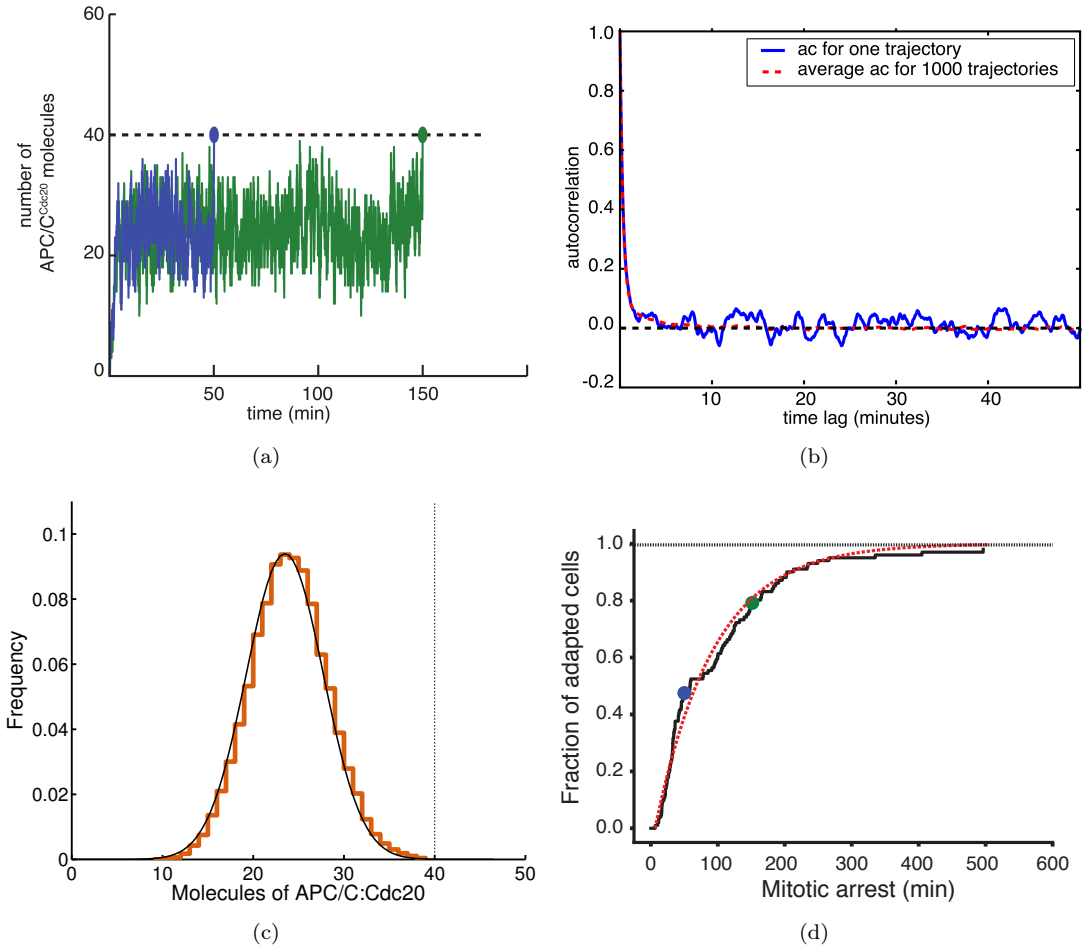

Figure 3.9: A model of the mitotic checkpoint reproduces adaptation dynamics
a) Simulated trajectories for APC/C^{Cdc20}. Each curve represents a single cell. Dashed line is the 'anaphase threshold' to be crossed for entry into anaphase. **b**) Autocorrelation of a single APC/C^{Cdc20} trajectory (blue) and of the average autocorrelation of 100 trajectories (red dashed) during the stationary phase using the wild type parameter settings. Dashed black line is 0. **c**) In orange, histogram of the simulated frequecies of APC/C^{Cdc20} values during the stationary phase. In black, a Gaussian distribution with the same mean and standard deviation. Dashed vertical line is the value of the 'anaphase threshold'. **d**) Simulated cumulative adaptation produced by the model in Figure 3.5 and equation (3.1). The circles display the adaptation time of the trajectories plotted in panel **a**. The cumulative adaptation curve (solid line), is fitted with an exponential (dotted line) after a delay.
Simulations performed by Fridolin Groß. Image adapted from Bonaiuti et al. [2017].

between the values assumed by the APC/C^{Cdc20} trajectories after the short transient and a Gaussian distribution with the same mean and variance (Figure 3.9(c)). Statistically, the Shapiro-Wilk test for normality cannot refuse the hypotesis of the APC/C^{Cdc20} trajectories being normally distributed ($p = 0.24$). Third, for what concerns the Markov property, Gillespie algorithm returns a Markov process (see Section 1.2.2 and Gillespie [1976]). However, the Markov process returned by the Gillespie algorithm is the dynamics of all the proteins, while it is not obvious that each of them is described by a Markov process. However, APC/C^{Cdc20} shares another property with Ornstein-Uhlenbeck process: in both the processes, the autocorrelation function decreases exponentially (Figure 3.9(b). This property also depends on the fact that Ornstein-Uhlenbeck process is a Markov process.

Altogether, these results show the similarity between APC/C^{Cdc20} and the Ornstein-Uhlenbeck pro-

cess. Since the 'anaphase threshold' is far from the mean value of APC/C^{Cdc20}(Figure 3.9(c)), we have a rationale for the presence of exponentially-distributed adaptation times. An important consequence of describing APC/C^{Cdc20} as an Ornstein-Uhlenbeck process is that in the latter the rate of the exponential curve of firs-passage times only depends on the distance between the mean and the threshold Nobile et al. [1985]. Both values, in our model, are the same in every cell. This finding supports the idea that the probability of adaptation, measured as the rate of the exponential cumulative distribution of adaptation times, is the same in the whole cell population.

3.2.5 Predictions of the model

The probability of adaptation depends on the distance between the steady state of APC/C^{Cdc20} and the 'anaphase threshold': the closer the steady state to the threshold, the higher the adaptation rate. According to our model (Figure 3.10(a)), the steady-state levels of APC/C^{Cdc20} increase with the production rate of Cdc20. This dependency is true as long as Mad3 and APC/C, binding partners of Cdc20, are in excess. In contrast, when the binding partners are limiting the dependency ceases, and APC/C^{Cdc20} levels become insensitive to further changes in Cdc20 production rate. Taken together, these results predict that adaptation rate increases with Cdc20 synthesis, until saturation is reached. Saturation depends on the low amount of total APC/C.

To explore the consequences of this prediction, based on the population average, on individual cells, we ran stochastic simulations of the model modulating the value of s, Cdc20 synthesis rate. As expected, stochastical numerical simulations show an increase in adaptation rates when increasing Cdc20 expression, an effect which becomes dimmer for high Cdc20 synthesis (Figure 3.10(b)). It is important to notice that, when APC/C^{Cdc20} steady state is close to the threshold, very small increases in its value have a noticeable impact on the mean adaptation time (see table in Figure 3.10).

The model also predicts that, as a consequence of the limited amount of Cdc20 interactors, during a SAC arrest APC/C^{Cdc20} steady-state levels cannot increase above the 'anaphase threshold'. This is true as long as all the SAC components are present. No matter how high we increase Cdc20 synthesis APC/C^{Cdc20} levels are on average below threshold (Figure 3.10(a)). In contrast, in the case of cells lacking SAC members, APC/C^{Cdc20} steady-state levels are not limited by the presence of an active SAC, and APC/C^{Cdc20} average value crosses the 'anaphase threshold' (see left panel in Figure 3.11). As a consequence, SAC-defective cells synchronously and quickly activate APC/C (see right panel in Figure 3.11). Summarizing, the model predicts that cells lacking SAC components and cells with increased synthesis of Cdc20 exibit different behavior in exit from mitosis in the presence of spindle damage.

How the checkpoint responds to increased Cdc20 synthesis depends on the topology of the SAC regulatory network, a subject further investigated in a manuscript in preparation to which I contributed Groß et al. [In preparation], presented in Appendix C. There, we analyze more rigorously

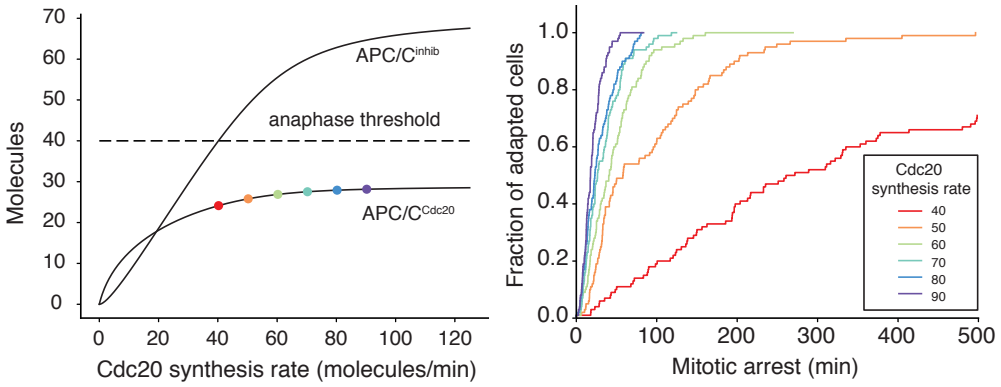

(a) (b)

color	Cdc20 synthesis rate (molecules/minute)	APC/C^{Cdc20} steady-state (molecules)	mean adaptation time (minutes)
red	40	24.0	222.0
orange	50	25.6	86.0
green	60	26.7	46.8
pale blue	70	27.4	35.1
blue	80	27.7	31.1
purple	90	27.9	20.6

Figure 3.10: Model prediction changing Cdc20 synthesis rate
a) Steady states for APC/C^{inhib} and APC/C^{Cdc20} as a function of Cdc20 synthesis rate, simulated by the model describing the protein network in Figure 3.5. The dotted line is the 'anaphase threshold' which needs to be crossed for cells to enter anaphase. With different filled dots, we mark different values of Cdc20 synthesis rate, see panel **b**. **b**) Stochastic simulations of the model in Figure 3.5, for the six different values of Cdc20 synthesis rate. **c**) The table summarizes the result obtained in the two other panels. Mean adaptation time is the reciprocal of the adaptation rate, estimated by fitting the simulated cumulative distributions in panel **b**. For high values of APC/C^{Cdc20}, small differences give significant reduction in mean adaptation time. Simulations performed by Fridolin Groß. Image adapted from Bonaiuti et al. [2017].

how the presence of two molecules of Cdc20 in MCC makes cells resistant to Cdc20 overexpression.

3.3 The SAC network is resistant to high Cdc20 levels

We have shown that stochastic simulations of the model give rise to adaptation dynamics that mirror the experimentally measured data for the wild-type condition. Moreover, the model predicts that, if wild-type has not saturated Mad3 and APC/C, increasing synthesis of Cdc20 causes an increase in adaptation rate, until no more free binding partners are available, and the system becomes insensitive to further increase of Cdc20 synthesis.

To experimentally investigate this effect, we modulated Cdc20 synthesis. It would have been possible to modulate synthesis using an artificial or an inducible promoter. However, endogenous synthesis of Cdc20 is tightly cell-cycle regulated (see Section 1.1.1), and we aimed at preserving this feature. So, we modulated Cdc20 synthesis by creating strains carrying 2, 3 or 5 copies of the gene, or diploid strains heterozygous for *CDC20*. In this way we could investigate values of Cdc20 synthesis both higher and smaller than the wild type, preserving all Cdc20 regulations.

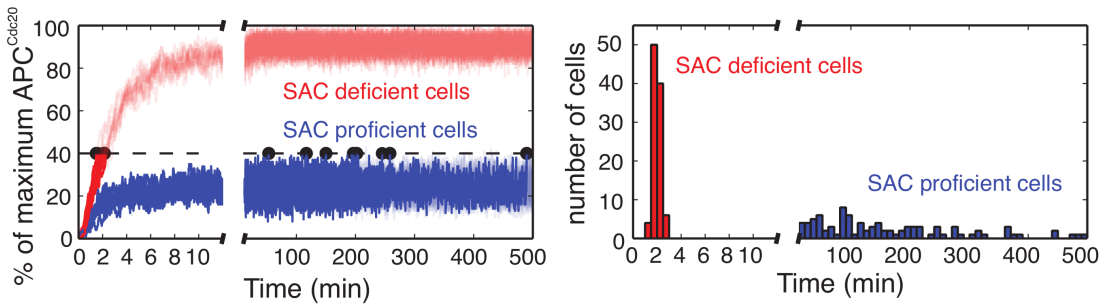

Figure 3.11: SAC proficient and deficient cells behavior according to the model
Left panel: stochastic simulations of APC/C^{Cdc20} levels in SAC-proficient (blue lines) or SAC-deficient (red lines) cells. Cells exit from mitosis once APC/C^{Cdc20} hits the 'anaphase threshold' (dashed line). Time of mitotic exit is indicated as black dot for each cell. APC/C^{Cdc20} levels are expressed as percentage of APC/C included in the complex, to underline the independency on the value of the 'anaphase threshold'. Right panel: histogram of times of exit from mitosis in 100 simulations of cells as in the left panel.
Simulations performed by Fridolin Groß. Image taken from Bonaiuti et al. [2017].

3.3.1 Results on strains carrying extra *CDC20*

We inserted 2, 3 and 5 copies of *CDC20* under the endogenous promoter, with the endogenous terminator (see Section 2.5 for details on quantification, and Figure 3.12(a) and Figure 3.12(b)), in cells expressing Clb2-mCherry and Mad2-GFP. We use *CDC20 NX* to denote the genotype of cells carrying more than 1 copy of *CDC20*. The amount of protein accumulated during a metaphase arrest scales with the number of genes (Figure 3.12(c)), and, accordingly, the activity of one individual *CDC20pr*, as defined in Figure 2.6 and in Section 2.8, is not lowered by the presence of additional copies of *CDC20pr* (Figure 3.12(d)).

The model predicts that cells overexpressing Cdc20 and SAC-defective cells respond in different way to a SAC-inducing stimulus. To test this prediction, we compared the experimental response to spindle poisons of *CDC20 NX* and SAC-defective *mad2*Δ and *mad3*Δ cells. *CDC20 NX* cells are much less sensitive than *mad2*Δ cells to benomyl, a microtubule-depolymerizing drugs, even if slightly more sensitive than wild type cells (Figure 3.13(a)). At single-cell level, *mad3*Δ cells show a much faster rebudding kinetics in nocodazole compared to *CDC20 5X* (Figure 3.13(b)). Collectively, these data indicate that the checkpoint as such is still functional in *CDC20 NX* strains.

To test the effect of increasing Cdc20 from wild-type value, we analysed the adaptation dynamics of *CDC20 NX* strains. We used the same experimental protocol and the same analysis pipeline that we used on wild-type strains to produce Figure 3.2(d) and Figure 3.4 (see details in Section 2.3). We arrested cells in G1, released them into nocodazole and imaged them with fluorescence microscope while growing in microfluidic devices. We observed that, as in the wild-type, most cells started to degrade Clb2 in the presence of localized Mad2 (Figure 3.14). We then measured adaptation time, and we noticed that cells adapted faster as the copy number increased. Noticeably, the major reduction in adaptation times took place going from one to two copies of *CDC20*, whereas further increasing copy number had less effect (Figure 3.15(a), summarized in Figure 3.17). This result is in agreement with

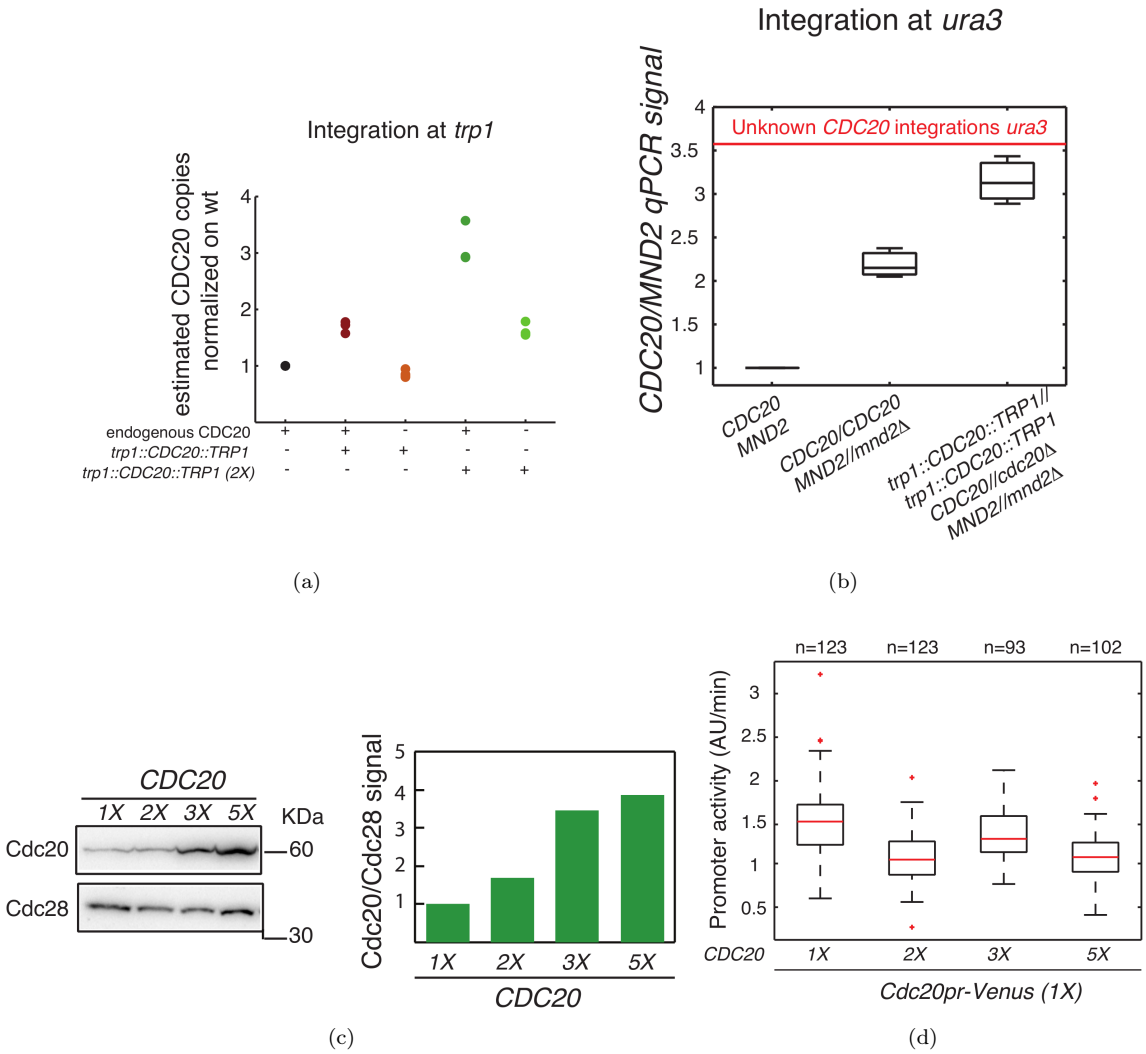

Figure 3.12: Characterization of strains carrying multiple *CDC20*
a) To estimate the number of *CDC20* copies integrated at the *TRP1* locus after transformation, we performed qPCR on genomic DNA for the indicated genotypes (yAC3202, yAC2398, yAC2435, yAC2400, yAC2450), and thus identified strains with two or three copies of *CDC20*. **b**) To estimate the number of *CDC20* copies integrated at *URA3* locus in yAC2675, we used as calibration set a group of three diploid strains with known *CDC20*-to-*MND2* ratio (yAC3202, yAC2621, yAC2622). *N*: 3. Transformation performed with Elena Chiroli. **c**) Cells expressing the indicated copy number of *CDC20* (yAC3202, yAC2398, yAC2400, yAC2991) were arrested in G1 and released into nocodazole at 23 °C. After 135 minutes protein extracts were prepared and analyzed by immunoblotting with *anti*-Cdc20 and *anti*-Cdc28 antibodies. Right panel: quantification of the signal normalized to *CDC20 1X* value. *N*: 2. Experiments performed by Elena Chiroli. **d**) Activity of the *CDC20pr*, as defined in Figure 2.6, in strains carrying one *CDC20pr*-Venus integrated in tandem with endogenous *CDC20*, and multiple copies of *CDC20* with their promoter and terminator (see Section 2.5 for details on strain construction, strains yAC3106, yAC3623, yAC3630, yAC3627). Cells were synchronized in G1 and released into nocodazole. Promoter activity was measured after *CDC20pr* was switched on and Venus signal started to increase. *N*: 3. Experiments performed with Elena Chiroli. Analysis performed with Andrea Ciliberto. Image taken from Bonaiuti et al. [2017].

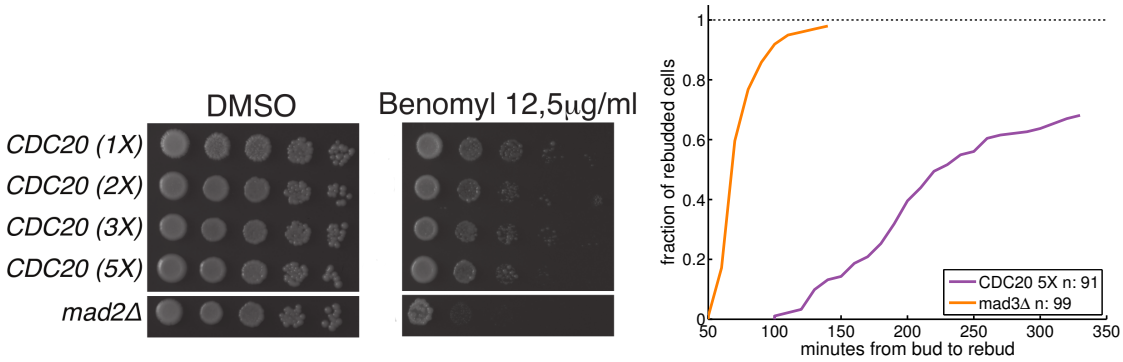

(a) (b)

Figure 3.13: *CDC20 NX* strains are SAC-proficient
a) Serial dilutions of the indicated strains (yAC1011, yAC2437, yAC2453, yAC2831, yAC1156) were spotted on YPD plates containing 1%DMSO or $12,5\,\mu g/ml$ benomyl. The picture was assembled from serial dilutions made on the same plate by splicing out the irrelevant strains. N: 2. Experiments performed by Elena Chiroli. **b**) Cumulative distributions of rebudding time of *CDC20 5X* and *mad3*Δ cells (yAC3552 and yAC3738). Cells were arrested in G1 and released into nocodazole in microfluidic devices, then bud-to-rebud time was measured (see Section 2.5 for details on the analysis). N: 2. Image taken from Bonaiuti et al. [2017].

the prediction of the model depicted in Figure 3.10(b).

3.3.2 Results on diploid strains

To test the effect of reducing the expression of Cdc20, we measured the length of mitotic arrest in diploid cells heterozygous for *CDC20* (see Section 2.6) and homozygous for Mad2-GFP and Clb2-mCherry. We kept track of the metaphase length by measuring the time between Clb2-mCherry rise and fall, as in haploid strains (see Section 2.3 for details).

Diploid cells could not be synchronized in G1, since they do not respond either to α- or a-factor. For this reason, we released cells into nocodazole with no prior synchronization. Given the absence of synchronization, the short duration of G1, and the fact that we acquired one image every 10 minutes, we could not have a clear negative control for Mad2 localization index. This prevented us from selecting cells based on Mad2 localization signal, as we did for haploids in Figure 3.4 and 3.15(a). Yet, we needed to exclude from the analysis those cells that were in mitosis at the time of nocodazole treatment, or entered mitosis before they could experience the effect of the drug. To this aim, we used results from synchronized haploids, where Clb2 levels started increasing from 50 minutes after nocodazole treatment (Figure 3.16). Thus, we included in the analysis of diploids only cells where Clb2 signal rises later than 50 minutes from nocodazole addition. We measured the time spent in mitosis as we did for the haploids: from Clb2 accumulation to its degradation.

Unlike haploids, a sizeable fraction of diploid cells died in metaphase, for reasons that are currently unknown: 13% of the observations included in the analysis over all the strains, 25% of the observations included in the heterozygous strain (for a complete overview of the database of observations included in the analysis see Table 4.2). For these cells we could measure the beginning of the mitotic arrest

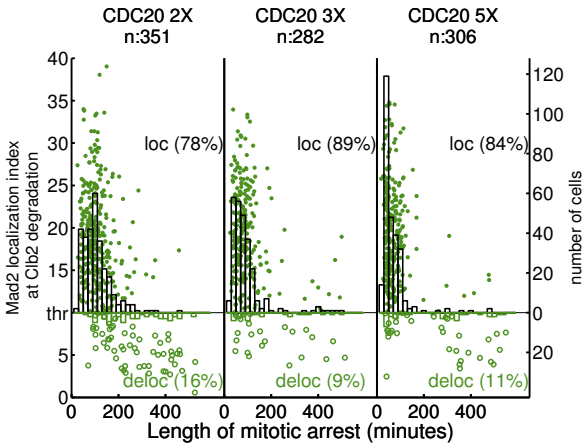

Figure 3.14: Clb2 degradation occurrs in the presence of Mad2 localized at kinetochores in *CDC20 NX* cells
Values of Mad2 localization index when Clb2 degradation starts, for the indicated strains (yAC3565, yAC3555, yAC3552). Each dot is a cell where Clb2 degradation is recorded, percentages refer to the whole set of cells (as in Figure 3.2(d)). N: 3; n: written for each genotype. (see Table 4.1 for details on the observation dataset). Image taken from Bonaiuti et al. [2017].

(Clb2 rise), but not its end, since they died before Clb2 degradation. In statistical analysis this kind of observations are called *censored*. Although we could not measure the duration of their mitotic arrest, we knew that these cells kept the arrest until they died. To include this information in the analysis, we changed the model used to estimate the propensity of cells to adapt. We did not fit the cumulative distributions with an exponential as we did with haploid cells, since this procedure would have ignored the censored observations. Instead, we used the Cox proportional hazard model, which keeps track also of cells dead during the metaphase arrest. We summarized the results using the hazard ratio, normalized to the *CDC20/CDC20* diploid.

In agreement with the predictions, heterozygous *CDC20/cdc20*Δ diploids showed a propensity to adapt that is 60% of the propensity of the homozygous *CDC20/CDC20* cells (hazard ratio = 0.60, Figure 3.15(b)).

3.3.3 Comparison of simulated and experimental data

In the previous sections (Section 3.3.1 and 3.3.2), we presented two different methods that we used to measure adaptation propensity in haploid and diploid strains. On haploids, we used the exponential fitting, while on diploids we used the Cox proportional model. To compare the two methods, we compared the results obtained on strains carrying similar genetic modifications in haploids and diploids (Figures 3.15(a) and 3.15(b)). The measure we used for comparison is the hazard ratio. For diploid strains, this value is returned from Cox model. For haploid strains, the hazard is the adaptation rate, interpreted as 'risk of adaptation per unit of time', and thus the hazard ratio is the adaptation rate of one particular strain divided by the adaptation rate of the wild-type. This value is presented also in the legend of Figure 3.15(a). We compared *CDC20 3X* with *CDC20 3X/CDC20 3X*, and *CDC20 5X* with *CDC20 5X/CDC20 5X*.

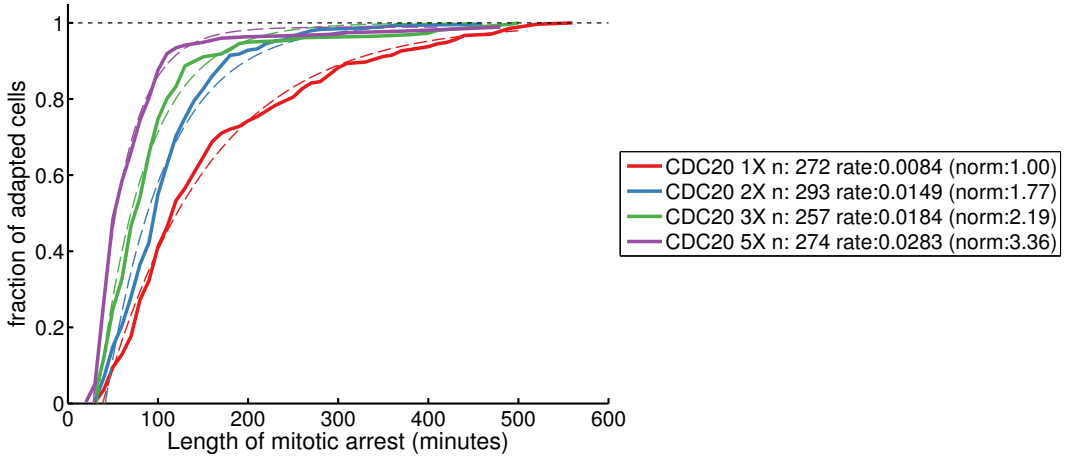

(a)

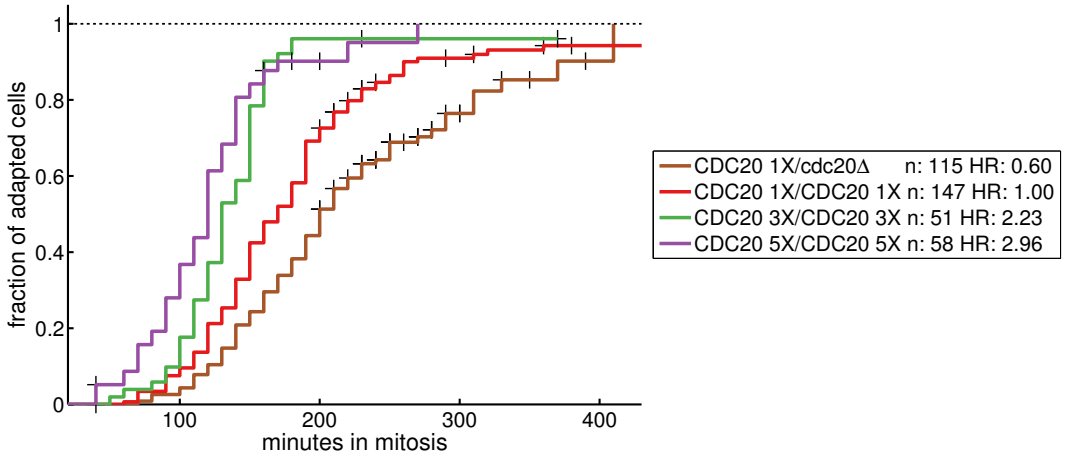

(b)

Figure 3.15: Effects of modulating *CDC20* copy number on adaptation rate
a) Haploid cells carrying MAD2-GFP CLB2-mCherry and 1, 2, 3, or 5 copies of *CDC20* (yAC3538, yAC3565, yAC3555, yAC3552) were arrested in G1 and released into nocodazole, as described for Figure 3.2. The cumulative distributions of times in metaphase (solid lines) are fitted with exponential curves (dotted lines) after a delay. Fitted adaptation rates, both raw and normalized on wild-type, are written in the legend, together with n. N: 3 (see Table 4.1 for details on the observation dataset). **b**) Diploid cells carrying in homozygosity MAD2-GFP CLB2-mCherry and homozygous for *CDC20* (yAC3801), *CDC20 3X* (yAC3802), *CDC20 5X* (yAC3803) or heterozygous for *CDC20* (yAC3804) were grown in microfluidic devices in the presence of nocodazole, without being synchronized in G1 (see also Section 2.6). In the plot, Kaplan-Meier estimate of their cumulative distribution function of adaptation times. A black cross marks the time interval where a censoring occurred (i.e., dead cell). Hazard ratio HR (with wild type as normalizer) and n are written in the legend. N: 2 (see Table 4.2 for details on the observation dataset). Image adapted from Bonaiuti et al. [2017].

analysis on haploids		analysis on diploids	
strain	**hazard ratio**	**hazard ratio**	**strain**
-	-	0.60	*CDC20/cdc20Δ*
CDC20 1X	1	1	*CDC20/CDC20*
CDC20 2X	1.77	-	-
CDC20 3X	2.19	2.23	*CDC20 3X/CDC20 3X*
CDC20 5X	3.36	2.96	*CDC20 5X/CDC20 5X*

Table 3.1: Comparison of haploid/diploid analysis
For haploid strains, we used the exponential fitting of mitotic time. 'Hazard ratio' is the rate of the exponential function normalized on the wild-type. Data from Figure 3.15(a).
For diploid strains, we used the hazard ratio from Cox proportional hazard model of mitotic time. Hazard ratio are computed with respect to the homozygous *CDC20/CDC20*. Data from Figure 3.15(b)

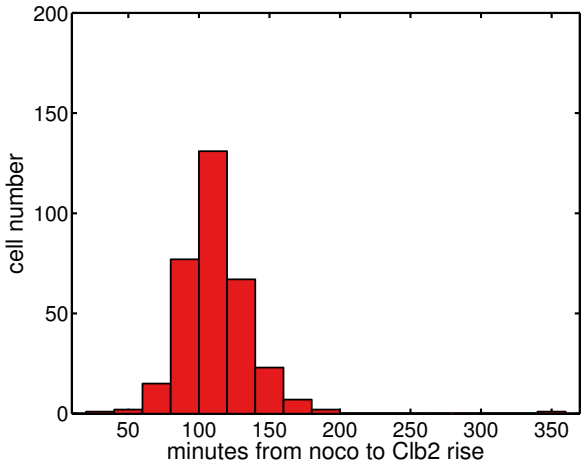

Figure 3.16: Histogram of Clb2 rise time
Haploid cells carrying MAD2-GFP CLB2-mCherry and endogenous *CDC20* were arrested in G1 and released into nocodazole. From the analysis of Clb2 signal explained in Section 2.3, we measured the time of Clb2 accumulation. N: 3; n: 326. For a complete overview of the database of observations see Table 4.1.

The results of this comparison are shown in Table 3.1. The strains carrying more than 2 copies of *CDC20*, either haploid or homozygous diploids, show similar hazard ratios. From this observation we conclude that the two methods give comparable results. Thus, we merged all the results, and presented them together, comparing them to the simulations (Figure 3.17). The global qualitative behavior of our model well recapitulates the dependency of adaptation kinetics with altered Cdc20 expression rate (Figure 3.17).

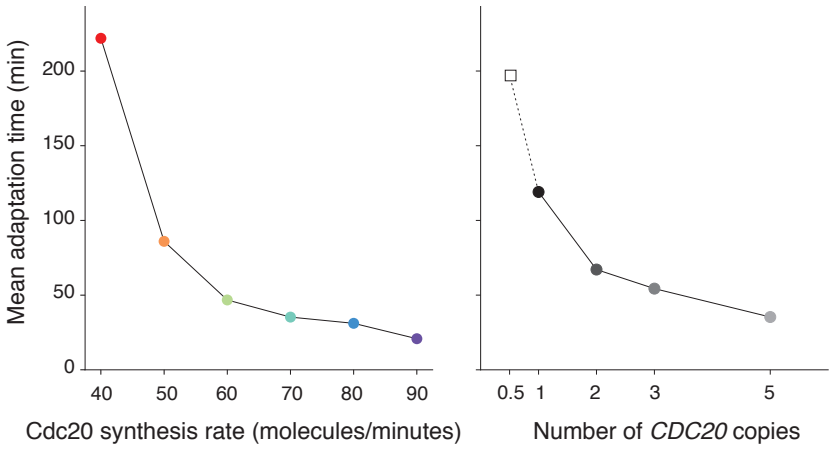

Figure 3.17: Simulated and experimental results are comparable when modulating Cdc20 synthesis
Mean adaptation time as a function of synthesis rate in the model (left, data from Figure 3.10(b)) and as a function of *CDC20* copy number in the experiment (right, data from Figure 3.15(a)). For copy number 0.5 we used the results obtained with diploids, which showed that the heterozygous *CDC20*/*cdc20*Δ, has 60% of propensity to adapt of wild type cells (Figure 3.15(b)). We marked this point using a different symbol (square) and a dashed line to emphasize the fact that this result was obtained in a different experimental system. Image taken from Bonaiuti et al. [2017].

In conclusion our data support the hypothesis that adaptation rate scales with Cdc20 synthesis up to *CDC20 X2* values. Above this value the dependency is reduced.

3.4 APC/C^{inhib} and MCC saturate with two copies of *CDC20*

Increasing Cdc20 expression did increase the chance of cells to adapt, but eventually the effect leveled off. According to the model, this saturation is due to the limited amount of Cdc20 interactors (Mads and APC/C), which are present in levels comparable to wild type Cdc20 (Figure 3.6(b) and Figure 3.6(c)). At the molecular level, the saturation of the interactors would lead to the saturation of the complexes, meaning that, after saturation, the levels of APC/C^{inhib}, APC/C^{Cdc20} and of MCC do not depend on Cdc20 synthesis (see Figure 3.10(a)). Since having more than 2 *CDC20* only mildly increases the adaptation rate, we expect that *CDC20 2X* strains have reached the saturation of the complexes. To experimentally test this hypothesis, we measured APC/C^{inhib} and MCC concentrations in strains carrying additional *CDC20* genes. We expect to measure higher levels of APC/C^{inhib} and MCC in *CDC20 2X* than in wild-type strains, and to measure similar levels in strains with 2 or more copies of *CDC20*.

To quantify APC/C^{inhib} and MCC in vivo, we used FCCS (see Section 1.3 for an introduction on the technique). For each of the two complexes, APC/C^{inhib} and MCC, we selected a protein pair (FCCS pair): Cdc23-mCherry/Mad2-GFP and Mad3-mCherry/Mad2-GFP, respectively.

3.4.1 Validation of FCCS as a tool to measure MCC and APC/C^{inhib}

Positive control has higher signal and shows better fit than negative controls

To test the choice of the protein pairs, we compared the cross-correlation signal in positive and negative controls. For the first, we induced the formation of the complexes of interest by releasing G1-arrested cells in nocodazole. For the negative controls, we chose three different conditions where the complexes do not form, and thus no cross-correlation signal is expected. The three conditions were: G1-arrested cells, large budded cycling cells, and cells treated with nocodazole but lacking one component of the MCC (*mad3*Δ cells for the Mad2/Cdc23 pair, *bub3*Δ for Mad2/Mad3). For both complexes, the protein pair in the positive control not only gave significantly higher concentrations than the negative ones (y-axis in Figure 3.18(a) and 3.18(b)), but also a better quality of the fitting (x-axis in the same Figures), implying a more reliable measurement of the concentrations (see Section 2.7.1 for a discussion on the quality of the fitting). It is worth noticing that the protein pair Mad3-mCherry/Mad2-GFP does not discriminate between free MCC and MCC in APC/C^{inhib}, and thus measures the total amount of MCC, which is also expected to saturate, according to the model.

FCCS measures known interactions between members of the MCC

As additional control of the accurate detection of protein complexes by FCCS, we measured the cross-correlation of pairs of other proteins taking part in MCC. At first, we investigated Mad2 and Bub3, tagged with GFP and mCherry, respectively. These two proteins interact not only as members of the MCC, but also at kinetochores, where they colocalize in the presence of spindle damage Kerscher

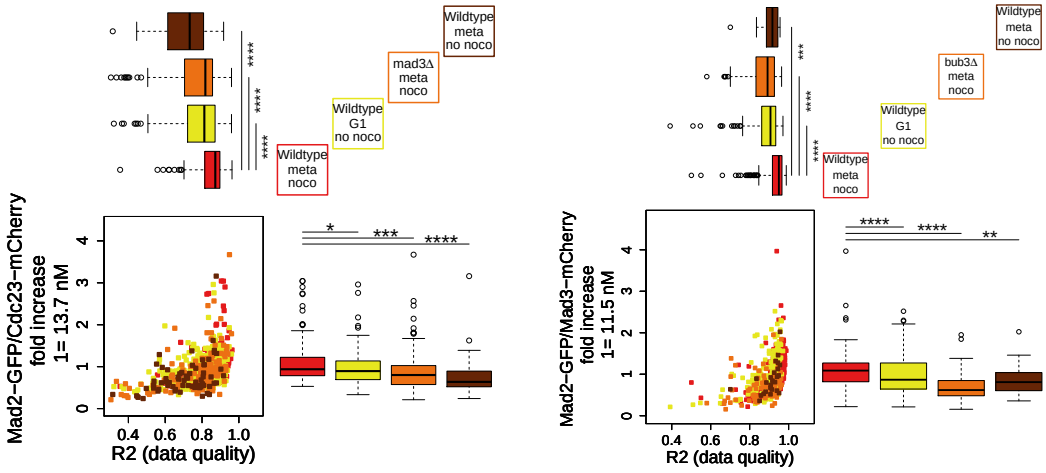

(a) (b)

Figure 3.18: Controls for FCCS as a tool to measure APC/C^{inhib} and MCC concentration
a-b) Four different conditions were used to test Mad2-GFP and Cdc23-mCherry (for APC/C^{inhib}, panel **a**) as well as Mad2-GFP and Mad3-mCherry (for MCC, panel **b**) as a protein pair for FCCS measurements. In the positive controls (red) we treated cells with nocodazole (yAC2886 for Mad2/Cdc23, yAC3268 for Mad2/Mad3). We compared this signal with three negative controls: G1-arrested cells (yellow), large-budded cycling cells (brown) and cells treated with nocodazole but lacking *MAD3* (yAC3103, for Mad2/Cdc23) or *BUB3* (yAC3127, for Mad2/Mad3) (orange). The signal is computed fitting the cross-correlation function and expressed as fold increase with respect to the signal measured in the positive control. See Section 2.7 for details on the protocol. In absolute concentrations, 1 corresponds to $13.7\,nM$ (panel **a**) and $11.5\,nM$ (panel **b**). Image taken from Bonaiuti et al. [2017].

et al. [2003], Gillett et al. [2004] (see Figure 3.1(b) and Section 1.1.2). We thus expect two sources of cross-correlation: unattached kinetochores and MCC. As positive control we thus used wild-type cells released into nocodazole, where both sources are present. As negative control we used the same cells, released in fresh medium, where neither Mad2 localization nor MCC formation are expected to take place. Another negative control are *mad1*Δ cells, since in this genetic background Mad2 localization at kinetochores is impaired Gillett et al. [2004] and thus MCC formation is not sustained. To uncouple the two sources of cross-correlation, we used *MAD3* deletion, that prevents MCC formation Hardwick et al. [2000], but retains Mad2 localization at kinetochore Gillett et al. [2004]. We thus expect to have no signal in both the negative controls, high signal in the positive, and only the signal from kinetochores in *mad3*Δ cells. Indeed, in nocodazole-arrested wild-type cells, the cross-correlation signal rises from G1 values, while it does not change in wild-type cells released in fresh medium and in *mad1*Δ cells. *mad3*Δ cells in nocodazole show the cross-correlation signal of Mad2 and Bub3 resulting from kinetochore colocalization only (Figure 3.19(a)). By comparing the signals from the positive control and *mad3*Δ cell, we notice that they are very similar. It might be due to the fact that, in the positive control, the signal emitted from the colocalization of Mad2 and Bub3 at kinetochores dominates the signal resulting from their codiffusion as MCC members. As previously mentioned, we did not use this pair of protein to measure MCC, but rather Mad2/Mad3, that codiffuse only as MCC members, since Mad3 does not localize at kinetochores (see Section 1.1.2).

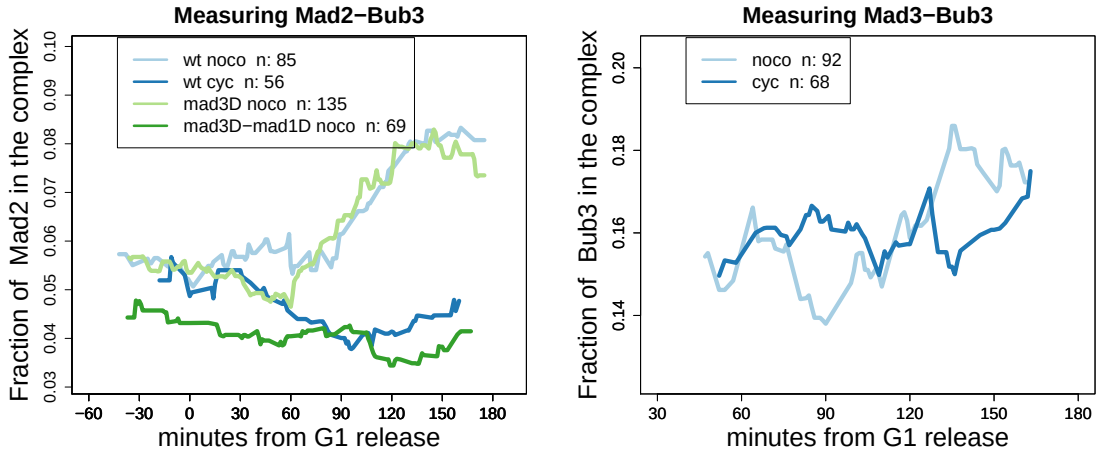

(a) (b)

Figure 3.19: FCCS correctly identifies known interactions of *MCC* members
a) Cells carrying Mad2-GFP and Bub3-mCherry were arrested in G1 and released either into nocodazole ('noco' in the legend) on into fresh medium ('cyc' in the legend). Strains are wild-type (wt, yAC2919) or *mad3*Δ (mad3D, yAC2994) or *mad3*Δ *mad1*Δ (mad3D-mad1D, yAC3042). The plot represent the cross-correlation signal, expressed as a fraction of Mad2 measured in the cell. N: 1. **b**) Cells carrying Bub3-GFP and Mad3-mCherry were arrested in G1 and released either into nocodazole ('noco' in the legend) on into fresh medium ('cyc' in the legend). The plot represent the cross-correlation signal, expressed as a fraction of Bub3 measured in the cell. N: 1.
See Section 2.7 for details on the protocol of both plots.

The second pair of proteins we used as control is composed by Mad3 and Bub3. Their interaction is not cell-cycle regulated Hardwick et al. [2000], thus we expect to see the same signal throughout an uncostrained cell cycle, and in the M-phase arrest due to the presence of spindle poison. Indeed, when we measured cross-correlation in cells carrying Mad3-mCherry and Bub3-GFP, we recorded the same signal at different time-points after G1 release, with a dynamic that did not depend on the presence of nocodazole (Figure 3.19(b)).

3.4.2 APC/C^{inhib} and MCC saturate with two copies of *CDC20*

We aimed at measuring APC/C^{inhib} and MCC since the model predicts that both the complexes saturate when increasing *CDC20* copy number (Figure 3.10(a), Section 3.2.5). When we measured the concentration of APC/C^{inhib} in *CDC20 NX* strains, we observed that the signal increased with one additional copy of *CDC20*, but reached saturation adding more copies (Figure 3.20(a)). The same happened when measuring MCC: it also saturates with two copies of *CDC20* (Figure 3.20(b)). These results demonstrate that increased expression of Cdc20 leads to saturation of MCC and of its interaction with APC/C, as expected from the model.

3.4.3 MCC reaches its maximal levels in *CDC20 NX* cells

According to the model, saturation of MCC and APC/C^{inhib} is a consequence of the limited amount of interactors, not a specific trait of strains overexpressing Cdc20. As a consequence, regardless of MCC and APC/C^{inhib} modulation, we cannot produce more of these complexes than *CDC20 NX*

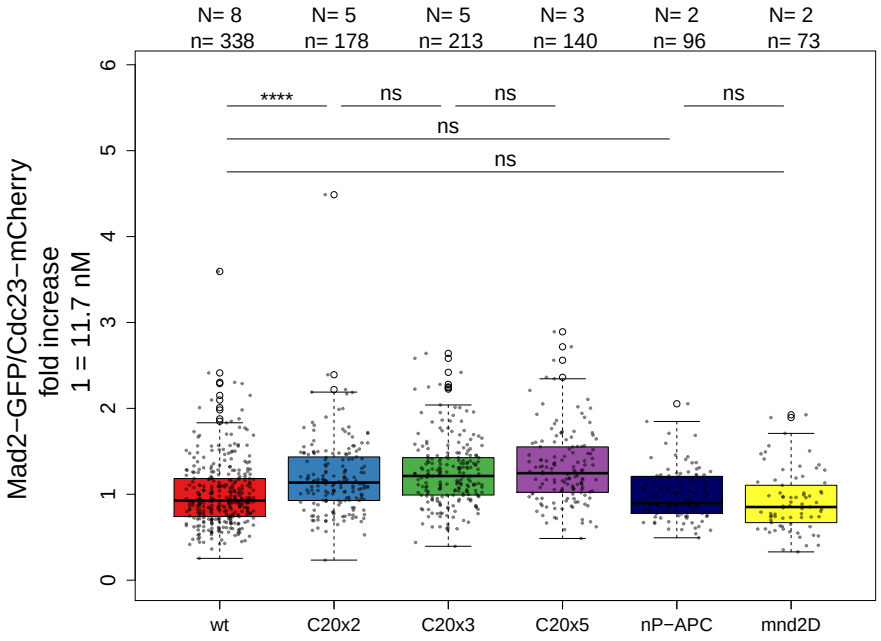

(a)

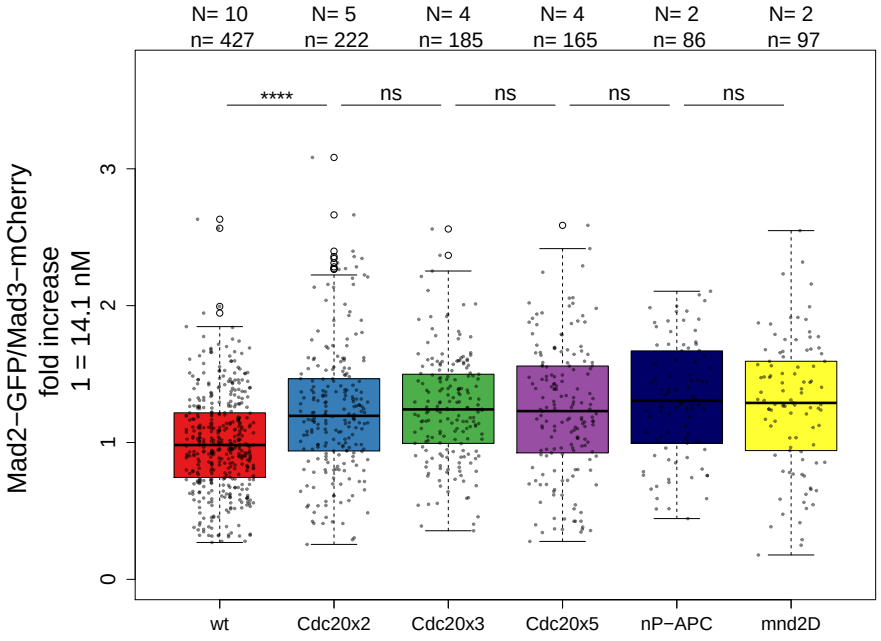

(b)

Figure 3.20: APC/C^{inhib} **and** MCC **saturate with two copies of** ***CDC20***
a-b) Cells carrying Mad2-GFP Cdc23-mCherry (panel **a**, strains yAC2886, yAC3179, yAC3176, yAC3384, yAC3312, yAC3400) or Mad2-GFP Mad3-mCherry (panel **b**, strains yAC3268,yAC3181, yAC3153, yAC3380, yAC3346, yAC3227), with 1, 2, 3, or 5 copies of *CDC20* or non-phosphorylatable forms of APC/C (nP-APC) or deletion of *MND2* (mnd2D) were released from G1 phase into synthetic low-fluorescent medium containing nocodazole and 1% peptone. Each measurement is expressed as fold increase with respect to the wild type strain measured on the same day. More precisely, we normalized the cross-correlation signal to the exponential of the mean value of the logarithmic transform of the wild type. See Section 2.7 for details on the protocol. Kolmogorov-Smirnov two-tails test was used for comparison. Circles are boxplots' outliers, included in the analyses. In panel **a** p-values are: for side-by-side comparisons from left to right: $6.35\,10^{-8}$, $8.01\,10^{-2}$, $6.6\,10^{-1}$ and $7.7\,10^{-2}$, for wt VS nP-APC $p = 6.1\,10^{-1}$, for wt VS mnd2D $p = 2.3\,10^{-1}$. In panel **b**, p-values are, for side-by-side comparison from left to right: $7.2\,10^{-9}$, $5.9\,10^{-1}$, $3.3\,10^{-1}$, $2.4\,10^{-1}$ and $9.2\,10^{-1}$.
Image adapted from Bonaiuti et al. [2017].

strains. To test this consequence of the model, we aimed at increasing MCC and APC/C^{inhib} in *CDC20 X1* strains, via two mechanisms that do not involve Cdc20 synthesis, but rather APC/C binding to Cdc20 and APC/C^{inhib} disassembly.

First, we used strains carrying non-phosphorylatable forms of two APC/C subunits, *CDC16-6A* and *CDC27-5A*. These mutations result in reduced affinity of APC/C to Cdc20 (Rudner and Murray [2000], and Section 1.1.1), which clogs the pathway for APC/C^{inhib} formation, reducing its levels. Since MCC disassembly depends on APC/C^{inhib}, MCC levels are expected to increase. The increase in MCC is limited, according to the model, by the limiting species interacting with Cdc20 in MCC formation. For this reason, this strain is expected to have the same amount of MCC as *CDC20 NX* strains, which should be the maximal possible level. The overall effect on APC/C^{inhib} formation is expected to be very mild, since the reduction in APC/C-MCC binding due to the lower affinity should be counterbalanced by an increase in MCC levels.

Indeed, when we measured MCC with FCCS, we found that the distribution of its values was statistically indistuinguishable from the one of *CDC20 5X* strain (Figure 3.20(b)). For what concerns APC/C^{inhib}, as expected, it was non-significantly different from wild-type (Figure 3.20(a)). These results verified a key prediction of the model, using a different perspective than the one used to build it, thus reinforcing the strength of its conclusions. Moreover, from a technical point of view, these results showed that it is possible to uncouple signals from MCC and APC/C^{inhib}, further confirming that FCCS is a valid tool for the analysis we are bringing off.

The second mutation we used to modulate MCC and APC/C^{inhib} was the deletion of *MND2*. *MND2* is a non-essential subunit of APC/C that promotes Cdc20 ubiquitination Foster and Morgan [2012], Mansfeld et al. [2011], Uzunova et al. [2012], Alfieri et al. [2016]. Thus, Mnd2 is the main responsible for the APC/C-dependent degradation of Cdc20. The reduced degradation of Cdc20 in *mnd2*Δ cells was explained with a reduced ability of APC/C to ubiquitinate Cdc20 [Foster and Morgan, 2012, Fig 4C]. Since Cdc20 ubiquitination induces the disassembly of APC/C^{inhib}, APC/C^{inhib} disassembly in this genetic background is expected to be reduced, and thus the overall levels of the complex to increase. On the other hand, the levels of free MCC are expected not to change, since Mnd2 does not contribute to its formation. In brief, we used this mutation to increase APC/C^{inhib} levels and test if, also in this genetic background, APC/C^{inhib} is limited as predicted by the model.

Surprisingly, when we measured APC/C^{inhib} and MCC in this genetic background, we found that APC/C^{inhib} levels are the same as in wild-type cells (Figure 3.20(a)), while MCC levels are as high as in *CDC20 5X* strains (Figure 3.20(b)). We discuss this surprising result hereafter. Here, we notice that in *mnd2*Δ cells the value of MCC is increased, but not more than in *CDC20 5X* strain, in line with the presence of limiting interactors.

As mentioned, in their work, Foster and Morgan do not explain the reduced degradation of

Cdc20 with reduced affinity between MCC and APC/C, but rather with the reduced ability of APC/C to ubiquitinate Cdc20 [Foster and Morgan, 2012, Fig 4C]. This implies that in *mnd2*Δ cells APC/C^{inhib} assembly is unchanged, while APC/C^{inhib} disassembly is reduced, resulting in higer APC/C^{inhib} levels. However, we directly measured APC/C^{inhib} levels in *MND2* and *mnd2*Δ cells, and they are not statistically different. This can be explained by a reduced assembly of the complex on APC/C, counterbalancing its reduced disassembly. The reduced formation rate of APC/C^{inhib} could also explain the high levels of MCC that we measured in *mnd2*Δ cells. This interpretation is in line with results found in fission yeast Sewart and Hauf [2017], where deletion of the *MND2* ortholog *APC15* causes defects in MCC-APC/C binding. On the other hand, Foster and Morgan interpretation is in line with results found in human cells: deletion of *APC15* increases the amount of MCC coimmunoprecipitated with Cdc27 Uzunova et al. [2012], an essential APC/C subunit. Further analysis are needed to understand whether, in budding yeast, deletion of *MND2* impacts on APC/C^{inhib} assembly or not.

3.4.4 Estimate of number of APC/C^{inhib} and MCC molecules in wild-type strains

So far we used FCCS to measure protein concentration. Of course, this information, together with an estimate of the volume where the reactions take place, can give us also an estimate of the actual number of reacting molecules, with a simple multiplication. Since Cdc23 is nuclear Melloy and Holloway [2004], we consider the ractions taking place in the nucleus. For the nuclear volume, we used $V_{nuc} = 4.2\mu m^3$ Therizols et al. [2010], as we did in the model simulations. The average concentration $\langle [ACMC] \rangle$ of APC/C^{inhib} in the wild-type strain is $11.7\,nM$ (Figure 3.20(a)), while MCC average concentration $\langle [MC] \rangle$ is $14.1\,nM$ (Figure 3.20(b))

We can get the average number N by multiplication:

$$N = \langle [\cdot] \rangle \; N_a \, V_{nuc}$$

where N_a is the Avogadro number, $6.022\,10^{23}\,Mol^{-1}$ and $\langle [\cdot] \rangle$ is the average concentration of the complex of interest. For APC/C^{inhib} in a wild type arrested cell we find:

$$\begin{aligned} N_{ACMC} &= 11.7\,nM \cdot 6.022 \cdot 10^{23}\,Mol^{-1} \cdot 4.2\mu m^3 \\ &= 11.7 \cdot 10^{-9}\,\frac{Mol}{L}\,\frac{6.022 \cdot 10^{23}}{Mol}\,4.2 \cdot 10^{-15}\,L \\ &= 11.7 \cdot 6.022 \cdot 4.2 \cdot 10^{-1} \\ &= 29.5 \end{aligned}$$

A similar computation for MCC leads to $N_{MCC} = 35.6$. Although we used several approximations, the order of magnitude is extremely low, as predicted by the model (see Figure 3.10).

3.5 Transient overexpression of Cdc20 induces adaptation in most cells, but not all

One key conclusion suggested by our model is that the adaptation rate only depends on the distance between the average APC/C^{Cdc20} steady-state levels and the 'anaphase threshold', and thus it is the same for all cells. Hence, transiently moving the APC/C^{Cdc20} steady-state closer to the threshold temporarily increases the adaptation rate in the population. The increase is reversible: once the transient is finished, adaptation rate returns to the endogenous value. Due to the limited amount of Cdc20 interactors, during a SAC arrest we cannot increase the average APC/C^{Cdc20} steady-state above the threshold, that would imply collective and synchronous adaptation as in SAC-defective cells (see Figure 3.11). Therefore, transient increase in adaptation rate is expected only to facilitate transition to anaphase, but not to drive all cells out of metaphase. Those cells that do not have chance to adapt during the brief overexpression are expected to return to the endogenous adaptation rate once the transient is over, since the half-life of Cdc20 is very short ($\sim$ 7 minutes, Figure 3.6(a) and Pan and Chen [2004], Foster and Morgan [2012]). In Figure 3.21 we can see a simulation of this effect. Green and blue lines represent two individual cells, simulated using the stochastic model. Adaptation is caused by APC/C^{Cdc20} hitting the 'anaphase threshold'. APC/C^{Cdc20} average steady-state levels (solid black line) increase as Cdc20 is overexpressed, remaining below the 'anaphase threshold'. The green cell adapts as a consequence of the overexpression, while the blue cell does not, even if the average APC/C^{Cdc20} value is the same in the two cells. The blue cell adapts during a subsequent overexpression of Cdc20.

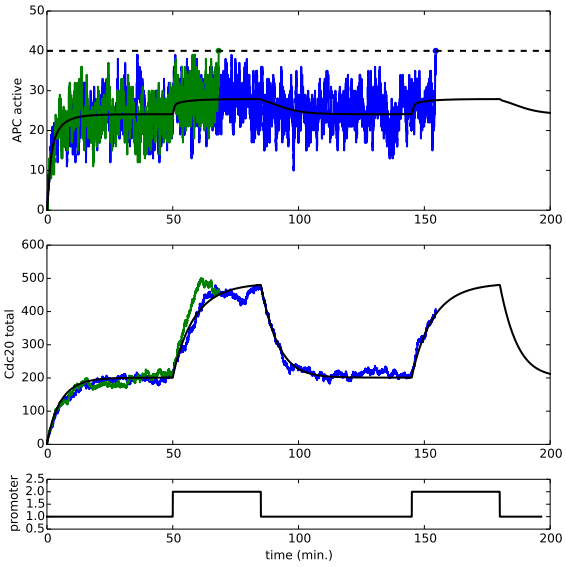

Figure 3.21: Simulation of two transients overexpressions of Cdc20
Simulations of the effect of two transient Cdc20 overexpressions on APC/C^{Cdc20} (upper panel) and Cdc20 total values (central panel). Green and blue lines are produced by the stochastic simulation, and represent the values of two individual cells until their adaptation. Cells adapt once APC/C^{Cdc20} hits the 'anaphase threshold'. Black solid lines are produced with the deterministic model, and thus represent the average levels in the the population. Dashed line is the 'anaphase threshold'. Promoter activation status is shown in the bottom panel. Simulations performed by Fridolin Groß.

To perform this experiment, we challenged arrested cells with exogenous pulses of Cdc20, and measured the response of cells to the overexpression. If the hypothesis is correct, overexpressing Cdc20 at different times should have the same effect. Moreover, if the adaptation propensity only depends on APC/C^{Cdc20} levels and not on the history of the cell, cells that mantain the arrest during a pulse respond to a second overexpression with the same dynamics as a population of cells that is exposed to extra Cdc20 levels for the first time (as the blue cell in Figure 3.21).

To control the exogenous expression of Cdc20, we placed *CDC20* under the control of the *MET3* promoter, which is triggered by the lack of methionine in the growth medium Charvin et al. [2010b]. To modulate the presence of methionine we grew cells in synthetic medium. Since in this medium nocodazole is not active Taylor-Mayer et al. [1988], we induced metaphase arrest by overexpressing Mad2 from the *GAL1* promoter Rossio et al. [2010]. It has been shown that Mad2 overexpression induces *MCC* amount comparable to what measured in nocodazole-arrested cells, indicating a *bona fide* SAC arrest Mariani et al. [2012].

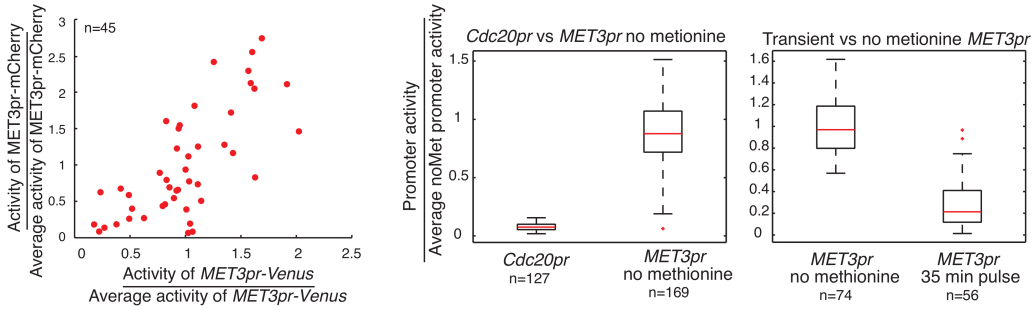

(a) (b)

Figure 3.22: Controls for *MET3pr* activity: coupling and strength
a) Cells carrying *MET3pr*-Venus, *MET3pr*-mCherry (yAC3112) were grown and synchronized in complete low-fluorescent synthetic medium with raffinose (SCR) and released from a G1 arrest in the same medium supplied with 2% galactose, to replicate the settings of the main experiment shown in Figure 3.23(a). During the experiment, cells were grown in microfluidic devices. The *MET3* promoters were activated by removal of methionine for 35 minutes. Synthesis rate is estimated as in Figure 2.6. N: 2. **b**) Indirect comparison of the *MET3pr* activated for 35 minutes and the endogenous *CDC20pr*. Cells carrying *GAL1pr-MAD2 HTB2*-mCherry and either *CDC20pr*-Venus^{degron}, *MET3pr*-Venus^{degron} (left boxplot, strains yAC3108, yAC3359) or *MET3pr*-Venus (right boxplot, strain yAC2341), were grown in galactose to induce Mad2 overexpression. (Left) After metaphase arrest, cells were kept under constant lack of methionine. (Right) After metaphase arrest, cells were kept under constant or transient (35 minutes) lack of methionine. For comparing the activity resulting from the transient induction of *MET3pr* and the activity of *CDC20pr*, both values were normalized to the activity of *MET3pr* under constant deprivation of methionine. The 35 min pulse produced a promoter expression on average 3 times weaker than under constant removal of methionine. The endogenous *CDC20* promoter was 11 times weaker than the *MET3* promoter under constant removal of methionine. N: 2.
Experiments performed by Elena Chiroli. Analysis performed by Andrea Ciliberto. Image taken from Bonaiuti et al. [2017].

Unfortunately, we could not directly tag the protein, since its high turnover prevents fluorophore maturation. Even fast-folding fluorescent proteins have barely the time to mature, resulting in dim and noisy signal (see Section 3.5.1). For this reason we indirectly monitored Cdc20 expression using the Venus^{degron} reporter under a *MET3* promoter, coupled with *MET3pr-CDC20* (see Section 2.8), similarly to what was done in Charvin et al. [2010b]. We confirmed that the activities of the two

MET3 promoters are well coupled (Figure 3.22(a), Pearson correlation coefficient = 0.7, $p = 8\,10^{-7}$, and Charvin et al. [2010b]). To measure adaptation time, we monitored nuclear division, which occurrs regularly in cells that adapt to Mad2 overexpression, and synchronously to Clb2 degradation Vernieri et al. [2013]. To this aim we tagged histone 2B with mCherry.

To test the prediction of the model, cells were arrested in G1, released in galactose to induce Mad2 overexpression and after 110 minutes, when they were arrested in metaphase with large buds, methionine was removed for 35 minutes to activate *MET3* promoter (see Section 2.8 for details on the protocol). In response to the pulse, $\sim 70\%$ of cells adapted rapidly (red histogram in 'Early pulse' lane in Figure 3.23(a)). The remaining $\sim 30\%$ (blue histogram) adapted late after the pulse, with dynamics similar to cells that never experienced Cdc20 overexpression ('No pulse' lane in Figure 3.23(a), direct comparison in Figure 3.23(c)).

It is interesting to notice that cells that respond to the pulse show similar activity of the *MET3pr* compared to cells that do not respond (Figure 3.23(d)). This lack of correlation is in agreement with the saturation of APC/C^{Cdc20} predicted by the model for high levels of Cdc20 synthesis (Figure 3.10(a)). The synthesis rate from the *MET3pr* is indeed 3 times higher than that from the endogenous *CDC20pr* (Figure 3.22(b)).

Adaptation rate depends on APC/C^{Cdc20} steady-state levels and as such not change in time, according to the model. To test this prediction, we activated *MET3pr* at a different time and measured the fraction of adapted cells. Giving the pulse after 170 minutes from G1 release ('Late pulse' lane in Figure 3.23(a)) resulted in a population split just as in the 'Early pulse' condition: one group ($\sim 70\%$) reacted to the pulse, the other adapted as if no pulse was given (direct comparison in Figure 3.23(c)).

To statistically test this claim, we measured the adaptation time as the time between the promoter activation and the nuclear divison in each cell (see definitions in Figure 2.6). In this way we took into account variability in the response of cells to the different pulses. The Kolmogorov-Smirnov two-tails test rejects the hypothesis that the distributions for 'Early pulse' and 'Late pulse' cells are different ($p = 0.46$).

This result reinforces the idea that cells are at steady-state. For this reason, and due to the short half-life of Cdc20, cells that do not adapt immediatly after the pulse are expected to return to the condition of those that never experienced the Cdc20 overexpression. To further confirm this idea, we tested whether cells that do not respond to a first pulse react to a subsequent pulse with the same dynamics as if they faced it for the first time (as the blue cell in Figure 3.21). We then treated cells with two consecutive pulses ('Double pulse' lane in Figure 3.23(a)). Cells reacted to the first as 'Early pulse' cells (Figure 3.23(b)), and those that resisted reacted to the second as 'Late pulse' cells (Figure 3.23(b)).

We cannot compare the effects of the second pulse on 'Late pulse' cells and on 'Double pulse' cells as we did on 'Early pulse' versus 'Late pulse'. Specifically, we cannot measure adaptation time starting from the promoter activation time, since we cannot measure this value in 'Double pulse' cells

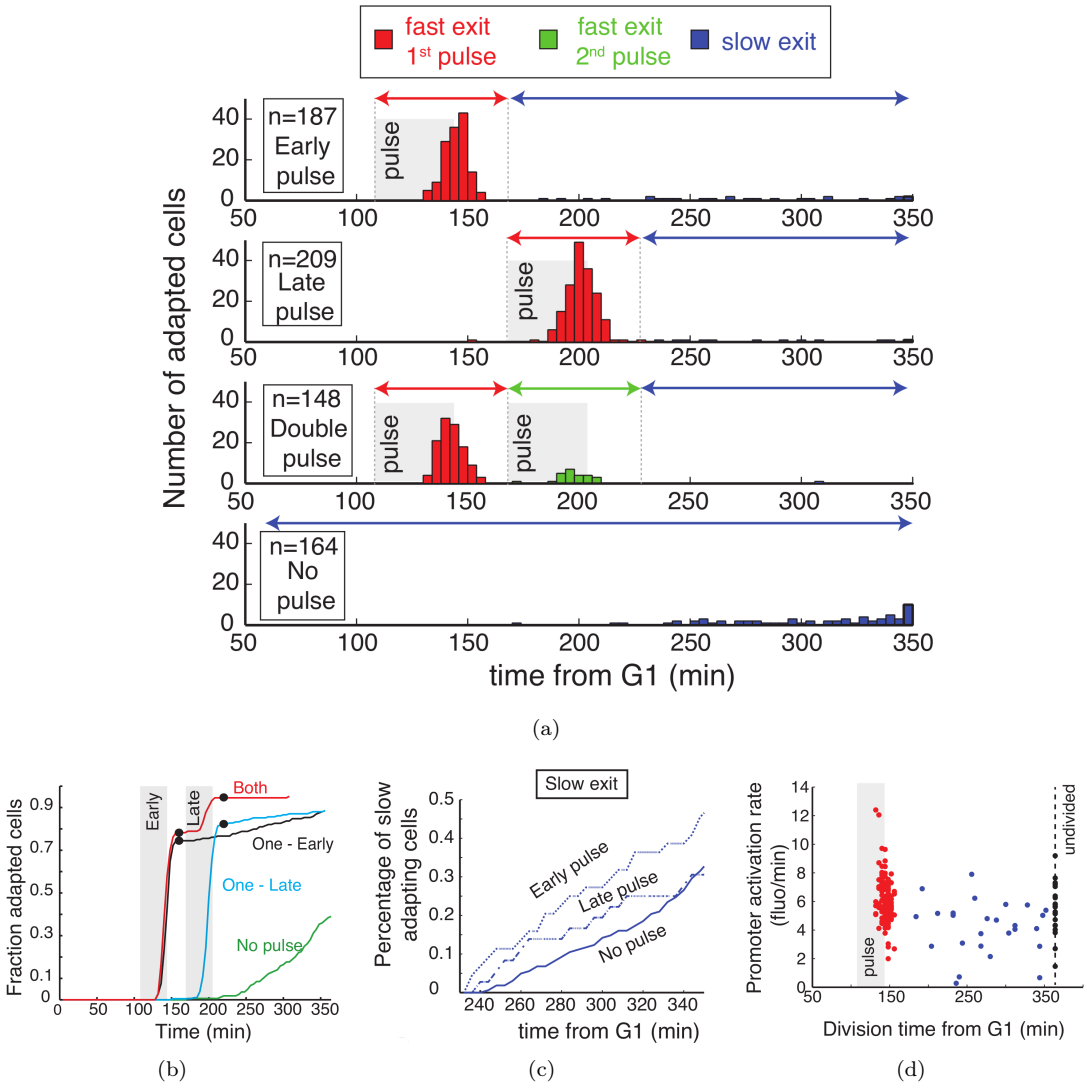

Figure 3.23: Transient overexpression of Cdc20 induces adaptation in most cells, but not all

MET3pr-CDC20 MET3pr-Venus *GAL1pr-MAD2 HTB2*-mCherrycells (yAC2341) were grown and synchronized in complete low-fluorescent synthetic medium with raffinose (SCR) and released from a G1 arrest in the same medium supplied with 2% galactose to activate the *GAL1* promoter. During the experiment, cells were grown in microfluidic devices. The *MET3* promoters were activated by removal of methionine (we call it 'pulse', shown as greyshaded rectangles in panel **a**), which occurred either early or late, the time difference being 1 hour. **a**) Histograms of adaptation times in the four conditions: 'Early pulse' are cells that experienced the 'pulse' 110 minutes after G1 release, 'Late pulse' at 170 minutes, 'Double pulse' both at 110 and 170 minutes, while 'No pulse' cells were grown in the presence of methionine. **b**) Cumulative empirical distributions of the histograms in panel **a**. **c**) Comparison between adaptation times, measured from G1 release, in cells that never switch on the *MET3* promoter ('No pulse') and cells that do not adapt under the early or late pulse. We only keep track of adaptation times occurring after the upper border of the second pulse, that is $t = 220\,min$. **d**) Scatterplot of adaptation times (x-axis) versus *MET3* promoter activity (y-axis) in the early pulse condition of panel **a**. Color code is the same for the two panels.
Experiments and analyses performed with Andrea Ciliberto and Elena Chiroli. Image taken from Bonaiuti et al. [2017].

responding to the second pulse. This is due to the high levels of fluorescence still present in the cells, as a consequece of the activation of *MET3pr*-Venus after the first pulse (Venus has a longer half-life than Cdc20). We then measured adaptation time starting from the beginning of the second pulse. The Kolmogorov-Smirnov two-tails test rejects the hypothesis that the two distributions are different ($p = 0.07$).

In summary, these experiments confirm that cells arrested in mitosis share the same propensity to adapt, which is largely independent on time. The adaptation rate does not depend on previous Cdc20 overexpression.

3.5.1 Tagging Cdc20 with fast-folding version of GFP does not enable accurate measurements

We aimed at measuring Cdc20 levels during a metaphase arrest. For this reason we tagged Cdc20 with a fast-folding version of GFP to allow fluorophore maturation before its degradation, which is very fast during a metaphase arrest (half-life is $\sim$ 7 minutes). See Section 2.9 for details on the strain construction.

Since Cdc20 levels are tightly regulated, we tested the effect of the tag. We arrested cells in G1, released them into fresh medium, and analyzed the protein levels via western blot analysis. The tagged version has similar dynamics compared with wild-type, albeit with slightly increased values (see Figure 3.24(a) and 3.24(b)).

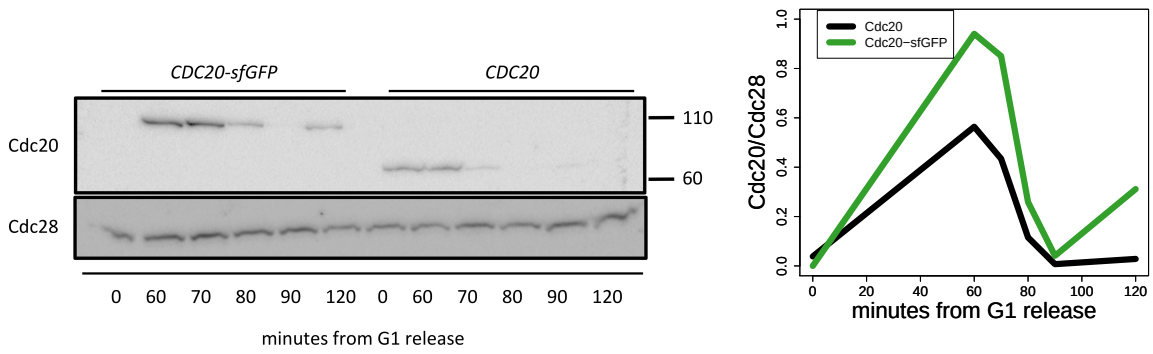

(a) (b)

Figure 3.24: Quality control of Cdc20-sfGFP
a) Western blot analysis of Cdc20 and Cdc28 in cells carrying Cdc20-sfGFP (strain yAC3456) or endogenous Cdc20 (strain yAC3202). Cells were arrested in G1, released into fresh medium and sampled at indicated time-points. **b**) Quantification of Cdc20/Cdc28 signal the gel in panel **a**.
N: 1

To relate metaphase length and Cdc20 levels, we performed single-cell experiments on strains carrying Clb2-mCherry and Cdc20-sfGFP. We arrested cells in G1 and released them into nocodazole in microfluidic devices. Metaphase length was measured with the same analysis used in Section 3.1

and 3.3, that relies on Clb2-mCherry mean signal. Its rise and fall mark the beginning and the end, respectively, of metaphase. Since Cdc20-sfGFP signal was much less clear, we needed a finer analysis. However, we will see, despite our efforts we could not extract reliable information from this tagged protein.

Cdc20-sfGFP protein levels cycle as expected (Figure 3.24(b)), but the fluorescent levels does not (Figure 3.25(a). To extract the dim nuclear signal visible by eye (Figure 3.25(c)), we took advantage of Clb2 signal. Using a k-means clustering on this value, we built a mask that identified nuclear pixels, and averaged Cdc20-sfGFP signal on those. In this way we could measure a signal higher than the mean (Figure 3.25(b)). However, this signal fades with time, independently of the time of mitotic exit (see an example in Figure 3.25(c), and the quantification in Figure 3.25(d)). This is in contrast with the known accumulation of Cdc20 in nocodazole Pan and Chen [2004]. This artefact likely depends on the fast degradation rate of Cdc20 ($\sim$ 7 minutes half-life, see Figure 3.6(a) and Pan and Chen [2004], Foster and Morgan [2012]) which is in the same order of magniture as the maturation time of sfGFP ($\sim$ 5 minutes Khmelinskii et al. [2012]). In other words, sfGFP does not fold fast enough to allow detection of Cdc20. *MND2* deletion slows down Cdc20 degradation by roughly a factor 2 Foster and Morgan [2012], and accordingly Cdc20-sfGFP signal is higher, but the artifact is still present (Figure 3.25(d)). We thus decided to avoid using this marker.

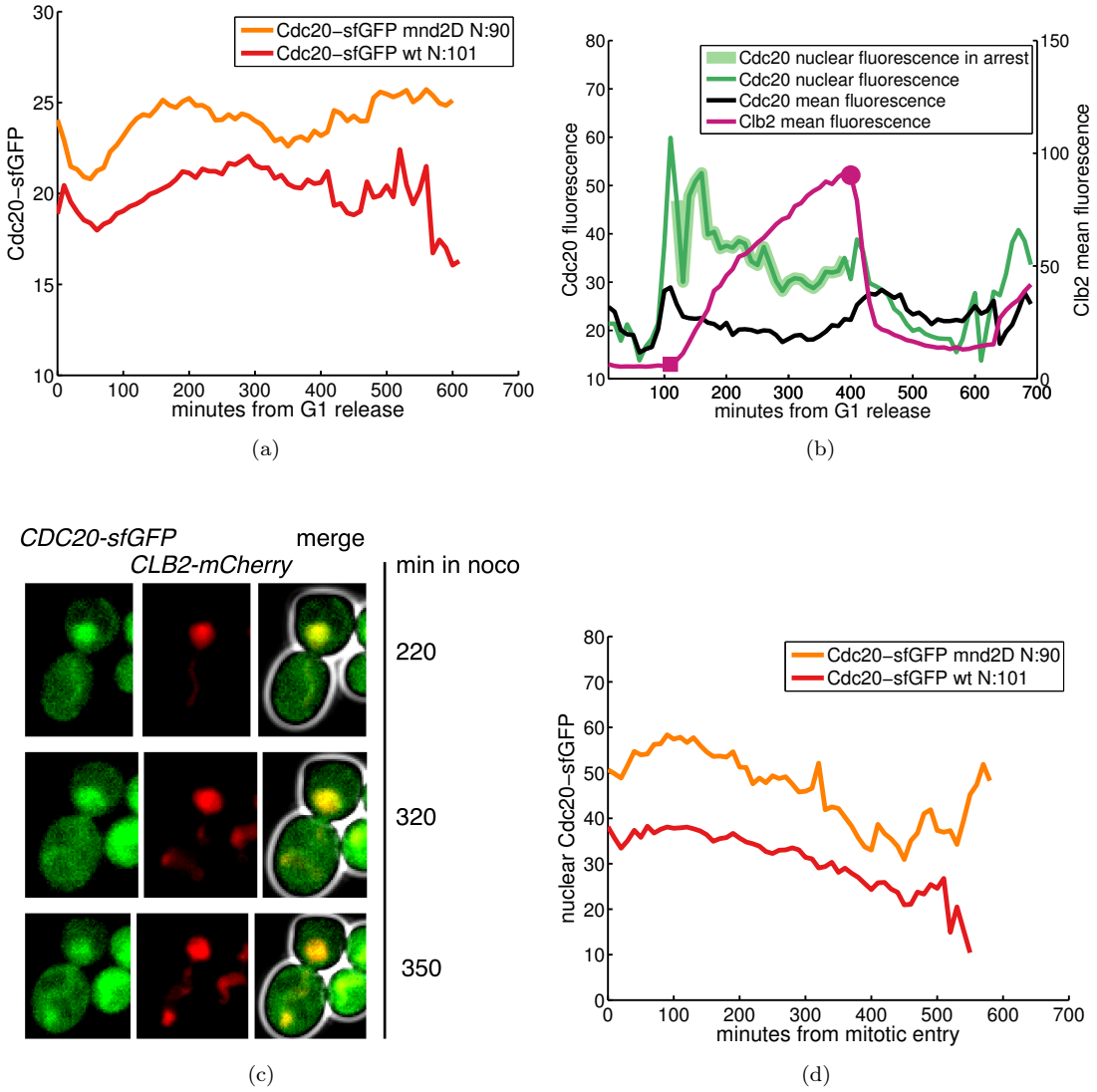

Figure 3.25: Quantification of Cdc20-sfGFP signal
Cells carrying Clb2-mCherry and Cdc20-sfGFP and either *MND2* (strain yAC3614) or *mnd2*Δ (strain yAC3612) were arrested in G1 and released into nocodazole. Data from one experiment, representative of two independent replicates. **a**) For each time-point, we computed the average of Cdc20-sfGFP value over all the cells still arrested in metaphase (that is: cells are included until Clb2 degradation). **b**) Example of mean and nuclear traces of Cdc20-sfGFP signals in wild-type cell. Clb2-cherry mean signal is used to identify the times of mitotic entry (purple square) and mitotic exit (purple dot), used to compute the plot in panel **c**. Thick green line represent Cdc20 nuclear signal between Clb2 accumulation and degradation, that is when the it is correctly identified. **c**) Example of wild-type cell at different time-points. **d**) Nuclear Cdc20-sfGFP signal is synchronized on the mitotic entry and considered only until mitotic exit (thick green line in panel **b**). Plot of the nuclear Cdc20-sfGFP value, averaged over the arrested cells (as in panel **a**), synchronized on the time of mitotic entry.

Chapter 4

Discussion

The phenomenon of adaptation to the SAC is still poorly understood. In this work, we addressed two of the questions regarding its nature: the presence or absence of SAC activity at adaptation; and the origin of the large variability in adaptation times.

Adaptation occurs in the presence of an active checkpoint

At adaptation, cells escape a mitotic arrest in the presence of the stimulus that induced SAC activation. However, it is not clear whether cells actually adapt to an active SAC or if the SAC is switched off, despite the presence of the stimuls, before entering into anaphase. The first scenario, at least in mammalian cells, was suggested in a seminal work by Brito and Rieder Brito and Rieder [2006]. On the other hand, work on mouse oocytes and mammalian cells invoked the second scenario, where the transit into anaphase is caused by SAC silencing, as a consequence of the Cdk1 inactivation driven by the slow degradation of Clb2 Rattani et al. [2014], Vazquez-Novelle et al. [2014]. In budding yeast, Vernieri and colleagues argued against this explanation, demonstrating that Cdk1 inactivation does not silence the SAC Vernieri et al. [2013].

Our data demostrate that budding-yeast cells adapt to an active SAC. Adaptation, measured with the degradation of the mitotic cyclin Clb2 during nocodazole-induced arrest, occurs in the presence of Mad2 localized at kinetochores. Moreover, Clb2 degradation, and the consequent reduction of Cdk1 activity, does not induce the delocalization of Mad2 from kinetochores in every cell. This latter result argues against the need of Cdk1 activity to mantain a SAC arrest, and is thus in agreement with the findings of Vernieri and colleagues.

Adaptation can be described with a stochastic model

The presence of an active SAC at the time of adaptation implies that the checkpoint does not fully inhibit APC/C. Since Cdh1 is dispensable for adaptation Vernieri et al. [2013], this process must be driven by APC/C^{Cdc20}. This finding sets the stage for a model in which APC/C^{Cdc20} is present, albeit at low levels, when an active SAC induces the formation of MCC and APC/C^{inhib}. In this

scenario, adaptation is driven by random fluctuations of APC/C^{Cdc20}, that bring this complex above the value needed for anaphase onset, that we called the 'anaphase threshold'. Random fluctuations are caused by the inherent stochasticity of chemical reactions, and cannot be neglected as a consequence of the low amount of Mad3 and APC/C molecules present in the cell. Despite its simplicity, the model can reproduce the experimentally measured adaptation dynamics (compare Figure 3.4 and Figure 3.9(d)).

Assumptions and properties of the model

The cumulative distribution of experimentally measured adaptation times shows an exponential behavior. The ability of our model to reproduce this beahvior is based on three assumptions, which we discuss hereafter: random fluctuations, steady state, and 'anaphase threshold'. These three properties are not obvious. First, random fluctuations are non-neglibible only in the presence of low number of proteins. We directly measured protein concentration using FCS. This method relies on tagged proteins whose concentration, in principle, could be affected by the tag. However, our measurements are in agreement with a proteome-wide Mass-Spectrometry analysis that included the proteins we investigated (Figure 3.6(b)). The measured concentrations were similar or smaller than ours, with the exception of Mad2 Kulak et al. [2014].

Second, the existence of a steady state, albeit in line with the fast turnover of Cdc20 during a SAC arrest, neglects other factors that could operate on slow time-scale and facilitate adaptation. For example, partially-polymerized microtubules can bind kinetochores and reduce the strength of the SAC signal, that depends on the number of signaling kinetochores Collin et al. [2013]; or cell-growth can reduce the kinetochore-to-cytoplasm ratio, that has been linked to SAC strength in *Caenorhabditis elegans* Galli and Morgan [2016]. Surely, a condition of SAC arrest is not a steady condition, in general terms, since cell growth does not stop. However, our data support the idea that the steady-state approximation is valid. First, the dynamics is well reproduced by an exponential distribution where the adaptation propensity is constant over time (Figure 3.4). Second, overexpressing Cdc20 at different time elicits the same response in terms of adaptation ('Early' and 'Late pulse' in Figure 3.23(a)), and thus the effects of slow time-scale dynamics can be neglected, at least in first approximation.

Third, in our model APC/C^{Cdc20} must overcome a fixed 'anaphase threshold' to induce the transition. This assumption may sound odd, but it underlies the idea that APC/C^{Cdc20} activation triggers positive-feedback loops inducing anaphase onset in a switch-like fashion (see Section 1.1.3). In essence, as mentioned when presenting the model, APC/C^{Cdc20} hitting the threshold in the model represents APC/C^{Cdc20} triggering the feedback loops in a real cell. Once the feedback loops are fired, the transition into anaphase becomes irreversible.

The model describes adaptation as a random event, whose probability to occur is the same in every cell. In this view, the large variability in adaptation times is caused by the stochasticity of the event,

not by intrinsic diversity of cells. This same large variability could also have suggested the presence of subpopulations of cells with different propensity to adapt. Instead, as a proof of homogeneity, we showed that a transient overexpression of Cdc20 elicits the same effect, regardless of previous overexpressions ('Early' and 'Late' *versus* 'Double pulse' in Figure 3.23(a)). In other words, the clustering elicited by the first 'pulse' of Cdc20 does not reflect a different ability to resist adaptation. Homogeneity in adaptation propensity does not exclude the presence of molecular mechanisms that facilitate adaptation, such as APC/C phosphorylation that increases APC/C^{Cdc20} formation. However, we believe that these mechanisms are enabling condition for adaptation, but they are not sufficient for driving adaptation.

Shortcomings of the model

The model cannot explain some observations. First, there is a small fraction of cells (13% over all strains) where the SAC is silenced before Clb2 degradation. We explained this behavior claiming that in these cells nocodazole effect has faded. However, we cannot exclude that these cells managed to escape the arrest via a different mechanism. It is important to notice that, as investigated in Appendix A, including these cells in the analyses does not change the exponential behavior of adaptation times, nor the saturation effect caused by increasing *CDC20* copy number.

Second, the levels of APC/C^{Cdc20}, indirectly deduced from APC/C^{inhib} and MCC levels, are the same in cells carrying 2 or more copies of *CDC20* (Figure 3.20). As a consequence, adaptation rate is expected to be the same in these strains. In contrast, measured adaptation rate increases adding more than 2 copies of *CDC20*, albeit the largest increase is observed from 1 to 2 copies (Figure 3.15(a)). We believe that the explanation for this fact lies in the extreme sensibility of the system to the distance between APC/C^{Cdc20} steady-state and the threshold. Differences in the distance of 1 or 2 molecules can give rise to different adaptation rates, as shown in Figure 3.10. The experimental setting we used may be not enough sensible to measure such small differences.

Third, the agreement between predicted and measured effect of increasing Cdc20 synthesis is only qualitative. Doubling *CDC20* in cells has a smaller effect than doubling Cdc20 synthesis rate in the model (see Figure 3.17). This discrepancy could be due to the fact that the actual production of Cdc20, although increased (Figure 3.12(c)), is not doubled in *CDC20 2X* cells with respect to wild-type. The potential reduction in Cdc20 production does not seem to involve transcription, since the presence of multiple *CDC20* promoters does not influence their activity (see Figure 3.12(d)). Other regulatory steps, downstream transcription, could be involved in regulating Cdc20 production. One possibility is that, in the presence of Cdc20 overexpression, Cdc20 folding cannot cope with synthesis and the protein is misfolded and degraded. This interpretation is in line with the fact that Cdc20 is folded by a chaperonin Camasses et al. [2003], which could become limiting under Cdc20 overexpression. This hypothesis needs to be verified. The mechanisms that oversee Cdc20 production and degradation during SAC-arrest are still poorly understood, and further investigation is needed to

better understand the regulation of Cdc20 synthesis and degradation.

If APC/C^{Cdc20} is substrate of APC/C^{inhib}, the system resists to Cdc20 overexpression

Increasing Cdc20 synthesis does not change the exponential behavior of adaptation times observed in wild-type strains, but only facilitates the transition. We explain this result by arguing that increasing *CDC20* gene copy number moves the steady-state value of APC/C^{Cdc20} closer to the threshold, but not above it. APC/C^{Cdc20} steady state below the 'anaphase threshold' implies that, as in wild-type cells, anaphase onset is triggered by random fluctuations, not by the average APC/C^{Cdc20} value. The distance to be covered by random fluctuation to hit the 'anaphase threshold' is smaller in *CDC20 NX* than in wild-type strains, since APC/C^{Cdc20} steady-state value is higher, and thus the triggering is more likely to occur. Thus, our results support the idea that the nature of adaptation in wild-type and *CDC20 NX* strains is the same.

Indeed, *CDC20 NX* strains adapt in the presence of SAC signaling (Figure 3.14), and show a fully functional checkpoint, as can be noticed by comparing serial dilutions of these strains with SAC-defifient *mad2*Δ on benomyl plates (Figure 3.13(a)). In agreement with our explanation, the average duration of metaphase arrest is reduced in *CDC20 5X* strain compared to wild-type, but not dramatically (from 149 minutes to 70 minutes), and *CDC20 5X* strain is still slower than SAC-defective *mad3*Δ strain (Figure 3.13(b)).

APC/C^{Cdc20} steady-state value saturates and remains below the threshold for high levels of Cdc20 synthesis. In other words, there is no increase in Cdc20 synthesis that can drive APC/C^{Cdc20} steady-state value above the threshold. This result may sound surprising, since Cdc20 is the target of the checkpoint, but it is the direct consequence of the wiring of the SAC network (Figure 3.5). In this wiring, newly synthesised Cdc20 goes either in MCC or in APC/C^{Cdc20}. The two bind and form APC/C^{inhib}. So, APC/C^{Cdc20} and APC/C^{inhib}, that are antagonist in driving or arresting the metaphase-to-anaphase transition, are balanced in an association/dissociation reaction (as we analysed in Section 1.2.1). In such reactions, adding one molecule of the substrate (APC/C^{Cdc20}) facilitates also the formation of a new molecule of the product (APC/C^{inhib}). For this reason, no one of the two species can exclude the other from APC/C, which is shared among them. Increasing Cdc20 leads at most to a 'frozen state' where there are no free Mads/Bubs partners to produce more MCC, nor free APC/C to create more APC/C^{Cdc20}. At this stage the system is no longer sensitive to further increase in Cdc20 Izawa and Pines [2015].

It is worth noticing that a reduced version of our model, including APC/C^{Cdc20} only, could be enough to reproduce the wild-type adaptation dynamics, as long as it retains the three characteristics mentioned previously: random fluctuations, steady state, and 'anaphase threshold'. In contrast, to predict the saturation of APC/C^{Cdc20} the model must include the whole molecular network, and

thus a realistic description of the SAC. This saturation, in particular, is the direct consequence of the recent finding that APC/C^{inhib} results from the binding of APC/C^{Cdc20} and MCC, and of the limiting amount of APC/C present in a cell.

Checkpoint deficiency and anticipated adaptation are not the same phenomenon

With the work presented here, we offer a way to distinguish between anticipated adaptation and SAC defectiveness. The first scenario is described thoroughly in these pages: the average APC/C^{Cdc20} value is kept below the 'anaphase threshold', but random fluctuations can drive individual cells into anaphase. The phenomenon shows large variability. On the other hand, in SAC defective cells, APC/C^{Cdc20} formation is not counteracted by APC/C^{inhib} assembly and Cdc20 degradation, and a large fraction of the total APC/C is activated by Cdc20, since no inhibitors are present. As a result, in these cells the average APC/C^{Cdc20} value is above the 'anaphase threshold', synchronously driving cells into anaphase. Here, stochastic fluctuations have no role, and the transition to anaphase is a deterministic event. Accordingly, the phenomenon is more coherent in time then adaptation, and faster. A simulation of the different scenarios can be found in Figure 3.11.

The distinction between adaptation and deficiency is very relevant for interpreting the response of cells to SAC-inducing stimuli. Overexpression of Cdc20, in our view, results in anticipated adaptation, while inhibition of MCC formation, by deletion of SAC-components or by mutations that impair the binding between MCC members, results in SAC-defectiveness. Along this argumentat, we can reconcile previous results on Cdc20 overexpression with ours. It has been shown that, in nocodazole, the dynamics of Pds1 degradation in budding-yeast cells overexpressing myc-tagged Cdc20 is halfway between wild-type and *mad2*Δ cells Pan and Chen [2004]. For this reason Cdc20-overexpressing cells were identified as checkpoint defective. In our view, these cells can be cathegorized as having anticipated adaptation. Similarly, budding-yeast cells overexpressing Cdc20 from the *GAL1* promoter have been identified as checkpoint defective. However, it takes roughly 30 minutes for these cells to degrade 50% of Pds1 during a nocodazole arrest [Shirayama et al., 1998, Fig. 7c]. This results is comparable with ours, since it takes 40 minutes for 50% of *CDC20 5X* cells to adapt. Thus, we suggest that cells overexpressing Cdc20 from the *GAL1* promoter have a proficient checkpoint, but anticipate adaptation.

Possible interpretation of the present work

As mentioned in Section 1.1.3, prolonged mitotic arrest is not likely to happen in nature. For this reason, the protein network driving the metaphase-to-anaphase transition has likely not been evolutionary shaped to behave optimally in these conditions. In this light, the prominent role of biochemical noise at adaptation could not sound surprising, since cells have not been selected to perform robustly in such conditions. In contrast, other transitions regularly occurring at each cell cycle have been shaped by evolutionary pressure, and so they robustly face biochemical noise, often by mean of feedback

loops Kapuy et al. [2009], Gérard et al. [2015], Skotheim et al. [2008].

In this view, it is possible that noise sensitivity is a common trait of transitions in non-physiological conditions, such as escape from prolonged arrests.

Future goals

The presence of an active SAC at adaptation time and the difference between anticipated adaptation and SAC defectiveness are not unique properties of budding yeast. Fission yeast as well responds to one extra copy of *CDC20* homolog with shorter mitotic arrest than wild-type, but still longer than *mad3*Δ cells Heinrich et al. [2013]. Interestingly, several colon-cancer cell-lines that overexpress Cdc20 (DLD-1, HT29, HCT-116 and LoVo), also show a robust checkpoint response Tighe et al. [2001]. Although both yeast and human cells show active SAC during adaptation, there are several important differences between the two organisms that prevent an automatic application to mammals of the model presented here. In particular, during mammalian SAC-arrest, Cyclin B is slowly degraded, and transcription is silenced. The presence of a fraction of active APC/C^{Cdc20} during an arrest could help explaining adaptation in mammals. Further work is thus needed, but expanding on mammalian cells the model presented here is an important goal.

The model presented here has interesting applications not only on cells adapting to a prolonged mitotic arrest, as investigated in these pages, but also on cells arrested with an active SAC and released from the arrest. In our model, during a SAC-arrest, average APC/C^{Cdc20} is close to the value needed to transit into anaphase. The removal of the SAC-inducing drug allows the correct kinetochore-to-microtubules attachment, increasing the levels of APC/C^{Cdc20} above the threshold, and inducing in this way anaphase. So, in a release from a SAC-arrest, APC/C^{Cdc20} increases and crosses the threshold starting from a value close to it. For a correct chromosome segregation, APC/C^{Cdc20} must cross the threshold in the presence of a complete kinetochore-to-microtubule attachment. However, it is known that SAC strength changes with the number of unattached kinetochores, working like a rheostate Collin et al. [2013]. Thus, cells could transit into anaphase before all sister chromatids are aligned, which induces mis-segreagation defects. It would be interesting to investigate this scenario by arresting cells with an active SAC and releasing them from the arrest. If the model is correct, cell-cycle resumption could take place before kinetochore-to-microtubule attachment is completed, and thus it could result in an increased mis-segregation rate.

Investigating the consequences of release from a SAC-arrest is an interesting topic, not only as a speculative question, but also in a cancer-treatment perspective. Indeed, spindle-depolymerizing chemotherapic agents are given with protocols that resemble the 'arrest and release' scenario. For example, vinorelbine is given to patients once a week for three weeks, and in the time between two administrations the drug is virtually absent from the blood of patients Caffo et al. [2013]. Investigating how SAC-release works, in the light of the present model, is an interesting plan.

Appendices

Appendix A

Mad2 localization: robustness analysis

The definition of the measure used to quantify Mad2 localization (the 'Mad2 localization index' presented in Section 2.3) is reasonable but arbitrary. For this reason, we analysed how much the results presented in Figures 3.2(d), 3.3, 3.4, 3.14 and 3.15(a), depend on the way we defined the localization index. To do so, we defined other 'localization indexes'. We call LI_0 the localization index used in the Results chapter, while the others are:

- $LI_1 = \frac{(mean\ of\ brightest\ 1\%\ of\ pixels\ in\ the\ raw\ image) - (mean\ of\ the\ raw\ image)}{standard\ deviation\ of\ the\ raw\ image}$, as in Primorac et al. [2013];
- LI_2 = the same definition as LI_1, but applied to an image filtered with the Laplacian of Gaussian presented in equation (2.1);
- LI_3 = the same definition as LI_1, but applied to an image filtered with a 3x3 matrix of ones;
- LI_4 = the value of the brightest pixel in the raw image.

We applied the analysis pipeline used in the Results (see Section 2.3), replacing LI_0 with each of the different 'localization indexes'. The resulting figures are very similar to those presented in the Results section. Also the hazard ratio, final output of this pipeline, are quantitatively very similar with every different variation. As an example, in Figures A.1(a)-A.1(d) are shown the figures obtained using LI_1 (since Figure 3.15(a) includes Figure 3.4, only the first is reproduced). The number n of cells included in Figure 3.15(a) and in Figure A.1(d) are different, since cells where Mad2 is not localized at the time of Clb2 degradation are excluded, and this definition depends on the localization index.

As an additional control, we ran the pipeline including in the analysis all the cells where Mad2 is not localized at the time of Clb2 degradation (step 6 in the pipeline). Also in this case, the results are quantitatively very similar (Figures A.1(e)-A.1(h)).

This analysis reinforces the idea that our results are independent on the specific measure of Mad2 localization status

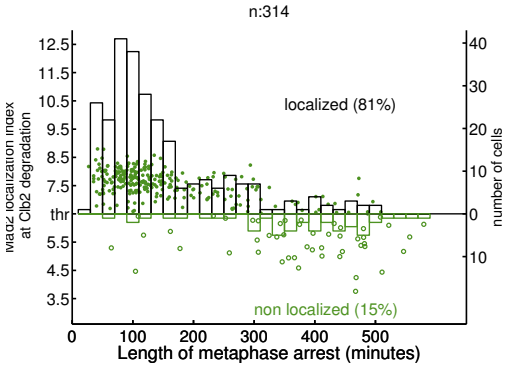

(a) as Figure 3.2(d)

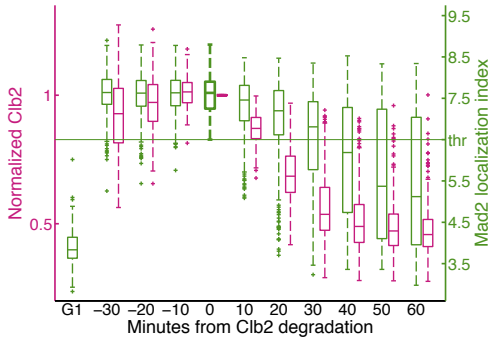

(b) as Figure 3.3

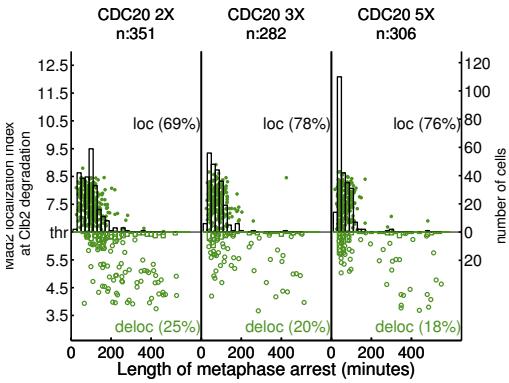

(c) as Figure 3.14

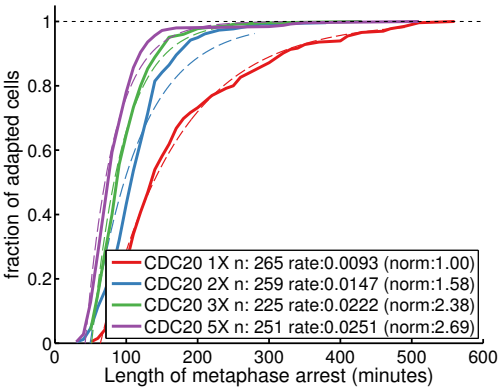

(d) as Figure 3.15(a)

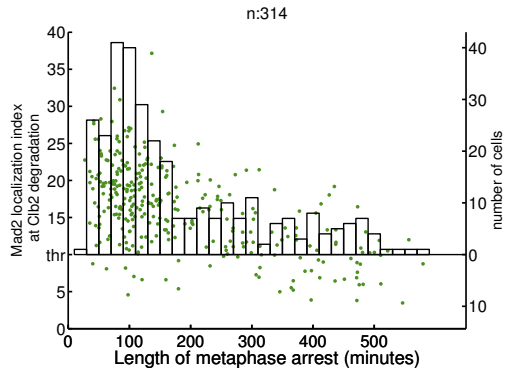

(e) as Figure 3.2(d)

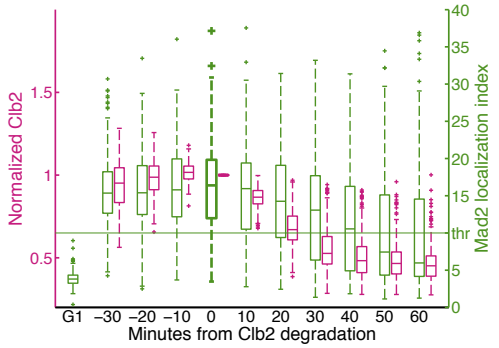

(f) as Figure 3.3

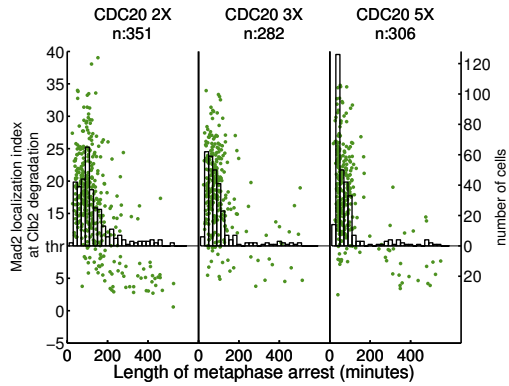

(g) as Figure 3.14

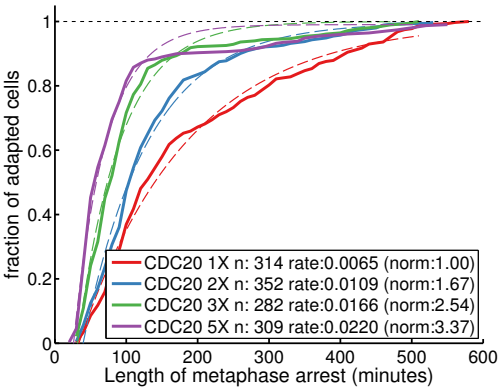

(h) as Figure 3.15(a)

Figure A.1: Results of Sections 3.1 and 3.3 do not depend on the definition of localization index.
Data from haploid experiments are analysed using the same pipeline presented in Section 2.3, but varying the steps related to Mad2 localization. Figures 3.2(d), 3.3, 3.14 and 3.15(a) are reproduced. Since the cumulative curve of wild-type haploid strain presented in Figure 3.4 is included in Figure 3.14, only the reproduction of the latter is presented here. **a-d**) Data from haploid experiments analysed using a different definition of Mad2 localization index (LI_1). **e-h**) Data from haploid experiments analysed without the exclusion of cells based on Mad2 localization status at the time of Clb2 degradation.

Appendix B

Evidence for the absence of subpopulations with different adaptation rates

The fact, observed in Section 3.2, that the empirical cumulative distribution of adaptation times is exponential, suggests that all cells share the same propensity to adapt. However, it is not obvious that based on this we can exclude the existence of subpopulations of cells with different propensities. To test it, we compared the 'simple model' of one exponential distribution (one adaptation rate θ describing the whole population) with a 'mixture model' of two exponential distributions (two adaptation rates θ_1 and θ_2, plus one parameter fixing the relative sizes of the subpopulations). Notice that the 'simple model' is a subcase of the 'mixture model' when either $\theta_1 = \theta_2$ or one of the two subpopulation is absent. We measured the performance of each model by estimating maximum likelihood using the `R` package `Renext` (https://CRAN.R-project.org/package=Renext).

First, we measured the performance of the 'simple model' on two groups of data: the experimentally measured adaptation time and an artificially generated set, drawn from a simple exponential distribution. We found that the performance is very similar (log-likelihood $= -1522$ for the experimental and -1515 ± 30 for the artificial data), thus confirming that our experimental data are in excellent agreement with the simple model.

Then, we fitted the experimental data set with the 'mixture model', resulting in $\theta_1 = \theta_2$. This implies that the 'mixture model' reduces to the 'simple' one, and thus that the two models give the same log-likelihood (horizontal dashed line in Figure B.1). We asked ourselves how sensible the 'mixture model' is in identifying mixed populations, when present. For this reason we generated artificial data sets where we imposed the presence of two subpopulations, drawn from exponential distributions and with the same size. We tuned the ratio r between the rates of the two populations

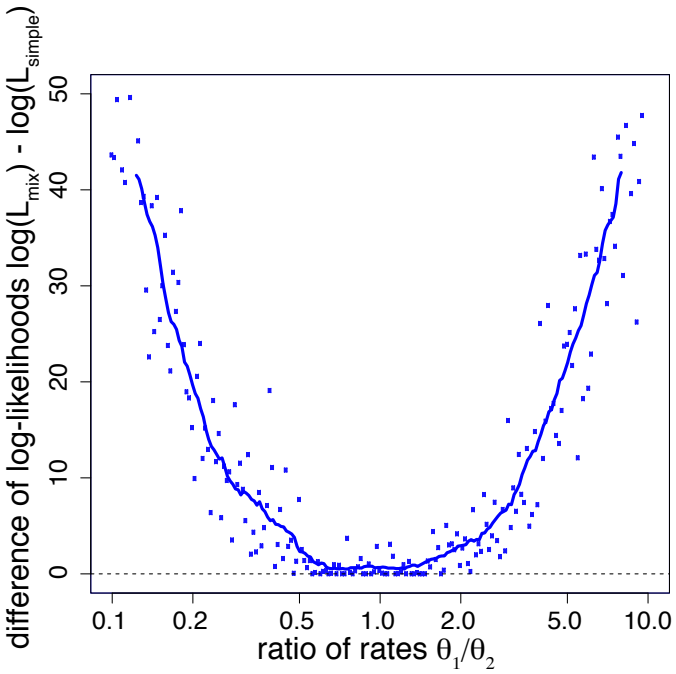

Figure B.1: Comparison of simple exponential model to a mixed model with two subpopulations.
Each dot corresponds to an artificially generated data set. Positive values on the y-axis indicate that the mixed model performs better. The thick blue line was obtained by smoothing the data with a moving average filter. Horizontal dashed line indicates the difference of log-likelihoods of the two models obtained on our data, which is 0. Simulation performed by Fridolin Groß.

and we measured the difference between the log-likelihood returned by the two models (blue dots in Figure B.1). If there are distinct subpopulations (that is: outside $r = 1$) the 'mixture model' outperforms the 'simple model'. The fact that the two models perform the same on experimental data provides evidence against the existence of two subpopulations.

Appendix C

An *in-silico* analysis of inhibitory logics in the mitotic checkpoint network

In the next pages we present the manuscript, in preparation, of a theoretical work aimed at investigating the effect of different topological networks of mitotic inhibition Groß et al. [In preparation].

An *in-silico* analysis of inhibitory logics in the mitotic checkpoint network

Fridolin Gross[1], Paolo Bonaiuti[1], Silke Hauf[2,3] and Andrea Ciliberto[1,4]

1- Istituto Firc di Oncologia Molecolare, IFOM, Via Adamello 16, 20139 Milano, Italy

2- Department of Biological Sciences, Virginia Tech, Blacksburg, VA 24061, USA

3- Biocomplexity Institute, Virginia Tech, Blacksburg, VA 24061, USA

4- Istituto di Genetica Molecolare, Consiglio Nazionale delle Ricerche (IGM-CNR), Via Abbiategrasso 207, 27100 Pavia, Italy

ABSTRACT

The mitotic checkpoint (also called spindle assembly checkpoint) is a signaling pathway that ensures faithful chromosome segregation. Mitotic checkpoint proteins inhibit the anaphase-promoting complex (APC/C) and its activator Cdc20 to prevent precocious anaphase. Checkpoint signaling leads to a complex of APC/C, Cdc20, and checkpoint proteins, in which the APC/C is inactive. Recent results have revealed that this inactive complex (APC/C^{MCC2}) contains two molecules of Cdc20 rather than one, as was long assumed. The regulatory implications of this discovery remain unexplored. APC/C^{MCC2} assembly can theoretically proceed through different sub-complexes, not all of which have been studied experimentally. Here, we systematically investigate different assembly pathways using mathematical models. We identify two distinct topologies with distinct behavior: 'sequential inhibition', which allows checkpoint function at both normal and abnormally high levels of Cdc20, and 'competitive inhibition', where the checkpoint functions at normal but fails at high levels of Cdc20. We find that the existence of one specific biochemical reaction can make or break checkpoint function at high Cdc20 levels. These findings could inform molecular strategies to treat cancers that exhibit Cdc20 overexpression.

INTRODUCTION

Faithful chromosome segregation requires that each sister chromatid moves towards a different daughter cell. This is guaranteed by the mitotic checkpoint (also known as spindle assembly checkpoint or SAC). As long as chromosomes are improperly attached to the mitotic spindle, the mitotic checkpoint inhibits the anaphase-promoting complex (APC/C) and its essential coactivator Cdc20, thereby preventing anaphase. Only when all attachments are correct, the checkpoint is lifted: APC/C^{Cdc20} becomes active, chromosome segregation can take place, and will now have a high chance of being executed correctly [1].

The mitotic checkpoint network has been investigated for decades, and likely all of the relevant players have been identified. Their interactions have been analyzed *in vivo* and *in vitro*, through both genetics and biochemistry. The concentrations of several network components have been determined in different organisms ([2-9, 10) Bonaiuti et al., in press), and the kinetics of the most relevant reactions have been studied in vitro {Faesen, 2017 #9, 11-15]. The resulting picture of the mitotic checkpoint network is complex [1, 16]. The network is composed of a cascade of association/dissociation reactions, which culminates in the formation of the inhibited form of APC/C. The ultimate effector of the checkpoint pathway is the mitotic checkpoint complex (MCC). The binding of the checkpoint protein Mad2 to Cdc20 is the first step in MCC assembly, and is limiting in forming the final inhibitor [17]. Subsequently, the checkpoint proteins Mad3/BubR1 and Bub3 bind to Mad2-Cdc20 to form the MCC. The MCC can bind the APC/C, a ubiquitin ligase, and prevent it from targeting its anaphase substrates – mitotic cyclins and securin – for degradation.

All these results have been solidly confirmed by multiple studies in several organisms, suggesting that we have reached a consensus picture of the main molecular actors in the pathway, as well as their interactions. Yet, our understanding of the SAC network was recently expanded by a key discovery: MCC bound to APC/C does not carry one molecule of Cdc20, as supposed for decades, but two [18, 19]. We call it MCC2, as opposed to MCC1 with only one Cdc20 (Figure 1). The two Cdc20 molecules are bound to two different KEN box motifs in the checkpoint protein Mad3/BubR1 [19-23]. Crucially, binding of both Cdc20 molecules is needed for APC/C inhibition [22-29].

The presence of two Cdc20 molecules in the inhibited APC/C challenges our understanding of the topology of the mitotic checkpoint network. In particular, it is not clear which reactions and intermediate species eventually lead to the formation of inhibited APC/C (Figure 1), and whether all possible assembly pathways support checkpoint activity. Here, we address this issue by systematically analyzing different topologies of the mitotic checkpoint network, using a formal quantitative framework. We show that the possible behaviors of this network can be traced back to two archetypal modes that represent two different inhibitory strategies.

RESULTS

APC/C^{MCC2} could be formed through different intermediates

The final product of the SAC network is the inhibited form of the APC/C which was recently shown to carry two molecules of Cdc20 (APC/C^{MCC2}) [19, 20, 23]. Its formation can follow two possible paths, which are not mutually exclusive: (i) as has been suggested [19], APC/C^{MCC2} is created by binding of MCC1 to APC/C^{Cdc20}; or (ii) the free

MCC2 complex binds to APC/C (Figure 1). Theoretically, there is the third possibility that binding of MCC1 to APC/C gives rise to APC/C^{MCC1}, which then picks up a second molecule of Cdc20 to become APC/C^{MCC2}. However, MCC1 binds the APC/C poorly when binding sites for the second Cdc20 molecule are mutated [22, 26, 30]. This suggests that APC/C^{MCC1} is unstable, and unlikely to be a precursor for APC/C^{MCC2}. We therefore do not include this last possibility in our analysis.

From the remaining two possibilities of forming APC/C^{MCC2}, we can assemble three networks (Figure 2). The two reactions common to all of them are the formation of MCC1 (reaction 1) and of APC/C^{Cdc20} (reaction 2). In network (i) APC/C^{MCC2} is directly formed from APC/C^{Cdc20} and MCC1 (reaction 3), whereas in network (ii) MCC1 first binds another Cdc20 (reaction 4) and this MCC2 then binds to free APC/C (reaction 5). Network (iii) includes the reactions of both (i) and (ii). One can arrive at network (iii) either by adding reactions 4 and 5 to network (i), or by adding reaction 3 to network (ii). In order to make the comparison between networks easier, we depict both versions in Figure 2.

Experimental evidence clearly supports possibility (i) [19], but the formation of free MCC2, not bound to the APC/C, has not been ruled out. Free MCC2 has been observed after deleting the APC/C subunit Apc15 in fission yeast [21, 22], but whether this species also exists in wild type cells remains unclear. This leaves (i) and (iii) as the most likely possibilities. To obtain a systematic understanding of the system, we also analyze (ii).

In the first network [Figure 2, (i)], inhibitory binding follows the formation of the active APC/C^{Cdc20} complex, we therefore call it ‘sequential inhibition’. In the second network

[Figure 2, (ii)], APC/C can either associate with MCC2 to form the inhibited form of the APC/C, or with Cdc20 to form the active form of the APC/C, but active APC/C^{Cdc20} never gets converted into the inactive APC/C^{MCC2}. Hence, MCC2 and Cdc20 compete for the APC/C. We call this 'competitive inhibition'. Finally, when (i) and (ii) are combined [Figure 2, (iii)], there is still the element of sequential inhibition, but Cdc20 and MCC2 now also compete for the APC/C. It is not obvious whether all these networks are expected to mount a SAC-mediated arrest, and how they will respond to perturbations.

The behavior of the SAC networks at different levels of Cdc20

We investigate the performance of the different networks by analyzing their behavior as a function of the total concentration of Cdc20 (which includes both free Cdc20 as well as Cdc20 within protein complexes). We chose Cdc20 because the concentration of this protein is dynamic, unlike the concentrations of the SAC proteins and the APC/C subunits, which have been found to be largely stable [10, 24, 27, 29, 31-37]. Moreover, Cdc20 is known to be overexpressed in several cancers [38-41], which calls for an investigation on the effect of high levels of Cdc20 in mitotically arrested cells.

Although it is known that Cdc20 is actively produced and degraded during a checkpoint arrest, the kinetics of this synthesis and degradation are incompletely examined [16, 42]. For example, it is not clear whether disassembly of APC/C^{MCC2}, driven by Cdc20 ubiquitination, gives rise to the complex APC/C/C^{Cdc20} or to the individual species APC/C and Cdc20. However, we can neglect the molecular details of Cdc20 synthesis and degradation and still obtain general conclusions if we focus on the steady state behavior of the SAC network where synthesis and degradation are balanced. We can then treat the total amount of Cdc20 as a free parameter in order to understand the

consequences of different expression levels for the behavior of the model. The steady state analysis comes at a price: we have to neglect potentially interesting transient behavior before the system reaches the steady state. Despite this limitation, the steady state is relevant for studying checkpoint behavior since it corresponds to the situation of checkpoint arrest.

We monitor the status of the SAC by keeping track of the active and inhibited forms of APC/C: APC/C^{Cdc20} and APC/C^{MCC2}, respectively. To interpret the concentrations of these complexes in terms of SAC proficiency or deficiency, we need to know the fraction of APC/C that must be in the active form for anaphase to occur. It is known that preventing anaphase requires a strong knock-down of Cdc20 [43, 44]. We thus distinguish between a state of SAC proficiency, where APC/C^{Cdc20} is kept low, and of SAC deficiency, where APC/C^{Cdc20} is high (Figure 3).

To simplify our models, we lumped Mad2 and Mad3 into one species (Mad) that binds Cdc20 (Figure 2). This simplification is justified because Mad2 and Mad3 bind sequentially to form MCC1 and Mad2-binding is rate-limiting (Figure 1). Relaxing this assumption does not qualitatively alter our results (Supplementary Material, Supplementary Figure 4).

Model parameters are set within a physiologically plausible range

The behavior of our models depends on several parameter values. Fortunately, many parameters of the mitotic checkpoint network have been measured experimentally. Concentrations vary in different organisms and across studies, but the ranges are similar (Table 1). In mammals, budding yeast and fission yeast, the APC/C seems to be similarly or less abundant than ‘free Mad2’ (not bound to Mad1) and Mad3, the two

species relevant for MCC formation. Cdc20 concentrations are in the range of, or higher than APC/C concentrations. In our simulations, we assume a 1 : 0.5 : 1 ratio of Mad, APC/C, and Cdc20. For simplicity, we rescale all concentrations to that of Mad.

For the simulations, we chose small dissociation constants ($1/100^{th}$ of protein concentration). Since SAC complexes are formed by proteins whose concentrations rarely exceed 100nM, this translates into K_Ds in the low nanomolar range. Such values are in agreement with published data for MCC formation and APC/C inhibition [17, 45]. In our simulations, we use identical K_Ds for all reactions, in order to focus on differences due to network topology only. Our analytical results allow us to understand how changing individual parameters would change the qualitative behavior (Supplementary Material).

Sequential inhibition does not allow APC/C^{Cdc20} to dominate

In order to compare the behavior of the different networks, we simulate the concentrations at steady state for varying levels of Cdc20. To understand the resulting curves, it is useful to consider the extreme situations, starting from the regime where Cdc20 is limiting (Cdc20 < Mad, APC/C). In the sequential inhibition model (i), APC/C^{MCC2} increases roughly linearly with Cdc20, whereas both APC/C^{Cdc20} and MCC1 increase proportional to the square root of total Cdc20 (Figure 3, Supplementary Figure 3). APC/C^{MCC2} dominates over APC/C^{Cdc20} due to a 'funneling effect': In the inhibitory pathway three binding reactions are required to form the inhibited species APC/C^{MCC2} (reactions 1,2, and 3), while only one reaction is used in the activating pathway to form APC/C^{Cdc20} (reaction 2). As long as the substrates for the inhibitor (i.e. Mad) are

available in sufficient amounts, Cdc20 is trapped in (funneled into) the inhibitory pathway because the effective binding strength of the combined reactions adds up. For small levels of Cdc20 this effect can easily be explained mathematically when making the reasonable assumption that most Mad and APC/C remains in its free form in this situation (Supplementary Material 3.1).

In the other extreme regime, where Mad and APC/C become limiting (Cdc20 > Mad2, APC/C), the binding reactions leading to MCC1 and APC/C^{Cdc20} production are saturated, and there is no significant amount of free APC/C or free Mad proteins [Figure 3, (i)]. Consequently, the concentrations of MCC1, APC/C^{MCC2} and APC/C^{Cdc20} stay constant if Cdc20 is increased further. The network is effectively reduced to the single binding reaction between MCC1 and APC/C^{Cdc20} [dashed box in Figure 3 (i)]. The validity of the approximation is confirmed by comparing the behavior of the full system to the simplified model (Supplementary Figure 3). Thus, at steady state we have an equilibrium between substrates (MCC1 and APC/C^{Cdc20}) and product (APC/C^{MCC2}), where both active and inactive species coexist. Assuming a reasonable stability of APC/C^{MCC2} (i.e., K_D smaller than total APC/C and total Mad), the inhibited APC/C^{MCC2} is in excess over APC/C^{Cdc20}, a condition that we associate with checkpoint proficiency.

We conclude that a crucial property of the sequential inhibition network is that APC/C^{Cdc20} never exceeds APC/C^{MCC2}, provided reasonably strong binding of all complexes. Furthermore, active APC/C^{Cdc20} and inactive APC/C^{MCC2} always co-exist, although at high Cdc20 concentrations the ratio is strongly biased towards APC/C^{MCC2}. Once Mad proteins and APC/C are saturated, the steady state concentrations of APC/C^{Cdc20} and APC/C^{MCC2} become insensitive to further increases of Cdc20.

Competitive inhibition leads to checkpoint failure at high Cdc20 concentrations

The competitive inhibition network (ii) behaves like the sequential inhibition network (i) for small values of Cdc20 (Cdc20 < APC/C, Mad), showing an efficient SAC arrest (Figure 3, (ii), and Supplementary Figure 3). APC/C^{MCC2} is in excess over APC/C^{Cdc20} even if we consider the symmetrical scenario where all individual species are present at identical levels (not shown). This result may seem surprising since Cdc20 and MCC2 have the same chance to bind APC/C. However, APC/C^{MCC2} is favored by the same funneling effect as in the sequential inhibition model, because there are three inhibitory reactions (1, 4, and 5), but only one activating reaction (2). The effect is indifferent to the order in which the complexes are formed, which is a straightforward consequence of mass action kinetics and a property of chemical reaction networks called “detailed balancing”. Accordingly, the behavior of the two networks for small values of Cdc20 is hardly distinguishable and can mathematically be understood in terms of the same approximation (Supplementary Material).

If we increase the total level of Cdc20, the system eventually runs out of free Mad. At this point, APC/C^{Cdc20} starts to increase at the expense of APC/C^{MCC2}. This change of equilibrium is driven by the increase of free Cdc20, which eventually wins the competition by detracting APC/C from APC/C^{MCC2}. Thus, in the competitive inhibition model, high concentrations of Cdc20 result in considerable formation of APC/C^{Cdc20}. In other words, cells become SAC deficient under Cdc20 overexpression. The network can be reduced to the smaller section shown in the dashed box of Figure 3 (ii), because reaction 1 and reaction 4 are saturated. A simplified model of this subnetwork well

approximates the behavior of the whole network for large concentrations of Cdc20 (Supplementary Figure 3).

Overall, the competitive inhibition model shows a steady state behavior that is consistent with an active SAC at low Cdc20 concentrations, but SAC failure at high Cdc20 concentrations.

The combined model behaves like competitive inhibition

Since it is not clear whether MCC1 – Cdc20 (reaction 4) and MCC2 – APC/C binding (reaction 5) co-exist in vivo with MCC1 – APC/C^{Cdc20} binding (reaction 3), we examined the combined network (iii) (Figure 2), which embeds all reactions of (i) and (ii). The behavior of the combined model cannot be easily predicted from the network's topology.

Our simulations show that for low levels of total Cd20 we again observe the linear increase of APC/C^{MCC2} and the square root increase of APC/C^{Cdc20} that was exhibited by both (i) and (ii). For high levels of Cdc20, the network exhibits the same behavior as the competitive inhibition model: APC/C^{Cdc20} starts exceeding APC/C^{MCC2} [Figure 3, (iii)]. To rationalize this result, we observe that (iii) can be formed from the competitive inhibition model (ii) by adding reaction 3 (Figure 2, 3). However, this addition is inconsequential in the high Cdc20 regime (Cdc20 in excess of Mad proteins and APC/C) because MCC1 is depleted at the expense of MCC2. Since the newly added reaction 3 is essentially inactive, there is no sequential inhibition, and APC/C^{Cdc20} prevails, just like in the competitive inhibition model. In this regime, the model therefore reduces to the same simplified model as (ii) (Supplementary Figure 3).

Interpreting (iii) as a modified sequential inhibition network (Figure 2, (iii) left side) is also interesting. Surprisingly, the APC/C^{Cdc20} 'wins it all' behavior for high Cdc20 levels

is present even if we introduce reaction 4 without reaction 5 (Figure 4), i.e. if MCC2 is formed but does not bind to APC/C. The reason is that for high Cdc20 concentrations, MCC2 becomes a dead-end for Mads, a condition that allows Cdc20 to freely bind APC/C. Thus, simply allowing the formation of free MCC2 is enough to turn a system capable of buffering extra Cdc20 levels into a system that is vulnerable to Cdc20 overexpression (Figure 4). However, checkpoint failure only occurs when Cdc20 is in excess, otherwise inhibited APC/C is still able to overcome active APC/C^{Cdc20} (Figure 4).

DISCUSSION

In this paper, we have theoretically analyzed the behavior of the mitotic checkpoint network given the new finding of an MCC complex with two Cdc20 molecules. This is the first time the consequences of this key feature are explored with a quantitative approach. In particular, we have analyzed three networks: one where APC/C^{Cdc20} is the precursor for APC/C^{MCC2} [(i) sequential inhibition], a second where Cdc20 and MCC2 compete for APC/C [(ii) competitive inhibition], and finally a third which is the combination of the first two [(iii) combined model]. While the competitive inhibition model can be formulated both with one or two molecules of Cdc20 in MCC, the sequential and combined models are a direct consequence of the discovery that two molecules of Cdc20 take part in APC/C^{MCC2} formation.

Based on intuitive assumptions, it has been suggested that free MCC2 formation, unbound to APC/C, is unlikely, because it would not be compatible with a robust checkpoint response [26]. The reasoning was that MCC1 should have a higher affinity for APC/C^{Cdc20} than for free Cdc20 in order to efficiently avoid APC/C^{Cdc20} formation. Our quantitative analysis now shows that allowing free MCC2 formation indeed creates

sensitivity to Cdc20 overexpression (Figure 3, 4). Simply by increasing the stability of the MCC2 complex, the combined network shifts from resistance to sensitivity towards extra Cdc20 levels (Figure 4).

Noticeably, however, and against the intuitive assumption, all three networks that we examined can mount a checkpoint response at non-saturating, physiological Cdc20 levels. This is due to what we called the 'funneling' effect, which is relevant when Cdc20 is limiting. In this regime, the three different networks employ different reactions, but all of them require three binding steps to produce APC/C^{MCC2}. The formation of APC/C^{Cdc20}, by contrast, requires only one binding step. Even using perfectly symmetrical networks (same K_Ds for all reactions and same concentrations for all species), this topological difference between the activating and inactivating branches of the SAC pathway results in Cdc20 being 'funneled' towards the inhibitory pathway. As a consequence, APC/C^{MCC2} exceeds APC/C^{Cdc20} for physiological levels of Cdc20. Our analytical results show that this is true as long as $[Mtotal]/(K_D\ [Atotl])<1$, i.e. provided that the complexes are reasonably stable and/or the total APC/C is not exceeding the Mads. Both conditions are reasonable, and largely verified experimentally (Table 1 and Supplementary Material, Parameters). Thus, for physiological levels of Cdc20, the SAC is expected to be operational even if free MCC2 formation is allowed.

Our analysis suggests that the different networks could be experimentally distinguished by studying the checkpoint response to Cdc20 overexpression. In several organisms, Cdc20 overexpression has been reported to induce precocious exit from a SAC-mediated arrest (Bonaiuti et al., in press, [8, 34, 46, 47]). However, we want to caution that this does not necessarily constitute evidence for a network that includes free MCC2

formation. In these experiments, cells exit mitosis with kinetics that are intermediate between the long mitotic delay of cells with normal Cdc20 levels and the extremely short mitosis of complete checkpoint failure (Bonaiuti et al, in press, [8, 34]). It has recently been demonstrated for budding yeast that the precocious escape from the SAC under Cdc20 overexpression does not constitute SAC failure, but is due to stochastic fluctuations of APC/C^{Cdc20} that reach levels high enough to drive cells into anaphase (Bonaiuti et al, in press). By contrast, the models that include stable, free MCC2 [(ii) and (iii)] predict that Cdc20 overexpression results in average levels of APC/C^{Cdc20} that are sufficient to drive cells into anaphase. Hence, cells are expected to escape from a checkpoint arrest synchronously and rapidly, in a deterministic fashion, similarly to SAC-deficient cells.

Our theoretical results have interesting translational implications. Cdc20 is overexpressed in a large variety of cancer cells [38-41]. Whether Cdc20 overexpression is a driver or a passenger of carcinogenesis is not yet clear. Yet, it is known that cancer cells are largely SAC proficient [39, 48-50]. We propose that Cdc20 overexpression could be used to specifically target these cells, as opposed to healthy cells with endogenous levels of Cdc20. According to our analysis, cancer cells are expected to have an unstable MCC2, and stabilization of MCC2 may provide a mechanism to selectively kill these cells by impairing the SAC.

It is important to remark that we have only analyzed the steady state behavior of the different networks. While this analysis did not find differences between the networks at physiological Cdc20 levels, we cannot exclude that the transient dynamics differ. To investigate this possibility, more detailed information about the mechanisms and

dynamics of Cdc20 production and degradation are required. This does not only include the kinetics of APC/C-mediated Cdc20 degradation while the checkpoint is active and Cdc20 is part of the MCC [51], but also potential regulation of Cdc20 synthesis, post-translational regulation, and APC/C-independent degradation [52-55]. Our fragmentary knowledge on these processes is currently the biggest impediment in understanding the dynamical behavior of the SAC network.

REFERENCES

FIGURE LEGENDS

Figure 1. A wiring diagram of possible reactions in the SAC. Only the most downstream reactions are considered. Network (i) purely considers APC/C^{MCC2} formation by MCC1 binding to APC/C^{Cdc20}. Network (ii) purely considers APC/C^{MCC2} formation by MCC2 binding to APC/C. Network (iii), depicted in Figure 2, contains both these possibilities.

Figure 2. Different networks for APC/C^{Cdc20} inhibition. (i) The sequential inhibition network, which is characterized by MCC1 binding to APC/C^{Cdc20}. (ii) The competitive inhibition network, which is characterized by competition between MCC2 and Cdc20 for APC/C binding. (iii) Different representations of the mixed network, containing the reactions of both (i) and (ii). Network (iii) can be generated by either adding reaction 5 and 4 (MCC2 formation and APC/C-MCC2 binding) to the sequential inhibition network, or by adding reaction 3 (MCC1 binding to APC/C^{Cdc20}) to the competitive inhibition network. Note that in networks (ii) and (iii), some species are listed more than once at different positions to be able to depict the overall structure of the network.

Figure 3 Steady state concentration of each species, dependent on the total Cdc20 concentration for each of the networks (i), (ii), and (iii). A Cdc20 value of 1 represents the wild type situation. APC/C and Mad concentrations are given relative to the wild-type level of Cdc20. The molecular species are organized into three groups: those that include Cdc20, APC/C, or Mad. The plots show how these three species are distributed among different complexes. While total APC/C and total Mad remain constant, total Cdc20 increases along the x-axis. MCC2 and APC/C^{MCC2} include two molecules of Cdc20, thus their concentration is counted twice in the plots representing the Cdc20-species. Models and parameters in the Supplementary Material.

Figure 4. Wiring (A) and bifurcation (B) diagram of the combined network [Figure 2 (iii)] without reaction 4, for different values of the association constant leading to MCC2 formation (reaction 5, marked in yellow). The dissociation constant is unchanged. Model and parameters in the Supplementary Material.

SUPPLEMENTARY FIGURES

Supplementary Figure 1. Data from Table 1, normalized to the value for Mad3 in each study. Plots show quartiles (box) and (whiskers).

Supplementary Figure 2. Binding reactions included in the models of Figure 2. In the first column, we list all reactions. In the remaining columns, we show those included in the individual models.

Supplementary Figure 3. Comparison between the simplified models (dashed lines), described in the Supplementary Material, and the full models (solid lines) described in Figure 2 and 3. Parameters and equations are described in Supplementary Material.

Supplementary Figure 4. Steady state concentration of APC/C^{Cdc20} and APC/C^{MCC2}, dependent on the total Cdc20 concentration, either assuming a lumped species, Mad, for Mad2 and Mad3 (solid lines), or assuming sequential Mad2 and Mad3 binding to Cdc20 (dashed lines).

Table 1. Experimental quantifications of Mad2, Mad3, APC/C, and Cdc20 in different model organisms.

REFERENCES

1. Lara-Gonzalez, P., Westhorpe, F.G., and Taylor, S.S. (2012). The spindle assembly checkpoint. In Curr Biol, Volume 22. pp. R966-980.
2. Luo, X., Tang, Z., Xia, G., Wassmann, K., Matsumoto, T., Rizo, J., and Yu, H. (2004). The Mad2 spindle checkpoint protein has two distinct natively folded states. Nat Struct Mol Biol *11*, 338-345.
3. Fang, G. (2002). Checkpoint protein BubR1 acts synergistically with Mad2 to inhibit anaphase-promoting complex. Mol Biol Cell *13*, 755-766.
4. Tang, Z., Bharadwaj, R., Li, B., and Yu, H. (2001). Mad2-Independent inhibition of APCCdc20 by the mitotic checkpoint protein BubR1. Dev Cell *1*, 227-237.
5. Sudakin, V., Chan, G.K., and Yen, T.J. (2001). Checkpoint inhibition of the APC/C in HeLa cells is mediated by a complex of BUBR1, BUB3, CDC20, and MAD2. J Cell Biol *154*, 925-936.
6. Howell, B.J., Moree, B., Farrar, E.M., Stewart, S., Fang, G., and Salmon, E.D. (2004). Spindle checkpoint protein dynamics at kinetochores in living cells. Curr Biol *14*, 953-964.
7. Poddar, A., Stukenberg, P.T., and Burke, D.J. (2005). Two complexes of spindle checkpoint proteins containing Cdc20 and Mad2 assemble during mitosis independently of the kinetochore in Saccharomyces cerevisiae. Eukaryot Cell *4*, 867-878.
8. Heinrich, S., Geissen, E.M., Kamenz, J., Trautmann, S., Widmer, C., Drewe, P., Knop, M., Radde, N., Hasenauer, J., and Hauf, S. (2013). Determinants of

robustness in spindle assembly checkpoint signalling. Nat Cell Biol *15*, 1328-1339.

9. Fava, L.L., Kaulich, M., Nigg, E.A., and Santamaria, A. (2011). Probing the in vivo function of Mad1:C-Mad2 in the spindle assembly checkpoint. EMBO J *30*, 3322-3336.

10. Nilsson, J., Yekezare, M., Minshull, J., and Pines, J. (2008). The APC/C maintains the spindle assembly checkpoint by targeting Cdc20 for destruction. Nat Cell Biol *10*, 1411-1420.

11. Kulukian, A., Han, J.S., and Cleveland, D.W. (2009). Unattached kinetochores catalyze production of an anaphase inhibitor that requires a Mad2 template to prime Cdc20 for BubR1 binding. Dev Cell *16*, 105-117.

12. Lad, L., Lichtsteiner, S., Hartman, J.J., Wood, K.W., and Sakowicz, R. (2009). Kinetic analysis of Mad2-Cdc20 formation: conformational changes in Mad2 are catalyzed by a C-Mad2-ligand complex. Biochemistry *48*, 9503-9515.

13. Simonetta, M., Manzoni, R., Mosca, R., Mapelli, M., Massimiliano, L., Vink, M., Novak, B., Musacchio, A., and Ciliberto, A. (2009). The influence of catalysis on mad2 activation dynamics. PLoS Biol *7*, e10.

14. Vink, M., Simonetta, M., Transidico, P., Ferrari, K., Mapelli, M., De Antoni, A., Massimiliano, L., Ciliberto, A., Faretta, M., Salmon, E.D., et al. (2006). In vitro FRAP identifies the minimal requirements for Mad2 kinetochore dynamics. Curr Biol *16*, 755-766.

15. Yang, M., Li, B., Liu, C.J., Tomchick, D.R., Machius, M., Rizo, J., Yu, H., and Luo, X. (2008). Insights into mad2 regulation in the spindle checkpoint revealed by the crystal structure of the symmetric mad2 dimer. PLoS Biol *6*, e50.

16. Musacchio, A. (2015). The Molecular Biology of Spindle Assembly Checkpoint Signaling Dynamics. Curr Biol *25*, R1002-1018.

17. Faesen, A.C., Thanasoula, M., Maffini, S., Breit, C., Muller, F., van Gerwen, S., Bange, T., and Musacchio, A. (2017). Basis of catalytic assembly of the mitotic checkpoint complex. Nature *542*, 498-502.

18. Primorac, I., and Musacchio, A. (2013). Panta rhei: the APC/C at steady state. J Cell Biol *201*, 177-189.

19. Izawa, D., and Pines, J. (2015). The mitotic checkpoint complex binds a second CDC20 to inhibit active APC/C. In Nature, Volume 517. pp. 631-634.

20. Alfieri, C., Chang, L., Zhang, Z., Yang, J., Maslen, S., Skehel, M., and Barford, D. (2016). Molecular basis of APC/C regulation by the spindle assembly checkpoint. Nature *536*, 431-436.

21. May, K.M., Paldi, F., and Hardwick, K.G. (2017). Fission Yeast Apc15 Stabilizes MCC-Cdc20-APC/C Complexes, Ensuring Efficient Cdc20 Ubiquitination and Checkpoint Arrest. Curr Biol *27*, 1221-1228.

22. Sewart, K., and Hauf, S. (2017). Different Functionality of Cdc20 Binding Sites within the Mitotic Checkpoint Complex. In Curr Biol, Volume 27. pp. 1213-1220.

23. Yamaguchi, M., VanderLinden, R., Weissmann, F., Qiao, R., Dube, P., Brown, N.G., Haselbach, D., Zhang, W., Sidhu, S.S., Peters, J.M., et al. (2016). Cryo-EM

of Mitotic Checkpoint Complex-Bound APC/C Reveals Reciprocal and Conformational Regulation of Ubiquitin Ligation. Mol Cell *63*, 593-607.

24. Burton, J.L., and Solomon, M.J. (2007). Mad3p, a pseudosubstrate inhibitor of APCCdc20 in the spindle assembly checkpoint. Genes Dev *21*, 655-667.

25. Diaz-Martinez, L.A., Tian, W., Li, B., Warrington, R., Jia, L., Brautigam, C.A., Luo, X., and Yu, H. (2015). The Cdc20-binding Phe box of the spindle checkpoint protein BubR1 maintains the mitotic checkpoint complex during mitosis. J Biol Chem *290*, 2431-2443.

26. Di Fiore, B., Wurzenberger, C., Davey, N.E., and Pines, J. (2016). The Mitotic Checkpoint Complex Requires an Evolutionary Conserved Cassette to Bind and Inhibit Active APC/C. Mol Cell *64*, 1144-1153.

27. King, E.M., van der Sar, S.J., and Hardwick, K.G. (2007). Mad3 KEN boxes mediate both Cdc20 and Mad3 turnover, and are critical for the spindle checkpoint. PLoS One *2*, e342.

28. Lara-Gonzalez, P., Scott, M.I., Diez, M., Sen, O., and Taylor, S.S. (2011). BubR1 blocks substrate recruitment to the APC/C in a KEN-box-dependent manner. J Cell Sci *124*, 4332-4345.

29. Sczaniecka, M., Feoktistova, A., May, K.M., Chen, J.S., Blyth, J., Gould, K.L., and Hardwick, K.G. (2008). The spindle checkpoint functions of Mad3 and Mad2 depend on a Mad3 KEN box-mediated interaction with Cdc20-anaphase-promoting complex (APC/C). J Biol Chem *283*, 23039-23047.

30. Tromer, E., Bade, D., Snel, B., and Kops, G.J. (2016). Phylogenomics-guided discovery of a novel conserved cassette of short linear motifs in BubR1 essential for the spindle checkpoint. Open Biol *6*.

31. Christiano, R., Nagaraj, N., Frohlich, F., and Walther, T.C. (2014). Global proteome turnover analyses of the Yeasts S. cerevisiae and S. pombe. Cell Rep *9*, 1959-1965.

32. Horikoshi, Y., Habu, T., and Matsumoto, T. (2013). An E2 enzyme Ubc11 is required for ubiquitination of Slp1/Cdc20 and spindle checkpoint silencing in fission yeast. Cell Cycle *12*, 961-971.

33. Pesin, J.A., and Orr-Weaver, T.L. (2008). Regulation of APC/C activators in mitosis and meiosis. Annu Rev Cell Dev Biol *24*, 475-499.

34. Pan, J., and Chen, R.H. (2004). Spindle checkpoint regulates Cdc20p stability in Saccharomyces cerevisiae. Genes Dev *18*, 1439-1451.

35. Schweizer, N., Ferras, C., Kern, D.M., Logarinho, E., Cheeseman, I.M., and Maiato, H. (2013). Spindle assembly checkpoint robustness requires Tpr-mediated regulation of Mad1/Mad2 proteostasis. J Cell Biol *203*, 883-893.

36. Yamada, H.Y., Matsumoto, S., and Matsumoto, T. (2000). High dosage expression of a zinc finger protein, Grt1, suppresses a mutant of fission yeast slp1(+), a homolog of CDC20/p55CDC/Fizzy. J Cell Sci *113 (Pt 22)*, 3989-3999.

37. Yu, H. (2007). Cdc20: a WD40 activator for a cell cycle degradation machine. Mol Cell *27*, 3-16.

38. Carter, S.L., Eklund, A.C., Kohane, I.S., Harris, L.N., and Szallasi, Z. (2006). A signature of chromosomal instability inferred from gene expression profiles predicts clinical outcome in multiple human cancers. Nat Genet *38*, 1043-1048.

39. Schvartzman, J.M., Sotillo, R., and Benezra, R. (2010). Mitotic chromosomal instability and cancer: mouse modelling of the human disease. Nat Rev Cancer *10*, 102-115.

40. Teixeira, J.H., Silva, P.M., Reis, R.M., Moura, I.M., Marques, S., Fonseca, J., Monteiro, L.S., and Bousbaa, H. (2014). An overview of the spindle assembly checkpoint status in oral cancer. Biomed Res Int *2014*, 145289.

41. Wang, Z., Wan, L., Zhong, J., Inuzuka, H., Liu, P., Sarkar, F.H., and Wei, W. (2013). Cdc20: a potential novel therapeutic target for cancer treatment. Curr Pharm Des *19*, 3210-3214.

42. Sivakumar, S., and Gorbsky, G.J. (2015). Spatiotemporal regulation of the anaphase-promoting complex in mitosis. Nat Rev Mol Cell Biol *16*, 82-94.

43. Huang, H.C., Shi, J., Orth, J.D., and Mitchison, T.J. (2009). Evidence that mitotic exit is a better cancer therapeutic target than spindle assembly. Cancer Cell *16*, 347-358.

44. Wolthuis, R., Clay-Farrace, L., van Zon, W., Yekezare, M., Koop, L., Ogink, J., Medema, R., and Pines, J. (2008). Cdc20 and Cks direct the spindle checkpoint-independent destruction of cyclin A. Mol Cell *30*, 290-302.

45. Foster, S.A., and Morgan, D.O. (2012). The APC/C subunit Mnd2/Apc15 promotes Cdc20 autoubiquitination and spindle assembly checkpoint inactivation. Mol Cell *47*, 921-932.

46. Hwang, L.H., Lau, L.F., Smith, D.L., Mistrot, C.A., Hardwick, K.G., Hwang, E.S., Amon, A., and Murray, A.W. (1998). Budding yeast Cdc20: a target of the spindle checkpoint. Science *279*, 1041-1044.

47. Mondal, G., Sengupta, S., Panda, C.K., Gollin, S.M., Saunders, W.S., and Roychoudhury, S. (2007). Overexpression of Cdc20 leads to impairment of the spindle assembly checkpoint and aneuploidization in oral cancer. Carcinogenesis *28*, 81-92.

48. Dominguez-Brauer, C., Thu, K.L., Mason, J.M., Blaser, H., Bray, M.R., and Mak, T.W. (2015). Targeting Mitosis in Cancer: Emerging Strategies. Mol Cell *60*, 524-536.

49. Funk, L.C., Zasadil, L.M., and Weaver, B.A. (2016). Living in CIN: Mitotic Infidelity and Its Consequences for Tumor Promotion and Suppression. Dev Cell *39*, 638-652.

50. Gascoigne, K.E., and Taylor, S.S. (2008). Cancer cells display profound intra- and interline variation following prolonged exposure to antimitotic drugs. Cancer Cell *14*, 111-122.

51. Musacchio, A., and Ciliberto, A. (2012). The spindle-assembly checkpoint and the beauty of self-destruction. Nat Struct Mol Biol *19*, 1059-1061.

52. Camasses, A., Bogdanova, A., Shevchenko, A., and Zachariae, W. (2003). The CCT chaperonin promotes activation of the anaphase-promoting complex through the generation of functional Cdc20. Mol Cell *12*, 87-100.

53. Novoa, I., Gallego, J., Ferreira, P.G., and Mendez, R. (2010). Mitotic cell-cycle progression is regulated by CPEB1 and CPEB4-dependent translational control. Nat Cell Biol *12*, 447-456.

54. Robbins, J.A., and Cross, F.R. (2010). Regulated degradation of the APC coactivator Cdc20. Cell Div *5*, 23.

55. Wang, R., Burton, J.L., and Solomon, M.J. (2017). Transcriptional and post-transcriptional regulation of Cdc20 during the spindle assembly checkpoint in S. cerevisiae. Cell Signal *33*, 41-48.

Figure 1
Gross et al

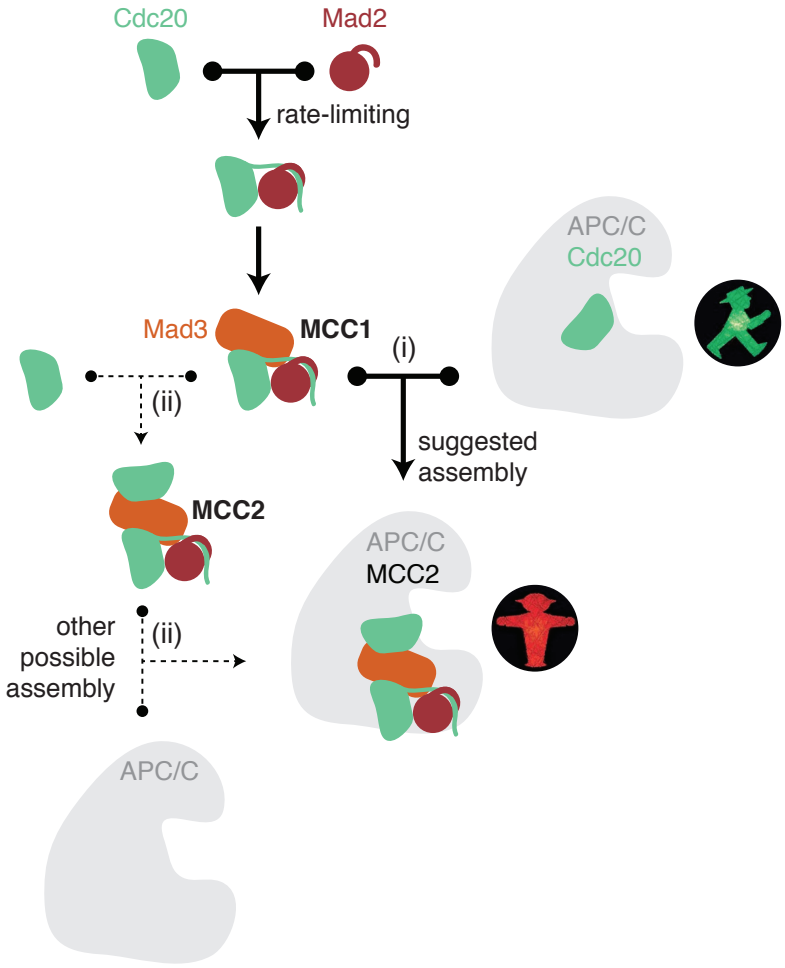

Figure 2
Gross et al

(i) Sequential inhibition

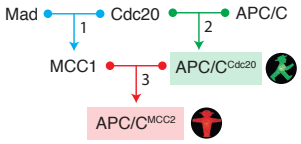

(ii) Competitive inhbition

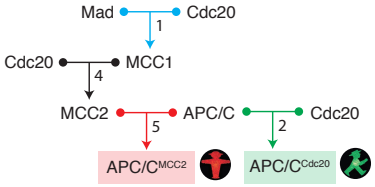

(iii) = (i) + (ii)

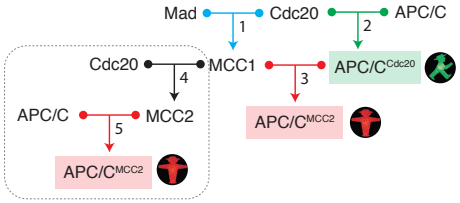

(iii) = (ii) + (i)

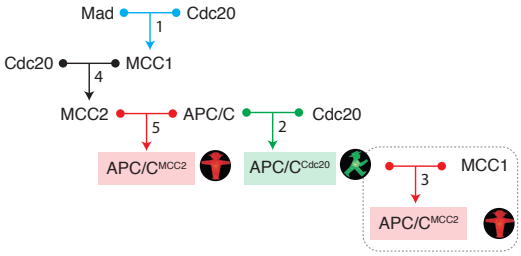

Figure 3
Gross et al

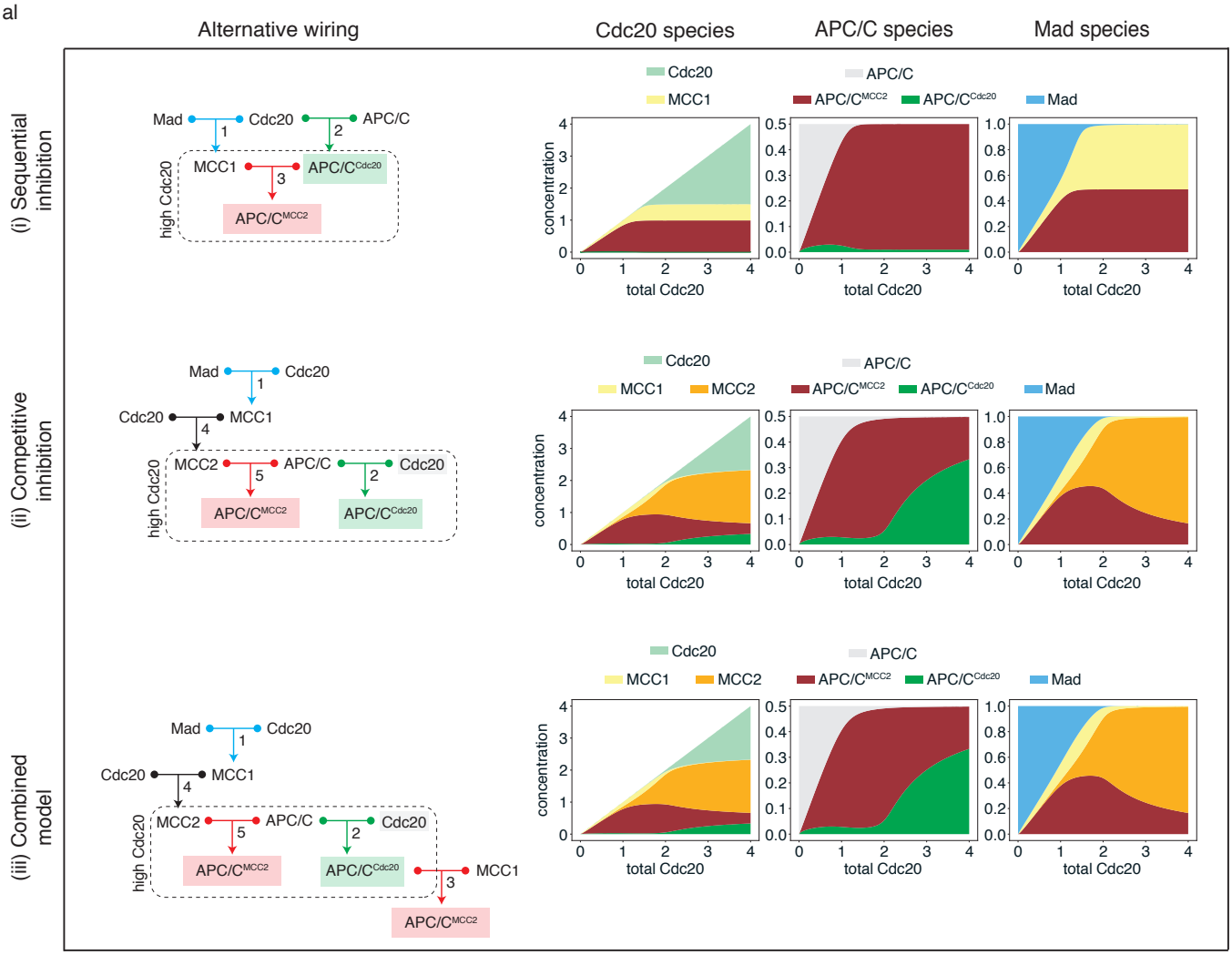

Figure 4
Gross et al

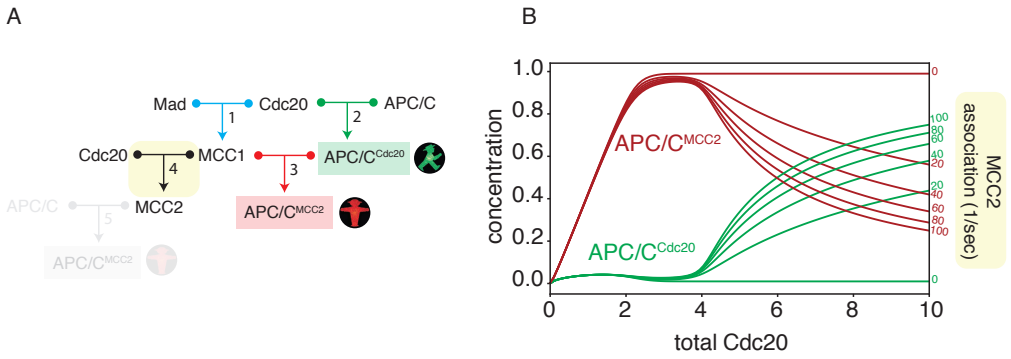

Supplementary Figure 1
Gross et al

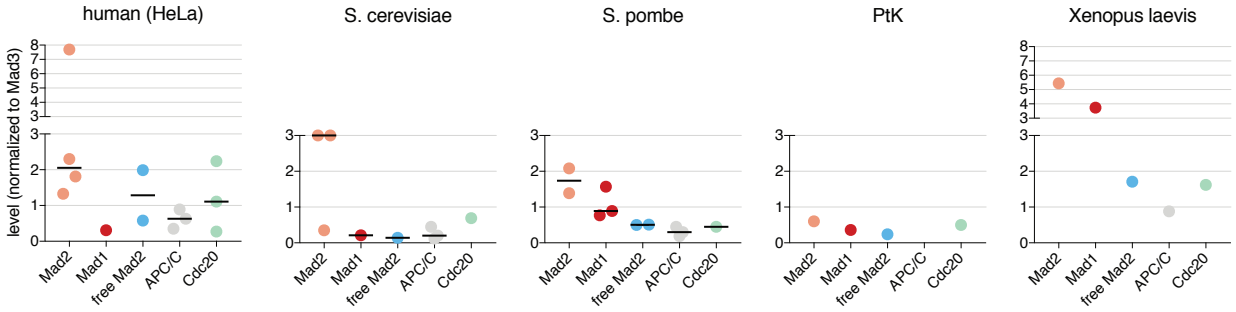

Figure S2
Gross et al

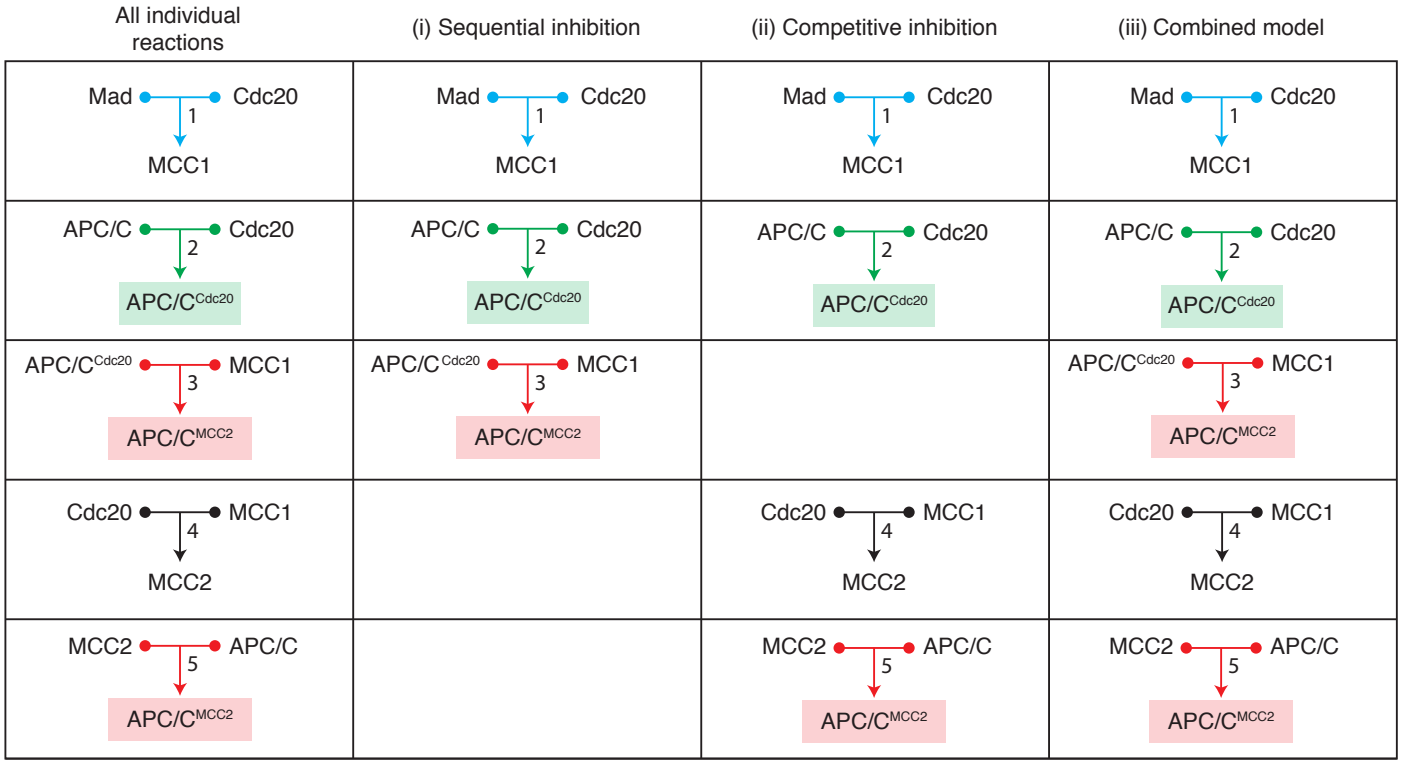

Suppl Fig 3
Gross et al

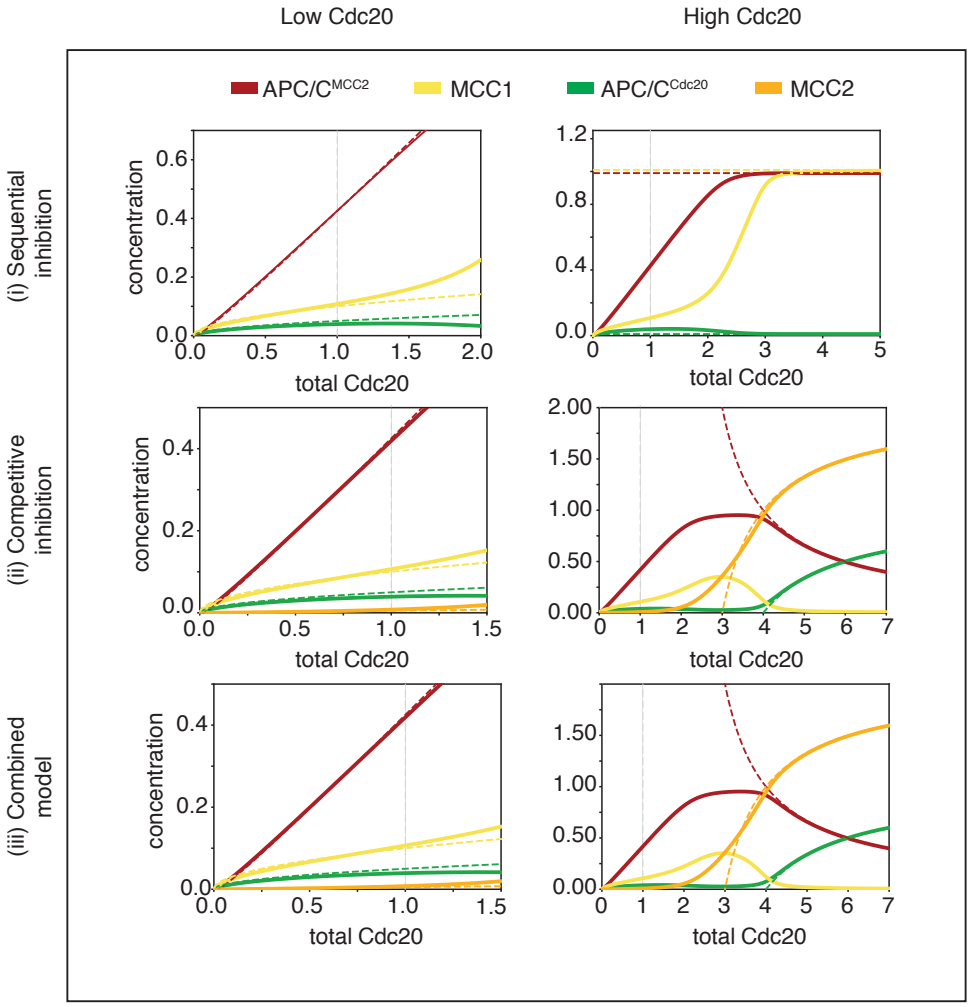

Suppl Fig 4
Gross et al

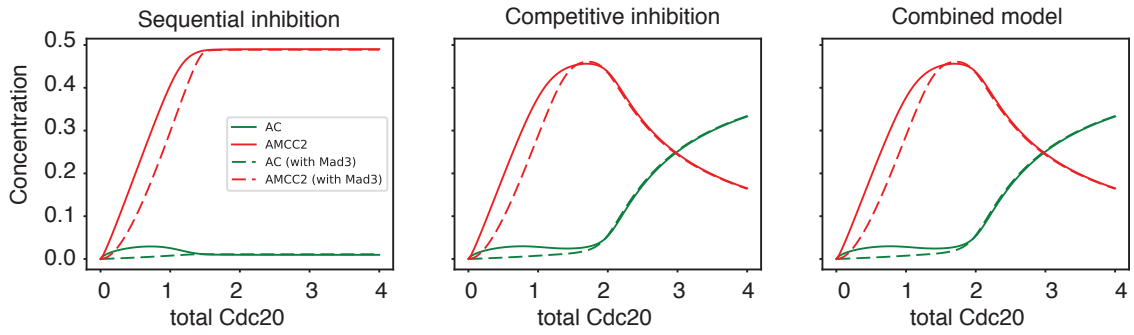

An *in-silico* analysis of inhibitory logics in the mitotic checkpoint network — Supplementary Information

Fridolin Gross, Paolo Bonaiuti, Silke Hauf and Andrea Ciliberto

Contents

1 Modeling Approach

In the following we give more detailed information on the modeling approach used in the article, and provide some analytical results in support of the generality of our conclusions.

Our models are straightforward translations of the wiring diagrams shown in Fig. 2 into ODEs using mass action kinetics. All binding reactions are assumed to be reversible. For the sake of readability we use the following abbreviations:

A	free APC/C
C	free Cdc20
M	free Mad2, Mad3
A_{total}	total APC/C
C_{total}	total Cdc20
M_{total}	total Mad2, Mad3
AC	APC/C^{Cdc20}
$MCC1$	MCC with one Cdc20 molecule
$MCC2$:	MCC with two Cdc20 molecules
$AMCC2$:	APC/C^{MCC2}

Furthermore, we use the following notation to refer to the net association and dissociation reaction of two species X and Y that can form a complex Z:

$$R_{X:Y\rightleftarrows Z} = k^{+}_{X:Y\rightleftarrows Z}[X]\cdot[Y] - k^{-}_{X:Y\rightleftarrows Z}[Z]\,, \tag{1}$$

where $[X]$ stands for the concentration of species X. To indicate the steady state level of X, we use the notation $[\hat{X}]$.

The dissociation constant is defined as

$$K_D^{X:Y} = \frac{k^{-}_{X:Y\rightleftarrows Z}}{k^{+}_{X:Y\rightleftarrows Z}} \quad , \tag{2}$$

For some derivations we assume that the rate is approximately the same for all reactions. In that case we will simply refer to it as K_D. We write down equations only for the concentrations of complexes. The concentrations of free A, M, and C can then be obtained from conservation relations that are justified by the observation that all checkpoint proteins and APC/C are stable and that total Cdc20 is at steady state.

All numerical simulations were carried out using the Python package "SloppyCell" [1, 2] and custom written Python functions.

2 Model Parameters

Table 1 lists experimental measurements of the relevant species in different organisms derived from a comprehensive survey of the scientific literature. A summary of the data in the form of boxplots is shown in Suppl. Fig. 1. Relevant for our model are the concentrations of free Mad2 (not bound to Mad1), Mad3, APC/C, and Cdc20. With very few exceptions, these concentrations do not differ by more than a factor of five. Different studies come to very different conclusions, illustrating the difficulty of accurately determining absolute values. As a general scheme, however, total levels of APC/C are typically lower than Mad2/3 and Cdc20. For the simulations we assumed that all dissociation constants are small (i.e. strong binding) and have the same value. Specifically, we used:

$$[C_{\text{total}}] = 1\,, \tag{3}$$

$$[M_{\text{total}}] = 1\,, \tag{4}$$

$$[A_{\text{total}}] = 0.5\,, \tag{5}$$

$$K_D = 0.01\,. \tag{6}$$

in dimensionless units (i.e. normalized to the total amount of Mad levels in wild type).

		Mad2		Mad1		free Mad2		Mad3		APC/C		Cdc20		ref.
organism	**unit**	**abs.**	**rel.**	**abs.**	**rel.**	**abs.**	**rel.**	**abs.**	**rel.**	**abs.**	**rel.**	**abs.**	**rel.**	
human (HeLa)	**nM**	202	229.5%	27	30.7%	175	198.9%	88	100%	31	35.2%	24	27.3%	[3]
	mol./cell	264,329		72,571		191,758				35,276		18,265		[4]
	nM	200		20		180								[5]
	rel. ratio	4		1										[6]
	nM	230	181.1%					127	100%			285	224.4%	[7]
	nM	120	133.3%					90	100%	80	88.9%	100	111.1%	[8]
	nM	400	769.2%			30	57.7%	52	100%	33	62.5%			[9]
S. cerevisiae	mol./cell	56		54		2				59		54		[10]
	mol./cell	9,600	300.0%					3,200	100%	375	11.7%	2,200	68.8%	[11]
	mol./cell	1,112	35.1%	656	20.7%	456	14.4%	3,171	100%	628	19.8%			[12]
	nM	201	300.0%					67	100%	30	44.8%			[13]
S. pombe	mol./cell			3,855	76.9%			5,012	100%	1,495	29.8%			[14]
	nM	154	208.1%	116	156.8%	38	51.4%	74	100%	14	18.9%			[15]
	nM	61	138.6%	39	88.6%	22	50.0%	44	100%	20	45.5%	20	45.5%	[15]
	mol./cell			832						341				[16]
PtK	nM	1,041	60.0%	625	36.0%	416	24.0%	1,735	100%			867	50.0%	[17]
X. laevis	nM	185	544.1%	127	373.5%	58	170.6%	34	100%	30	88.2%	55	161.8%	[18]

Table 1: Experimental measurements of molecular species involved in the SAC network. Both absolute (**abs.**) and relative (**rel.**) amounts are shown. Relative amounts are normalized to Mad3. Values of free Mad2 are calculated as Mad2 − Mad1.

3 Analytical Results

3.1 Sequential Inhibition Model

Equations

The wiring diagram in Fig. 2 (i) corresponds to the following set of equations:

$$\frac{d[AC]}{dt} = R_{A:C \rightleftarrows AC} - R_{AC:MCC1 \rightleftarrows AMCC2}\,, \tag{7}$$

$$\frac{d[MCC1]}{dt} = R_{M:C \rightleftarrows MCC1} - R_{AC:MCC1 \rightleftarrows AMCC2}\,, \tag{8}$$

$$\frac{d[AMCC2]}{dt} = R_{AC:MCC1 \rightleftarrows AMCC2}\,. \tag{9}$$

Furthermore, we have the following conservation relations:

$$[A_{\text{total}}] = [A] + [AC] + [AMCC2]\,, \tag{10}$$

$$[M_{\text{total}}] = [M] + [MCC1] + [AMCC2]\,, \tag{11}$$

$$[C_{\text{total}}] = [C] + [AC] + [MCC1] + 2 \cdot [AMCC2]\,. \tag{12}$$

Approximation for small Cdc20

In the following we will often exploit the fact that the models we consider are detailed balanced. This means that at steady state all forward reactions are individually balanced against their corresponding reverse reactions, or

$$R_{X:Y \rightleftarrows Z} = 0\,, \tag{13}$$

which directly leads to

$$[\hat{Z}] = \frac{[\hat{X}][\hat{Y}]}{K_D^{X:Y}}\,. \tag{14}$$

For the sequential inhibition model, detailed balancing can easily be shown. Setting (9) to zero, we immediately get

$$R_{AC:MCC1 \rightleftarrows AMCC2} = 0\,. \tag{15}$$

But then it follows from (7) and (8) that both other reactions are also detailed balanced.

Therefore, we obtain

$$[\hat{AC}] = \frac{[\hat{A}][\hat{C}]}{K_D^{A:C}}\,, \tag{16}$$

$$[\hat{MCC1}] = \frac{[\hat{M}][\hat{C}]}{K_D^{M:C}}\,, \tag{17}$$

$$[\hat{AMCC2}] = \frac{[\hat{AC}][\hat{MCC1}]}{K_D^{AC:MCC1}} = \frac{[\hat{A}][\hat{M}][\hat{C}]^2}{K_D^{A:C} K_D^{M:C} K_D^{AC:MCC1}}\,. \tag{18}$$

For small levels of C_{total} we can use the approximation $[\hat{A}] \approx [A_{\text{total}}]$ and $[\hat{M}] \approx [M_{\text{total}}]$. From (16) and (17) we immediately get

$$\frac{[\hat{AC}]}{[\hat{MCC1}]} \approx \frac{[A_{\text{total}}]}{[M_{\text{total}}]} \frac{K_D^{M:C}}{K_D^{A:C}}\,. \tag{19}$$

Thus, in this regime the relative amounts of AC and $MCC1$ are directly related to the total amounts and the corresponding binding reactions. Furthermore, using (19) we can rewrite (18) as

$$[\hat{AMCC2}] = \frac{[M_{\text{total}}][\hat{AC}]^2 K_D^{A:C}}{[A_{\text{total}}] K_D^{M:C} K_D^{AC:MCC1}}\,, \tag{20}$$

or

$$[A\hat{MCC}2] \approx \frac{1}{k}[\hat{AC}]^2 \quad \text{with} \quad k = \frac{[A_{\text{total}}]}{[M_{\text{total}}]} \frac{K_D^{M:C} K_D^{AC:MCC1}}{K_D^{A:C}} \,. \tag{21}$$

The quadratic dependence means that $AMCC2$ will dominate for [AC] larger than k. But k is a small number if binding is generally strong and/or $[M_{\text{total}}] > [A_{\text{total}}]$. Note that k is small even if all reactions have the same binding strength and and $[M_{\text{total}}] = [A_{\text{total}}]$. This is because there are two binding reactions leading to the inhibited, but only one reaction leading to the active species. Mathematically this is reflected by the product of two K_Ds in the numerator of (21). Together this explains the "funneling" effect that we observe for small levels of Cdc20.

To even better understand the qualitative behavior of the Figure 3, we can exploit the conservation relation

$$[C_{\text{total}}] = [\hat{C}] + [\hat{AC}] + [\hat{MCC}1] + 2[A\hat{MCC}2] \,. \tag{22}$$

In the limit of strong binding $[A\hat{MCC}2]$ dominates this sum. As (19) shows, $[\hat{AC}]$ and $[\hat{MCC}1]$ are of similar order. $[\hat{C}]$ is even smaller, which follows e.g. from (16):

$$[\hat{C}] \approx \frac{K_D^{A:C}}{[A_{\text{total}}]} [\hat{AC}] \,. \tag{23}$$

Therefore, we have

$$[A\hat{MCC}2] \approx \frac{[C_{\text{total}}]}{2} \,, \tag{24}$$

which explains the initially approximately linear behavior of APC/C$^{\text{MCC2}}$ in Figure 3 (i). Based on this approximation we can use Equations (16)–(18) to derive expressions for the other species as well:

$$[\hat{C}] \approx \sqrt{\frac{K_D^{A:C} K_D^{M:C} K_D^{AC:MCC1}}{2[A_{\text{total}}][M_{\text{total}}]}} \sqrt{[C_{\text{total}}]} \,, \tag{25}$$

$$[\hat{AC}] \approx \sqrt{\frac{1}{2} \frac{[A_{\text{total}}]}{[M_{\text{total}}]} \frac{K_D^{M:C} K_D^{AC:MCC1}}{K_D^{A:C}}} \sqrt{[C_{\text{total}}]} \,, \tag{26}$$

$$[\hat{MCC}1] \approx \sqrt{\frac{1}{2} \frac{[M_{\text{total}}]}{[A_{\text{total}}]} \frac{K_D^{A:C} K_D^{AC:MCC1}}{K_D^{M:C}}} \sqrt{[C_{\text{total}}]} \,. \tag{27}$$

From this we can understand how the steady state concentrations for small levels of Cdc20 depend on parameters and concentrations. Moreover, we can explain the approximately linear dependence of APC/C$^{\text{MCC2}}$ and the square root dependence of the other species.

Approximation for large Cdc20

If C_{total} is large, then every free molecule of M or A will quickly bind to a free molecule of C. With the approximation that this binding is instantaneous and $M \approx A \approx 0$, we can directly calculate the steady state values for the remaining species. For this it is sufficient to look at the three species $MCC1$, AC, and $AMCC2$, and the only reaction left to be considered is

$$\frac{d[AMCC2]}{dt} = R_{AC:MCC1 \rightleftarrows AMCC2}\,, \tag{28}$$

because the other two species are then determined by the conservation relations. At steady state we have

$$[A\hat{M}CC2] = \frac{[\hat{AC}] \cdot [M\hat{C}C1]}{K_D^{AC:MCC1}} = \frac{([A_{\text{total}}] - [A\hat{M}CC2])([M_{\text{total}}] - [A\hat{M}CC2])}{K_D^{AC:MCC1}}\,.$$

From this we get

$$([A_{\text{total}}] - [A\hat{M}CC2])([M_{\text{total}}] - [A\hat{M}CC2]) - K_D^{AC:MCC1} \cdot [A\hat{M}CC2] = 0\,, \tag{29}$$

which is a quadratic equation in $[A\hat{M}CC2]$ whose solution is

$$[A\hat{M}CC2] = \frac{1}{2}\left([A_{\text{total}}] + [M_{\text{total}}] + K_D^{AC:MCC1}\right) \pm \sqrt{\left(\frac{[A_{\text{total}}] + [M_{\text{total}}] + K_D^{AC:MCC1}}{2}\right)^2 - [A_{\text{total}}][M_{\text{total}}]}\,. \tag{30}$$

Only the "$-$" solution ensures that $[A\hat{M}CC2] \leq [M_{\text{total}}], [A_{\text{total}}]$. The relative amounts of $[A\hat{M}CC2]$ and $[\hat{AC}] \approx [A_{\text{total}}] - [A\hat{M}CC2]$ mainly depend on the strength of AC binding to $MCC1$. For weak binding ($K_D^{AC:MCC1} \gg [M_{\text{total}}], [A_{\text{total}}]$) we get $AMCC2 \approx 0$, while for strong binding we get $[\hat{AC}] \approx 0$. In general, both species co-exist and their levels becomes insensitive to changes in C_{total}.

In Suppl. Fig. 3 (i) the simulated steady state concentrations for the sequential model are shown together with the analytical approximations for small and large Cdc20.

3.2 Competitive Inhibition Model

Equations:

The competitive inhibition model includes the additional species $MCC2$ which is formed by $MCC1$ binding an additional molecule of C. The inhibited species $AMCC2$ is then formed by $MCC2$ binding

to a free molecule of A. We therefore have to consider four equations:

$$\frac{d[AC]}{dt} = R_{A:C \rightleftarrows AC}\,, \tag{31}$$

$$\frac{d[MCC1]}{dt} = R_{M:C \rightleftarrows MCC1} - R_{MCC1:C \rightleftarrows MCC2}\,, \tag{32}$$

$$\frac{d[MCC2]}{dt} = R_{MCC1:C \rightleftarrows MCC2} - R_{A:MCC2 \rightleftarrows AMCC2}\,, \tag{33}$$

$$\frac{d[AMCC2]}{dt} = R_{A:MCC2 \rightleftarrows AMCC2}\,, \tag{34}$$

together with the following conservation relations:

$$[A_{\text{total}}] = [A] + [AC] + [AMCC2]\,, \tag{35}$$

$$[M_{\text{total}}] = [M] + [MCC1] + [MCC2] + [AMCC2]\,, \tag{36}$$

$$[C_{\text{total}}] = [C] + [AC] + [MCC1] + 2 \cdot ([MCC2] + [AMCC2])\ . \tag{37}$$

Approximation for small Cdc20

In the same way as before we can show that detailed balancing holds, and we get at steady state

$$[\hat{AC}] = \frac{[\hat{A}][\hat{C}]}{K_D^{A:C}}\,, \tag{38}$$

$$[\hat{MCC}1] = \frac{[\hat{M}][\hat{C}]}{K_D^{M:C}}\,, \tag{39}$$

$$[\hat{MCC}2] = \frac{[\hat{MCC}1][\hat{C}]}{K_D^{MCC1:C}} = \frac{[\hat{M}][\hat{C}]^2}{K_D^{M:C} K_D^{MCC1:C}}\,, \tag{40}$$

$$[\hat{AMCC}2] = \frac{[\hat{A}][\hat{MCC}2]}{K_D^{A:MCC2}} = \frac{[\hat{A}][\hat{M}][\hat{C}]^2}{K_D^{M:C} K_D^{MCC1:C} K_D^{A:MCC2}}\,. \tag{41}$$

Equations (38) and (39) are identical to (16) and (17), and the only difference between (41) and (18) is one of the dissociation constants. Moreover, $[\hat{MCC}2]$ is very small for small levels of C_{total} and strong binding because from (40) and (41) we get

$$\frac{\hat{MCC}2}{\hat{AMCC}2} \approx \frac{K_D^{AC:MCC2}}{[A_{\text{total}}]}\,. \tag{42}$$

So the model effectively reduces to the same equations as the sequential inhibition model. This explains why for small levels of Cdc20 the steady state behavior is basically the same for sequential and competitive inhibition. In particular, we see from the calculations that the funneling effect is indifferent to the order in which the complexes are formed. This is a straightforward consequence of mass action kinetics and detailed balancing.

In exactly the same way as before, we can derive approximations for all species:

$$[A\hat{M}CC2] \approx \frac{[C_{\text{total}}]}{2}\,, \tag{43}$$

$$[\hat{C}] \approx \sqrt{\frac{K_D^{M:C} K_D^{MCC1:C} K_D^{A:MCC2}}{2[A_{\text{total}}][M_{\text{total}}]}}\sqrt{[C_{\text{total}}]}\,, \tag{44}$$

$$[\hat{AC}] \approx \sqrt{\frac{1}{2}\frac{[A_{\text{total}}]}{[M_{\text{total}}]}\frac{K_D^{M:C} K_D^{MCC1:C} K_D^{A:MCC2}}{(K_D^{A:C})^2}}\sqrt{[C_{\text{total}}]}\,, \tag{45}$$

$$[M\hat{C}C1] \approx \sqrt{\frac{1}{2}\frac{[M_{\text{total}}]}{[A_{\text{total}}]}\frac{K_D^{MCC1:C} K_D^{A:MCC2}}{K_D^{M:C}}}\sqrt{[C_{\text{total}}]}\,, \tag{46}$$

$$[M\hat{C}C2] \approx \frac{K_D^{A:MCC2}}{2[A_{\text{total}}]}[C_{\text{total}}]\,. \tag{47}$$

Again we reproduce the approximately linear behavior of APC/C$^{\text{AMCC2}}$ and the square root behavior of the other species (with the exception for free $MCC2$, which increases linearly, but with a very small slope).

Approximation for large Cdc20

For high levels of C_{total}, we can assume that

$$[M_{\text{total}}] \approx [AMCC2] + [MCC2]\,, \tag{48}$$

$$[A_{\text{total}}] \approx [AMCC2] + [AC]\,, \tag{49}$$

meaning that all species that bind to free C (i.e. A, M, and MCC) are approximately zero. With the help of the conversation relation (37) we can then immediately derive

$$[C_{\text{total}}] \approx 2 \cdot [M_{\text{total}}] + [AC] + [C]\,. \tag{50}$$

This means that the system effectively reduces to a simple competition model where the inhibitor $MCC2$ competes with C for free A.

It can be easily shown that the inhibited species will always lose the competition if levels of Cdc20 are high. First of all, note that if $[C_{\text{total}}] \to \infty$, then also $[C] \to \infty$. From detailed balancing, we then get

$$[A] = \frac{K_D^{A:C}[AC]}{[C]} < \frac{K_D^{A:C}[A_{\text{total}}]}{[C]} \to 0\,, \tag{51}$$

which entails

$$[AMCC2] = \frac{[A][MCC2]}{K_D^{A:MCC2}} < \frac{[A][M_{\text{total}}]}{K_D^{A:MCC2}} \to 0\,. \tag{52}$$

For the special case of $K_D = K_D^{A:MCC2} = K_D^{A:C}$, we can derive simple expressions for $[\hat{AC}]$ and $[A\hat{MCC}2]$ as functions of $[C_{\text{total}}]$. Given detailed balancing, Eq. (48) leads to

$$[M_{\text{total}}] \approx \frac{[\hat{A}][M\hat{C}C2]}{K_D} + [M\hat{C}C2] = \frac{K_D + [\hat{A}]}{K_D} \cdot [M\hat{C}C2]\,, \tag{53}$$

or

$$[M\hat{C}C2] \approx [M_{\text{total}}] \frac{K_D}{K_D + [\hat{A}]}\,. \tag{54}$$

From Eq. (50) we can derive an analogous expression for $[\hat{C}]$:

$$[C_{\text{total}}] - 2 \cdot [M_{\text{total}}] \approx \frac{K_D + [\hat{A}]}{K_D} \cdot [\hat{C}]\,, \tag{55}$$

or

$$[\hat{C}] \approx ([C_{\text{total}}] - 2 \cdot [M_{\text{total}}]) \frac{K_D}{K_D + [\hat{A}]}\,. \tag{56}$$

Furthermore, rewriting (49) and afterwards substituting (54) and (56), we get

$$\begin{aligned}[A_{\text{total}}] &\approx \frac{[\hat{A}][M\hat{C}C2]}{K_D} + \frac{[\hat{A}][\hat{C}]}{K_D} \\ &\approx [\hat{A}] \cdot \left(\frac{[M_{\text{total}}]}{K_D + [\hat{A}]} + \frac{[C_{\text{total}}] - 2 \cdot [M_{\text{total}}]}{K_D + [\hat{A}]} \right)\,,\end{aligned} \tag{57}$$

from which we obtain

$$\frac{[\hat{A}]}{K_D + [\hat{A}]} \approx \frac{[A_{\text{total}}]}{[C_{\text{total}}] - [M_{\text{total}}]}\,. \tag{58}$$

Combining (54), (56), and (58), we finally get

$$[AMCC2] = \frac{[\hat{A}][M\hat{C}C2]}{K_D} \approx \frac{[A_{\text{total}}][M_{\text{total}}]}{[C_{\text{total}}] - [M_{\text{total}}]} \tag{59}$$

and

$$[AC] = \frac{[\hat{A}][\hat{C}]}{K_D} \approx \frac{[A_{\text{total}}]([C_{\text{total}}] - 2 \cdot [M_{\text{total}}])}{[C_{\text{total}}] - [M_{\text{total}}]}\,. \tag{60}$$

Note that these expressions depend only on the total amounts and not on the association/dissociation parameters (for this derivation we did not use the assumption of strong binding). Most importantly, and as already shown, we will always get $AC \to A_{\text{total}}$ and $AMCC2 \to 0$ for $C_{\text{total}} \to \infty$. In other words, the

competitive inhibition model always becomes checkpoint deficient for sufficiently high levels of Cdc20.

The approximations for the competitive inhibition model are shown in Suppl. Fig. 3 (ii).

3.3 Combined Model

Equations

The combined model includes both ways of producing the inhibited species $AMCC2$. The corresponding set of equations is

$$\frac{d[AC]}{dt} = R_{A:C \rightleftarrows AC} - R_{AC:MCC1 \rightleftarrows AMCC2}\,, \tag{61}$$

$$\frac{d[MCC1]}{dt} = R_{M:C \rightleftarrows MCC1} - R_{MCC1:C \rightleftarrows MCC2} - R_{AC:MCC1 \rightleftarrows AMCC2}\,, \tag{62}$$

$$\frac{d[MCC2]}{dt} = R_{MCC1:C \rightleftarrows MCC2} - R_{A:MCC2 \rightleftarrows AMCC2}\,, \tag{63}$$

$$\frac{d[AMCC2]}{dt} = R_{A:MCC2 \rightleftarrows AMCC2} + R_{AC:MCC1 \rightleftarrows AMCC2}\,. \tag{64}$$

The conservation relations are the same as (35), (36), and (37). For this network the detailed balancing property does not follow directly from the equations, but requires certain restricting conditions on the rate constants. It can be shown that the condition for detailed balancing for this model is

$$K_D^{A:C} \cdot K_D^{AC:MCC1} = K_D^{MCC1:C} \cdot K_D^{A:MCC2} \tag{65}$$

(a procedure for deriving this condition can be found for instance in [19]). For our analysis we assume that detailed balancing holds. The condition is obviously fulfilled in the special case that all K_Ds are the same.

Approximation for small Cdc20

Given detailed balancing, the derivation of steady state expressions can be carried out in the same way as in the case of the competitive inhibition model in Section 3.2. This directly explains why the behavior of the combined model for small Cdc20 is the same as in the other two models.

Approximation for large Cdc20

As in Section 3.2, we can assume that all reactions involving free C are saturated. In particular, we have $MCC1 \approx 0$, which means that the sequential production of the inhibitor $R_{AC:MCC1 \rightleftarrows AMCC2}$, that is added with respect to the competitive inhibition model, is not active at all. As a consequence, the behavior of the combined model at saturating levels of Cdc20 is the same as the competitive inhibition model.

The approximations for the combined model are shown in Suppl. Fig. 3 (iii).

3.4 Model with Mad3 as a separate species

Equations:

To incorporate Mad3 as a separate species, we assume that first Mad2 ($M2$) binds to Cdc20 (C) to form Mad2:Cdc20 ($M2C$). Afterwards this complex binds to free Mad3 ($M3$) to form $MCC1$. This translates to the following equations for the competitive inhibition case:

$$\frac{d[M2C]}{dt} = R_{M2:C \rightleftarrows M2C} - R_{M2C:M3 \rightleftarrows MCC1} \,, \tag{66}$$

$$\frac{d[MCC1]}{dt} = R_{M2C:M3 \rightleftarrows M2C} - R_{MCC1:C \rightleftarrows MCC2} \,, \tag{67}$$

and to

$$\frac{d[M2C]}{dt} = R_{M2:C \rightleftarrows M2C} - R_{M2C:M3 \rightleftarrows MCC1} \,, \tag{68}$$

$$\frac{d[MCC1]}{dt} = R_{M2C:M3 \rightleftarrows M2C} - R_{AC:MCC1 \rightleftarrows AMCC2} \,, \tag{69}$$

for the sequential inhibition case. The equations for $[AC]$, $[MCC2]$, and $[AMCC2]$ are unchanged with respect to 3.1 and 3.2.

As before, the concentrations of the free species can be obtained from conservation relations:

$$[A_{\text{total}}] = [A] + [AC] + [AMCC2] \,, \tag{70}$$

$$[M2_{\text{total}}] = [M2] + [M2C] + [MCC1] + [MCC2] + [AMCC2] \,, \tag{71}$$

$$[M3_{\text{total}}] = [M3] + [MCC1] + [MCC2] + [AMCC2] \,, \tag{72}$$

$$[C_{\text{total}}] = [C] + [AC] + [M2C] + [MCC1] + 2 \cdot ([MCC2] + [AMCC2]) \,. \tag{73}$$

Approximation for small Cdc20

We can use the same strategy as before, based on the property of detailed balancing, to derive steady state expressions for AC and $AMCC2$. But whereas the expression for AC is unchanged:

$$[\hat{AC}] \approx \frac{[A_{\text{total}}][\hat{C}]}{K_D^{A:C}} \,, \tag{74}$$

due to the additional species we now get

$$[\hat{AMCC2}] \approx \frac{[A_{\text{total}}][M2_{\text{total}}][M3_{\text{total}}][\hat{C}]^2}{K_D^{A:C} K_D^{M2:C} K_D^{M2C:M3} K_D^{AC:MCC1}} \tag{75}$$

for sequential inhibition, and

$$[A\hat{MCC}2] \approx \frac{[A_{\text{total}}][M2_{\text{total}}][M3_{\text{total}}][\hat{C}]^2}{K_D^{M2:C} K_D^{M2C:M3} K_D^{MCC1:C} K_D^{A:MCC2}} \tag{76}$$

for competitive inhibition.

As a result, we get the following relationship between active and inhibited species:

$$[A\hat{MCC}2] \approx \frac{1}{k}[A\hat{MCC}2]^2\,, \tag{77}$$

where

$$k = \frac{[A_{\text{total}}]}{[M2_{\text{total}}][M3_{\text{total}}]} \frac{K_D^{M2:C} K_D^{M2C:M3} K_D^{AC:MCC1}}{K_D^{A:C}} \tag{78}$$

for sequential inhibition, and

$$k = \frac{[A_{\text{total}}]}{[M2_{\text{total}}][M3_{\text{total}}]} \frac{K_D^{M2:C} K_D^{M2C:M3} K_D^{MCC1:C} K_D^{A:MCC2}}{(K_D^{A:C})^2} \tag{79}$$

for competitive inhibition.

Comparing this to (21), the corresponding equation for the model without $M3$, we see that the constant k is now even smaller (provided that the K_Ds are smaller than M2 and M3) because there are four reactions to build the inhibited species. This means that the funneling effect is even more pronounced in a model with Mad3 as a separate species. This can be seen in Suppl. Fig. 4.

Approximation for large Cdc20

For large levels of Cdc20 the model including Mad3 behaves very similarly to the simpler models, provided that $[M3_{\text{total}}] = [M_{\text{total}}]$, i.e. $M3$ is limiting.

For the competitive inhibition scenario, the model is approximated by exactly the same reduced network as the model in 3.2. This is because $MCC1 \approx 0$, and therefore also $M3, M2C \approx 0$ (using again detailed balancing).

In the case of sequential inhibition we are left with two remaining reactions: $R_{M2C:M3 \rightleftarrows MCC1}$ and $R_{AC:MCC1 \rightleftarrows AMCC2}$. Thus there is again an equilibrium between AC and $AMCC2$, but the levels are slightly shifted because $[MCC1] < [M3_{\text{total}}]$. Under the assumption that binding of $M2C$ to $M3$ is strong, the asymptotic levels of AC and $AMCC2$ are very close to those in 3.1, as can be seen in Suppl. Fig. 4.

Supplemental References

[1] Gutenkunst RN, Atlas JC, Casey FP, Daniels BC, Kuczenski RS, Waterfall JJ, Myers CR, Sethna JP (2007) SloppyCell, `http://sloppycell.sourceforge.net/`

[2] Myers CR, Gutenkunst RN, Sethna JP (2007) Python unleashed on systems biology. *Comput Sci Eng* **9**: 34–37

[3] Hein MY, Hubner NC, Poser I, Cox J, Nagaraj N, Toyoda Y, Gak IA, Weisswange I, Mansfeld J, Buchholz F, Hyman AA, Mann M (2015) A Human Interactome in Three Quantitative Dimensions Organized by Stoichiometries and Abundances. *Cell* **163**: 712–723

[4] Kulak NA, Pichler G, Paron I, Nagaraj N, Mann M (2014) Minimal, encapsulated proteomic-sample processing applied to copy-number estimation in eukaryotic cells. *Nat Methods* **11**: 319–324

[5] Shah J, Botvinick E, Bonday Z, Furnari F, Berns M, Cleveland DW (2004) Dynamics of Centromere and Kinetochore Proteins: Implications for Checkpoint Signaling and Silencing. *Curr Biol* **14**: 942–952

[6] Luo X, Tang Z, Xia G, Wassmann K, Matsumoto T, Rizo J, Yu H (2004) The Mad2 spindle checkpoint protein has two distinct natively folded states. *Nat Struct Mol Biol* **11**: 338–345

[7] Fang G (2002) Checkpoint Protein BubR1 Acts Synergistically with Mad2 to Inhibit Anaphase-promoting Complex. *Mol Biol Cell* **13**: 755–766

[8] Tang Z, Bharadwaj R, Li B, Yu H (2001) Mad2-Independent inhibition of APCCdc20 by the mitotic checkpoint protein BubR1. *Dev Cell* **1**: 227–237

[9] Sudakin V, Chan GK, Yen TJ (2001) Checkpoint inhibition of the APC/C in HeLa cells is mediated by a complex of BUBR1, BUB3, CDC20, and MAD2. *J Cell Biol* **154**: 925–936

[10] Chong YT, Koh JL, Friesen H, Duffy SK, Cox MJ, Moses A, Moffat J, Boone C, Andrews BJ (2015) Yeast Proteome Dynamics from Single Cell Imaging and Automated Analysis. *Cell* **161**: 1413–1424

[11] Poddar A, Stukenberg PT, Burke DJ (2005) Two Complexes of Spindle Checkpoint Proteins Containing Cdc20 and Mad2 Assemble during Mitosis Independently of the Kinetochore in *Saccharomyces cerevisiae*. *Eukaryot Cell* **4**: 867–878

[12] Ghaemmaghami S, Huh WK, Bower K, Howson RW, Belle A, Dephoure N, O'Shea EK, Weissman JS (2003) Global analysis of protein expression in yeast. *Nature* **425**: 737–741

[13] Bonaiuti P, Cairoli E, Gross F, Corno A, Vernieri C, Štefl M, Cosentino Lagomarsino M, Knop M, Ciliberto A (forthcoming) Cells escape an operational mitotic checkpoint through a stochastic process. *Curr Biol*

[14] Carpy A, Krug K, Graf S, Koch A, Popic S, Hauf S, Macek B (2014) Absolute Proteome and Phosphoproteome Dynamics during the Cell Cycle of Schizosaccharomyces pombe (Fission Yeast). *Mol Cell Proteomics* **13**: 1925–1936

[15] Heinrich S, Geissen EM, Kamenz J, Trautmann S, Widmer C, Drewe P, Knop M, Radde N, Hasenauer J, Hauf S (2013) Determinants of robustness in spindle assembly checkpoint signalling. *Nature Cell Biol* **15**: 1328–1339

[16] Marguerat S, Schmidt A, Codlin S, Chen W, Aebersold R, Bähler J (2012) Quantitative Analysis of Fission Yeast Transcriptomes and Proteomes in Proliferating and Quiescent Cells. *Cell* **151**: 671–683

[17] Howell BJ, Moree B, Farrar EM, Stewart S, Fang G, Salmon ED (2004) Spindle Checkpoint Protein Dynamics at Kinetochores in Living Cells. *Curr Biol* **14**: 953–964

[18] Wühr M, Freeman Jr RM, Presler M, Horb ME, Peshkin L, Gygi S, Kirschner MW (2015) Deep Proteomics of the Xenopus laevis Egg using an mRNA-derived Reference Database. *Curr Biol* **24**: 1467–1475

[19] Feinberg M (1989) Necessary and Sufficient Conditions for Detailed Balancing in Mass Action Systems of Arbitrary Complexity. *Chem Eng Sci* **44**: 1819–1827

number of observation per strain					description of each category	category included in each figure					
CDC20						**Figures and strain included in it**					
ALL	**X1**	**X2**	**X3**	**X5**		3.2(d) **X1**	3.3 **X1**	2.3 **ALL**	3.4 **X1**	3.15(a) **ALL**	3.14 **X1, X2, X5**
1092	272	292	257	271	Mad is localized at Clb2 degradation	x	x	x	x	x	x
161	42	59	25	35	Mad2 is not localized at Clb2 degradation	x		x			x
4	0	1	0	3	Cell die before Clb2 degradation			x	x	x	
53	12	21	6	14	Mad2 is delocalized - Clb2 does not degrade			x			
1310	326	373	288	323	**TOTAL**	314	272	1310	272	1096	939

Table 4.1: Observation dataset for nocodazole experiments in haploids.

number of observation per strain					description of each category
		CDC20			
ALL	**X1/X1**	**X3/X3**	**X5/X5**	**X1/Δ**	
320	132	49	53	86	Clb2 is degraded
2	2	0	0	0	Movie ends before Clb2 degradation
50	13	2	5	29	Cell die before Clb2 degradation
372	147	51	58	115	**TOTAL**

Table 4.2: Observation dataset for nocodazole experiments in diploids.
All the observations are included in Figure 3.15(b).

parameter	Value (deterministic)	Value (stochastic)	References
s (wt)	$20nM \cdot min^{-1}$	$50\,molecules \cdot min^{-1}$	Pan and Chen [2004], Foster and Morgan [2012], Fig 3.6(a)
D	$0.5\,min^{-1}$	$0.5\,min^{-1}$	
a_{MC}	$0.05\,nM^{-1}\,min^{-1}$	$0.02\,molecules^{-1}\,min^{-1}$	estimated from Simonetta et al. [2009]
$K_{D,MC}$	$10\,nM$	$25\,molecules$	Faesen et al. [2017]
a_{AC}	$0.05\,nM^{-1}\,min^{-1}$	$0.02\,molecules^{-1}\,min^{-1}$	estimated from Chang et al. [2014]
$K_{D,AC}$	$10\,nM$	$25\,molecules$	
a_{ACMC}	$0.05\,nM^{-1}\,min^{-1}$	$0.02\,molecules^{-1}\,min^{-1}$	
$K_{D,ACMC}$	$10\,nM$	$25\,molecules$	estimated from Foster and Morgan [2012]
D_{bkg}	$0.1\,min^{-1}$	$0.1\,min^{-1}$	
M_{total}	$80\,nM$	$200\,molecules$	Fig 3.6(b)
A_{total}	$40\,nM$	$100\,molecules$	Fig 3.6(b), Fig 3.7, Primorac and Musacchio [2013]

Table 4.3: Table of parameters.
Parameters used in the deterministic and stochastic numerical simulations, with their references. See Section 3.2.2 for all the details about parameter estimation.

Table 4.4: Table of strains.

strain	genotype	source
yAC1011	*MATalpha*	
yAC1070	*MATa, his3-11,15::HIS3tetR-GFP (single integration), ura3::3XURA3tetO112*	
yAC1156	*MATalpha, mad2::TRP1*	
yAC2341	*MATa, trp1::MET3pr-yEVenus::TRP1, htb2::HTB2-mCherry::HIS3, leu2-3::LEU2::GAL1-MAD2 (multiple copies), ura3::MET3-CDC20::URA3*	
yAC2398	*MATa, trp1::CDC20::TRP1*	
yAC2400	*MATa, trp1::CDC20::TRP1 (x2)*	
yAC2435	*MATalpha, cdc20::LEU2, trp1::CDC20::TRP1*	
yAC2437	*MATalpha, trp1::CDC20::TRP1*	
yAC2450	*MATa, trp1::CDC20::TRP1 (x2), cdc20::LEU2*	
yAC2453	*MATalpha, trp1::CDC20::TRP1 (x2)*	
yAC2621	*MATa/alpha, pds1::18MYC-Pds1::LEU2 /leu2, MND2/mnd2::KanMX6*	
yAC2622	*MATa/alpha, mnd2::KanMX6 /MND2, cdc20::LEU2/CDC20, trp1::CDC20::TRP1/trp1::CDC20::TRP1*	
yAC2675	*MATa, ura3::CDC20::URA3 (x2)*	
yAC2831	*MATalpha, trp1::CDC20::TRP1(x2), ura3::CDC20::URA3 (x2), scc1::Scc1-3mCherryFP::NAT*	
yAC2886	*MATa, ADE2, mad2::MAD2-3myeGFP-dcu::NAT cdc23::CDC23-3mCherry-dcu::hphNT1*	
yAC2919	*MATa, ADE2, mad2::MAD2-3myeGFP-dcu::NAT bub3::BUB-3mCherry-dcu::hphNT1*	
yAC2932	*MATa, ADE2, cdc23::CDC23-3mCherry-dcu::hphNT1, apc5::APC5-3myeGFP-dcu::NAT*	
yAC2940	*MATa, ADE2, bub3::BUB3-3myeGFP-dcu::NAT mad3::MAD3-3mCherry-dcu::hphNT1*	
yAC2954	*MATa, ADE2, cdc16::CDC16-3myeGFP-dcu::NAT, cdc23::CDC23-3mCherry-dcu::hphNT1*	
yAC2991	*MATa, trp1::CDC20::TRP1 (2X), ura3::CDC20::URA3 (2X)*	
yAC2994	*MATa, ADE2, mad2::MAD2-3myeGFP-dcu::NAT, bub3::BUB3-3mCherry-dcu::hphNT1, mad3::kanMX*	
yAC3042	*MATa, ADE2, mad2::MAD2-3myeGFP-dcu::NAT, bub3::BUB3-3mCherry-dcu::hphNT1, mad3::kanMX, mad1::HIS3*	
yAC3103	*MATa, ADE2, mad2::MAD2-3myeGFP-dcu::NAT, cdc23::CDC23-3mCherry-dcu::hphNT1, mad3::kanMX*	
yAC3106	*MATa, cdc20::CDC20pr::yEVenus^{degron}-TRP1::CDC20, htb2::HTB2-mCherry::HIS3*	
yAC3108	*MATa, cdc20::CDC20pr::yEVenus^{degron}-TRP1::CDC20, htb2::HTB2-mCherry::HIS3, leu2-3::LEU2::GAL1-MAD2 (multiple copies)*	

Table 4.4: Table of strains (continued)

strain	genotype	source
yAC3112	*MATa, trp1::MET3pr-yEVenus::TRP1, ura3::MET3pr-mCherry::URA3*	
yAC3127	*MATa, ADE2, mad3::MAD3-3mCherry-dcu::hphNT1, mad2::MAD2-3myeGFP-dcu::NAT, bub3::LEU2*	
yAC3153	*MATa, ADE2, mad3::MAD3-3mCherry-dcu::hphNT1, mad2::MAD2-3myeGFP-dcu::NAT, trp1::CDC20::TRP1 (2X)*	
yAC3176	*MATa, ADE2, cdc23::CDC23-3mCherry-dcu::hphNT1, mad2::MAD2-3myeGFP-dcu::NAT, trp1::CDC20::TRP1 (2X)*	
yAC3179	*MATa, ADE2, cdc23::CDC23-3mCherry-dcu::hphNT1, mad2::MAD2-3myeGFP-dcu::NAT, trp1::CDC20::TRP1*	
yAC3181	*MATa, ADE2, mad3::MAD3-3mCherry-dcu::hphNT1, mad2::MAD2-3myeGFP-dcu::NAT, trp1::CDC20::TRP1*	
yAC3202	*MATa*	
yAC3227	*MATa, ADE2, mad3::MAD3-3mCherry-dcu::hphNT1, mad2::MAD2-3myeGFP-dcu::NAT mnd2::HIS3*	
yAC3261	*MATa, apc4::APC4myc9-TRP1*	
yAC3262	*MATa, apc5::APC5myc9-TRP1*	
yAC3266	*MATa bub3::BUB3-3Cherry::hphNT1, mad2::MAD2-3GFP-KanMX6*	
yAC3268	*MATa, ADE2, mad3::MAD3-3mCherry-dcu::hphNT1, mad2::MAD2-3myeGFP-dcu::NAT*	
yAC3307	*MATa, cdc20::Myc9-CDC20-TRP1*	
yAC3312	*MATa, ADE2, cdc23::CDC23-3mCherry-dcu::hphNT1, mad2::MAD2-3myeGFP-dcu::NAT, cdc16:CDC16-6A-TRP1, cdc27::CDC27-5A-KAN*	
yAC3346	*MATa, ADE2, mad3::MAD3-3mCherry-dcu::hphNT1, mad2::MAD2-3myeGFP-dcu::NAT, cdc16:CDC16-6A-TRP1, cdc27::CDC27-5A-KAN*	
yAC3353	*MATa, cdc20::Myc9-CDC20-TRP1, cdc27::CDC27myc9-TRP1*	
yAC3359	*MATa, leu2-3::LEU2::GAL1-MAD2 (multiple copies), htb2::HTB2-mCherry::HIS3, MET3pr-yEVenus^{degron}::TRP1(single integration)*	
yAC3365	*MATa cdc27::CDC27myc9-TRP1*	
yAC3367	*MATa, cdc23::CDC23myc9-LEU2, cdc20::Myc9-CDC20-TRP1*	
yAC3371	*MATa, cdc23::CDC23myc9-LEU2*	
yAC3380	*MATa, ADE2, mad3::MAD3-3mCherry-dcu::hphNT1, mad2::MAD2-3myeGFP-dcu::NAT, trp1::CDC20::TRP1 (2X), ura3::CDC20::URA3 (2X)*	
yAC3384	*MATa, ADE2, cdc23::CDC23-3mCherry-dcu::hphNT1, mad2::MAD2-3myeGFP-dcu::NAT, trp1::CDC20::TRP1 (2X), ura3::CDC20::URA3 (2X)*	
yAC3400	*MATa, ADE2, cdc23::CDC23-3mCherry-dcu::hphNT1, mad2::MAD2-3myeGFP-dcu::NAT, mnd2::HIS3*	
yAC3415	*MATa, sfGFPΔC-URA3-NOP1pr-sfGFP-CDC20*	

Table 4.4: Table of strains (continued)

strain	genotype	source
yAC3427	*MATa, apc4::APC4myc9-TRP1, cdc23::CDC23myc9-LEU2*	
yAC3429	*MATalpha, leu2::NatNT2-GAL1pr-I-SCEI*	
yAC3430	*MATa, apc5::APC5myc9-TRP1, cdc23::CDC23myc9-LEU2*	
yAC3436	*MATa cdc27::CDC27myc9-TRP1*	
yAC3456	*MATa, CDC20::sfGFP-CDC20*	
yAC3509	*MATa, clb2::CLB2-3mCherry-dcu::hphNT1*	
yAC3536	*MATalpha clb2::Clb2-3mCherry-dcu-hphNT1 CDC20::sfGFP-CDC20*	
yAC3538	*MATa, clb2::CLB2-3mCherrydcu::hphNT1, mad2::MAD2-3GFP-KanMX6*	
yAC3552	*MATa, clb2::CLB2-3mCherry-dcu::hphNT1, mad2::MAD2-3GFP-KanMX6, trp1::CDC20::TRP1 (2X), ura3::CDC20::URA3 (2X),*	
yAC3555	*MATa, clb2::CLB2-3mCherry-dcu::hphNT1, mad2::MAD2-3GFP-KanMX6, trp1::CDC20::TRP1 (2X)*	
yAC3565	*MATa, clb2::CLB2-3mCherry-dcu::hphNT1, mad2::MAD2-3GFP-KanMX6, trp1::CDC20::TRP1*	
yAC3612	*MATa, ADE2, clb2::Clb2-3mCherry-dcu-hphNT1, CDC20::sfGFP-CDC20, mnd2::HIS3*	
yAC3614	*MATa, ADE2, clb2::Clb2-3mCherry-dcu-hphNT1, CDC20::sfGFP-CDC20*	
yAC3623	*MATa, cdc20::CDC20pr::yEVenus^{degron}-TRP1::CDC20, htb2::HTB2-mCherry::HIS3, trp1::CDC20::TRP1*	
yAC3627	*MATa, cdc20::CDC20pr::yEVenus^{degron}-TRP1::CDC20, htb2::HTB2-mCherry::HIS3, trp1::CDC20::TRP1 (2X), ura3::CDC20::URA3 (2X)*	
yAC3630	*MATa, trp1::CDC20::TRP1 (2X), cdc20::CDC20pr::yEVenus^{degron}-TRP1::CDC20, htb2::HTB2-mCherry::HIS3*	
yAC3738	*MATa, clb2::CLB2-3mCherrydcu::hphNT1, mad2::MAD2-3GFP-KanMX6, mad3::TRP1*	
yAC3801	*MATa/alpha, clb2::CLB2-3mCherry-dcu::hphNT1/clb2::CLB2-3mCherry-dcu::hphNT1, mad2::MAD2-3GFP-KanMX6/mad2::MAD2-3GFPKanMX6*	
yAC3802	*MATa/alpha, clb2::CLB2-3mCherry-dcu::hphNT1/clb2::CLB2-3mCherry-dcu::hphNT1, mad2::MAD2-3GFP-KanMX6/mad2::MAD2-3GFPKanMX6, trp1::CDC20::TRP1 (2X)/trp1::CDC20::TRP1 (2X)*	
yAC3803	*MATa/alpha, clb2::CLB2-3mCherry-dcu::hphNT1/clb2::CLB2-3mCherry-dcu::hphNT1, mad2::MAD2-3GFP-KanMX6/mad2::MAD2-3GFPKanMX6, trp1::CDC20::TRP1 (2X)/trp1::CDC20::TRP1 (2X), ura3::CDC20::URA3 (2X)/ura3::CDC20::URA3 (2X)*	
yAC3804	*MATa/alpha, clb2::CLB2-3mCherry-dcu::hphNT1/clb2::CLB2-3mCherry-dcu::hphNT1, mad2::MAD2-3GFP-KanMX6/mad2::MAD2-3GFPKanMX6, CDC20/cdc20::HIS3*	

name	description	origin
pAC97	*CDC20pr-yEVenus^{degron}::TRP1*	this study
pAC130	*MET3pr-CDC20*	this study
pAC136	*MET3pr-yEVenus::TRP1*	this study
pAC138	*CDC20pr-CDC20-CDC20ter (TRP1)*	this study
pAC142	*CDC20pr-CDC20-CDC20ter (URA3)*	this study
pAC156	*MET3pr-mCherry (URA3)*	this study
pST70	*3mCherry-dcu-hphNT1*	Boeke et al. [2014]
pST72	*3myeGFP-dcu-natNT1*	Boeke et al. [2014]
pMaM189	N-sfGFPΔC-I-SceI^{site}-*CYC1term-URA3-NOP1pr*-I-SceI^{site}-sfGFP	Khmelinskii et al. [2011]
pND32	*GAL1pr*-I-SCEI	Khmelinskii et al. [2011]
pRS402	*ADE2*	Brachmann et al. [1998]

Table 4.5: Table of plasmids used in this study

Declaration of contributions

I performed the experiments and analyses presented in this thesis, except where otherwise stated. In particular, I received help on the following topics. Elena Chiroli performed with me the transformations that led to the creation of *CDC20 NX* strains, and together with Federica Natali they produced the *CDC20*-sfGFP strain. Mattia Pavani helped me in tagging proteins for FCS/FCCS experiments. Considering APC/C^{Cdc20} fluctuations as an Ornstein-Uhlenbeck process is an idea of Marco Cosentino Lagomarsino. The mathematical model was developed in many discussions with Andrea Ciliberto and Fridolin Groß, who performed all numerical simulations.

Bibliography

G Aletti, D Morale, A Micheletti, and M Burger. *Math everywhere - Deterministic and stochastic modelling in biomedicine, economics and industry*. Springer, Berlin, Heidelberg, New York, 2006.

C. Alfieri, L. Chang, Z. Zhang, J. Yang, S. Maslen, M. Skehel, and D. Barford. Molecular basis of APC/C regulation by the spindle assembly checkpoint. *Nature*, 536(7617):431–6, 2016. ISSN 1476-4687 (Electronic) 0028-0836 (Linking). doi: 10.1038/nature19083. URL https://www.ncbi.nlm.nih.gov/pubmed/27509861.

P. Aravamudhan, R. Chen, B. Roy, J. Sim, and A. P. Joglekar. Dual mechanisms regulate the recruitment of spindle assembly checkpoint proteins to the budding yeast kinetochore. *Mol Biol Cell*, 2016. ISSN 1939-4586 (Electronic) 1059-1524 (Linking). doi: 10.1091/mbc.E16-01-0007. URL http://www.ncbi.nlm.nih.gov/pubmed/27170178.

K. Bacia and P. Schwille. Practical guidelines for dual-color fluorescence cross-correlation spectroscopy. *Nat Protoc*, 2(11):2842–56, 2007. ISSN 1750-2799 (Electronic) 1750-2799 (Linking). doi: 10.1038/nprot.2007.410. URL http://www.ncbi.nlm.nih.gov/pubmed/18007619.

K. Bacia, S. A. Kim, and P. Schwille. Fluorescence cross-correlation spectroscopy in living cells. *Nat Methods*, 3(2):83–9, 2006. ISSN 1548-7091 (Print) 1548-7091 (Linking). doi: 10.1038/nmeth822. URL http://www.ncbi.nlm.nih.gov/pubmed/16432516.

J. Bloom and F. R. Cross. Multiple levels of cyclin specificity in cell-cycle control. *Nat Rev Mol Cell Biol*, 8(2):149–60, 2007. ISSN 1471-0072 (Print) 1471-0072 (Linking). doi: 10.1038/nrm2105. URL https://www.ncbi.nlm.nih.gov/pubmed/17245415.

D. Boeke, S. Trautmann, M. Meurer, M. Wachsmuth, C. Godlee, M. Knop, and M. Kaksonen. Quantification of cytosolic interactions identifies Ede1 oligomers as key organizers of endocytosis. *Mol Syst Biol*, 10(11):756, 2014. ISSN 1744-4292 (Electronic) 1744-4292 (Linking). doi: 10.15252/msb.20145422. URL http://www.ncbi.nlm.nih.gov/pubmed/25366307.

P. Bonaiuti, E. Chiroli, F. Gross, A. Corno, C. Vernieri, M. Stefl, M. Cosentino Lagomarsino, M. Knop, and A. Ciliberto. Cells escape an operational mitotic checkpoint through a stochastic process. *Curr*

Biol, 2017. ISSN 1879-0445 (Electronic) 0960-9822 (Linking). doi: 10.1016/j.cub.2017.11.031. URL https://www.ncbi.nlm.nih.gov/pubmed/29249657.

C. B. Brachmann, A. Davies, G. J. Cost, E. Caputo, J. Li, P. Hieter, and J. D. Boeke. Designer deletion strains derived from Saccharomyces cerevisiae S288C: a useful set of strains and plasmids for PCR-mediated gene disruption and other applications. *Yeast*, 14(2):115–32, 1998. ISSN 0749-503X (Print) 0749-503X (Linking). doi: 10.1002/(SICI)1097-0061(19980130)14:2<115::AID-YEA204>3.0.CO;2-2. URL https://www.ncbi.nlm.nih.gov/pubmed/9483801.

D. M. Brady and K. G. Hardwick. Complex formation between Mad1p, Bub1p and Bub3p is crucial for spindle checkpoint function. *Curr Biol*, 10(11):675–8, 2000. ISSN 0960-9822 (Print) 0960-9822 (Linking). URL http://www.ncbi.nlm.nih.gov/pubmed/10837255.

D. A. Brito and C. L. Rieder. Mitotic checkpoint slippage in humans occurs via cyclin B destruction in the presence of an active checkpoint. *Curr Biol*, 16(12):1194–1200, 2006. URL http://eutils.ncbi.nlm.nih.gov/entrez/eutils/elink.fcgi?dbfrom=pubmed&id=16782009&retmode=ref&cmd=prlinks.

O. Caffo, M. Dipasquale, V. Murgia, A. Veccia, and E. Galligioni. An evaluation of the pharmacokinetics and clinical use of vinorelbine for NSCLC treatment. *Expert Opin Drug Metab Toxicol*, 9(8):1037–51, 2013. ISSN 1744-7607 (Electronic) 1742-5255 (Linking). doi: 10.1517/17425255.2013.804065. URL https://www.ncbi.nlm.nih.gov/pubmed/23705788.

A. Camasses, A. Bogdanova, A. Shevchenko, and W. Zachariae. The CCT chaperonin promotes activation of the anaphase-promoting complex through the generation of functional Cdc20. *Mol Cell*, 12(1):87–100, 2003. ISSN 1097-2765 (Print) 1097-2765 (Linking). URL https://www.ncbi.nlm.nih.gov/pubmed/12887895.

L. F. Chang, Z. Zhang, J. Yang, S. H. McLaughlin, and D. Barford. Molecular architecture and mechanism of the anaphase-promoting complex. *Nature*, 513(7518):388–393, 2014. ISSN 1476-4687 (Electronic) 0028-0836 (Linking). doi: 10.1038/nature13543. URL https://www.ncbi.nlm.nih.gov/pubmed/25043029.

W. C. Chao, K. Kulkarni, Z. Zhang, E. H. Kong, and D. Barford. Structure of the mitotic checkpoint complex. *Nature*, 484(7393):208–13, 2012. ISSN 1476-4687 (Electronic) 0028-0836 (Linking). doi: 10.1038/nature10896. URL http://www.ncbi.nlm.nih.gov/pubmed/22437499.

G. Charvin. PhyloCell. https://github.com/gcharvin/phyloCell, 2017.

G. Charvin, F. R. Cross, and E. D. Siggia. A microfluidic device for temporally controlled gene expression and long-term fluorescent imaging in unperturbed dividing yeast cells. *PloS one*, 3(1):e1468, 2008. URL <GotoISI>://MEDLINE:18213377.

G. Charvin, C. Oikonomou, and F. Cross. Long-term imaging in microfluidic devices. *Methods Mol Biol*, 591:229–42, 2010a. ISSN 1940-6029 (Electronic) 1064-3745 (Linking). doi: 10.1007/978-1-60761-404-3_14. URL https://www.ncbi.nlm.nih.gov/pubmed/19957134.

G. Charvin, C. Oikonomou, E. D. Siggia, and F. R. Cross. Origin of irreversibility of cell cycle start in budding yeast. *PLoS Biol*, 8(1):e1000284, 2010b. ISSN 1545-7885 (Electronic) 1544-9173 (Linking). doi: 10.1371/journal.pbio.1000284. URL http://www.ncbi.nlm.nih.gov/pubmed/20087409.

O. Cohen-Fix and D. Koshland. Pds1p of budding yeast has dual roles: inhibition of anaphase initiation and regulation of mitotic exit. *Genes Dev*, 13(15):1950–9, 1999. ISSN 0890-9369 (Print) 0890-9369 (Linking). URL https://www.ncbi.nlm.nih.gov/pubmed/10444593.

P. Collin, O. Nashchekina, R. Walker, and J. Pines. The spindle assembly checkpoint works like a rheostat rather than a toggle switch. *Nat Cell Biol*, 15(11):1378–85, 2013. ISSN 1476-4679 (Electronic) 1465-7392 (Linking). doi: 10.1038/ncb2855. URL https://www.ncbi.nlm.nih.gov/pubmed/24096242.

V. D'Angiolella, C. Mari, D. Nocera, L. Rametti, and D. Grieco. The spindle checkpoint requires cyclin-dependent kinase activity. *Genes Dev*, 17(20):2520–5, 2003. ISSN 0890-9369 (Print) 0890-9369 (Linking). doi: 10.1101/gad.267603. URL https://www.ncbi.nlm.nih.gov/pubmed/14561775.

A. De Antoni, C. G. Pearson, D. Cimini, J. C. Canman, V. Sala, L. Nezi, M. Mapelli, L. Sironi, M. Faretta, E. D. Salmon, and A. Musacchio. The Mad1/Mad2 complex as a template for Mad2 activation in the spindle assembly checkpoint. *Curr Biol*, 15(3):214–25, 2005. ISSN 0960-9822 (Print) 0960-9822 (Linking). doi: 10.1016/j.cub.2005.01.038. URL http://www.ncbi.nlm.nih.gov/pubmed/15694304.

A. E. Dick and D. W. Gerlich. Kinetic framework of spindle assembly checkpoint signalling. *Nat Cell Biol*, 15(11):1370–7, 2013. ISSN 1476-4679 (Electronic) 1465-7392 (Linking). doi: 10.1038/ncb2842. URL http://www.ncbi.nlm.nih.gov/pubmed/24096243.

A. Edelstein, N. Amodaj, K. Hoover, R. Vale, and N. Stuurman. Computer control of microscopes using microManager. *Curr Protoc Mol Biol*, Chapter 14:Unit14 20, 2010. ISSN 1934-3647 (Electronic) 1934-3647 (Linking). doi: 10.1002/0471142727.mb1420s92. URL https://www.ncbi.nlm.nih.gov/pubmed/20890901.

A. C. Faesen, M. Thanasoula, S. Maffini, C. Breit, F. Müller, S. van Gerwen, T. Bange, and A. Musacchio. Basis of catalytic assembly of the mitotic checkpoint complex. *Nature*, 542(7642):498–502, 2017. ISSN 1476-4687 (Electronic) 0028-0836 (Linking). doi: 10.1038/nature21384. URL https://www.ncbi.nlm.nih.gov/pubmed/28102834.

I. T. Foe, S. A. Foster, S. K. Cheung, S. Z. DeLuca, D. O. Morgan, and D. P. Toczyski. Ubiquitination of Cdc20 by the APC occurs through an intramolecular mechanism. *Curr Biol*, 21(22):1870–7,

2011. ISSN 1879-0445 (Electronic) 0960-9822 (Linking). doi: 10.1016/j.cub.2011.09.051. URL http://www.ncbi.nlm.nih.gov/pubmed/22079111.

S. A. Foster and D. O. Morgan. The APC/C subunit Mnd2/Apc15 promotes Cdc20 autoubiquitination and spindle assembly checkpoint inactivation. *Mol Cell*, 47(6):921–32, 2012. ISSN 1097-4164 (Electronic) 1097-2765 (Linking). doi: 10.1016/j.molcel.2012.07.031. URL http://www.ncbi.nlm.nih.gov/pubmed/22940250.

R. Fraschini, E. Formenti, G. Lucchini, and S. Piatti. Budding yeast Bub2 is localized at spindle pole bodies and activates the mitotic checkpoint via a different pathway from Mad2. *J Cell Biol*, 145 (5):979–91, 1999. ISSN 0021-9525 (Print) 0021-9525 (Linking). URL https://www.ncbi.nlm.nih.gov/pubmed/10352016.

R. Fraschini, A. Beretta, L. Sironi, A. Musacchio, G. Lucchini, and S. Piatti. Bub3 interaction with Mad2, Mad3 and Cdc20 is mediated by WD40 repeats and does not require intact kinetochores. *EMBO J*, 20(23):6648–59, 2001. ISSN 0261-4189 (Print) 0261-4189 (Linking). doi: 10.1093/emboj/20.23.6648. URL http://www.ncbi.nlm.nih.gov/pubmed/11726501.

M. Galli and D. O. Morgan. Cell size determines the strength of the spindle assembly checkpoint during embryonic development. *Dev Cell*, 36(3):344–52, 2016. ISSN 1878-1551 (Electronic) 1534-5807 (Linking). doi: 10.1016/j.devcel.2016.01.003. URL https://www.ncbi.nlm.nih.gov/pubmed/26859356.

K. E. Gascoigne and S. S. Taylor. Cancer cells display profound intra- and interline variation following prolonged exposure to antimitotic drugs. *Cancer Cell*, 14(2):111–22, 2008. ISSN 1878-3686 (Electronic) 1535-6108 (Linking). doi: 10.1016/j.ccr.2008.07.002. URL https://www.ncbi.nlm.nih.gov/pubmed/18656424.

K. E. Gascoigne and S. S. Taylor. How do anti-mitotic drugs kill cancer cells? *J Cell Sci*, 122(Pt 15):2579–85, 2009. ISSN 0021-9533 (Print) 0021-9533 (Linking). doi: 10.1242/jcs.039719. URL https://www.ncbi.nlm.nih.gov/pubmed/19625502.

C. Gérard, J. J. Tyson, D. Coudreuse, and B. Novák. Cell cycle control by a minimal Cdk network. *PLoS Comput Biol*, 11(2):e1004056, 2015. ISSN 1553-7358 (Electronic) 1553-734X (Linking). doi: 10.1371/journal.pcbi.1004056. URL https://www.ncbi.nlm.nih.gov/pubmed/25658582.

G. Giaever, A. M. Chu, L. Ni, C. Connelly, L. Riles, S. Veronneau, S. Dow, A. Lucau-Danila, K. Anderson, B. Andre, A. P. Arkin, A. Astromoff, M. El-Bakkoury, R. Bangham, R. Benito, S. Brachat, S. Campanaro, M. Curtiss, K. Davis, A. Deutschbauer, K. D. Entian, P. Flaherty, F. Foury, D. J. Garfinkel, M. Gerstein, D. Gotte, U. Guldener, J. H. Hegemann, S. Hempel, Z. Herman, D. F. Jaramillo, D. E. Kelly, S. L. Kelly, P. Kotter, D. LaBonte, D. C. Lamb, N. Lan, H. Liang, H. Liao, L. Liu, C. Luo, M. Lussier, R. Mao, P. Menard, S. L. Ooi, J. L. Revuelta, C. J. Roberts, M. Rose,

P. Ross-Macdonald, B. Scherens, G. Schimmack, B. Shafer, D. D. Shoemaker, S. Sookhai-Mahadeo, R. K. Storms, J. N. Strathern, G. Valle, M. Voet, G. Volckaert, C. Y. Wang, T. R. Ward, J. Wilhelmy, E. A. Winzeler, Y. Yang, G. Yen, E. Youngman, K. Yu, H. Bussey, J. D. Boeke, M. Snyder, P. Philippsen, R. W. Davis, and M. Johnston. Functional profiling of the Saccharomyces cerevisiae genome. *Nature*, 418(6896):387–91, 2002. ISSN 0028-0836 (Print) 0028-0836 (Linking). doi: 10.1038/nature00935. URL https://www.ncbi.nlm.nih.gov/pubmed/12140549.

D. T. Gillespie. A general method for numerically simulating the stochastic time evolution of coupled chemical reactions. *Journal of Computational Physics*, 22:403–434, 1976.

D. T. Gillespie. Exact stochastic simulation of coupled chemical reactions. *Journal of physical chemistry*, 1977.

E. S. Gillett, C. W. Espelin, and P. K. Sorger. Spindle checkpoint proteins and chromosome-microtubule attachment in budding yeast. *The Journal of cell biology*, 164(4):535–46, 2004. ISSN 0021-9525. URL <GotoISI>://MEDLINE:14769859.

G. H. Goto, A. Mishra, R. Abdulle, C. A. Slaughter, and K. Kitagawa. Bub1-mediated adaptation of the spindle checkpoint. *PLoS Genet*, 7(1):e1001282, 2011. ISSN 1553-7404 (Electronic) 1553-7390 (Linking). doi: 10.1371/journal.pgen.1001282. URL http://www.ncbi.nlm.nih.gov/pubmed/21298086.

F. Groß, P. Bonaiuti, S. Hauf, and A. Ciliberto. An *in-silico* analysis of inhibitory logics in the mitotic checkpoint network. In preparation.

S. Gruber, C. H. Haering, and K. Nasmyth. Chromosomal cohesin forms a ring. *Cell*, 112(6):765–77, 2003. ISSN 0092-8674 (Print) 0092-8674 (Linking). URL http://www.ncbi.nlm.nih.gov/pubmed/12654244.

C M Guldberg and P Waage. Studier i affiniteten. *Forhandelinger: Videnskabs-Selskabet i Christiana*, 35, 1864.

R.N. Gutenkunst, J.C. Atlas, F.P. Casey, B.C. Daniels, R.S. Kuczenski, J.J. Waterfall, C.R. Myers, and J.P. Sethna. SloppyCell. http://sloppycell.sourceforge.net/., 20107.

K. G. Hardwick, E. Weiss, F. C. Luca, M. Winey, and A. W. Murray. Activation of the budding yeast spindle assembly checkpoint without mitotic spindle disruption. *Science*, 273(5277):953–6, 1996. ISSN 0036-8075 (Print) 0036-8075 (Linking). URL https://www.ncbi.nlm.nih.gov/pubmed/8688079.

K. G. Hardwick, R. C. Johnston, D. L. Smith, and A. W. Murray. MAD3 encodes a novel component of the spindle checkpoint which interacts with Bub3p, Cdc20p, and Mad2p. *J Cell Biol*, 148(5):

871–82, 2000. ISSN 0021-9525 (Print) 0021-9525 (Linking). URL http://www.ncbi.nlm.nih.gov/pubmed/10704439.

S. Heinrich, H. Windecker, N. Hustedt, and S. Hauf. Mph1 kinetochore localization is crucial and upstream in the hierarchy of spindle assembly checkpoint protein recruitment to kinetochores. *J Cell Sci*, 125(Pt 20):4720–7, 2012. ISSN 1477-9137 (Electronic) 0021-9533 (Linking). doi: 10.1242/jcs.110387. URL http://www.ncbi.nlm.nih.gov/pubmed/22825872.

S. Heinrich, E. M. Geissen, J. Kamenz, S. Trautmann, C. Widmer, P. Drewe, M. Knop, N. Radde, J. Hasenauer, and S. Hauf. Determinants of robustness in spindle assembly checkpoint signalling. *Nature Cell Biology*, 15(11):1328–U155, 2013. ISSN 1465-7392. doi: Doi10.1038/Ncb2864. URL <GotoISI>://WOS:000326680700009.

M. A. Hoyt, L. Totis, and B. T. Roberts. S. cerevisiae genes required for cell cycle arrest in response to loss of microtubule function. *Cell*, 66(3):507–17, 1991. ISSN 0092-8674 (Print) 0092-8674 (Linking). URL https://www.ncbi.nlm.nih.gov/pubmed/1651171.

B. Huang and T. C. Huffaker. Dynamic microtubules are essential for efficient chromosome capture and biorientation in S. cerevisiae. *J Cell Biol*, 175(1):17–23, 2006. ISSN 0021-9525 (Print) 0021-9525 (Linking). doi: 10.1083/jcb.200606021. URL https://www.ncbi.nlm.nih.gov/pubmed/17030980.

J. N. Huang, I. Park, E. Ellingson, L. E. Littlepage, and D. Pellman. Activity of the APC(Cdh1) form of the anaphase-promoting complex persists until S phase and prevents the premature expression of Cdc20p. *J Cell Biol*, 154(1):85–94, 2001. ISSN 0021-9525 (Print) 0021-9525 (Linking). URL https://www.ncbi.nlm.nih.gov/pubmed/11448992.

F. Huber, M. Meurer, D. Bunina, I. Kats, C. I. Maeder, M. Štefl, C. Mongis, and M. Knop. PCR duplication: A one-step cloning-free method to generate duplicated chromosomal loci and interference-free expression reporters in yeast. *PLoS One*, 9(12):e114590, 2014. ISSN 1932-6203 (Electronic) 1932-6203 (Linking). doi: 10.1371/journal.pone.0114590. URL http://www.ncbi.nlm.nih.gov/pubmed/25493941.

L. H. Hwang, L. F. Lau, D. L. Smith, C. A. Mistrot, K. G. Hardwick, E. S. Hwang, A. Amon, and A. W. Murray. Budding yeast Cdc20: a target of the spindle checkpoint. *Science*, 279(5353):1041–4, 1998. ISSN 0036-8075 (Print) 0036-8075 (Linking). URL http://www.ncbi.nlm.nih.gov/pubmed/9461437.

D. Izawa and J. Pines. The mitotic checkpoint complex binds a second CDC20 to inhibit active APC/C. *Nature*, 2015. ISSN 1476-4687 (Electronic) 0028-0836 (Linking). doi: 10.1038/nature13911. URL http://www.ncbi.nlm.nih.gov/pubmed/25383541.

C. Janke, M. M. Magiera, N. Rathfelder, C. Taxis, S. Reber, H. Maekawa, A. Moreno-Borchart, G. Doenges, E. Schwob, E. Schiebel, and M. Knop. A versatile toolbox for PCR-based tagging of

yeast genes: new fluorescent proteins, more markers and promoter substitution cassettes. *Yeast*, 21(11):947–62, 2004. ISSN 0749-503X (Print) 0749-503X (Linking). doi: 10.1002/yea.1142. URL http://www.ncbi.nlm.nih.gov/pubmed/15334558.

S. Kaisari, D. Sitry-Shevah, S. Miniowitz-Shemtov, and A. Hershko. Intermediates in the assembly of mitotic checkpoint complexes and their role in the regulation of the anaphase-promoting complex. *Proc Natl Acad Sci U S A*, 2016. ISSN 1091-6490 (Electronic) 0027-8424 (Linking). doi: 10.1073/pnas.1524551113. URL http://www.ncbi.nlm.nih.gov/pubmed/26755599.

N. G. van Kampen. *Stochastic processes in physics and chemistry*. North-Holland personal library. Elsevier, Amsterdam ; Boston ; London, 3rd edition, 2007. ISBN 9780444529657 (pbk.) 0444529659 (pbk.).

P. Kapusta, R. Macháň, A. Benda, and M. Hof. Fluorescence Lifetime Correlation Spectroscopy (FLCS): concepts, applications and outlook. *Int J Mol Sci*, 13(10):12890–910, 2012. ISSN 1422-0067 (Electronic) 1422-0067 (Linking). doi: 10.3390/ijms131012890. URL https://www.ncbi.nlm.nih.gov/pubmed/23202928.

O. Kapuy, E. He, S. Lopez-Aviles, F. Uhlmann, J. J. Tyson, and B. Novak. System-level feedbacks control cell cycle progression. *FEBS Lett*, 583(24):3992–8, 2009. ISSN 1873-3468 (Electronic) 0014-5793 (Linking). doi: 10.1016/j.febslet.2009.08.023. URL https://www.ncbi.nlm.nih.gov/pubmed/19703449.

S. Kemmler, M. Stach, M. Knapp, J. Ortiz, J. Pfannstiel, T. Ruppert, and J. Lechner. Mimicking Ndc80 phosphorylation triggers spindle assembly checkpoint signalling. *EMBO J*, 28(8):1099–110, 2009. ISSN 1460-2075 (Electronic) 0261-4189 (Linking). doi: 10.1038/emboj.2009.62. URL https://www.ncbi.nlm.nih.gov/pubmed/19300438.

O. Kerscher, L. B. Crotti, and M. A. Basrai. Recognizing chromosomes in trouble: association of the spindle checkpoint protein Bub3p with altered kinetochores and a unique defective centromere. *Mol Cell Biol*, 23(18):6406–18, 2003. ISSN 0270-7306 (Print) 0270-7306 (Linking). URL http://www.ncbi.nlm.nih.gov/pubmed/12944469.

A. Khmelinskii, M. Meurer, N. Duishoev, N. Delhomme, and M. Knop. Seamless gene tagging by endonuclease-driven homologous recombination. *PLoS One*, 6(8):e23794, 2011. ISSN 1932-6203 (Electronic) 1932-6203 (Linking). doi: 10.1371/journal.pone.0023794. URL http://www.ncbi.nlm.nih.gov/pubmed/21915245.

A. Khmelinskii, P. J. Keller, A. Bartosik, M. Meurer, J. D. Barry, B. R. Mardin, A. Kaufmann, S. Trautmann, M. Wachsmuth, G. Pereira, W. Huber, E. Schiebel, and M. Knop. Tandem fluorescent protein timers for in vivo analysis of protein dynamics. *Nat Biotechnol*, 30(7):708–14, 2012. ISSN

1546-1696 (Electronic) 1087-0156 (Linking). doi: 10.1038/nbt.2281. URL http://www.ncbi.nlm.nih.gov/pubmed/22729030.

E. M. King, S. J. van der Sar, and K. G. Hardwick. Mad3 KEN boxes mediate both Cdc20 and Mad3 turnover, and are critical for the spindle checkpoint. *PLoS One*, 2(4):e342, 2007. ISSN 1932-6203 (Electronic) 1932-6203 (Linking). doi: 10.1371/journal.pone.0000342. URL http://www.ncbi.nlm.nih.gov/pubmed/17406666.

T. Kiyomitsu, H. Murakami, and M. Yanagida. Protein interaction domain mapping of human kinetochore protein Blinkin reveals a consensus motif for binding of spindle assembly checkpoint proteins Bub1 and BubR1. *Mol Cell Biol*, 31(5):998–1011, 2011. ISSN 1098-5549 (Electronic) 0270-7306 (Linking). doi: 10.1128/MCB.00815-10. URL https://www.ncbi.nlm.nih.gov/pubmed/21199919.

N. A. Kulak, G. Pichler, I. Paron, N. Nagaraj, and M. Mann. Minimal, encapsulated proteomic-sample processing applied to copy-number estimation in eukaryotic cells. *Nat Methods*, 11(3):319–24, 2014. ISSN 1548-7105 (Electronic) 1548-7091 (Linking). doi: 10.1038/nmeth.2834. URL https://www.ncbi.nlm.nih.gov/pubmed/24487582.

R. Li and A. W. Murray. Feedback control of mitosis in budding yeast. *Cell*, 66(3):519–31, 1991. ISSN 0092-8674 (Print) 0092-8674 (Linking). URL https://www.ncbi.nlm.nih.gov/pubmed/1651172.

H. Liang, H. H. Lim, A. Venkitaraman, and U. Surana. Cdk1 promotes kinetochore bi-orientation and regulates Cdc20 expression during recovery from spindle checkpoint arrest. *EMBO J*, 31(2):403–16, 2012. ISSN 1460-2075 (Electronic) 0261-4189 (Linking). doi: 10.1038/emboj.2011.385. URL https://www.ncbi.nlm.nih.gov/pubmed/22056777.

H. H. Lim, P. Y. Goh, and U. Surana. Cdc20 is essential for the cyclosome-mediated proteolysis of both Pds1 and Clb2 during M phase in budding yeast. *Curr Biol*, 8(4):231–4, 1998. ISSN 0960-9822 (Print) 0960-9822 (Linking). URL https://www.ncbi.nlm.nih.gov/pubmed/9501986.

N. London and S. Biggins. Signalling dynamics in the spindle checkpoint response. *Nat Rev Mol Cell Biol*, 15(11):736–47, 2014a. ISSN 1471-0080 (Electronic) 1471-0072 (Linking). doi: 10.1038/nrm3888. URL http://www.ncbi.nlm.nih.gov/pubmed/25303117.

N. London and S. Biggins. Mad1 kinetochore recruitment by Mps1-mediated phosphorylation of Bub1 signals the spindle checkpoint. *Genes Dev*, 2014b. ISSN 1549-5477 (Electronic) 0890-9369 (Linking). doi: gad.233700.113[pii]10.1101/gad.233700.113. URL http://www.ncbi.nlm.nih.gov/pubmed/24402315.

N. London, S. Ceto, J. A. Ranish, and S. Biggins. Phosphoregulation of Spc105 by Mps1 and PP1 regulates Bub1 localization to kinetochores. *Curr Biol*, 22(10):900–6, 2012. ISSN 1879-0445 (Elec-

tronic) 0960-9822 (Linking). doi: 10.1016/j.cub.2012.03.052. URL http://www.ncbi.nlm.nih.gov/pubmed/22521787.

M. S. Longtine, 3rd McKenzie, A., D. J. Demarini, N. G. Shah, A. Wach, A. Brachat, P. Philippsen, and J. R. Pringle. Additional modules for versatile and economical PCR-based gene deletion and modification in Saccharomyces cerevisiae. *Yeast*, 14(10):953–61, 1998. ISSN 0749-503X (Print) 0749-503X (Linking). doi: 10.1002/(SICI)1097-0061(199807)14:10<953::AID-YEA293>3.0.CO;2-U. URL https://www.ncbi.nlm.nih.gov/pubmed/9717241.

D. Lu, J. Y. Hsiao, N. E. Davey, V. A. Van Voorhis, S. A. Foster, C. Tang, and D. O. Morgan. Multiple mechanisms determine the order of APC/C substrate degradation in mitosis. *J Cell Biol*, 207(1):23–39, 2014. ISSN 1540-8140 (Electronic) 0021-9525 (Linking). doi: 10.1083/jcb.201402041. URL https://www.ncbi.nlm.nih.gov/pubmed/25287299.

X. Luo and H. Yu. Protein metamorphosis: the two-state behavior of Mad2. *Structure*, 16(11): 1616–25, 2008. ISSN 0969-2126 (Print) 0969-2126 (Linking). doi: 10.1016/j.str.2008.10.002. URL https://www.ncbi.nlm.nih.gov/pubmed/19000814.

T. R. Maarleveld, B. G. Olivier, and F. J. Bruggeman. StochPy: a comprehensive, user-friendly tool for simulating stochastic biological processes. *PLoS One*, 8(11):e79345, 2013. ISSN 1932-6203 (Electronic) 1932-6203 (Linking). doi: 10.1371/journal.pone.0079345. URL https://www.ncbi.nlm.nih.gov/pubmed/24260203.

R. Macháň, P. Kapusta, and M. Hof. Statistical filtering in fluorescence microscopy and fluorescence correlation spectroscopy. *Anal Bioanal Chem*, 406(20):4797–813, 2014. ISSN 1618-2650 (Electronic) 1618-2642 (Linking). doi: 10.1007/s00216-014-7892-7. URL https://www.ncbi.nlm.nih.gov/pubmed/24908406.

C. I. Maeder, M. A. Hink, A. Kinkhabwala, R. Mayr, P. I. Bastiaens, and M. Knop. Spatial regulation of Fus3 MAP kinase activity through a reaction-diffusion mechanism in yeast pheromone signalling. *Nat Cell Biol*, 9(11):1319–26, 2007. ISSN 1465-7392 (Print) 1465-7392 (Linking). doi: 10.1038/ncb1652. URL http://www.ncbi.nlm.nih.gov/pubmed/17952059.

M. Maldonado and T. M. Kapoor. Constitutive Mad1 targeting to kinetochores uncouples checkpoint signalling from chromosome biorientation. *Nature cell biology*, 13(4):475–82, 2011. ISSN 1476-4679 (Electronic) 1465-7392 (Linking). doi: 10.1038/ncb2223ncb2223[pii]. URL http://www.ncbi.nlm.nih.gov/pubmed/21394085.

J. Mansfeld, P. Collin, M. O. Collins, J. S. Choudhary, and J. Pines. APC15 drives the turnover of MCC-CDC20 to make the spindle assembly checkpoint responsive to kinetochore attachment. *Nat Cell Biol*, 13(10):1234–43, 2011. ISSN 1476-4679 (Electronic) 1465-7392 (Linking). doi: 10.1038/ncb2347. URL https://www.ncbi.nlm.nih.gov/pubmed/21926987.

M. Mapelli, L. Massimiliano, S. Santaguida, and A. Musacchio. The Mad2 conformational dimer: structure and implications for the spindle assembly checkpoint. *Cell*, 131(4):730–43, 2007. ISSN 0092-8674 (Print) 0092-8674 (Linking). doi: 10.1016/j.cell.2007.08.049. URL https://www.ncbi.nlm.nih.gov/pubmed/18022367.

L. Mariani, E. Chiroli, L. Nezi, H. Muller, S. Piatti, A. Musacchio, and A. Ciliberto. Role of the Mad2 dimerization interface in the spindle assembly checkpoint independent of kinetochores. *Curr Biol*, 22(20):1900–8, 2012. ISSN 1879-0445 (Electronic) 0960-9822 (Linking). doi: 10.1016/j.cub.2012.08.028. URL http://www.ncbi.nlm.nih.gov/pubmed/23000150.

D. Marr and E. Hildreth. Theory of edge detection. *Proc R Soc Lond B Biol Sci*, 207(1167):187–217, 1980. ISSN 0950-1193 (Print) 0950-1193 (Linking). URL https://www.ncbi.nlm.nih.gov/pubmed/6102765.

P. G. Melloy and S. L. Holloway. Changes in the localization of the Saccharomyces cerevisiae anaphase-promoting complex upon microtubule depolymerization and spindle checkpoint activation. *Genetics*, 167(3):1079–94, 2004. ISSN 0016-6731 (Print) 0016-6731 (Linking). doi: 10.1534/genetics.103.025478. URL http://www.ncbi.nlm.nih.gov/pubmed/15280225.

C. Michaelis, R. Ciosk, and K. Nasmyth. Cohesins: chromosomal proteins that prevent premature separation of sister chromatids. *Cell*, 91(1):35–45, 1997. ISSN 0092-8674 (Print) 0092-8674 (Linking). URL http://www.ncbi.nlm.nih.gov/pubmed/9335333.

D. O. Morgan. *The cell cycle: principles of control*. Primers in biology. New Science Press ; Sinauer Associates, London Sunderland, MA, 2007. ISBN 9780199206100 (pbk. Oxford University Press) 0199206104 (pbk. Oxford University Press) 9780953918126 (pbk. New Science Press) 0953918122 (pbk. New Science Press) 9780878935086 (pbk. Sinauer Associates) 0878935088 (pbk. Sinauer Associates).

C. Myers, R. Gutenkunst, and J. Sethna. Python unleashed on systems biology. *Computing in Science and Engineering*, 9(3):34–37, 5 2007. ISSN 1521-9615. doi: 10.1109/MCSE.2007.60.

W. Nijenhuis, E. von Castelmur, D. Littler, V. De Marco, E. Tromer, M. Vleugel, M. H. van Osch, B. Snel, A. Perrakis, and G. J. Kops. A TPR domain-containing N-terminal module of MPS1 is required for its kinetochore localization by Aurora B. *J Cell Biol*, 201(2):217–31, 2013. ISSN 1540-8140 (Electronic) 0021-9525 (Linking). doi: 10.1083/jcb.201210033. URL https://www.ncbi.nlm.nih.gov/pubmed/23569217.

J. Nilsson, M. Yekezare, J. Minshull, and J. Pines. The APC/C maintains the spindle assembly checkpoint by targeting Cdc20 for destruction. *Nat Cell Biol*, 10(12):1411–20, 2008. ISSN 1476-4679 (Electronic) 1465-7392 (Linking). doi: 10.1038/ncb1799ncb1799[pii]. URL http://www.ncbi.nlm.nih.gov/pubmed/18997788.

G. Nishimura and M. Kinjo. Dead-time distortion in fluorescence correlation measurements. *Appl Opt*, 44(17):3458–67, 2005. ISSN 0003-6935 (Print) 0003-6935 (Linking). URL https://www.ncbi.nlm.nih.gov/pubmed/16007843.

A. G. Nobile, L. M. Ricciardi, and L Sacerdote. Exponential trends of Ornstein-Uhlenbeck first-passage-time densities. *Journal of Applied Probability*, 22(2):360–369, 1985. doi: 10.2307/3213779.

L Ornstein and G. E. Uhlenbeck. On the theory of brownian motion. *Physical review*, 36:823–841, 1930. doi: 10.1103/PhysRev.36.823.

W. J. Palframan, J. B. Meehl, S. L. Jaspersen, M. Winey, and A. W. Murray. Anaphase inactivation of the spindle checkpoint. *Science*, 313(5787):680–4, 2006. ISSN 1095-9203 (Electronic) 0036-8075 (Linking). doi: 10.1126/science.1127205. URL https://www.ncbi.nlm.nih.gov/pubmed/16825537.

J. Pan and R. H. Chen. Spindle checkpoint regulates Cdc20p stability in Saccharomyces cerevisiae. *Genes & development*, 18(12):1439–51, 2004. ISSN 0890-9369 (Print) 0890-9369 (Linking). doi: 10.1101/gad.118420418/12/1439[pii]. URL http://www.ncbi.nlm.nih.gov/pubmed/15198982.

N. Pavelka and G. Rancati. Never in neutral: a systems biology and evolutionary perspective on how aneuploidy contributes to human diseases. *Cytogenet Genome Res*, 139(3):193–205, 2013. ISSN 1424-859X (Electronic) 1424-8581 (Linking). doi: 10.1159/000348303. URL http://www.ncbi.nlm.nih.gov/pubmed/23446188.

I. Primorac and A. Musacchio. Panta rhei: the APC/C at steady state. *J Cell Biol*, 201(2):177–89, 2013. ISSN 1540-8140 (Electronic) 0021-9525 (Linking). doi: 10.1083/jcb.201301130. URL http://www.ncbi.nlm.nih.gov/pubmed/23589490.

I. Primorac, J. R. Weir, E. Chiroli, F. Groß, I. Hoffmann, S. van Gerwen, A. Ciliberto, and A. Musacchio. Bub3 reads phosphorylated MELT repeats to promote spindle assembly checkpoint signaling. *Elife*, 2:e01030, 2013. ISSN 2050-084X (Electronic). doi: 10.7554/eLife.01030. URL http://www.ncbi.nlm.nih.gov/pubmed/24066227.

S. Prinz, E. S. Hwang, R. Visintin, and A. Amon. The regulation of Cdc20 proteolysis reveals a role for APC components Cdc23 and Cdc27 during S phase and early mitosis. *Curr Biol*, 8(13):750–60, 1998. ISSN 0960-9822 (Print) 0960-9822 (Linking). URL http://www.ncbi.nlm.nih.gov/pubmed/9651679.

E. Queralt, C. Lehane, B. Novák, and F. Uhlmann. Downregulation of PP2A(Cdc55) phosphatase by separase initiates mitotic exit in budding yeast. *Cell*, 125(4):719–32, 2006. ISSN 0092-8674 (Print) 0092-8674 (Linking). doi: 10.1016/j.cell.2006.03.038. URL https://www.ncbi.nlm.nih.gov/pubmed/16713564.

J. M. Raser and E. K. O'Shea. Noise in gene expression: origins, consequences, and control. *Science*, 309(5743):2010–3, 2005. ISSN 1095-9203 (Electronic) 0036-8075 (Linking). doi: 10.1126/science.1105891. URL https://www.ncbi.nlm.nih.gov/pubmed/16179466.

A. Rattani, P. K. Vinod, J. Godwin, K. Tachibana-Konwalski, M. Wolna, M. Malumbres, B. Novák, and K. Nasmyth. Dependency of the spindle assembly checkpoint on Cdk1 renders the anaphase transition irreversible. *Curr Biol*, 24(6):630–7, 2014. ISSN 1879-0445 (Electronic) 0960-9822 (Linking). doi: 10.1016/j.cub.2014.01.033. URL https://www.ncbi.nlm.nih.gov/pubmed/24583015.

S Redner. *A guide to first-passage processes*. Cambridge University Press, Cambridge ; New York, 2001. ISBN 0521652480.

C. L. Rieder, R. W. Cole, A. Khodjakov, and G. Sluder. The checkpoint delaying anaphase in response to chromosome monoorientation is mediated by an inhibitory signal produced by unattached kinetochores. *J Cell Biol*, 130(4):941–8, 1995. ISSN 0021-9525 (Print) 0021-9525 (Linking). URL https://www.ncbi.nlm.nih.gov/pubmed/7642709.

J. Ries, Z. Petrasek, A. Garcia-Suez, and P. Schwille. A comprehensive framework for fluorescence cross-correlation spectroscopy. *New Journal of Physics*, 2010.

R. Rigler and E. Elson. *Fluorescence correlation spectroscopy: theory and applications*. Springer series in chemical physics,. Springer, Berlin ; New York, 2001. ISBN 9783642640186 3540674330 (hc. alk. paper) 0172-6218 ;. URL SpringerLinkhttp://dx.doi.org/10.1007/978-3-642-59542-4MITAccessOnly.

J. A. Robbins and F. R. Cross. Regulated degradation of the APC coactivator Cdc20. *Cell Div*, 5:23, 2010. ISSN 1747-1028 (Electronic) 1747-1028 (Linking). doi: 10.1186/1747-1028-5-23. URL http://www.ncbi.nlm.nih.gov/pubmed/20831816.

V. Rossio, E. Galati, M. Ferrari, A. Pellicioli, T. Sutani, K. Shirahige, G. Lucchini, and S. Piatti. The RSC chromatin-remodeling complex influences mitotic exit and adaptation to the spindle assembly checkpoint by controlling the Cdc14 phosphatase. *The Journal of cell biology*, 191(5):981–97, 2010. URL <GotoISI>://MEDLINE:21098112.

RStudio Team. *RStudio: Integrated Development Environment for R*. RStudio, Inc., Boston, MA, 2015. URL http://www.rstudio.com/.

A. D. Rudner and A. W. Murray. Phosphorylation by Cdc28 activates the Cdc20-dependent activity of the anaphase-promoting complex. *J Cell Biol*, 149(7):1377–90, 2000. ISSN 0021-9525 (Print) 0021-9525 (Linking). URL http://www.ncbi.nlm.nih.gov/pubmed/10871279.

S. Santaguida and A. Musacchio. The life and miracles of kinetochores. *EMBO J*, 28(17):2511–31, 2009. ISSN 1460-2075 (Electronic) 0261-4189 (Linking). doi: 10.1038/emboj.2009.173. URL http://www.ncbi.nlm.nih.gov/pubmed/19629042.

S. Santaguida, C. Vernieri, F. Villa, A. Ciliberto, and A. Musacchio. Evidence that Aurora B is implicated in spindle checkpoint signalling independently of error correction. *EMBO J*, 30(8):1508–19, 2011. ISSN 1460-2075 (Electronic) 0261-4189 (Linking). doi: 10.1038/emboj.2011.70. URL https://www.ncbi.nlm.nih.gov/pubmed/21407176.

J. Schindelin, I. Arganda-Carreras, E. Frise, V. Kaynig, M. Longair, T. Pietzsch, S. Preibisch, C. Rueden, S. Saalfeld, B. Schmid, J. Y. Tinevez, D. J. White, V. Hartenstein, K. Eliceiri, P. Tomancak, and A. Cardona. Fiji: an open-source platform for biological-image analysis. *Nat Methods*, 9(7):676–82, 2012. ISSN 1548-7105 (Electronic) 1548-7091 (Linking). doi: 10.1038/nmeth.2019. URL https://www.ncbi.nlm.nih.gov/pubmed/22743772.

C. A. Schneider, W. S. Rasband, and K. W. Eliceiri. NIH Image to ImageJ: 25 years of image analysis. *Nat Methods*, 9(7):671–5, 2012. ISSN 1548-7105 (Electronic) 1548-7091 (Linking). URL https://www.ncbi.nlm.nih.gov/pubmed/22930834.

P. Schwille and E. Hausten. *Fluorescence Correlation Spectroscopy: An Introduction to its Concepts and Applications*. Biophysics Book Online, 2002. URL http://www.biophysics.org/portals/1/pdfs/education/schwille.pdf.

K. Sewart and S. Hauf. Different functionality of Cdc20 binding sites within the mitotic checkpoint complex. *Curr Biol*, 27(8):1213–1220, 2017. ISSN 1879-0445 (Electronic) 0960-9822 (Linking). doi: 10.1016/j.cub.2017.03.007. URL https://www.ncbi.nlm.nih.gov/pubmed/28366743.

L. A. Shepperd, J. C. Meadows, A. M. Sochaj, T. C. Lancaster, J. Zou, G. J. Buttrick, J. Rappsilber, K. G. Hardwick, and J. B. Millar. Phosphodependent recruitment of Bub1 and Bub3 to Spc7/KNL1 by Mph1 kinase maintains the spindle checkpoint. *Curr Biol*, 22(10):891–9, 2012. ISSN 1879-0445 (Electronic) 0960-9822 (Linking). doi: 10.1016/j.cub.2012.03.051. URL https://www.ncbi.nlm.nih.gov/pubmed/22521786.

M. Shirayama, W. Zachariae, R. Ciosk, and K. Nasmyth. The Polo-like kinase Cdc5p and the WD-repeat protein Cdc20p/fizzy are regulators and substrates of the anaphase promoting complex in Saccharomyces cerevisiae. *EMBO J*, 17(5):1336–49, 1998. ISSN 0261-4189 (Print) 0261-4189 (Linking). doi: 10.1093/emboj/17.5.1336. URL http://www.ncbi.nlm.nih.gov/pubmed/9482731.

M. Simonetta, R. Manzoni, R. Mosca, M. Mapelli, L. Massimiliano, M. Vink, B. Novák, A. Musacchio, and A. Ciliberto. The influence of catalysis on Mad2 activation dynamics. *PLoS Biol*, 7(1):e10, 2009. ISSN 1545-7885 (Electronic) 1544-9173 (Linking). doi: 10.1371/journal.pbio.1000010. URL http://www.ncbi.nlm.nih.gov/pubmed/19143472.

J. M. Skotheim, S. Di Talia, E. D. Siggia, and F. R. Cross. Positive feedback of g1 cyclins ensures coherent cell cycle entry. *Nature*, 454(7202):291–6, 2008. ISSN 1476-4687 (Electronic) 0028-

0836 (Linking). doi: 10.1038/nature07118nature07118[pii]. URL http://www.ncbi.nlm.nih.gov/pubmed/18633409.

B. D. Slaughter and R. Li. Toward quantitative "in vivo biochemistry" with fluorescence fluctuation spectroscopy. *Mol Biol Cell*, 21(24):4306–11, 2010. ISSN 1939-4586 (Electronic) 1059-1524 (Linking). doi: 10.1091/mbc.E10-05-0451. URL https://www.ncbi.nlm.nih.gov/pubmed/21160072.

V. Sudakin, G. K. Chan, and T. J. Yen. Checkpoint inhibition of the APC/C in HeLa cells is mediated by a complex of BUBR1, BUB3, CDC20, and MAD2. *J Cell Biol*, 154(5):925–36, 2001. ISSN 0021-9525 (Print) 0021-9525 (Linking). doi: 10.1083/jcb.200102093. URL https://www.ncbi.nlm.nih.gov/pubmed/11535616.

M. Sullivan and D. O. Morgan. Finishing mitosis, one step at a time. *Nat Rev Mol Cell Biol*, 8(11): 894–903, 2007. ISSN 1471-0080 (Electronic) 1471-0072 (Linking). doi: 10.1038/nrm2276. URL https://www.ncbi.nlm.nih.gov/pubmed/17912263.

U. Surana, H. Robitsch, C. Price, T. Schuster, I. Fitch, A. B. Futcher, and K. Nasmyth. The role of CDC28 and cyclins during mitosis in the budding yeast S. cerevisiae. *Cell*, 65(1):145–61, 1991. ISSN 0092-8674 (Print) 0092-8674 (Linking). URL https://www.ncbi.nlm.nih.gov/pubmed/1849457.

T. U. Tanaka, N. Rachidi, C. Janke, G. Pereira, M. Galova, E. Schiebel, M. J. Stark, and K. Nasmyth. Evidence that the Ipl1-Sli15 (Aurora kinase-INCENP) complex promotes chromosome bi-orientation by altering kinetochore-spindle pole connections. *Cell*, 108(3):317–29, 2002. ISSN 0092-8674 (Print) 0092-8674 (Linking). URL http://www.ncbi.nlm.nih.gov/pubmed/11853667.

T. U. Tanaka, M. J. Stark, and K. Tanaka. Kinetochore capture and bi-orientation on the mitotic spindle. *Nat Rev Mol Cell Biol*, 6(12):929–42, 2005. ISSN 1471-0072 (Print) 1471-0072 (Linking). doi: 10.1038/nrm1764. URL https://www.ncbi.nlm.nih.gov/pubmed/16341079.

Y. C. Tang and A. Amon. Gene copy-number alterations: a cost-benefit analysis. *Cell*, 152(3):394–405, 2013. ISSN 1097-4172 (Electronic) 0092-8674 (Linking). doi: 10.1016/j.cell.2012.11.043. URL https://www.ncbi.nlm.nih.gov/pubmed/23374337.

R. E. Taylor-Mayer, V. W. Mayer, and C. J. Goin. Effect of treatment medium on induction of aneuploidy by nocodazole in Saccharomyces cerevisiae. *Environ Mol Mutagen*, 11(3):323–31, 1988. ISSN 0893-6692 (Print) 0893-6692 (Linking). URL http://www.ncbi.nlm.nih.gov/pubmed/3281826.

P. Therizols, T. Duong, B. Dujon, C. Zimmer, and E. Fabre. Chromosome arm length and nuclear constraints determine the dynamic relationship of yeast subtelomeres. *Proc Natl Acad Sci U S A*, 107 (5):2025–30, 2010. ISSN 1091-6490 (Electronic) 0027-8424 (Linking). doi: 10.1073/pnas.0914187107. URL https://www.ncbi.nlm.nih.gov/pubmed/20080699.

A. Tighe, V. L. Johnson, M. Albertella, and S. S. Taylor. Aneuploid colon cancer cells have a robust spindle checkpoint. *EMBO Rep*, 2(7):609–14, 2001. ISSN 1469-221X (Print) 1469-221X (Linking). doi: 10.1093/embo-reports/kve127. URL https://www.ncbi.nlm.nih.gov/pubmed/11454737.

K. Uzunova, B. T. Dye, H. Schutz, R. Ladurner, G. Petzold, Y. Toyoda, M. A. Jarvis, N. G. Brown, I. Poser, M. Novatchkova, K. Mechtler, A. A. Hyman, H. Stark, B. A. Schulman, and J. M. Peters. APC15 mediates CDC20 autoubiquitylation by APC/C(MCC) and disassembly of the mitotic checkpoint complex. *Nat Struct Mol Biol*, 19(11):1116–23, 2012. ISSN 1545-9985 (Electronic) 1545-9985 (Linking). doi: 10.1038/nsmb.2412. URL http://www.ncbi.nlm.nih.gov/pubmed/23007861.

M. D. Vazquez-Novelle, L. Sansregret, A. E. Dick, C. A. Smith, A. D. McAinsh, D. W. Gerlich, and M. Petronczki. Cdk1 inactivation terminates mitotic checkpoint surveillance and stabilizes kinetochore attachments in anaphase. *Curr Biol*, 24(6):638–45, 2014. ISSN 1879-0445 (Electronic) 0960-9822 (Linking). doi: 10.1016/j.cub.2014.01.034. URL https://www.ncbi.nlm.nih.gov/pubmed/24583019.

C. Vernieri, E. Chiroli, V. Francia, F. Groß, and A. Ciliberto. Adaptation to the spindle checkpoint is regulated by the interplay between Cdc28/Clbs and PP2ACdc55. *The Journal of cell biology*, 202 (5):765–78, 2013. ISSN 1540-8140 (Electronic) 0021-9525 (Linking). doi: 10.1083/jcb.201303033jcb.201303033[pii]. URL http://www.ncbi.nlm.nih.gov/pubmed/23999167.

J. M. Vilar, C. C. Guet, and S. Leibler. Modeling network dynamics: the lac operon, a case study. *J Cell Biol*, 161(3):471–6, 2003. ISSN 0021-9525 (Print) 0021-9525 (Linking). doi: 10.1083/jcb.200301125. URL https://www.ncbi.nlm.nih.gov/pubmed/12743100.

R. Visintin, K. Craig, E. S. Hwang, S. Prinz, M. Tyers, and A. Amon. The phosphatase Cdc14 triggers mitotic exit by reversal of Cdk-dependent phosphorylation. *Molecular cell*, 2(6):709–18, 1998. ISSN 1097-2765. URL <GotoISI>://MEDLINE:9885559.

R. Visintin, E. S. Hwang, and A. Amon. Cfi1 prevents premature exit from mitosis by anchoring Cdc14 phosphatase in the nucleolus. *Nature*, 398(6730):818–23, 1999. ISSN 0028-0836. URL <GotoISI>://MEDLINE:10235265.

J. Šteflova, M. Štefl, S. Walz, M. Knop, and O. Trapp. Comprehensive study on critical micellar concentrations of SDS in acetonitrile-water solvents. *Electrophoresis*, 37(10):1287–95, 2016. ISSN 1522-2683 (Electronic) 0173-0835 (Linking). doi: 10.1002/elps.201500553. URL https://www.ncbi.nlm.nih.gov/pubmed/26842727.

M. Wachsmuth, C. Conrad, J. Bulkescher, B. Koch, R. Mahen, M. Isokane, R. Pepperkok, and J. Ellenberg. High-throughput fluorescence correlation spectroscopy enables analysis of proteome dynamics in living cells. *Nat Biotechnol*, 33(4):384–9, 2015. ISSN 1546-1696 (Electronic) 1087-0156 (Linking). doi: 10.1038/nbt.3146. URL http://www.ncbi.nlm.nih.gov/pubmed/25774713.

C. D. Warren, D. M. Brady, R. C. Johnston, J. S. Hanna, K. G. Hardwick, and F. A. Spencer. Distinct chromosome segregation roles for spindle checkpoint proteins. *Mol Biol Cell*, 13(9):3029–41, 2002. ISSN 1059-1524 (Print) 1059-1524 (Linking). doi: 10.1091/mbc.E02-04-0203. URL https://www.ncbi.nlm.nih.gov/pubmed/12221113.

R. Wäsch and F. R. Cross. APC-dependent proteolysis of the mitotic cyclin Clb2 is essential for mitotic exit. *Nature*, 418(6897):556–62, 2002. ISSN 0028-0836 (Print) 0028-0836 (Linking). doi: 10.1038/nature00856. URL https://www.ncbi.nlm.nih.gov/pubmed/12152084.

F. M. Yeong, H. H. Lim, C. G. Padmashree, and U. Surana. Exit from mitosis in budding yeast: biphasic inactivation of the Cdc28-Clb2 mitotic kinase and the role of Cdc20. *Mol Cell*, 5(3):501–11, 2000. ISSN 1097-2765 (Print) 1097-2765 (Linking). URL https://www.ncbi.nlm.nih.gov/pubmed/10882135.

W. Zachariae, M. Schwab, K. Nasmyth, and W. Seufert. Control of cyclin ubiquitination by CDK-regulated binding of Hct1 to the anaphase promoting complex. *Science*, 282(5394):1721–4, 1998. ISSN 0036-8075 (Print) 0036-8075 (Linking). URL https://www.ncbi.nlm.nih.gov/pubmed/9831566.

Z. Zhang, S. M. Roe, M. Diogon, E. Kong, H. El Alaoui, and D. Barford. Molecular structure of the N-terminal domain of the APC/C subunit Cdc27 reveals a homo-dimeric tetratricopeptide repeat architecture. *J Mol Biol*, 397(5):1316–28, 2010. ISSN 1089-8638 (Electronic) 0022-2836 (Linking). doi: 10.1016/j.jmb.2010.02.045. URL https://www.ncbi.nlm.nih.gov/pubmed/20206185.

Acknowledgements

In chronological order, I'd like to thank the supervisors of my MSc thesis, Simone Paleari, Andrea Gamba and Tiziano Penati. I got to molecular biology, and to the application of mathematics to molecular biology, thanks to the work done with them.
Then, I want to thank Pamela Minicozzi, from Istituto Nazionale dei Tumori in Milano, that taught me the importance of every step of data analysis, including data acquisition!, and how rich good databases can be.
Finally, I'm deeply grateful to Andrea Ciliberto, for the trust and the supervision, in the highest meaning, he gave me in these years. He led me from applied mathematics to this work, which is a long way, believe me!, wisely balancing freedom and mentoring, trust and suggestions, listening and speaking. Thanks a lot.

If I am asked to, I'd say that all the wet-lab biology I know, has been taught me by Elena Chiroli. One of my first day in the lab I asked her: "Wait, five-prime, three-prime...what does it mean?", and she patiently explained me DNA structure, how PCR works, how western blots work...and the list is long. Many thanks.
Martin Štefl, at Michael Knop's lab at ZMBH in Heidelberg, introduced me to spectroscopy techniques, and I am grateful to both of them for the opportunity they gave me. I also want to thank the members of Knop's lab that helped me during the months I spent in Heidelberg: Daniel Kirrmaier, Matthias Meurer and Cyril Mongis.
I would also like to thank the people that contributed to this work: Fridolin Groß, Elena Chiroli and Andrea Ciliberto, mentioned in several figures, but also Mattia Pavani, Federica Natali and Marco Cosentino Lagomarsino, who physically and scientifically helped me in some steps of this work. I want to thank all the present and former members of Ciliberto's lab, for all the helpful discussions and the amazing lab life: Andrea, Elena, Fridolin, Mattia and Federica, already mentioned, but also Andrea Corno, Tiziana Lischetti, Claudio Vernieri, Valentina Francia and Emanuele Martini. Thanks for these years together.

Last, I want to thank my friends and my family, that supported my life in these years. A special thanks is for Chiara, who has always been close to me, and Irene, born between figure 1 and 5.